



STOCHASTIC MODELING AND SIMULATION OF THE COUPLED
AXIAL-TORSIONAL VIBRATION OF A DRILL-STRING

Daniel de Moraes Lobo

Dissertação de Mestrado apresentada ao Programa de Pós-graduação em Engenharia Mecânica, COPPE, da Universidade Federal do Rio de Janeiro, como parte dos requisitos necessários à obtenção do título de Mestre em Engenharia Mecânica.

Orientadores: Thiago Gamboa Ritto
Daniel Alves Castello

Rio de Janeiro
Março de 2019

STOCHASTIC MODELING AND SIMULATION OF THE COUPLED
AXIAL-TORSIONAL VIBRATION OF A DRILL-STRING

Daniel de Moraes Lobo

DISSERTAÇÃO SUBMETIDA AO CORPO DOCENTE DO INSTITUTO
ALBERTO LUIZ COIMBRA DE PÓS-GRADUAÇÃO E PESQUISA DE
ENGENHARIA (COPPE) DA UNIVERSIDADE FEDERAL DO RIO DE
JANEIRO COMO PARTE DOS REQUISITOS NECESSÁRIOS PARA A
OBTENÇÃO DO GRAU DE MESTRE EM CIÊNCIAS EM ENGENHARIA
MECÂNICA.

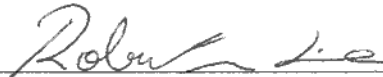
Examinada por:



Prof. Thiago Gamboa Ritto, D.Sc.



Prof. Daniel Alves Castello, D.Sc.



Prof. Roberta de Queiroz Lima, D.Sc.



Prof. Marcelo Areias Trindade, D.Sc.

RIO DE JANEIRO, RJ – BRASIL
MARÇO DE 2019

Lobo, Daniel de Moraes

Stochastic modeling and simulation of the coupled axial-torsional vibration of a drill-string/Daniel de Moraes Lobo.

– Rio de Janeiro: UFRJ/COPPE, 2019.

XVII, 166 p.: il.; 29, 7cm.

Orientadores: Thiago Gamboa Ritto

Daniel Alves Castello

Dissertação (mestrado) – UFRJ/COPPE/Programa de Engenharia Mecânica, 2019.

Bibliografia: p. 104 – 114.

1. Drill-string. 2. Bit-Rock Interaction. 3. Axial-Torsional vibration. 4. Stochastic. I. Ritto, Thiago Gamboa *et al.* II. Universidade Federal do Rio de Janeiro, COPPE, Programa de Engenharia Mecânica. III. Título.

*“So the problem is not so much
to see what nobody has yet seen,
as to think what nobody has yet
thought concerning that which
everybody sees.”
(Arthur Schopenhauer)*

Acknowledgements

At first, I would like to thank my family. To my wife for all the love, affection and comprehension during this journey. To my parents for the love, unceasing encouragement and all the investment made in my education since childhood. Thank you for always believing on me, for comforting me in difficult times and celebrating my achievements.

Besides my family, I wish to express my sincere thanks to my advisors Prof. Thiago Ritto and Prof. Daniel Castello, for their continuous support of my M.Sc. study and related research, for their patience, motivation, and immense knowledge. Their guidance helped me in all the time of research and writing of this dissertation. I would also like to express my gratitude to Prof. Thiago Ritto for providing me an opportunity to join his team as a researcher, which gave me the support I needed to develop this work.

I am also very grateful to Prof. Edson Cataldo from Universidade Federal Fluminense for sharing his expertise with me. Our discussions about some topics of this work served as a valuable guidance for me.

I thank my fellow labmates for the stimulating discussions, for the encouragement and for all the fun we have had in the last two years. I would also like to express my gratitude to everyone from the Department of Mechanical Engineering for their help and support.

To my father, in memory... Thank you so much! It is all because of you.

Resumo da Dissertação apresentada à COPPE/UFRJ como parte dos requisitos necessários para a obtenção do grau de Mestre em Ciências (M.Sc.)

MODELAGEM E SIMULAÇÃO ESTOCÁSTICA DA VIBRAÇÃO ACOPLADA AXIAL-TORCIONAL DE UMA COLUNA DE PERFURAÇÃO

Daniel de Moraes Lobo

Março/2019

Orientadores: Thiago Gamboa Ritto
Daniel Alves Castello

Programa: Engenharia Mecânica

Esta dissertação investiga a vibração axial-torcional acoplada de uma coluna de perfuração na presença de incertezas litológicas. Este trabalho tem três objetivos principais: (i) realizar uma investigação numérica determinística através de um modelo acoplado axial-torsional contínuo, considerando as não-linearidades geométricas e a interação broca-rocha; (ii) propor um novo modelo estocástico para descrever incertezas na interação bit-rock usando as equações diferenciais estocásticas de Itô e; (iii) analisar a influência dos principais parâmetros na resposta estocástica comparando as estatísticas obtidas a partir dos resultados. O modelo contínuo é discretizado por meio do método dos elementos finitos, considerando as não-linearidades geométricas e um modelo de interação broca-rocha que é qualitativamente validado com resultados experimentais. Os resultados determinísticos mostraram que as não linearidades geométricas não afetaram a resposta e, portanto, são ignoradas nas análises subsequentes. O modelo é reduzido usando a base modal e os resultados são analisados. Em seguida, um modelo estocástico é construído para descrever a heterogeneidade litológica. Este modelo considera dois processos estocásticos: processo de Ornstein-Uhlenbeck e um novo processo acoplado. O novo processo é capaz de descrever melhor a física quando ocorre *stick-slip* severo. As estatísticas da resposta mostram que a heterogeneidade na formação rochosa induz vibrações mais severas na broca. Além disso, as diferenças entre os processos são pequenas quando a broca não trava, mas o novo processo resulta em vibrações mais severas quando há períodos de travamento da broca.

Abstract of Dissertation presented to COPPE/UFRJ as a partial fulfillment of the requirements for the degree of Master of Science (M.Sc.)

STOCHASTIC MODELING AND SIMULATION OF THE COUPLED
AXIAL-TORSIONAL VIBRATION OF A DRILL-STRING

Daniel de Moraes Lobo

March/2019

Advisors: Thiago Gamboa Ritto
Daniel Alves Castello

Department: Mechanical Engineering

This dissertation investigates the coupled axial-torsional vibration of drill-strings in the presence of lithology uncertainties. This work has three main objectives: (i) to perform a deterministic numerical investigation through a continuous axial-torsional coupled model, considering the geometric nonlinearities and the bit-rock interaction; (ii) to propose a novel stochastic model to describe uncertainties on bit-rock interaction by using Itô stochastic differential equations, and; (iii) to analyze the influence of the main parameters on stochastic response by comparing the statistics obtained from the results. The continuous model is discretized by means of the finite element method, considering the geometric nonlinearities and a bit-rock interaction model that is qualitatively validated with experimental results. The deterministic results showed that the geometric nonlinearities did not affect the response and, thus, are ignored in the subsequent analyses. The model is reduced using the modal basis and the results are analyzed. Then, a stochastic model is constructed to describe lithology heterogeneity. This model considers two stochastic processes: Ornstein-Uhlenbeck process and a novel coupled process. The novel process is capable of describing better the physics when severe stick-slip happens. The statistics of the response show that the heterogeneity on rock formation induces severer vibrations at the bit. Also, the differences between the processes are small when bit does not stick, but the novel process causes worse vibrations when bit sticks.

Contents

List of Figures	x
1 Introduction	1
1.1 Motivation	1
1.2 Dissertation objective and organization	2
1.3 Overview of a drilling rig	2
1.4 Drilling operation	4
1.5 Vibrations in drill-strings	5
1.5.1 Axial vibration	6
1.5.2 Torsional vibration	7
1.5.3 Lateral vibration	8
2 Literature review	11
2.1 Drill-string modeling and control	11
2.2 Bit-rock interaction model	16
2.3 Uncertainty quantification in drill-string vibration	27
2.4 Experimental investigation of drill-string vibration	29
3 Deterministic numerical investigation	34
3.1 Base model	34
3.2 Initial prestressed configuration	39
3.3 Bit-rock interaction model	40
3.4 Boundary conditions	42
3.5 Reduced-order model	42
3.6 Numerical Results	44
3.6.1 Evaluation of nonlinear stiffness influence	45
3.6.2 Modal analysis	49
3.6.3 Dynamical response	53
3.6.4 Parametric analysis	62

4	Stochastic numerical investigation	69
4.1	Stochastic model for bit-rock interaction	71
4.1.1	Ornstein–Uhlenbeck process	72
4.1.2	Coupled process	75
4.2	Stochastic system of equations	77
4.3	Stochastic numerical results	78
4.3.1	Stochastic process generation	79
4.3.2	Stochastic system response	85
4.3.3	Parametric analysis	97
5	Conclusions	102
	Bibliography	104
A	Bit-rock interaction model validation with experimental data	115
A.1	Experimental set-up	116
A.2	Mechanical model	118
A.3	Experimental results	119
A.4	Numerical results	122
B	An introduction to stochastic differential equations (SDE)	129
B.1	Brownian Motion	130
B.2	Stochastic Integrals	132
B.2.1	Riemann Sums	134
B.2.2	Itô integral	137
B.3	Stochastic Differential Equations	146
B.3.1	Solutions of SDE	147
B.3.2	Applications of SDE	157
C	Scalar linear stochastic differential equations	160
D	Numerical integration method	163
E	Program structure	164

List of Figures

1.1	A schematic view of a drilling rig. Reproduced from LEINE and VAN CAMPEN [2].	3
1.2	Drill-string vibration modes.	6
1.3	An example of optimum zone. [3]	6
1.4	BHA whirl. Red dot represents stationary point on pipe section to describe its rotation. Dashed circle represents the whirling motion. Adopted from [10].	9
2.1	Bit-rock interaction model proposed by LIN and WANG [5], where $f(\dot{\phi})$ actually represents $t_{bit}(\dot{\theta}_{bit})$	17
2.2	Experimental data for bit-rock interaction obtained by BRETT [19] .	18
2.3	Experimental data in E-S diagram presented by DETOURNAY and DEFOURNY [29]	19
2.4	Instantaneous torque at the bit presented by PAVONE and DES-PLANS [41]	19
2.5	Bit-rock interaction proposed by TUCKER and WANG [23]	20
2.6	Bit-rock interaction model proposed by TUCKER and WANG [26] . .	21
2.7	Bit-rock interaction proposed by NAVARRO-LÓPEZ <i>et al.</i> [8]	22
2.8	Relation between TOB and bit angular velocity obtained by GER-MAY <i>et al.</i> [35]	23
2.9	Bit-rock interaction law proposed by HONG <i>et al.</i> [40]	25
2.10	Bit-rock interaction law and stability map proposed by RITTO <i>et al.</i> [45]. The second figure represents the stability map: the colored gradient is stick-slip severity; y-axis is the WOB; and x-axis is the speed on surface. The red dot represents the unstable measured data and the black dot is stable one.	26
2.11	Hysteretic bit-rock interaction model and experimental data for one stick-slip cycle. Adopted from [46].	27
3.1	Schematic view of the system.	34
3.2	Displacement Field. Adapted from [52].	36

3.3	Element.	37
3.4	Bit-rock interaction model. $\mathcal{W}_{ob} = \bar{W}_{ob} = 100$ kN.	41
3.5	Convergence of the 20th natural frequency.	45
3.6	Results for model 1 with $\Omega = 95.5$ RPM and $\bar{W}_{ob} = 100$ kN. (a) Rotational speed at the bit; (b) Axial speed at the bit.	46
3.7	Results for model 2 with $\Omega = 95.5$ RPM and $\bar{W}_{ob} = 100$ kN. (a) Rotational speed at the bit; (b) Axial displacement at the bit.	47
3.8	Results for model 2 with $\Omega = 95.5$ RPM and $\bar{W}_{ob} = 100$ kN. (a) Rotational speed at the bit; (b) Axial displacement at the bit.	48
3.9	Deformation per element through the time. Each line correponds to one element. (a) Axial deformation; (b) Angular deformation. $\Omega =$ 95.5 RPM, $\bar{W}_{ob} = 100$ kN.	49
3.10	Comparison between complete and reduced-order models for the ro- tational speed at the bit. $\bar{W}_{ob} = 100$ kN, $\Omega = 95.5$ RPM.	50
3.11	Axial vibration modes. (a) 4th mode and (b) 6th mode.	51
3.12	Axial vibration modes. (a) 9th mode and (b) 11th mode.	51
3.13	Torsional vibration modes. (a) 2nd mode and (b) 3rd mode.	51
3.14	Torsional vibration modes. (a) 5th mode and (b) 7th mode.	52
3.15	Torsional vibration modes. (a) 8th mode and (b) 10th mode.	52
3.16	Torsional vibration modes. 12th mode.	52
3.17	Vibration modes. (a) 33th mode (torsional - 12.75Hz) and (b) 29th mode (axial - 11.15Hz).	53
3.18	Axial deformation du/dx along drill-string length at each position x . (a) $\bar{W}_{ob} = 100$ kN; (b) $\bar{W}_{ob} = 65$ kN.	54
3.19	(a) Axial speed at the bit; (b) Rotational speed at the top and at the bit. $\bar{W}_{ob} = 65$ kN, $\Omega = 95.5$ RPM.	54
3.20	(a) Angular relative displacement of the bit with the top angular position as reference. (b) Torque-On-Bit (TOB). $\bar{W}_{ob} = 65$ kN, $\Omega =$ 95.5 RPM.	55
3.21	Fast Fourier Transform (fft) of (a) Bit rotational speed and (b) Bit axial speed. $\bar{W}_{ob} = 65$ kN, $\Omega = 95.5$ RPM.	55
3.22	(a) Axial speed at the bit; (b) Rotational speed at the top and at the bit. $\bar{W}_{ob} = 100$ kN, $\Omega = 95.5$ RPM.	56
3.23	Rotational speed at the bit and torque applied by top rotary system compared to the torque on bit due to bit-rock interaction.	57
3.24	(a) Axial displacement of the bit; (b) Torsional displacement at the top and the bit. $\bar{W}_{ob} = 100$ kN, $\Omega = 95.5$ RPM.	58
3.25	Angular relative displacement of the bit with the top angular position as reference. $\bar{W}_{ob} = 100$ kN, $\Omega = 95.5$ RPM.	58

3.26	Phase Portrait at the bit. $\bar{W}_{ob} = 100$ kN, $\Omega = 95.5$ RPM.	59
3.27	Phase Portrait along drill-string length. $\bar{W}_{ob} = 100$ kN, $\Omega = 95.5$ RPM.	59
3.28	Torque applied at the top by the top rotary system (rotary table or top drive). $\bar{W}_{ob} = 100$ kN, $\Omega = 95.5$ RPM.	60
3.29	Drill-string dynamics and interaction forces. From the top to the bottom, respectively: Rotational speed at the bit (Bit Speed); Depth-of-Cut (DOC); Torque on bit (t_{bit}) and; Axial force on bit (f_{bit}). $\bar{W}_{ob} = 100$ kN, $\Omega = 95.5$ RPM.	61
3.30	Bit-rock interaction. $\bar{W}_{ob} = 100$ kN, $\Omega = 95.5$ RPM.	62
3.31	Fast Fourier Transform (fft) of (a) Bit rotational speed and (b) Bit axial speed. $\bar{W}_{ob} = 100$ kN, $\Omega = 95.5$ RPM.	62
3.32	Stability map for stick-slip severity. (a) 2D; (b) 3D.	63
3.33	Stability map for stick-slip severity. $\alpha = 0.4$ and $\beta = 0.008$. (a) 2D; (b) 3D.	64
3.34	Rotational speed at the bit for $\Omega = 95.5$ RPM and $\bar{W}_{ob} = 110$ kN. (a) $\alpha = 0.1$ and $\beta = 0.00008$; (b) $\alpha = 0.4$ and $\beta = 0.008$	65
3.35	Parametric analysis of bit-rock interaction ($\mathcal{W} = \bar{W}_{ob} = 100$ kN). Varying (a) b1; (b) b2.	66
3.36	Parametric analysis of bit-rock interaction ($\mathcal{W} = \bar{W}_{ob} = 100$ kN). Varying (a) b3; (b) b4.	66
3.37	Parametric analysis of bit-rock interaction ($\mathcal{W} = \bar{W}_{ob} = 100$ kN). Varying b5.	66
3.38	Bit rotational speed for $\bar{W}_{ob} = 100$ kN and $\Omega = 95.5$ RPM. Varying (a) b3 and (b) b4.	67
3.39	Parametric analysis of bit-rock interaction ($\mathcal{W} = \bar{W}_{ob} = 100$ kN). Varying together (a) b1 and b5; (b) b2 and b4.	67
3.40	Parametric analysis of bit-rock interaction ($\mathcal{W} = \bar{W}_{ob} = 100$ kN). Varying together (a) b3 and b4; (b) b2, b3 and b4.	68
3.41	Bit rotational speed for $\bar{W}_{ob} = 100$ kN and $\Omega = 95.5$ RPM. Varying (a) b3 and (b) b4.	68
4.1	Rock Strength by the depth of well. (a) Adopted from [76]; (b) Adopted from [77].	70
4.2	Correlation between unconfined compressive strength q and specific energy ϵ . (a) Adopted from [29]; (b) Adopted from [78].	70
4.3	Measurements of intrinsic specific energy during a scratch test. (a) Adopted from [29]; (b) Adopted from [79].	71

4.4	Power Spectral Density of process $\mathbf{P}(t)$ for several values of b_1 and b_2 . (a) Without normalization; (b) With normalization. Case 1: $b_1 = 1.0$, $b_2 = 0.05$; Case 2: $b_1 = 0.5$, $b_2 = 0.0125$; Case 3: $b_1 = 0.5$, $b_2 = 0.05$; Case 4: $b_1 = 1.0$, $b_2 = 0.1$	73
4.5	Convergence of the second moment of $\mathbf{Y}(t)$: (a) over the number of simulations and step time size Δt , and; (b) over time step size Δt for 1000 simulations.	79
4.6	Convergence of the second moment of $\mathbf{A}_4(t) = a_{4m}(h_{OU} + \mathbf{Y}(t))^2$ over the number of simulations and step time size Δt	80
4.7	(a) Second moment of $\mathbf{Y}(t)$ over time; (b) One realization of stochas- tic process $\mathbf{Y}(t)$	80
4.8	(a) Probabilistic envelope of $\mathbf{A}_4(t) = a_{4m}(h_{OU} + \mathbf{Y}(t))^2$ for three times the standard variation σ_{A4} around mean μ_{A4} . (b) Five realizations of the process $\mathbf{A}_4(t) = a_{4m}(h_{OU} + \mathbf{Y}(t))^2$	81
4.9	Power Spectral Density of process $\mathbf{Y}(t)$ for simulated data and ana- lytical solution.	81
4.10	Normalized Power Spectral Density of process $\mathbf{A}_4(t) = a_{4m}(h_{OU} +$ $\mathbf{Y}(t))^2$ for simulated data and analytical solution.	82
4.11	Convergence of the second moment of $\mathbf{G}(t)$: (a) over the number of simulations and step time size Δt , and; (b) over time step size Δt for 1000 simulations.	83
4.12	Convergence of the second moment of $\mathbf{A}_4(t) = a_{4m}(h_{CP} + \mathbf{G}(t))^2$ over the number of simulations and step time size Δt	83
4.13	Top graph: rotational speed at the bit used as input for the generation of stochastic process $\mathbf{G}(t)$; Bottom graph: 3 realizations and the probabilistic envelope of $\mathbf{A}_4(t) = a_{4m}(h_{CP} + \mathbf{G}(t))^2$ for three times the standard variation σ_{A4} around the mean μ_{A4} . The time intervals in which bit is almost stopped are highlighted by green rectangles. . .	84
4.14	(a) Fast Fourier Transform (fft) of process $\mathbf{G}(t)$ for when bit is almost stationary (stick phase) and when bit is rotating (slip phase).; (b) Spectrogram of process $\mathbf{A}_4(t) = a_{4m}(h_{CP} + \mathbf{G}(t))^2$ for simulated data.	85
4.15	Deterministic rotational speed at the bit used as initial condition for stochastic simulation. (a) $\Omega = 95.5$ RPM and $\bar{W}_{ob} = 100$ kN; (b) $\Omega = 95.5$ RPM and $\bar{W}_{ob} = 68$ kN	86
4.16	Convergence of stochastic drill-string dynamical response. $\Omega = 95.5$ RPM and $\bar{W}_{ob} = 100$ kN. (a) O-U process, and; (b) CP process. . . .	87
4.17	Convergence of stochastic drill-string dynamical response for the num- ber of simulations. $\Omega = 95.5$ RPM and $\bar{W}_{ob} = 100$ kN. (a) O-U process, and; (b) CP process.	87

4.18	Validation of CP Process properties with fully coupled system. One realization and the probabilistic envelope of $\mathbf{A}_4(t) = a_{4m}(h_{CP} + \mathbf{G}(t))^2$ for three times the standard deviation σ_{A4} around mean μ_{A4} . $\Omega = 95.5$ RPM and $\bar{W}_{ob} = 100$ kN.	88
4.19	Simulations in which the bit achieves negative axial speeds. (a) O-U process, and; (b) CP process.	89
4.20	One simulation of the stochastic response at the bit with uncertainties modeled by CP Process. (a) Rotational Speed, and; (b) Axial Speed. $\Omega = 95.5$ RPM and $\bar{W}_{ob} = 100$ kN.	89
4.21	Probabilistic envelope of 95% for the rotational speed at the bit. (a) O-U Process; (b) CP Process. $\Omega = 95.5$ RPM and $\bar{W}_{ob} = 100$ kN.	90
4.22	Probabilistic envelope of 95% for 1500 seconds of stochastic results with uncertainties modeled by CP Process. (a) Rotational speed, and; (b) Axial speed. $\Omega = 95.5$ RPM and $\bar{W}_{ob} = 100$ kN.	91
4.23	One simulation of the TOB by the stochastic model with uncertainties modeled by (a) O-U process and (b) CP process. $\Omega = 95.5$ RPM and $\bar{W}_{ob} = 100$ kN.	92
4.24	Stochastic bit-rock interaction graph with uncertainties modeled by CP Process. (a) One simulation of 250 seconds, and; (b) Probabilistic envelope of 95%. $\Omega = 95.5$ RPM and $\bar{W}_{ob} = 100$ kN.	93
4.25	Fast Fourier Transform (fft) of stochastic response with uncertainties modeled by CP process. (a) Bit rotational speed, and; (b) Bit axial speed. $\Omega = 95.5$ RPM and $\bar{W}_{ob} = 100$ kN.	93
4.26	One simulation of the stochastic response at the bit with uncertainties modeled by CP Process. (a) Rotational Speed, and; (b) Axial Speed. $\Omega = 95.5$ RPM and $\bar{W}_{ob} = 68$ kN.	94
4.27	Probabilistic envelope of 95% stochastic response with the uncertainties modeled by CP Process. (a) Bit rotational speed, and; (b) Bit axial speed. $\Omega = 95.5$ RPM and $\bar{W}_{ob} = 68$ kN.	95
4.28	Stochastic bit-rock interaction graph with uncertainties modeled by CP Process. (a) One simulation of 250 seconds, and; (b) Probabilistic envelope of 95%. $\Omega = 95.5$ RPM and $\bar{W}_{ob} = 68$ kN.	95
4.29	Fast Fourier Transform (fft) of stochastic bit rotational speed with uncertainties modeled by CP process. $\Omega = 95.5$ RPM and $\bar{W}_{ob} = 68$ kN.	96
4.30	Empirical Cumulative Density Function of stick-slip severity factor. $\Omega = 95.5$ RPM. (a) $\bar{W}_{ob} = 100$ kN and; (b) $\bar{W}_{ob} = 68$ kN.	97

4.31	(a) Stick-slip severity factor (S_{SS}) for $\Omega = 95.5$ RPM according to the applied \bar{W}_{ob} . (b) Standard deviation of the stick-slip severity according to the applied \bar{W}_{ob}	98
4.32	Fast Fourier Transform (fft) of bit rotational speed for a bigger damping. $\Omega = 95.5$ RPM, $\alpha = 0.4$ and $\beta = 0.008$. (a) $\bar{W}_{ob} = 82$ kN, and; (b) $\bar{W}_{ob} = 110$ kN.	99
4.33	Empirical cumulative distribution function (CDF) of the stick-slip severity factor (S_{SS}) for $\Omega = 95.5$ RPM. Case 1 (C1): $\bar{W}_{ob} = 100$ kN, $\alpha = 0.1$ and $\beta = 0.00008$; Case 2 (C2): $\bar{W}_{ob} = 110$ kN, $\alpha = 0.4$ and $\beta = 0.008$; Case 3 (C3): $\bar{W}_{ob} = 68$ kN, $\alpha = 0.1$ and $\beta = 0.00008$; Case 4 (C4): $\bar{W}_{ob} = 88$ kN, $\alpha = 0.4$ and $\beta = 0.008$	100
4.34	Probabilistic envelope of TOB against the bit rotational speed for $\Omega = 95.5$ RPM when the uncertainties are modeled by CP process. Case 1 (C1): $\nu_1 = 0.01$, $\nu_2 = 0.005$; Case 2 (C2): $\nu_1 = 0.005$, $\nu_2 = 0.005$; Case 3 (C3): $\nu_1 = 0.01$, $\nu_2 = 0.01$. (a) $\bar{W}_{ob} = 68$ kN, and; (b) $\bar{W}_{ob} = 100$ kN.	101
4.35	Empirical cumulative distribution function (CDF) of stick-slip severity factor (S_{SS}). $\Omega = 95.5$ RPM. Case 1 (C1): $b_1 = 1.0$, $b_2 = 0.05$, $\nu_1 = 0.01$, $\nu_2 = 0.005$; Case 2 (C2): $b_1 = 0.5$, $b_2 = 0.05$, $\nu_1 = 0.005$, $\nu_2 = 0.005$; Case 3 (C3): $b_1 = 1.0$, $b_2 = 0.1$, $\nu_1 = 0.01$, $\nu_2 = 0.01$. (a) $\bar{W}_{ob} = 68$ kN, and; (b) $\bar{W}_{ob} = 100$ kN	101
A.1	Experimental test-rig developed and described in [73]. On the left: a general view of the test-rig; On the right: a close view of the bottom part, including the measured variables.	116
A.2	Concrete test-body after experiment.	117
A.3	Schematic view of mechanical model for (a) torsional dynamics and (b) axial dynamics.	118
A.4	Experimental data for one experimental run of 60 seconds (sample 105) with an average top rotational speed of 78 RPM and bit diameter of 12 mm. The red box is related to the 3s time interval taken for analysis.	120
A.5	Experimental data from sample 105 for the time interval of 37 to 40 seconds.	121
A.6	Bit-rock interaction graphs for sample 105 ($37 < t < 40$). (a) TOB versus Bit speed (b) WOB versus Bit speed. The red arrows show the path direction during acceleration and deceleration.	122

A.7	Numerical results for the 1-DOF model compared to experimental data from 37 to 40 seconds. $b_0 = 0.0022$ m, $b_1 = 1.5$ s/rad, $b_2 = 1.5$ and $b_3 = 0.01$ s ² /rad ²	124
A.8	(a) TOB versus Bit speed and (b) Fast Fourier Transform (fft) of the bit rotational speed for the numerical results of the 1-DOF model compared to experimental data from 37 to 40 seconds. $b_0 = 0.0022$ m, $b_1 = 1.5$ s/rad, $b_2 = 1.5$ and $b_3 = 0.01$ s ² /rad ²	124
A.9	Numerical results for the 2-DOF model compared to experimental data from 37 to 40 seconds. $a_1 = 0.0026$ m/s, $a_2 = 5 \times 10^6$ m/s/N, $a_3 = 2.0610 \times 10^{-4}$ m/rad, $a_4 = 8751.6$ N.rad, $a_5 = 0.0875$ N.m, $e = 1$ rad ² /s ²	125
A.10	Fast Fourier Transform (fft) of the bit rotational speed for the numerical results of the 2-DOF model compared to experimental data from 37 to 40 seconds. $a_1 = 0.0026$ m/s, $a_2 = 5 \times 10^6$ m/s/N, $a_3 = 2.0610 \times 10^{-4}$ m/rad, $a_4 = 8751.6$ N.rad, $a_5 = 0.0875$ N.m, $e = 1$ rad ² /s ²	126
A.11	(a) TOB versus Bit speed and (b) WOB versus Bit speed for the numerical results of the 2-DOF model compared to experimental data from 37 to 40 seconds. $a_1 = 0.0026$ m/s, $a_2 = 5 \times 10^6$ m/s/N, $a_3 = 2.0610 \times 10^{-4}$ m/rad, $a_4 = 8751.6$ N.rad, $a_5 = 0.0875$ N.m, $e = 1$ rad ² /s ² . The arrows show the path direction during acceleration and deceleration. The green arrows are for the experimental data and the red ones are for the numerical results.	126
A.12	(a) TOB versus Bit speed and (b) WOB versus Bit speed for the numerical results of the 2-DOF model compared to experimental data from 37 to 40 seconds. $a_1 = 0.0011$ m/s, $a_2 = 5 \times 10^6$ m/s/N, $a_3 = 9.16 \times 10^{-5}$ m/rad, $a_4 = 6732$ N.rad, $a_5 = 0.3471$ N.m, $e = 1.5$ rad ² /s ² . The arrows show the path direction during acceleration and deceleration. Green arrow are for experimental data and the red ones are for numerical results.	127
A.13	Numerical results for the 2-DOF model compared to experimental data from 37 to 40 seconds. $a_1 = 0.0011$ m/s, $a_2 = 5 \times 10^6$ m/s/N, $a_3 = 9.16 \times 10^{-5}$ m/rad, $a_4 = 6732$ N.rad, $a_5 = 0.3471$ N.m, $e = 1.5$ rad ² /s ²	128
B.1	(a) Three sample paths of brownian motion with $dt = 0.002$ s. (b) Five paths of $U(t)$ and mean value with $dt=0.002$ s.	131
B.2	Stochastic integrals of W dW following (a) Itô definition and (b) Stratonovich definition.	135

B.3	Stochastic chain rule demonstration.	141
B.4	(a) Simulation of X_1 ($\lambda_1 = 2$; $\mu_1 = 1$) and X_2 ($\lambda_2 = 3$; $\mu_2 = 1.5$). (b) Solutions for $X_1 X_2$	144
B.5	Euler-Maruyama method demonstration.	152
B.6	(a) Strong and (b) weak convergence of EM method.	154
B.7	One sample path of a Brownian Bridge.	158
B.8	One sample path of Langevin's equation.	159
E.1	Simplified structure of program PRINCIPAL.m.	164
E.2	Simplified structure of program DRILLDYN.m.	165
E.3	Simplified structure of program sub_normalmodes.m.	165
E.4	Simplified structure of program sub_dyn.m.	166

Chapter 1

Introduction

1.1 Motivation

Vibrations are unavoidable in operations such as drilling because of the nature of the external forces acting on the drill-string, especially the one generated by the cutting action of the drill-bit that has many uncertainties. The new scenario faced by drilling companies worsen the vibrations experienced by drill-strings due to its longer length, harder formations, bore-hole instabilities and so on. The vibrations and shocks steal energy from the drilling operation, reducing the amount of available energy used to drill the rock and thus reducing the efficiency. The worst problem related to vibrations is the failure of downhole equipment.

Downhole failures of the drill-string can result in a complete separation of the drill-string or the bottom hole assembly (BHA). In extreme cases, the recovery of the remaining equipment is not possible through an operation commonly called fishing. When it occurs, it is necessary to drill a hole parallel to the section occupied by the abandoned drill-string. This operation is called sidetrack and can take from 2 to 12 days to complete and typically costs on the order of one million dollars (data from 2007, according to [1]). The cost of detecting and avoiding the final separation is dramatically lower. The detection can be done analyzing subtle changes in pressure and flow rate, for example [1].

Due to modeling uncertainties and variations in environmental factors, like lithology, it is a good idea to consider the interactions of the drill-string with the borehole within a stochastic framework. The consideration of such uncertainties can give rise to more realistic operation ranges with risk evaluation. Therefore, stochastic analysis of drill-string vibration can play an important role in achieving a more efficient and safer operation.

1.2 Dissertation objective and organization

The objectives of this work are: (i) to perform a deterministic numerical investigation through a continuous axial-torsional coupled model which is discretized by means of the finite element method that considers the bit-rock interaction and geometric nonlinearities. This investigation includes the determination of the influence of geometric nonlinearities on response, the study of vibration modes, the analysis of deterministic response for a set of parameters and the parametric analysis to evaluate the influence of the main parameters on system's response; (ii) to propose a novel stochastic model to describe uncertainties on bit-rock interaction by using Itô stochastic differential equations, and; (iii) to analyze the influence of the main parameters on stochastic response by comparing the statistics obtained from the results.

In Chapter 1, a brief introduction about drilling operation is presented. In Chapter 2, the most relevant works in literature are reviewed under three points of view: 1 - Drill-string modeling, control and data analysis; 2 - Bit-rock interaction models and; 3 - Uncertainty quantification in drill-string vibration. In Chapter 3, the deterministic investigation is presented, including the mathematical model development, hypothesis made and the deterministic results which include the vibration modes and drill-string response. Chapter 4 is about the stochastic investigation. In this chapter, two stochastic processes are proposed and the stochastic formulation is presented. The stochastic results are also presented, including the stochastic processes generation, the stochastic response of drill-string and a parametric analysis. Chapter 5 concludes this work and discuss some possible future works.

In Appendix A, a validation of the bit-rock interaction model considered in this work is performed based on experimental results. In Appendix B, the subject of stochastic differential equations is discussed. In Appendix C, the differential equations governing the first and seconds moments of linear stochastic differential equations is derived. In Appendix D, the numerical procedure used to solve the stochastic system of equations is explained.

1.3 Overview of a drilling rig

The production of oil and gas out of fossil fuel reservoirs demands a rotary machine called drilling rig which is used to create holes in earth subsurface. The term rig refers to the complex set of equipment used to penetrate the surface. A common drilling rig is shown in Fig.1.1 and it is made of the following main systems: Drill-string; Hoisting system; Top rotary system; and Drilling mud. Furthermore, the drilling rig involves equipment pertaining to additional functions, such as power

generators and blow-out preventer (BOP).

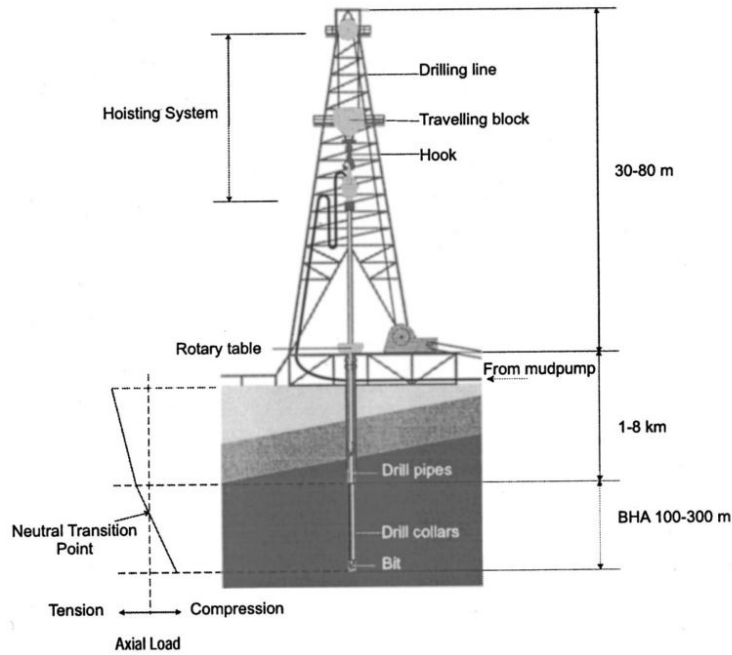


Figure 1.1: A schematic view of a drilling rig. Reproduced from LEINE and VAN CAMPEN [2].

Drill-strings of more than 9 km are used today to reach ultra-deep wells. Such systems are slender with a diameter-to-length ratio much less than a human hair. The majority of drill-string is made of slender tubes called drill-pipes, responsible for transmitting the rotational motion from the top to the hole bottom and for conducting the drilling mud to the bit. The lower part of the drill-string is called Bottom Hole Assembly (BHA) and comprises of: drill collars which are heavy pipes responsible for applying the Weight-on-bit (WOB); a Drill-bit that is the rock-cutting tool in charge of drilling the rock formation; stabilizers designed to minimize lateral motion during drilling; heavyweight drill pipe (HWDP) used to provide a flexible transition between drill collars and drill-pipe in order to reduce fatigue failures; and a variety of equipments used to many purposes like measurement (MWD tools), deviation control, shocking subs, among others.

The hoisting system is responsible for controlling the hook load. This force acts on the top of drill-string in order to hang the drill-string weight. This way, the majority of drill-string is held in tension, while the remainder is intentionally placed in compression to provide the necessary weight-on-bit to drill the rock. Horizontal drilling requires a different approach where the entire horizontal portion of the drill-string is put in compression.

The energy to drive the drill-bit is generated by the top rotary system that is mostly an electrical motor. This system can be of two types: a rotary table or a top

drive.

A substance called drilling mud is injected at the top of drill-string and it is conducted to the bit. After it achieves the bottom of drill-string, it returns through the annulus between the drill-string and the borehole wall. The mud usually consists of water or oil with viscosifiers and weight materials. This mud is used to cool down and lubricate the bit and also to provide the pressure in the borehole to assure its stability, among other functionalities.

1.4 Drilling operation

The drilling process is steered by three major things:

- Hook Load: axial force reaction at the top of drill-string;
- Rotary Speed: rotational speed provided by the top rotary system; and
- Flow Rate: the volume of pumped drilling mud per time.

Observations are also important to indicate the drilling progress and its states. These observations are interpreted by drilling engineers in order to take important decisions. The three common observations are:

- Rate of Penetration (ROP): the axial speed of the top of drill-string gives a measurement of the rate rock is penetrated.
- Torque at the Top Rotary System: the current consumed by the electric motor used in the top rotary system gives a direct measure of the torque applied to the drill-string, in the case of a DC motor; and
- Pressure drop: the pressure drop in flowline from the pumps to the top of drill-string.

Some typical values for the parameters in drilling operations can be useful to understand drilling dynamics. The weight-on-bit generally ranges from 0 to 250 kN. At the surface, the hook load can achieve 3000 kN. Torque on bit can range from 0.5 to 10 kNm while the torque applied to drill-string at the surface can achieve 70 kNm due to borehole interactions. Rotational speeds range from 50 to 200 rpm and rates of penetration vary from 1 to 50 m/h. [1]

1.5 Vibrations in drill-strings

Vibrations are usually considered detrimental to the drilling process, except for some specific cases where vibration is desired, like percussive drilling for example. Vibrations often induce premature wear and damages to drill-string. It can also increase the chances of fatigue failures. The vibration can be induced by interactions with the environment or be self-induced. Many other problems can result from vibrations. It can interfere or even damage MWD tools, induce wellbore instabilities reducing direction control and reduce the ROP because of energy losses due to vibration and due to the friction along drill-string.

Drill-string vibrations are commonly classified according to the direction they occur. Three main types of vibration are identified, as depicted in Fig. 1.2: axial, lateral and torsional. A brief definition is given for each of them:

- Axial vibration: Drill-string moves along its axis of rotation. The critical situation is called bit-bounce and it occurs when bit impacts the formation and gets loose at high speed. Typical frequencies are 1–10 Hz [1].
- Lateral vibration: Drill-string moves laterally to its rotation axis in the annular gap. The critical situation is called whirl and it occurs when the center of rotation moves laterally as it rotates. The whirl can be forward (section rotates around borehole in the same direction drill-string rotates around its own axis), backward (section rotates around borehole in the opposite direction drill-string rotates around its own axis) or chaotic (section impacts borehole wall in a chaotic manner). Typical Frequencies are 0.5 to tens of Hz [1].
- Torsional vibration: Drill-string rotates irregularly downhole while it rotates at an almost constant speed on the surface. The most harmful torsional vibration is called stick-slip. In this mode, the bit becomes stuck in rock formation while the top rotary system continues to rotate. When the energy stored in drill-string becomes high enough, drill-bit is released and achieves high speeds, reaching even 10 times top rotary speed. Typical frequencies are 0.05–0.5 Hz [1].

In general, the three modes explained above occur simultaneously while drilling. It occurs because of the coupling between them through the interactions with borehole and the geometric coupling. Despite this, a fully coupled model with all boundary conditions usually results in high computational costs and lack of clarity about parameters influence.

In order to reduce the presence of harmful vibration during drilling, the concept of an optimum zone is used to define BHA components and drilling parameters. This

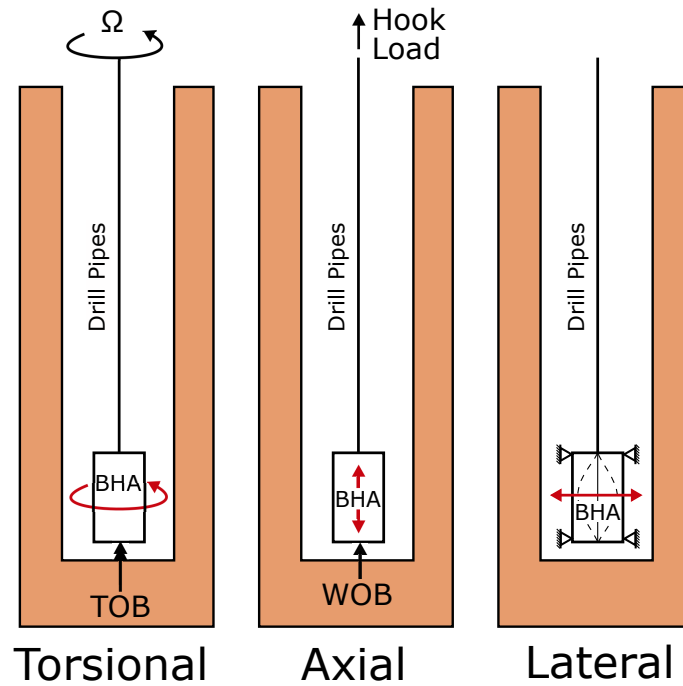


Figure 1.2: Drill-string vibration modes.

concept consists of a map that indicates where vibration is more likely to occur. In this map, the central zone is called the optimum zone because vibrations are unlikely to occur inside it. An example of an optimum zone is given in Fig.1.3.

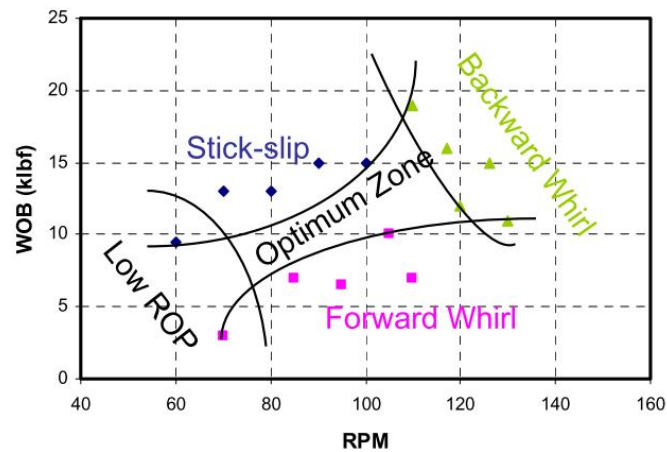


Figure 1.3: An example of optimum zone. [3]

1.5.1 Axial vibration

Axial vibrations can be detrimental or beneficial to drilling operation depending on how they affect WOB and thus ROP. They are beneficial when using percussive drilling, for example. When it is detrimental, they exhibit large amplitudes due to resonance, the bit lifts off from the formation and drilling process becomes erratic,

and thus reducing ROP. MWD tools are capable of detecting a wide and frequent WOB fluctuation. In extreme cases, WOB rapidly vanishes periodically. It usually means that bit lost contact with the formation and this phenomenon is called bit-bounce.

Two primary causes of axial vibration were identified in the literature. The first is due to the irregularities on formation surface caused by the indentation pattern caused by tricone bits. The second is related to the frequency tuning of mud pressure with the axial frequencies. Bit-bounce is a harmful vibration and can result in low ROP, downhole equipment failure and even well damage.

1.5.2 Torsional vibration

Drill-string torsional vibration remained undetected for a long time. It has been suggested that the large inertia of rotary table caused this, as it attenuates torsional vibrations traveling upward. However, large amplitude variations were observed in applied torque. Today, downhole measurements clearly show that the bit does not have a steady rotational motion despite the constant speed applied by the top rotary system. Actually, the drill-bit angular motion experiences large fluctuation in time. This difference between the motion of drill-bit and the top of drill-string is due to the large torsional flexibility of the structure.

Several factors can make drill-bit to stop, like a sudden WOB increase or environmental causes as a tight hole, significant drag, severe dog-legs and key-seatings. As drill-bit gets stuck, drill-string continues to rotate and stores torsional energy. When the available torque reaches a level that bit can no longer resist, the bit comes loose and rotates at a very high speed that can reach ten times the rotary table speed. When bit rotates, it releases the energy that was trapped in drill-string and the rotational speed decreases. Then, drill-bit sticks again and the cycle repeats. This phenomenon is called stick-slip and happens during as much as 50% of drilling time [4].

Although the term stick-slip is formally used to describe only the situation in which bit stops completely, this term is also used by the industry to refer to all the severe torsional vibrations that occur during drilling operations, even when bit does not stops completely. This industry jargon is going to be used in this dissertation.

The stick-slip cause is usually attributed to the relationship of torque on bit (TOB) with drill-bit rotational speed. It is usually taken within modeling perspectives by mean of dry-friction models because of the similarity between the behavior of the two phenomena. It has been also suggested that stick-slip only occurs when drill-string is longer than a critical length and that the severity of stick-slip increases with the length. It makes sense because drill-string becomes more flexible. Many

works on this area [2, 4–6] also stated that stick-slip disappears above a critical speed.

This type of vibration is very harmful to drilling operation as it can decrease the ROP by 25% [7]. Other problems can also be originated from this kind of vibration [8]: drill-pipe fatigue problems; drill-string components failure; wellbore instability and; bit damage.

Several remedies were proposed in the last years to suppress stick-slip vibrations. These include increase drill-string stiffness, increase rotational speed, decrease WOB, increase BHA inertia, and reduce the difference between static and dynamic friction coefficients [6]. MWD tools are now capable of giving real-time information about downhole status, although it is still not possible to transmit real-time measurement data. The information about downhole status permits the control of rotational behavior of drilling assembly by varying WOB and rotational speed, modifying mud properties and changing the drill-bit or BHA composition [7]. A different approach was also suggested regarding the control of the torque oscillations in the top rotary system. This method claimed to damp torsional waves traveling up drill-string in order to suppress stick-slip oscillations [9].

1.5.3 Lateral vibration

Lateral vibrations are also called as transverse, bending, or flexural vibrations. They are widely recognized as a major cause of drill-string and BHA failures. Despite this, lateral vibration of drill-strings remained unknown for a long time because most of this vibration does not travel to the surface. It is due to the stabilizers that suppress most of the lateral motion where they are placed. Thus, lateral vibrations rapidly attenuate while propagating towards the surface. Therefore, it is very difficult to detect it only by surface measurements. Advances in MWD tools helped to identify this kind of vibration and its impact on equipment failures. Despite the damaging nature of this vibration, it can be beneficial in directional drilling in order to control the direction of drill-bit and increase ROP [7].

The major causes of lateral vibrations are the contact and friction at borehole/drill-string and bit/formation interaction, imbalance, eccentricity and initial curvature in drill collar section. Consequences of this kind of vibration are reduced ROP and early failure of downhole equipment. Also, it contributes to drill-collar wear and connection failures. Furthermore, it can initiate severe and repeated contacts with borehole wall resulting in surface abrasion of drilling equipment, deterioration of the well condition and damaging borehole wall. Finally, it can affect drilling direction and initiate other modes of vibration (axial and torsional).

During drilling, most of BHA operates in compression, which facilitates buckling

and whirling to occur. An important subset of lateral vibration is the BHA whirl. Whirl is the condition when the center of rotation of a drill-collar section is not located in the center of rotation of drill-string that is typically on the center of the hole. BHA whirl is illustratively shown in Fig. 1.4 and it can be classified into forward, backward or chaotic.

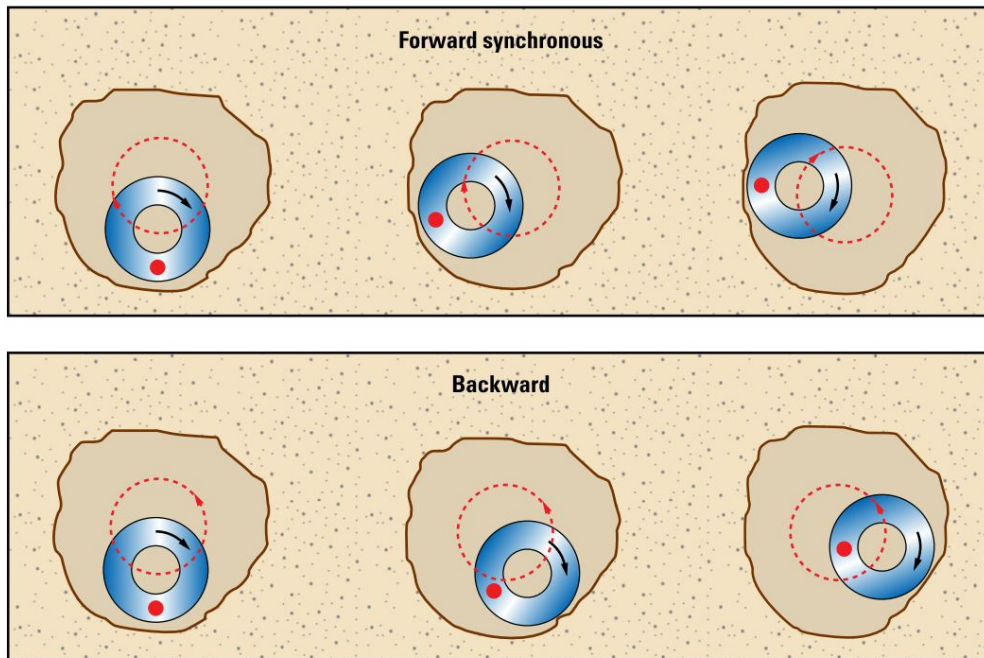


Figure 1.4: BHA whirl. Red dot represents stationary point on pipe section to describe its rotation. Dashed circle represents the whirling motion. Adopted from [10].

Forward whirl occurs when drill-collar section rotates around borehole in the same direction as drill-string is rotated by the top rotary system. In this regime, the same side of drill-collar may be in constant contact with the borehole wall, resulting in flat-spots on collar joints. Forward whirl may develop in common drilling operations and it is usually caused by out-of-balance mass but unlikely to occur if eccentricity is less than stabilizer clearance [11]. Furthermore, depending on down-hole conditions and drilling parameters, forward synchronous whirl can evolve to backward whirl [7].

The whirl is classified as backward if the drill-collars rotates around borehole in the opposite direction as drill-string is rotated by the top rotary system. It can be originated from the friction between stabilizers and borehole wall. Backward whirl can achieve rates much higher than rotary speed, resulting in fatigue life shortening. It occurs because backward whirl induces fluctuating bending moments with periodically change of sign and high amplitudes.

Extreme cases of non-synchronous whirl are called chaotic whirl. In this case, the motion is irregular and depends strongly on initial conditions. This motion is

induced by nonlinear fluid forces, stabilizer clearance and borehole wall interactions [7]. In the presence of chaotic whirl, drill-collar sections may impact the borehole wall many times. Thus, it can severely damage downhole equipment.

Chapter 2

Literature review

A literature review of the most important contributions for this research is presented in this chapter. The first topic is about the dynamical model of the drill-string and the control strategies proposed to reduce vibrations. A very important subject concerning drill-string modeling is the bit-rock interaction. Because of this, a dedicated section in the literature review is dedicated to this part of the model. Next, the uncertainty quantification in drill-string vibrations is discussed because of the random nature of external forces, especially those related to the interaction with the well-bore. At last, the experimental studies regarding drill-string vibrations are outlined and discussed.

2.1 Drill-string modeling and control

The vibration of drill-strings was first addressed in 1960 when BAILEY and FINNIE [12] performed the first modal analysis of a continuous system with longitudinal and torsional vibrations. The authors presented an analytical study and calculated the natural frequencies using a graphical method. The numerical results were compared to experimental data obtained in 1960 by FINNIE and BAILEY [13].

Eight years later, in 1968, DAREING and LIVESAY [14] proposed a model to calculate longitudinal and angular vibrations that is very similar to [12]. The main difference of the adopted model is the inclusion of a linear viscous damping along the drill-string. The solution was compared to field data and the model appeared to predict reasonably well the vibration of drill-strings under those conditions. For validation, only the frequency response was compared.

In 1982, BELOKOBYL and PROKOPOV [15] introduced an analytical analysis of the torsional vibration of drill-strings. The authors proposed a 1-DOF model considering a concentrated inertia in the lower segment and a linear torsional spring between the rotary table and the inertia. The bit-rock interaction was included as

a drag torque and the torsional vibration was analyzed as a friction-induced self-excited vibration.

In 1986, HALSEY *et al.* [16] presented an analytical method for calculating the torsional natural frequencies in a drill-string. The drill-string was modeled as a continuous system like in [14] but the friction torque along the drill-string was modeled as a constant torque plus a viscous torque. The bit-rock interaction was neglected assuming that it has no influence on the natural frequencies. The authors compared the frequencies calculated with the ones obtained experimentally in a 1000m deep, nearly vertical well. A correction factor in the wavenumber was used to incorporate the drillpipe joints effect into the calculation. The calculated frequencies were in good agreement with the experimental data. The natural frequencies were practically not affected by rotation rate, weight-on-bit and damping effects.

In 1987, DAWSON *et al.* [6] used a 1-DOF model with a linear behavior in the slip phase in friction model. They analyzed experimental data obtained in a directional deep well and have observed fluctuations in the torque at the driving system in the presence of stick-slip. The data also suggested an increase in magnitude and frequency of the vibration when the rotational speed is higher. The authors concluded that stick-slip oscillations disappear above a certain critical rotary speed. They also proposed a reduction in the static friction as a solution for this phenomenon.

One year later (1988), KYLLINGSTAD and HALSEY [17] used the same model as DAWSON *et al.* [6] but neglecting the viscous effect on TOB. The analytical solution was formulated for stick-slip motion. The authors claimed that the model describes a nonlinear self-excitation of the lowest torsional mode and that the frequency of stick-slip oscillation is a bit lower than the natural pendulum frequency. Also, the time during stick and the frequency of stick-slip are dependent on the rotary rate. The model was validated against experimental data and they claimed that controlling the rotary speed in a way that dampens torsional oscillations can be a solution for stick-slip vibration.

In the same year, HALSEY *et al.* [9] presented the first control system to mitigate stick-slip oscillation, called torque feedback. The system was designed to keep the rotary speed and the torque as constant as possible. This way, it can prevent the rotary system from being an effective reflector of torsional waves and then reduce or prevent stick-slip oscillations. The disadvantage of this system is the additional sensors required. Field experiments on a full-scale research drilling rig showed that torque feedback was effective for those conditions it was tested for.

LIN and WANG [18] published two papers in 1990 and 1991 about the stick-slip phenomenon. The authors also considered a 1-DOF torsional pendulum model as other authors had mentioned before. They were one of the first to solve the problem numerically in the time domain and to calibrate some constants using field data.

They concluded, among other things, that the amplitude of stick-slip oscillation amplifies as the rotary speed increases but vanishes when the rotary speed reaches a critical value.

Regarding the lateral motion, JANSEN [11] was the first to investigate drill-string vibrations using non-linear rotor dynamics in 1991. The proposed model considered a section of whirling drill collars with 2 DOF and took into account the influence of drilling mud, stabilizers clearance and friction. The author considered this model quite simple to give a quantitative description of drill collar dynamics but the qualitative analysis was considered very helpful. The main conclusions were: Fluid damping and stabilizer friction reduce the whirl amplitude; Fluid added mass and stabilizer clearance reduces critical speed at which whirl amplitude is maximum, and; instabilities can result from stabilizer clearance.

In 1992, BRETT [19] proposed a model similar to [6, 16, 17]. The differences are that the dynamics of the rotary table is explicitly taken into account and it allows an arbitrary relationship for the boundary condition at the bit. The solution is presented in the time domain and no analytical closed form is presented. Three important conclusions were presented by the author about torsional vibration: (1) it can occur in shallow vertical holes where the friction is low; (2) it is more common with PDC bit than with three-cone bits; and (3) it is more severe in hard rocks, at higher WOB, lower rotary speed and duller bits.

In 1995, JANSEN and VAN DEN STEEN [20] used the same concept of HALSEY *et al.* [9] of active damping stick-slip vibration with a feedback control in the drive system. This new proposal uses only electrical variables in the feedback control and does not need any expensive sensors. The model adopted is a simple torsional pendulum with 2 DOF. This control resulted in a less velocity threshold value at which stick-slip disappears.

YIGIT and CHRISTOFOROU [21] investigated the transverse vibration induced by axial motion of drill-strings in 1996. The drill-string was modeled as a non-rotating slender beam with a simply-supported lower part. The model also considers nonlinear coupling terms and intermittent contact between drills-string and the wellbore wall. Only the lower part of the drill-string was considered to have transverse and axial vibration because it is under compression. The upper part is under tension and only axial vibration was considered. It was shown that the fully coupled equations resulted in lower critical axial loads. When the axial load becomes larger than the critical value, multiple impacts with wellbore wall are detected and the response becomes chaotic.

In 1997, the same authors extended the model for a rotating drill-string and they also considered a parametric excitation due to bit-rock interaction and an unbalanced mass. In addition, a non-linear damping was included and contact with

wellbore wall now considers the friction. Due to the non-linearities of the model, the dynamic response becomes non-periodic and suggests a chaotic behavior. Torsional vibrations were neglected.

TUCKER and WANG [23] proposed an integrated model for drill-string dynamics in 1999. The model is based on a Cosserat rod model and considers six independent DOF: three for the location of the centroid and three related to the dynamical state to be expressed in terms of flexural, torsional and shear strain, together with dilation and stretch. The model also includes constitutive relations that can describe the modes of vibration that are associated with the motion of drill-string in straight and curved boreholes. The BHA and rotary tables are modeled as mass points with rotary inertia. The objective of this article is to discuss the stability of axisymmetric drill-string configuration in a vertical borehole under coupled torsional, axial and lateral vibrations as well as extreme conditions of whirl.

In 1999, TUCKER and WANG [24] designed a torque feedback control as an alternative to soft-torque using the model proposed in [9]. The two control methods were compared and the proposed mechanism eliminated many of the volatilities suffered by soft torque.

In 2000, CHALLAMEL [25] studied the stability of a drill-string using the direct method of Liapounov through discrete models. At first, only the torsional motion is considered in a 1-DOF model. Next, torsional and axial motions are coupled through bit-rock interaction and the author concludes that stick-slip can be described adequately by considering a quasi-static axial evolution instead of studying the coupled vibration.

In 2002, LEINE and VAN CAMPEN [2] attributed stick-slip and lateral whirl vibration to the fluid forces of the drilling mud. The model considered three degrees of freedom: two for the lateral vibration and one for torsional. The coupling takes place through the fluid force and contact with the borehole. Bifurcation diagrams were calculated and analyzed. A hysteresis effect was seen in the transition between stick-slip and lateral whirl for changes in the rotational speeds.

In 2003, TUCKER and WANG [26] extended the work done in 1999 and proposed a rectification torque control on the bit. The authors presented a table comparing different control strategies and apparently the bit torsional rectification presented the best results.

In the same year, CHRISTOFOROU and YIGIT [27] proposed a fully coupled model to describe drill-string dynamics. The coupling was done by bit/rock and drill-string/borehole interactions as well as by geometric and dynamic nonlinearities. The authors also proposed a feedback control to try to control stick-slip resulting in lower critical rotational speeds. This was considered important because high rotational speeds resulted in severe lateral vibration.

In 2004, NAVARRO-LÓPEZ *et al.* [8] presented a new control strategy to suppress stick-slip vibration. The proposed model is discrete and has 2 torsional DOFS, one for BHA and one for the top drive. Two methods of control are proposed: (i) control the weight-on-bit; and (ii) introduce a shock sub in the BHA. The main disadvantage of these methods is the necessity of real-time downhole measurements which is very difficult due to data transfer speed and harmful environment.

Also in 2004, RICHARD *et al.* [28] proposed a discrete model with axial and torsional DOF and a new bit-rock interaction model using the concepts developed by DETOURNAY and DEFOURNY [29]. The coupling between torsional and axial modes was done through the bit-rock interaction.

In 2005, KHULIEF and AL-NASER [30] contributed with a finite element model for the full dynamics of drill-string. The drill-string was discretized into finite shaft element with 12 degrees of freedom each. The model considered the gyroscopic effect, torsional/bending inertia coupling and the effect of the gravitational force field. A modal transformation was also used to build a reduced model. The interactions of the drill-string with the borehole were not considered and important dynamic effects were neglected.

In the next year, YIGIT and CHRISTOFOROU [31] simplified the model proposed in [27] to consider only torsional and axial vibration. The model includes the mutual dependence of torsional and axial motion through the bit-rock interaction law. The objective was to study the interaction between stick-slip and bit-bounce under varying operating conditions. The results suggested that the rotary control is not enough to suppress vibration. Therefore, a control of the hook load is suggested to control axial motion as well.

In 2007, KHULIEF *et al.* [32] included axial-bending coupling and bit-rock interaction in the formulation presented in 2005. The coupling between axial and torsional motions was also included in bit-rock interaction through the dependence of TOB on the WOB. In this analysis, it was assumed that bit never loses contact with the formation.

Also in this year, ZAMANIAN *et al.* [33] included the damping due to drilling mud, active damping system (as the one proposed by [20]) and moment of inertia of rotary table in the model proposed by RICHARD *et al.* [28]. It was concluded that changes in the parameters introduced can affect the stability of the bit. Also, stick-slip vibrations can be avoided by the appropriate selection of those parameters.

In the same year, SAMPAIO *et al.* [34] proposed a finite element model to study the coupling of axial and torsional vibrations. The model took into account the geometrical non-linearities in the finite element formulation. A comparison between linear and non-linear models was performed and showed considerable differences in quantitative and qualitative manners. Otherwise, these differences appeared only

after a certain number of periods of stick-slip.

In 2009, GERMAY *et al.* [35] extended the study started in [28, 36] to include multiple modes rather than 2 degrees of freedom. The authors based the formulation on a continuum representation and discretized the problem with finite element method. The angular velocity was considered constant at the top as in [28, 36]. The conclusions were very similar to the ones in [28, 36] but more modes were captured using this approach.

RITTO *et al.* [37] proposed, in the same year, a non-linear model using Timoshenko beam theory. The equations of motions were discretized by means of the finite element method. The model also included bit-rock interaction, fluid-structure interaction and impacts with the borehole wall.

In 2013, LIU *et al.* [38] proposed a new model that takes into account torsional, lateral and axial motion on an 8-DOF discrete model. The model also considers dry friction, loss of contact and collisions. The time and frequency responses were assessed and a bifurcation diagram was drawn to identify chaotic and periodic regimes.

In 2014, KAMEL and YIGIT [39] extended the work done in [31] by including the hoisting system which control the axial velocity and WOB.

In 2016, HONG *et al.* [40] proposed the utilization of Kalman estimator to predict downhole conditions based on surface measurements. The objective was to facilitate the usage of active control systems used to prevent severe vibrations that are based on downhole conditions. A lumped parameter model considering torsional motion along the drill-string and lateral motion at drill collars was proposed.

2.2 Bit-rock interaction model

This section is devoted to discussing the bit-rock interaction models. The graphs shown below are obtained directly from the articles mentioned. The equations were rewritten in order to standardize the notation used in this work.

The first time bit-rock interaction was included in the drill-string model was in 1982 by BELOKOBYL and PROKOPOV [15]. They included a drag torque at the concentrated inertia on the bottom of drill-string. The friction was considered as a nonlinear function of the angular velocity of the drill bit as in Eq. 2.1, where t_{bit} represents the torque-on-bit (TOB), $\dot{\theta}_{bit}$ is bit angular speed and M_0 , ϵ and k are constants. The problem was formulated based on the well-known problem of vibrations of a load held by a spring on an endless tape moving at a constant velocity.

$$t_{bit}(\dot{\theta}_{bit}) = M_0[1 + (\epsilon - 1)e^{-k\dot{\theta}_{bit}}] \quad (2.1)$$

In 1987, DAWSON *et al.* [6] also modeled the bit-rock interaction as friction torque. They attributed stick-slip oscillations to the friction effects at the bit, more precisely because of the difference between static and dynamic friction coefficients. The slip phase of friction was modeled using a linear function of the bit rotational speed. One year later, KYLLINGSTAD and HALSEY [17] modeled bit-rock interaction using coulomb friction without the decaying behavior with bit rotational speed. The law proposed in [17] was formulated as a system of equations as in Eq.2.2 where τ_C and $\Delta\tau$ are constants.

$$t_{bit}(\dot{\theta}_{bit}) \begin{cases} < \tau_C + \Delta\tau, & \text{if } \dot{\theta}_{bit} = 0 \\ = \tau_C, & \text{if } \dot{\theta}_{bit} > 0 \end{cases} \quad (2.2)$$

LIN and WANG [5] proposed another dry friction model to describe bit-rock interaction. The authors pointed out that dry friction model should meet two characteristics: (i) The static friction coefficient is greater than the kinetic friction coefficient, and; (ii) The friction gradually tends to a constant value as the relative speed of two contacting bodies increases. For the authors best knowledge there was not an accurate model that could fit these characteristics and describe bit-rock interaction effectively. Therefore, the authors proposed a continuous exponential law to describe bit-rock interaction. The formulation is presented in Fig.2.1 and in Eq. 2.3 where f_1 , f_2 , γ and ϵ are constants.

$$t_{bit}(\dot{\theta}_{bit}) = f_2 + (f_1 - f_2) \exp(-\gamma \dot{\theta}_{bit})^\epsilon \quad (2.3)$$

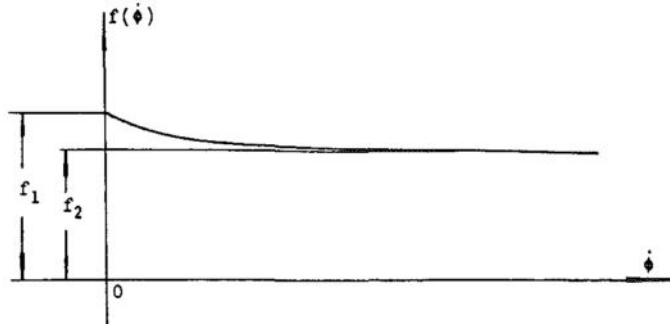


Figure 2.1: Bit-rock interaction model proposed by LIN and WANG [5], where $f(\dot{\phi})$ actually represents $t_{bit}(\dot{\theta}_{bit})$.

BRETT [19] investigate the torsional vibration using experimental data obtained on laboratory, on a full-scale research rig and on the field with PDC bit. It was concluded that PDC bits have the inherent characteristic of reduction of torque with increased rotary speed. It was also concluded that the interaction is affected by WOB, lithology and bit condition (sharp or dull). This behavior can be seen in Fig. 2.2. This work shows that this characteristic can excite severe torsional

vibration, even though the rotation is smooth when the bit is off bottom. The model's prediction was in good agreement to field data in terms of magnitude and frequency with the bit-rock interaction law observed in the tests.

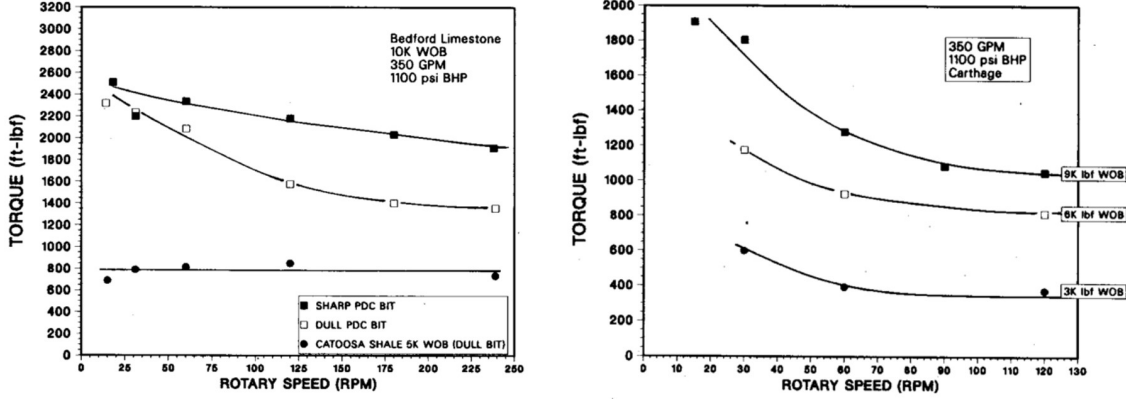


Figure 2.2: Experimental data for bit-rock interaction obtained by BRETT [19]

In 1992, DETOURNAY and DEFOURNY [29] performed a study on the mechanics of cutting mechanism of PDC bits. They proposed to decompose the TOB ($t_{bit} = T_c + T_f$) and WOB ($W_{ob} = W_c + W_f$) in two terms: cutting (T_c and W_c) and friction (T_f and W_f). The cutting components were modeled depending on the depth-of-cut as in Eqs. 2.4, 2.5 and 2.6. And a linear constraint (Eq. 2.7) was proposed between TOB and WOB in the frictional term. The authors tested the model against experimental data through an E-S diagram, where E represents the specific energy ($E = 2t_{bit}/a^2\delta_c$) and S represents the drilling strength ($S = W_{ob}/a\delta_c$). It was concluded that the model was in good agreement with experimental data because data points cluster along a line in the E-S diagram, as shown in Fig. 2.3. The parameter \dot{u}_{bit} is the ROP, r_b is the bit radius, ϵ is a constant called intrinsic specific energy, γ is a constant related to the bit, μ is the friction coefficient at the wearflat/rock contact and ξ is the ratio of S over E when there is no friction.

$$\delta_c = 2\pi \frac{\dot{u}_{bit}}{\dot{\theta}_{bit}} \quad (2.4)$$

$$T_c = \frac{1}{2}\epsilon\delta_c r_b^2 \quad (2.5)$$

$$W_c = \zeta\epsilon\delta_c r_b^2 \quad (2.6)$$

$$T_f = \frac{1}{2}\gamma\mu r_b W_f \quad (2.7)$$

In 1994, PAVONE and DESPLANS [41] performed high sampling rate downhole measurements that are fully synchronized to all other signals. The measured data suggested that stick-slip occurs because of the relation between the torque at the bit and rotary speed. This relationship shows that torque decreases when the ro-

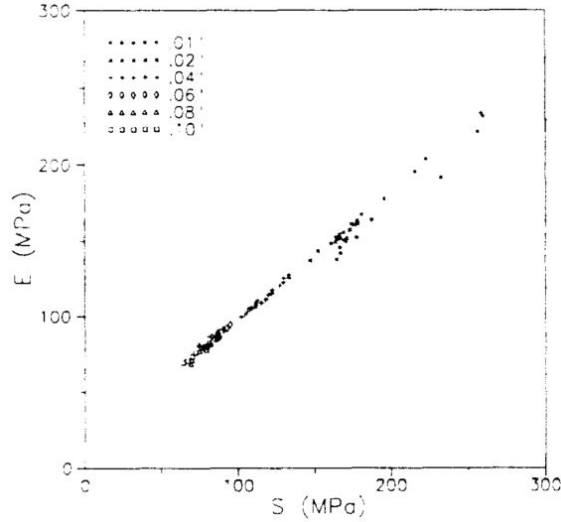


Figure 2.3: Experimental data in E-S diagram presented by DETOURNAY and DEFOURNY [29]

tary speed increases and remains constant when rotary speed decreases, as seen in Fig. 2.4. The author claims that is possible to simulate drill-string dynamics with a simple model if actual friction laws are used at the bit level and along the drill-string. Based on the experimental results, PAVONE and DESPLANS [41] proposed Eq. 2.8 for the interaction law, where $\dot{\phi}_0$ is a constant. They also suggested a solution for stick-slip: to use a downhole tool to create a positive slope that can counteract the negative slope of the bit-rock interaction.

$$t_{bit} = 23.6(\mathcal{W}_{ob})^{1.1}(\dot{\theta}_{bit})^{-0.3} \left[1 - e^{-\frac{\dot{\theta}_{bit}}{\phi_0}} \right] \quad (2.8)$$

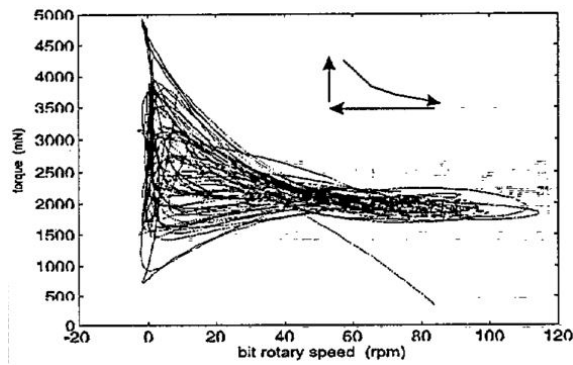


Figure 2.4: Instantaneous torque at the bit presented by PAVONE and DESPLANS [41]

In 1999, TUCKER and WANG [23] used a four parameter expression to simulate a Coulomb friction at the bit. The expression was based on the velocity-weakening effect as well as observed before on the field and as the other developed models. Figure 2.5 shows the profile of the frictional torque for a typical field operation

using Eq. 2.9 where A , B , a and b are constants.

$$t_{bit}(\dot{\theta}_{bit}) = AB\dot{\theta}_{bit}(ab^2 + b^2 + B^2\dot{\theta}_{bit}^2)/(b^2 + B^2\dot{\theta}_{bit}^2)\sqrt{1 + B^2\dot{\theta}_{bit}^2} \quad (2.9)$$

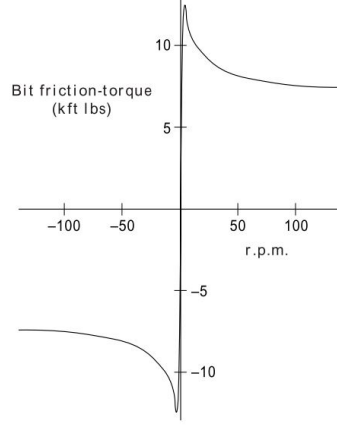


Figure 2.5: Bit-rock interaction proposed by TUCKER and WANG [23]

In 2000, CHALLAMEL [25] based the bit-rock interaction formulation on the work developed by DETOURNAY and DEFOURNY [29]. The TOB was then calculated considering only the cutting mechanism described in [29] and reproduced in Eq. 2.10. The depth-of-cut, as expressed in Eq. 2.4, explodes when bit velocity tends to zero, which is not true. Due to this effect, a correction is proposed and TOB is then calculated with a linear dependence on ROP and an exponential dependence on bit velocity as in Eq. 2.11. To complete bit-rock interaction model, WOB is computed accordingly to Eq.2.12 as a linear function of TOB as can be deduced from [29] if only cutting forces are considered. In eqs. 2.10, 2.11 and 2.12, the variables ϵ , ζ , α and μ are constants.

$$t_{bit} = \pi\epsilon r_b^2 \frac{\dot{u}_{bit}}{\dot{\theta}_{bit}} \quad (2.10)$$

$$t_{bit} = \begin{cases} \zeta \dot{u}_{bit} e^{-\alpha \dot{\theta}_{bit}}, & \text{if } \dot{\theta}_{bit} \geq 0 \\ -\zeta \dot{u}_{bit}, & \text{if } \dot{\theta}_{bit} < 0 \end{cases} \quad (2.11)$$

$$\mathcal{W}_{ob} = \mu t_{bit} \quad (2.12)$$

In 2003, TUCKER and WANG [26] proposed a relation for axial-torsional coupling on the bit that depends on the bit rotary speed, Torque-on-Bit, Weight-on-Bit, Depth-of-Cut and Rate of Penetration. These relations were based on the correlations found in drilling measurements under stable drilling conditions and they are shown in Eqs. 2.13, 2.14 and 2.15. It also has the same variables used in the formulation proposed by [29] based on rock mechanics. The TOB and WOB are functions

of DOC plus a constant as in [29]. In order to regularize the DOC calculation, a regularization function (Eq. 2.16) is proposed and multiplies the right side of Eqs. 2.13, 2.14 and 2.15. The behavior of the torque at the drill-bit as a function of its rotary speed in RPM for three different constant values of WOB in kN is displayed in Fig. 2.6. The variables a_i and ϵ in eqs. 2.13, 2.14, 2.15 and 2.16 are constants.

$$\dot{u}_{bit} = -a_1 + a_2 \mathcal{W}_{ob} + a_3 \dot{\theta}_{bit} \quad (2.13)$$

$$t_{bit} = a_4 \delta_c + a_5 \quad (2.14)$$

$$\delta_c = \frac{\dot{u}_{bit}}{\dot{\theta}_{bit}} \quad (2.15)$$

$$F(\Omega) = \frac{\dot{\theta}_{bit}}{\sqrt{\dot{\theta}_{bit}^2 + \epsilon^2}} \quad (2.16)$$

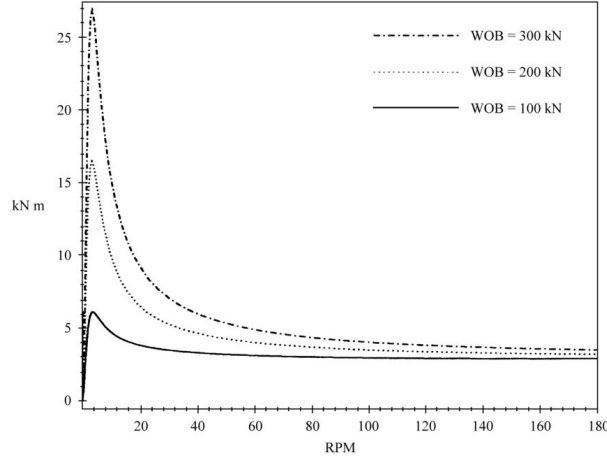


Figure 2.6: Bit-rock interaction model proposed by TUCKER and WANG [26]

In the same year, CHRISTOFOROU and YIGIT [27] proposed a bit-rock interaction law that considers a stiffness (k_c) at the bottom and calculate WOB as a function of the difference between bit axial position (x) and the formation surface (s) that is modeled as an harmonic function that varies on bit angular position and according to the bit's number of blades. This hypothesis is linked to roller-cone bits due to the lobe pattern this bit causes on rock formation [42]. In this model, WOB has an influence on TOB but torsional vibration has no effect on axial vibration. The TOB is expressed in terms of ROP, DOC, bit radius, a friction coefficient (μ) and a velocity-weakening function ($f(\dot{\theta}_{bit})$). ROP is calculated as a function of the applied WOB and the average bit speed (ω_d). The DOC is already regularized in this model by the velocity-weakening function. The formulation is shown in Eqs. 2.17, 2.18, 2.19, 2.20 and 2.21. The variables that have not been mentioned are constants.

$$\mathcal{W}_{ob} = \begin{cases} k_c(x - s) & \text{if } x \geq s, \\ 0 & \text{if } x < s, \end{cases} \quad (2.17)$$

$$t_{bit} = F(x, \theta_{bit})[\mu f(\dot{\theta}_{bit}) + \zeta \sqrt{r_h \delta_c}] \quad (2.18)$$

$$\delta_c = \frac{2\pi \dot{u}_{bit}}{\omega_d} \quad (2.19)$$

$$\dot{u}_{bit} = c_1 F_0 \sqrt{\omega_d} + c_2 \quad (2.20)$$

$$f(\dot{\theta}_{bit}) = \tanh(\dot{\theta}_{bit}) + \frac{\alpha_1 \dot{\theta}_{bit}}{(1 + \alpha_2 \dot{\theta}_{bit}^2)} \quad (2.21)$$

In 2004, NAVARRO-LÓPEZ *et al.* [8] considered two bit-rock interaction laws. They were both non-regularized dry friction torques which decays with bit velocity. The difference relies on the consideration of a WOB as constant or as an harmonic function that varies with time. The interaction law is shown in Fig.2.7 and in Eq. 2.22 where T_{eb} is the torque for equilibrium, D_v is constant and defines the zero velocity band, $\dot{\theta}_{bit}$ is bit speed, T_{sb} is the maximum static friction torque, T_{cb} is the kinetic friction torque and γ_b is a constant.

$$t_{bit} = \begin{cases} T_{eb} & , \dot{\theta}_{bit} < D_v \text{ and } |T_{eb}| < T_{sb} \\ T_{sb} \text{sign}(T_{eb}) & , \dot{\theta}_{bit} < D_v \text{ and } |T_{eb}| > T_{sb} \\ T_{cb} + (T_{sb} - T_{cb})e^{-\gamma_b \theta_{bit}} \text{sign}(\dot{\theta}_{bit}) & , \dot{\theta}_{bit} > D_v \end{cases} \quad (2.22)$$

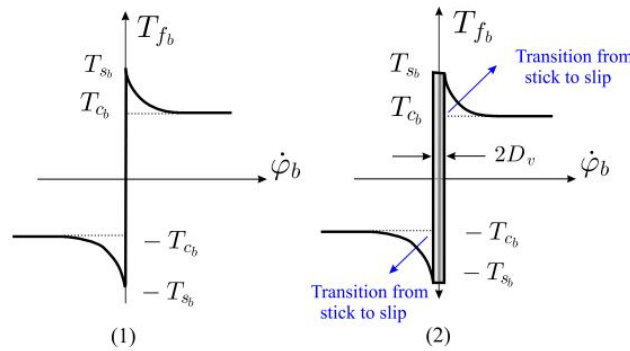


Figure 2.7: Bit-rock interaction proposed by NAVARRO-LÓPEZ *et al.* [8]

In 2004, RICHARD *et al.* [28] presented a coupling between torsional and axial modes done through the bit-rock interaction and using the concepts developed in [29]. The bit-rock interaction was modeled by joining the cutting and friction forces as in Eqs. 2.5, 2.6 and 2.7. The cutting forces are modeled in terms of the depth of cut that depend on the bit position (u_{bit}) at a previous time, thus introducing delay

differential equation in the system as in Eq. 2.23. This previous time ($t - t_n$) is calculated in order to respect Eq. 2.24 and corresponds to the instant in which the blade was in the same angular position as the previous blade at the current time. Later on, in 2007, RICHARD *et al.* [36] investigated a little further the effects of this model in drill-string dynamics with a linear stability analysis and linking the model to E-S diagrams and experimental observations. In 2009, GERMAY *et al.* [35] presented the relation between TOB and bit speed for one stick-slip cycle as reproduced in Fig. 2.8.

$$\delta_c = u_{bit}(t) - u_{bit}(t - t_n) \quad (2.23)$$

$$\theta_{bit}(t) - \theta_{bit}(t - t_n) = 2\pi/n \quad (2.24)$$

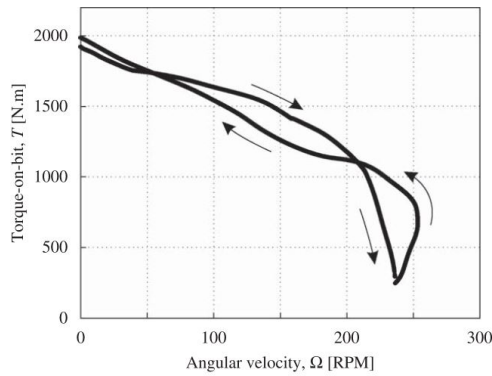


Figure 2.8: Relation between TOB and bit angular velocity obtained by GERMAY *et al.* [35]

In 2006, YIGIT and CHRISTOFOROU [31] proposed a modification on the bit-rock interaction law presented in [27]. It was included a linear term in the velocity-weakening function on the bit-rock interaction law. This way, the term $\mu f(\dot{\theta}_{bit})$ becomes $\mu(\dot{\theta}_{bit})$ as in Eq. 2.25. Although this modeling is associated to roller cone bits, the authors used parameters for typical PDC bit drilling on hard formations in the simulations.

$$\mu(\dot{\theta}_{bit}) = \mu_0 \left(\tanh(\dot{\theta}_{bit}) + \frac{\alpha_1 \dot{\theta}_{bit}}{(1 + \alpha_2 \dot{\theta}_{bit}^{2\gamma})} + \nu \dot{\theta}_{bit} \right) \quad (2.25)$$

In 2007, KHULIEF *et al.* [32] assumed that WOB (W) fluctuates around a mean value (W_0) with a frequency related to DOC and ROP. After some manipulations, it is stated that WOB actually fluctuates according to the angular position of the bit (θ_{bit}) and it can be calculated as in Eq. 2.26. The torque on the bit was modeled as a friction torque and it was a function of WOB, a coefficient of friction (μ) and the continuous function proposed in [27] and reproduced in Eq. 2.21.

$$\mathcal{W}_{ob} = \mathcal{W}_0 + k_f \delta_c (1 - \sin(\theta_{bit})) \quad (2.26)$$

$$t_{bit} = \mu \mathcal{W}_{ob} f(\dot{\theta}_{bit}) \quad (2.27)$$

In 2013, LIU *et al.* [38] used a bit-rock interaction law based on the formulation proposed by [35] but the authors included a velocity-weakening effect on the friction part of both TOB and WOB. This effect was included by multiplying the original formula by the function reproduced in Eq. 2.28, where ϵ , f_0 , f_1 and α are constants.

$$Z(\dot{\theta}_{bit}) = \frac{2}{\pi} \arctan(\epsilon \dot{\theta}_{bit}) \left(\frac{f_1 - f_0}{1 + \alpha |\dot{\theta}_{bit}|} + f_0 \right) \quad (2.28)$$

In 2014, KAMEL and YIGIT [39] proposed a modification of the bit-rock interaction model presented in [36] to account for phases I and II of the cutting model proposed by [43]. The authors also used a Heaviside function (Eq. 2.31) in the friction part of WOB to avoid the singularity. Another Heaviside function (Eq. 2.32) was included in frictional TOB to account for negative velocities. The new frictional TOB and WOB are reproduced in Eqs. 2.29 and 2.30. The variable δ_c^* is a critical DOC where the transition between phases occurs, l is the wearflat length and the other variables are constants obtained experimentally.

$$W_f = \begin{cases} 0 & \text{if } \delta_c \leq 0, \\ k_c \delta_c & \text{if } \delta_c < \delta_c^*, \\ r_b \sigma l f(\dot{u}_{bit}) & \text{if } \delta_c \geq \delta_c^*, \end{cases} \quad (2.29)$$

$$T_f = \gamma (W_f) \frac{r_b}{2} \mu f(\dot{\theta}_{bit}) \quad (2.30)$$

$$f(\dot{u}_{bit}) = \frac{1}{1 + e^{a_1 \dot{u}_{bit} + b_1}} \quad (2.31)$$

$$f(\dot{\theta}) = \tanh(a_2 \dot{\theta}_{bit} + b_2) \quad (2.32)$$

In 2016, HONG *et al.* [40] presented a new bit-rock interaction law based on the experimental data presented in [2] and the observation made by [41] that the relation between TOB and bit speed presents a hysteresis effect. A hysteretic dry friction formulation was used with velocity-weakening effect as shown in Fig. 2.9. When the velocity is increasing, the model is the same used in [27] and the function $f_+(\dot{\theta}_{bit})$ was already reproduced in Eq. 2.21 as $f(\dot{\theta}_{bit})$. When it decreases, a new function is proposed (Eq. 2.35) and a much lower friction torque is reached when bit sticks. Accordingly to Eq. 2.33, when bit is stuck, the torque is calculated in order to maintain the equilibrium at the bit (T_d).

$$t_{bit} = \begin{cases} T_d & \text{if } |\dot{\theta}_{bit}| < D_v \text{ and } T_f \geq |T_d|, \\ T_f & \text{else} \end{cases} \quad (2.33)$$

$$T_f = \begin{cases} \mathcal{W}_{ob} r_b f_+(\dot{\theta}_{bit}) & \text{if } \text{sign}(\dot{\theta}_{bit} \ddot{\theta}_{bit}) > 0, \\ \mathcal{W}_{ob} r_b f_-(\dot{\theta}_{bit}, \ddot{\theta}_{bit}) \text{sign}(\dot{\theta}_{bit}) & \text{if } \text{sign}(\dot{\theta}_{bit} \ddot{\theta}_{bit}) < 0, \end{cases} \quad (2.34)$$

$$f_-(\dot{\theta}_{bit}, \ddot{\theta}_{bit}) = 0.97 - \frac{f + \Delta f \frac{1}{1 + \frac{|\dot{\theta}_{bit}|}{\nu}} - f_2}{f_2 \left(1 + \left(\frac{\dot{\theta}_{bit} - \tau \ddot{\theta}_{bit}}{\nu} \right)^2 \right)} \quad (2.35)$$

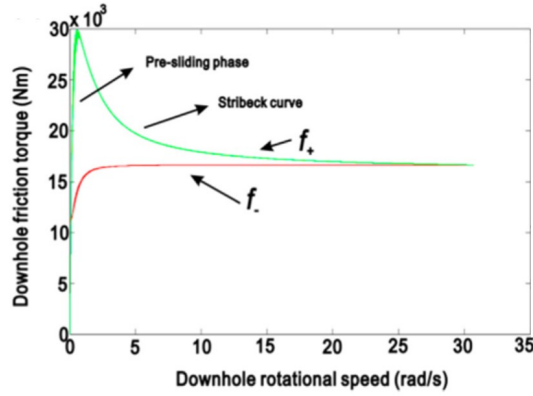


Figure 2.9: Bit-rock interaction law proposed by HONG *et al.* [40]

In 2017, QIU *et al.* [44] modeled a drill-string using the finite element method and the bit-rock interaction was based on the model developed by RICHARD *et al.* [28]. They proposed a modification on the formulation of DOC: it is calculated in terms of the axial displacement at each time step rather than using the delay approach as proposed in [28].

Also in this year, RITTO *et al.* [45] proposed a different function for the bit-rock interaction (Fig. 2.10) based on field measurements acquired at 50 Hz. The bit-rock interaction law consisted of three bit speed regions, according to Eq. 2.36. A linear function was used to fit bit-rock interaction in the first two regions and a cubic function for the last region. The authors used a lumped parameter model to describe drill-string torsional dynamics and the results presented a good agreement with field measurements. A stability map was calculated using the fitted model and it could predict the severity of the field measurements. It was concluded that a simple torsional lumped parameter model can tackle the problem of torsional stability.

$$t_{bit} = \begin{cases} r_b(a_0 + a_1\dot{\theta}_{bit})1.36 & \text{for } \dot{\theta}_{bit} \in [0.0, 3.5] \\ r_b(a_2 + a_3\dot{\theta}_{bit})1.36 & \text{for } \dot{\theta}_{bit} \in [3.5, 8.0] \\ r_b(a_4 + a_5\dot{\theta}_{bit} + a_6\dot{\theta}_{bit}^2 + a_7\dot{\theta}_{bit}^3)1.36 & \text{for } \dot{\theta}_{bit} \in [8.0, 240] \end{cases} \quad (2.36)$$

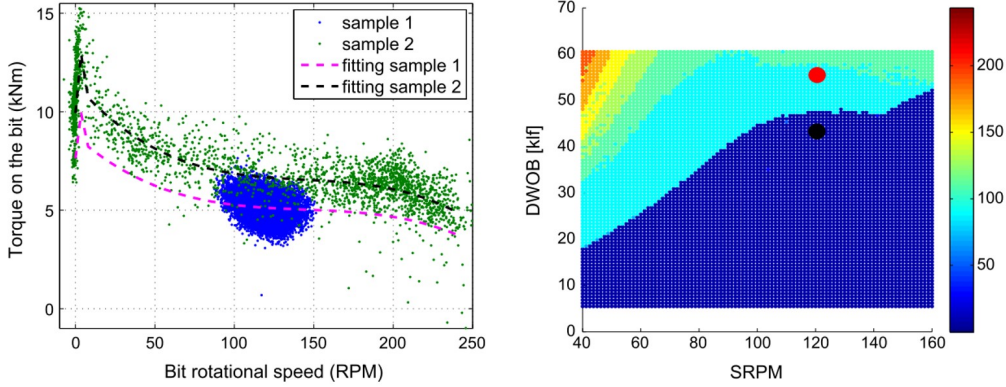


Figure 2.10: Bit-rock interaction law and stability map proposed by RITTO *et al.* [45]. The second figure represents the stability map: the colored gradient is stick-slip severity; y-axis is the WOB; and x-axis is the speed on surface. The red dot represents the unstable measured data and the black dot is stable one.

In 2018, REAL *et al.* [46] proposed a novel hysteretic bit-rock interaction model for the torsional dynamics of drill-strings. The authors present some experimental data that indicates that the TOB depends not only on bit speed, but also on bit acceleration. The bit-rock interaction model is reproduced in Eq. 2.37, in which b_0 to b_5 are positive constants, $\text{sign}(x) = \frac{x}{|x|}$ and $H(\dot{\theta}_{bit}, \ddot{\theta}_{bit})$ is hysteretic function defined in Eq. 2.38, in which β_1 and β_2 are positive constants. Figure 2.11 shows the proposed bit-rock interaction model against experimental data of one stick-slip cycle.

$$t_{bit} = b_0 \left(\tanh(b_1 \dot{\theta}_{bit}) + \frac{b_2 |\dot{\theta}_{bit}|^{b_4} \text{sign}(\dot{\theta}_{bit})}{1 + b_3 |\dot{\theta}_{bit}|^{b_5}} (1 + H(\dot{\theta}_{bit}, \ddot{\theta}_{bit})) \right), \quad (2.37)$$

$$H(\dot{\theta}_{bit}, \ddot{\theta}_{bit}) = \beta_1 \tanh(\beta_2 \ddot{\theta}_{bit}) \text{sign}(\dot{\theta}_{bit}) \quad (2.38)$$

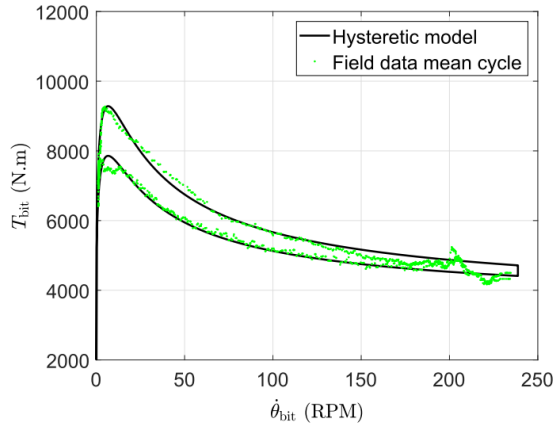


Figure 2.11: Hysteretic bit-rock interaction model and experimental data for one stick-slip cycle. Adopted from [46].

2.3 Uncertainty quantification in drill-string vibration

The first probability approach dates back to 1958, when BOGDANOFF and GOLDBERG [47] considered random forces acting at the bit. The model considered axial and torsional vibrations. The authors assumed that random forces acted at the bit and discussed the advantage of this approach over a deterministic analysis. In 1961, the same authors published the continuation of this investigation. In this new approach, the forces acting at the sides of the pipes were also considered random. The objective was to investigate the stresses in BHA and discuss the advantages of statistical analysis.

DAREING and LIVESAY [14] analyzed experimental data in 1968 and concluded that the acceleration on the bit was random and that it was probably caused by bit teeth impacting a rock of random hardness. This observation increased the perception of the role of randomness in the drill-string dynamics.

In 1997, KOTSONIS and SPANOS [49] studied the random lateral vibration of drill-strings taking into account the fluid damping, wall contact, eccentric collars and initial curvature of the collar. The difference from other models relies on the consideration of dynamic WOB that is time variant with zero mean and described by a stationary random process. The chaotic and random whirling are then assessed.

In 2002, SPANOS *et al.* [50] proposed a stochastic approach to study lateral vibrations of a drill-string considering the lateral excitation of the BHA as uncertain. A finite element model was used accounting for the string-wall interaction and the standard deviation of the lateral motion of drill-bit has been calculated.

In 2009, RITTO *et al.* [37] studied the random vibration of a drill-string. Uncertainties were included in the bit-rock interaction using the non-parametric method

introduced by SOIZE [51]. This method consists of the usage of random matrices inside the finite element formulation. It was shown that uncertainties considerably affect the system response.

In 2010, RITTO *et al.* [52] introduced a robust optimization of drilling parameters with the objective to maximize the mean ROP respecting the integrity limits. The optimization was said to be robust because the model considers uncertainties on the bit-rock interaction. The model considered axial and torsional motion and the drill-string was discretized through finite element method.

In 2013, QIU and YANG [53] studied the random vibration of a drill-string using the Euler-Bernoulli beam theory together with the finite element method to describe drill-string dynamics. The model was axial-torsional and lateral-torsional coupled. The bit-rock interaction law was modeled as in [31]. The randomness was included by adding a Gaussian white noise in the excitation part of the equations. The stochastic results were analyzed through the mean and standard deviation of bit speed.

In 2014, PERCY [54] studied the vibration of drill-string considering the torsional and lateral dynamics. The model is constructed based on Euler-Bernoulli beam theory and the finite element method is applied to obtain the numerical solution. At first, the results from the deterministic model are investigated and the influence of different parameters is assessed. After, the author modeled some geometric parameters as random variables and analyzed the influence of such uncertainties on vibration modes. Finally, one parameter of bit-rock interaction is also modeled as a random variable and the stochastic dynamical response is analyzed through statistics of the stick-slip severity.

In 2017, QIU *et al.* [44] investigated the random vibration of drill-strings by considering a random excitation in the bit-rock interaction. The excitation was treated as a Gaussian white noise. A statistical linearization was applied in order to use the Newmark algorithm to solve the dynamic system. The results were compared to Monte Carlo simulations and the statistics of the results were assessed.

Also in 2017, LOBO *et al.* [55] presented a stochastic analysis of the torsional dynamics of a drill-string when there is a transition between two rock layers. A simple model with 1 DOF was used. The transition was modeled with 3 different functions and the parameters of the transition were considered uncertain. They concluded that different shapes of transition imply in different dynamic responses. These differences are clearer in stochastic response.

In the same year, REAL *et al.* [56] proposed a new strategy for modeling uncertainties in the substructures and interfaces of dynamical systems. This strategy is based on the Craig-Bampton method and on the nonparametric probabilistic approach proposed by SOIZE [51]. The main contribution relies on the possibility of

introducing uncertainties on inner and interface degrees of freedom separately. The authors applied this strategy to the torsional dynamics of drill-strings. The deterministic model is constructed by means of the finite element method. The mass, damping and stiffness matrices are then modeled as stochastic matrices and the proposed strategy is compared to another two classical strategies. For the same level of uncertainties, all the strategies presented results very similar, indicating that the proposed strategy is consistent. Finally, an investigation is carried out to determine the effect of each uncertainty on the dynamical response.

In 2018, NOGUEIRA and RITTO [57] investigated the stochastic torsional stability of a drill-string. The authors used a mathematical model based on classical torsion theory discretized by means of the finite element model. The variables considered random were the mud density, the friction constant of bit-rock interaction, the confined compressive strength of the rock and the damping ratios. The distribution used to describe each variable is derived by using the maximum entropy principle. Finally, Monte Carlo simulations are carried out to construct a stochastic stability map. The influence of each random variable is assessed.

In 2019, DO [58] considered the parameters of bit-rock interaction as Lévy processes. This process is decomposed into three components: a constant drift, a Brownian motion and a pure jump process. The main idea relies on the modeling of the uncertainties in bit-rock interaction plus the jump effect when the rock is cracked during an operation. The crack of the rock will cause the force and moment acting on the bit to change abruptly. A Lyapunov-type theorem is developed to study well-posedness, stability in moment, and almost sure stability of nonlinear stochastic differential equations. Finally, a robust and an adaptive controllers are designed using this theorem and the backstepping method.

2.4 Experimental investigation of drill-string vibration

One of the first experimental investigations of drill-string dynamics available in literature dates back to 1960 and was performed by FINNIE and BAILEY [13]. They developed an equipment to measure axial force, torque and axial and rotational motions at the top of a drill string. In [13], they described the equipment developed. The natural frequencies measured during the operation were much different from those predicted in [12]. According to the authors, the most interesting phenomenon was the interaction between torsional and axial motions. It was clear that surface measurements were not enough to understand the dynamic behavior of the drill-string. Moreover, in 1994, DYKSTRA *et al.* [59] verified that the amplitude of

vibrations at the bit rapidly diminished with the distance from the bit which confirms the need for downhole data.

DEILY *et al.* [60] developed in 1968 a self-contained tool to measure forces and motions during the actual drilling process. It was the first time that forces were measured downhole. The tool recorded eight signals on a magnetic tape in offline mode: axial, torsional and bending loads; axial, angular and lateral accelerations; and internal and annular pressure. The authors noted weight variations in excess of 3.5 times the mean value due to bit bounce. In normal drilling, the weight variations were about 25 to 50 percent of the mean value. The torque variations were generally less than weight variations but a coupling between these two variables was found. This work provided evidence of the differences between surface and downhole vibration modes.

CUNNINGHAM [61] presented a paper with some additional discussions on the measurements acquired using the equipment described by DEILY *et al.* [60]. The author noted stick-slip vibration for the first time, where the RPM reached values from 0 to 96 rpm. He also noted large losses of rotary power along the drill-string. The author identified two sources of axial fluctuations: rotation of the drill-string with bottom disturbances that can cause a vibration with frequency three times the rotational speed with a three-cutter bit; and the pulsation of mud pump pressure fluctuations.

In 1991, DUFEYTE and HENNEUSE [4] published an article where they investigated 3500 hours of field data obtained between 1988 and 1990. They observed stick-slip oscillation in roughly 50% of the time. In these situations, maximum downhole rotational speed could reach 10 times the speed at the surface. The data showed how destructive this phenomenon is and its consequences. At the surface, this phenomenon was characterized by variations in torque (as observed by DAWSON *et al.* [6]). These variations are linked to the length of the drill pipes and the rotational speed. The authors also analyzed the effect of several parameters on the dynamics. The lithology appeared to have the most influence on the development of stick-slip oscillations. As a solution for stick-slip, the authors suggest to increase the rotational speed and reduce WOB as a first aid, but a permanent solution would be to control the drive (as suggested by other authors) and to use lubrication.

In 1992, DETOURNAY and DEFOURNY [29] investigated the drilling response of PDC bits. The authors studied the relations between weight-on-bit (WOB), torque on bit (TOB), bit rotational speed and rate of penetration. The bit-rock interaction forces are decomposed into cutting and frictional components. The cutting component is proportional to the depth-of-cut and the frictional components of TOB and WOB are linearly related. Two quantities are proposed to study the relations under investigation: specific energy and drilling strength. Experimental

data shows that the data points cluster along a line in the diagram constructed by these two quantities.

In 1994, DYKSTRA *et al.* [59] performed laboratory and field tests to investigate the dynamics of a drill bit and a drill-string. The field test suggested that bit whirl was not detectable at the surface and the stabilizers played an important role in diminishing vibration magnitude. The vibration generated by PDC bits were much worse than by roller cone bits. Otherwise, it was concluded that anti-whirl PDC bits vibrate with amplitudes around an order of magnitude less than conventional PDC bits. Based on the experiments, other operational guidelines and drill-string configurations were suggested in order to reduce downhole vibration.

In 2003, MELAKHESSOU *et al.* [62] studied the nonlinear interaction between drill-string and wellbore wall through numerical and experimental approaches. The experimental rig is designed to represent the portion of BHA which is under compression. The rig is composed of an electrical motor that is connected to a torquemeter and a rod. In the middle of the rod, a disc is attached to represent tool-joint. This disc is inside a cylinder that represents the wellbore wall. At the end of the rod, a break is placed in order to provide torque. The lateral displacements were measured by two optoelectronic cameras. The test-rig was capable of reproducing forward and backward whirl. The backward whirl was obtained only by increasing the friction between the disc and the cylinder by adding rubber to cylinder inner surface.

In 2008, RAYMOND *et al.* [63] designed a test-rig to investigate drill-string axial vibrations and find the best operational parameters that eliminate this vibration. The experimental actually drills a rock sample in the laboratory.

In 2009, KHULIEF and AL-SULAIMAN [64] presented an experimental test-rig capable of simulating the drill-string vibration for a variety of excitation mechanisms: stick-slip, well-borehole contact and drilling fluid interaction. The setup consists of a variable speed motor, a stainless steel vertical shaft, a Plexiglas pipe as a wellbore with fluid inside, a magnetic brake to simulate stick-slip and a shaker used to excite drill-string axially. The constructed test-rig was successfully used to tune model parameters.

In 2010, FRANCA [65] presented a new model for the drilling response of roller-cone bits (RC bits). The author inspired himself on the work of DETOURNAY and DEFOURNY [29]. In order to validate the model, the author performed a series of laboratory tests with an in-house designed drilling rig. The upper assembly is composed by a geared brushless motor and a linear actuator which together can provide a precise rate of penetration from 0.01 mm/s to 100 mm/s. The bit assembly is composed by a roller-cone bit, a shaft and sophisticated anvil. In this test-rig, the rock sample is driven at a constant speed while the bit and shaft are stationary.

In 2012, ESMAEILI *et al.* [66] constructed a fully automated laboratory scale

drilling rig called the CDC miniRig. The experimental setup actually drills rock samples and consists of a steel frame, drawwork, top drive, weights, measurement sensors, drill-string, drill bit and a control unit. Several experimental runs were carried out and the influence of each parameter was assessed.

In 2013, VLAJIC *et al.* [67] studied the torsional vibration of a rotor enclosed within a stator subjected to dry friction. The experimental results showed forward and backward whirl, as well as impacting motions. The experimental results are compared to simulations of a finite dimensional model and it was concluded that the numerical simulations are found to capture the phenomena observed in experiments.

In 2015, KAPITANIAK *et al.* [68] presents a novel experimental rig capable of reproducing all major types of drill-string vibrations, such as stick-slip oscillations, whirling, drill bit bounce and helical buckling. The experimental rig uses commercial drill-bits and rock samples. Furthermore, a low-dimensional model is developed and calibrated based on a torsional pendulum. In addition, a more sophisticated model is also constructed by means of the finite element method. The experimental and numerical results demonstrate the predictive capabilities of the mechanical models proposed.

In 2015, CAYRES *et al.* [69] proposed a test-rig to simulate the torsional vibration of drill-strings. This test-rig is composed by a slender shaft in horizontal position and two breaking discs: one simulates the bit-rock interaction and the other simulates the contact with the wellbore wall.

In 2017, WIERCIGROCH *et al.* [70] reviewed the development and the analysis of the axial-torsional coupled 2-DOF model which assumes a state-dependent delay and a viscous damping. The authors used the experimental data obtained in test-rig described by [68] to analyze this model and propose a new one that considers a non-uniform distribution of blades which is intended to avoid unrealistic regenerative types of instabilities.

In 2017, LIU *et al.* [71] developed a small-scale drilling rig to drive a parametric study of the stick-slip phenomenon. The parametric study involved two flexible shafts with different mechanical properties. The results showed that varying some of the mechanical properties could drive the nature of the stick-slip oscillations.

In 2018, KAPITANIAK *et al.* [72] investigated forward and backward whirls on the very same test-rig proposed in [68]. The experimental results showed the co-existence of both whirling motions and characterized the parameter space in which different whirls can be observed.

In 2018, REAL *et al.* [73] developed a novel low-cost test-rig capable of reproducing drill-string torsional vibration, including stick-slip. The test-rig is mainly composed by a DC motor, a flexible shaft, an inertial disk and a masonry bit. At the bottom, a concrete test-body is lifted by an electrical jack in order to simu-

late the drilling procedure. The experimental results obtained are in agreement with experimental studies found in the literature. This is the test-rig in which the Appendix A is based on.

Chapter 3

Deterministic numerical investigation

3.1 Base model

The drill-string model is represented in Fig. 3.1. It is composed of two main parts: Drill-pipes and BHA. Each part has different characteristics and a node is placed in the transition between them in the problem formulation. At the top, a constant speed is imposed by the rotary table and an axial force (Hook Load) is applied to sustain part of the drill-string weight. At the bottom, the forces due to bit-rock interaction are added. Each part of this model will be explained in the following.

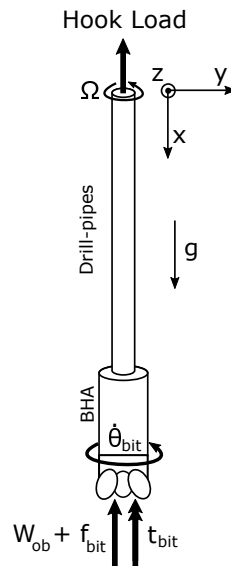


Figure 3.1: Schematic view of the system.

The equations of motion for the system are derived through Hamilton's principle. It states that the development in time for a mechanical system is such that the integral of the difference between the kinetic and the potential energy is stationary,

i.e. the variation is zero. The extended Hamilton's principle accounts for non-conservative forces and can be written as:

$$\delta\Pi = \int_{t_1}^{t_2} (\delta U - \delta T - \delta W) dt = 0, \quad (3.1)$$

where U is the potential strain energy, T is the kinetic energy and W is the work done by the nonconservative forces and the forces not accounted in the potential energy. At this point, only the internal forces and gravity are going to be considered in the following formulation. The boundary conditions and external forces are included at the end of the formulation, after the finite element discretization. The kinetic energy is written as:

$$T = \frac{1}{2} \int_0^L (\rho A \dot{u}^2 + \rho I_p \dot{\theta}_x^2) dx, \quad (3.2)$$

where u is the axial displacement, θ_x is the angular displacement, x is the position along drill-string, ρ is the mass density, A is the cross sectional area, I_p is the cross sectional polar moment of inertia, L is the length of drill-string. The variation of kinetic energy is expressed by:

$$\delta T = - \int_0^L (\rho A \dot{u} \delta u + \rho I_p \ddot{\theta}_x \delta \theta_x) dx. \quad (3.3)$$

The work done by gravity force is accounted for in W calculation as:

$$W = \int_0^L \rho g A u dx, \quad (3.4)$$

where g is the gravity acceleration. The variation of Eq. 3.4 is given as:

$$\delta W = \int_0^L \rho g A \delta u dx. \quad (3.5)$$

The last term of Hamilton's Principle formulation is the strain energy that is written as:

$$U = \frac{1}{2} \int_V \boldsymbol{\epsilon}^T [S] dV, \quad (3.6)$$

where V is the volume, $\boldsymbol{\epsilon}$ is the Green-Lagrange strain tensor in Voigt notation, $[S]$ is the second Piola-Kirchoff stress tensor in Voigt notation. To calculate the potential strain energy, the Green-Lagrangian strain tensor is used and it is expressed as a function of the displacements by:

$$\mathbf{E} = \frac{1}{2} \left[\left(\frac{d\mathbf{p}}{d\mathbf{x}_{ref}} \right) + \left(\frac{d\mathbf{p}}{d\mathbf{x}_{ref}} \right)^T + \left(\frac{d\mathbf{p}}{d\mathbf{x}_{ref}} \right)^T \left(\frac{d\mathbf{p}}{d\mathbf{x}_{ref}} \right) \right], \quad (3.7)$$

where \mathbf{p} is the displacement field vector. It depends on the point reference coordinates $\mathbf{x}_{ref} = (x, y, z)$, where x is in the axial direction and y and z are perpendicular to the axial direction, and on the coordinates after deformation, called \mathbf{x} . The displacements due to torsion and traction are illustrated in Fig. 3.2 and they are written as:

$$\mathbf{p} = \begin{bmatrix} u_x \\ u_y \\ u_z \end{bmatrix} = \mathbf{x} - \mathbf{x}_{ref} = \begin{bmatrix} u \\ y \cos(\theta_x) - z \sin(\theta_x) - y \\ y \sin(\theta_x) + z \cos(\theta_x) - z \end{bmatrix} \quad (3.8)$$

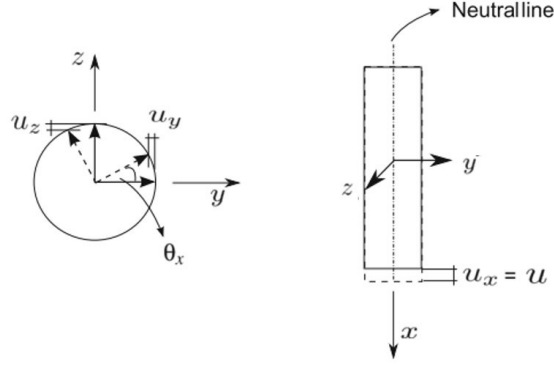


Figure 3.2: Displacement Field. Adapted from [52].

The components of the Green-Lagrangian strain tensor are calculated and only the non-zero terms are considered. Finite strains are considered. The strain tensor non-zero components are given as:

$$\epsilon_{xx} = u_{x,x} + \frac{1}{2}(u_{x,x}^2 + u_{y,x}^2 + u_{z,x}^2) \quad (3.9)$$

$$\epsilon_{xy} = \frac{1}{2}(u_{y,x} + u_{x,y} + u_{x,x}u_{x,y} + u_{y,x}u_{y,y} + u_{z,x}u_{z,y}) \quad (3.10)$$

$$\epsilon_{xz} = \frac{1}{2}(u_{z,x} + u_{x,z} + u_{x,x}u_{x,z} + u_{y,x}u_{y,z} + u_{z,x}u_{z,z}) \quad (3.11)$$

Considering the constitutive equation $\mathbf{S} = [C]\boldsymbol{\epsilon}$ and substituting it into Eq. 3.6, the variation of potential strain energy can be calculated as:

$$\delta U = \int_V \delta \boldsymbol{\epsilon}^T [C] \boldsymbol{\epsilon} dV = \int_V \delta \boldsymbol{\epsilon}^T \begin{bmatrix} E & 0 & 0 \\ 0 & G & 0 \\ 0 & 0 & G \end{bmatrix} \boldsymbol{\epsilon} dV, \quad (3.12)$$

where $\boldsymbol{\epsilon} = [\epsilon_{xx} \quad 2\epsilon_{xy} \quad 2\epsilon_{xz}]^T$. The Eqs. 3.9, 3.10 and 3.11 are substituted inside Eq. 3.12 and it can now be expressed by a sum of two terms: linear (δU_L) and non-linear (δU_{NL}):

$$\delta U_L = \int_0^L [\delta u'(EAu') + \delta \theta'(GI_0\theta')] dx, \quad (3.13)$$

$$\begin{aligned} \delta U_{NL} = \int_0^L \delta u' \left[\frac{EA}{2}(3u'^2 + u'^3) + \frac{EI_0}{2}(\theta'^2 + u'\theta'^2) \right] dx + \\ \int_0^L \delta \theta' \left[\frac{EI_0}{2}(2u' + u'^2)\theta' + \frac{EI_{02}}{2}\theta'^3 \right] dx, \end{aligned} \quad (3.14)$$

where I_0 is the moment of inertia, and; I_{02} is a generalized cross-sectional constant defined by $I_{02} = \int_A (y^2 + z^2)^2 dA$. The equation of motion is discretized by mean of the finite element method (FEM). One element is illustrated in Fig. 3.3, where $\xi = x/l_e$ is the transformed coordinate and l_e is the length of the element. The elementary displacement vector is given by $\mathbf{u}_e = [u_1 \ \theta_1 \ u_2 \ \theta_2]^T$, where u_i and θ_i are the axial and torsional displacements in node i , respectively.

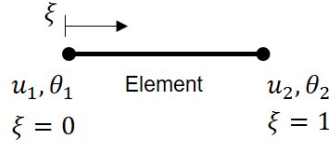


Figure 3.3: Element.

The displacement field for this element is a function of the time and space. This displacement and its derivative in space ($d/d\xi$) are calculated according to the following equations:

$$u = \mathbf{n}_u(\xi)\mathbf{u}_e(t), \quad \theta = \mathbf{n}_\theta(\xi)\mathbf{u}_e(t), \quad (3.15)$$

$$u' = \frac{1}{l_e}\mathbf{n}'_u\mathbf{u}_e(t), \quad \theta' = \frac{1}{l_e}\mathbf{n}'_\theta\mathbf{u}_e(t), \quad (3.16)$$

where $\mathbf{n}_u = [1 - \xi \ 0 \ \xi \ 0]$, $\mathbf{n}_\theta = [0 \ 1 - \xi \ 0 \ \xi]$, $\mathbf{n}'_u = [-1 \ 0 \ 1 \ 0]$ and $\mathbf{n}'_\theta = [0 \ -1 \ 0 \ 1]$. Substituting the expressions above in the variational formulation, one gets:

$$\begin{aligned} \delta T^e &= \delta \mathbf{u}_e^T [M^e] \ddot{\mathbf{u}}_e, \\ \delta U_L^e &= \delta \mathbf{u}_e^T [K_e^e] \mathbf{u}_e, \\ \delta U_{NL}^e &= \delta \mathbf{u}_e^T [K_g^e] \mathbf{u}_e, \\ \delta W^e &= \delta \mathbf{u}_e^T \mathbf{f}_g^e, \end{aligned} \quad (3.17)$$

where $[M^e]$ is the mass matrix, K_e^e is the linear stiffness matrix, K_g^e is the nonlinear

stiffness matrix and \mathbf{f}_g^e is the gravity force vector. After some manipulations, those matrices and vector result in:

$$[M^e] = \int_0^1 (\rho A l_e \mathbf{n}_u^T \mathbf{n}_u + \rho I_0 l_e \mathbf{n}_\theta^T \mathbf{n}_\theta) d\xi, \quad (3.18)$$

$$[K_e^e] = \int_0^1 \left(\frac{EA}{l_e} \mathbf{n}_u'^T \mathbf{n}_u' + \frac{GI_0}{l_e} \mathbf{n}_\theta'^T \mathbf{n}_\theta' \right) d\xi, \quad (3.19)$$

$$\begin{aligned} [K_g^e] = & \int_0^1 \frac{EA}{2l_e} (3\mathbf{n}_u'^T \mathbf{n}_u' u' + \mathbf{n}_u'^T \mathbf{n}_u' u'^2) d\xi \\ & \int_0^1 \frac{EI_0}{2l_e} (\mathbf{n}_u'^T \mathbf{n}_\theta' \theta' + \mathbf{n}_u'^T \mathbf{n}_\theta' u' \theta') d\xi \\ & \int_0^1 \frac{EI_0}{2l_e} (2\mathbf{n}_\theta'^T \mathbf{n}_\theta' u' + \mathbf{n}_\theta'^T \mathbf{n}_u' u' \theta') d\xi \\ & \int_0^1 \frac{EI_{02}}{2l_e} (\mathbf{n}_\theta'^T \mathbf{n}_\theta' \theta'^2) d\xi \end{aligned}, \quad (3.20)$$

$$\mathbf{f}_g^e = \int_0^1 \rho g A l_e \mathbf{n}_u^T d\xi. \quad (3.21)$$

After calculating the integrals above, the mass and stiffness matrices and the force vector are obtained and shown in Eqs. 3.22, 3.23, 3.24 and 3.25. The nonlinear stiffness matrix remains in function of the space derivative of displacements that need to be calculated for every step of time in numerical integration.

$$[M^e] = \frac{\rho l_e}{6} \begin{bmatrix} 2A & 0 & A & 0 \\ 0 & 2I_0 & 0 & I_0 \\ A & 0 & 2A & 0 \\ 0 & I_0 & 0 & 2I_0 \end{bmatrix} \quad (3.22)$$

$$[K_e^e] = \frac{1}{l_e} \begin{bmatrix} EA & 0 & -EA & 0 \\ 0 & GI_0 & 0 & -GI_0 \\ -EA & 0 & EA & 0 \\ 0 & -GI_0 & 0 & GI_0 \end{bmatrix} \quad (3.23)$$

$$\begin{aligned}
[K_g^e] = & \frac{EA}{2l_e}(3u' + u'^2) \begin{bmatrix} 1 & 0 & -1 & 0 \\ 0 & 0 & 0 & 0 \\ -1 & 0 & 1 & 0 \\ 0 & 0 & 0 & 0 \end{bmatrix} + \frac{EI_0}{2l_e} \begin{bmatrix} 0 & \theta' & 0 & -\theta' \\ \theta' & u' & -\theta' & -u' \\ 0 & -\theta' & 0 & \theta' \\ -\theta' & -u' & \theta' & u' \end{bmatrix} \\
& + \frac{EI_0}{2l_e} \begin{bmatrix} 0 & \theta'u' & 0 & -\theta'u' \\ \theta'u' & 0 & -\theta'u' & 0 \\ 0 & -\theta'u' & 0 & \theta'u' \\ -\theta'u' & 0 & \theta'u' & 0 \end{bmatrix} + \frac{EI_{02}}{2l_e} \begin{bmatrix} 0 & 0 & 0 & 0 \\ 0 & \theta' & 0 & -\theta' \\ 0 & 0 & 0 & 0 \\ 0 & -\theta' & 0 & \theta' \end{bmatrix}
\end{aligned} \tag{3.24}$$

$$\mathbf{f}_g^e = \frac{\rho g A l_e}{2} [1 \ 0 \ 1 \ 0]^T \tag{3.25}$$

After assembling the elementary matrices and vector into the global ones, the external forces are included in the formulation and the equation of motion is finally expressed in Eq. 3.26.

$$[M]\ddot{\mathbf{u}}(t) + ([K_e] + [K_g(\mathbf{u}(t))])\mathbf{u}(t) = \mathbf{f}_g + \mathbf{f}_f + \mathbf{f}_T(\dot{u}_{bit}(t), \dot{\theta}_{bit}(t)), \tag{3.26}$$

where $\mathbf{f}_f = [0 \ \dots \ 0 \ -\bar{W}_{ob} \ 0]^T$ represents the axial force at the bit in which \bar{W}_{ob} is the desired weight-on-bit; and $\mathbf{f}_T(\dot{u}_{bit}(t), \dot{\theta}_{bit}(t)) = [0 \ \dots \ 0 \ -f_{bit}(\dot{u}_{bit}(t), \dot{\theta}_{bit}(t)) \ -t_{bit}(\dot{u}_{bit}(t), \dot{\theta}_{bit}(t))]^T$ represents the force and torque at the bit due to bit-rock interaction in which $t_{bit}(\dot{u}_{bit}(t), \dot{\theta}_{bit}(t))$ is the torque and $f_{bit}(\dot{u}_{bit}(t), \dot{\theta}_{bit}(t))$ is the axial force variation around the desired value for WOB. Note that the axial force and torque on the bit depends on the axial speed of the bit $\dot{u}_{bit}(t)$ and on the rotational speed of the bit $\dot{\theta}_{bit}(t)$, which are obtained by extracting the two last terms of $\dot{\mathbf{u}}(t)$. The total weight-on-bit is called $\mathcal{W}_{ob} = f_{bit} + \bar{W}_{ob}$.

3.2 Initial prestressed configuration

In order to simplify the problem, the change of variables $\mathbf{u}(t) = \mathbf{u}_d(t) + \mathbf{u}_s$ is used to evaluate the dynamics ($\mathbf{u}_d(t)$) around an initial prestressed configuration (\mathbf{u}_s). To calculate the equilibrium point, the angular motion is fixed at the top and the axial motion is fixed at the bit. This boundary condition is chosen based on the situation when the top motor is locked (i.e. drill-string is not rotating) and drill-string is in touch with bottom-hole in a way that the desired weight-on-bit is achieved and drill-bit cannot move downward. To implement this boundary condition, the second and (2n-1)th lines and columns are removed from all matrices and vectors, where

n is the number of nodes. The equilibrium point is static, thus all derivatives in time vanishes and the bit-rock interaction model is not considered. The nonlinear stiffness matrix is also ignored because the drill-string is not under torsion and $[K_g(\mathbf{u}(t))]$ is neglectable. The point is then calculated in Eq. 3.27 considering the desired weight-on-bit and the gravity force.

$$\mathbf{u}_s = [K_e]^{-1}(\mathbf{f}_g + \mathbf{f}_f). \quad (3.27)$$

After the computation of \mathbf{u}_s , the fixed DOFs need to be reinserted into the vector by adding zero elements in the 2nd and (2n-1)th positions. Then, the equation of motion can be expressed in terms of the new variables defined above and the full matrices (i.e. without boundary conditions):

$$[M]\ddot{\mathbf{u}}_d(t) + ([K_e] + [K_g(\mathbf{u}_s + \mathbf{u}_d(t))])\mathbf{u}_d(t) = \mathbf{f}_T(\dot{u}_{bit}(t), \dot{\theta}_{bit}(t)) - [K_g(\mathbf{u}_s + \mathbf{u}_d(t))]\mathbf{u}_s. \quad (3.28)$$

A proportional damping matrix is included in the equations and it is calculated as $[D] = \alpha[M] + \beta[K_e]$. The complete equation of motion can then be written as:

$$[M]\ddot{\mathbf{u}}_d(t) + [D]\dot{\mathbf{u}}_d(t) + ([K_e] + [K_g(\mathbf{u}_s + \mathbf{u}_d(t))])\mathbf{u}_d(t) = \mathbf{f}_T(\dot{u}_{bit}(t), \dot{\theta}_{bit}(t)) - [K_g(\mathbf{u}_s + \mathbf{u}_d(t))]\mathbf{u}_s. \quad (3.29)$$

3.3 Bit-rock interaction model

The next step is to define the bit-rock interaction model. The model chosen for this work is the one proposed by TUCKER and WANG [26]. This model is chosen because it considers the coupling between torsional and axial dynamics and it is a continuous regularized model, which is good for the computational cost. In addition, this model was calibrated using experimental data by TUCKER and WANG [26]. This model takes into account the coupling between axial and torsional vibrations. Based on drilling measurements under stable drilling conditions, the correlation between the main variables is defined as:

$$\dot{u}_{bit}(t) = -a_1 + a_2(\mathcal{W}_{ob}(\dot{u}_{bit}(t), \dot{\theta}_{bit}(t))) + a_3\dot{\theta}_{bit}(t), \quad (3.30)$$

$$t_{bit}(\dot{u}_{bit}(t), \dot{\theta}_{bit}(t)) = a_4 \frac{\dot{u}_{bit}(t)}{\dot{\theta}_{bit}(t)} + a_5. \quad (3.31)$$

The ratio $\dot{u}_{bit}(t)/\dot{\theta}_{bit}(t)$ represents the depth-of-cut and the coefficients are set as: $a_1 = 3.429 \cdot 10^{-3} \text{ m s}^{-1}$; $a_2 = 5.672 \cdot 10^{-8} \text{ m N}^{-1} \text{ s}^{-1}$; $a_3 = 1.374 \cdot 10^{-4} \text{ m rad}^{-1}$;

$$a_4 = 9.537 \cdot 10^6 \text{ N rad}; a_5 = 1.475 \cdot 10^3 \text{ N m}.$$

It is noticed that $t_{bit}(\dot{u}_{bit}(t), \dot{\theta}_{bit}(t))$ goes to infinite if the bit have zero rotational speed. Thus, it is necessary to regularize the calculation of the torque and axial speed at the bit in order to make it go to zero when rotational speed approaches zero. To do this, the following regularization function is defined:

$$Z(\dot{\theta}_{bit}(t)) = \frac{\dot{\theta}_{bit}(t)}{\sqrt{\dot{\theta}_{bit}^2(t) + \epsilon^2}}, \quad (3.32)$$

where ϵ is the regularization parameter set as $\epsilon = 2 \text{ rad/s}$. The torque and axial force at the bit can then be finally isolated and calculated according to:

$$f_{bit}(\dot{u}_{bit}(t), \dot{\theta}_{bit}(t)) = \frac{\dot{u}_{bit}(t)}{a_2 Z^2(\dot{\theta}_{bit}(t))} - \frac{a_3 \dot{\theta}_{bit}(t)}{a_2 Z(\dot{\theta}_{bit}(t))} + \frac{a_1}{a_2} - \bar{W}_{ob} \quad (3.33)$$

$$t_{bit}(\dot{u}_{bit}(t), \dot{\theta}_{bit}(t)) = a_4 Z^2(\dot{\theta}_{bit}(t)) \frac{\dot{u}_{bit}(t)}{\dot{\theta}_{bit}(t)} + a_5 Z(\dot{\theta}_{bit}(t)) \quad (3.34)$$

Fixing the WOB on 100 kN, i.e. $\mathcal{W}_{ob} = \bar{W}_{ob} = 100 \text{ kN}$, we can construct the classical TOBx $\dot{\theta}_{bit}$ curve for bit-rock interaction (Fig. 3.4).

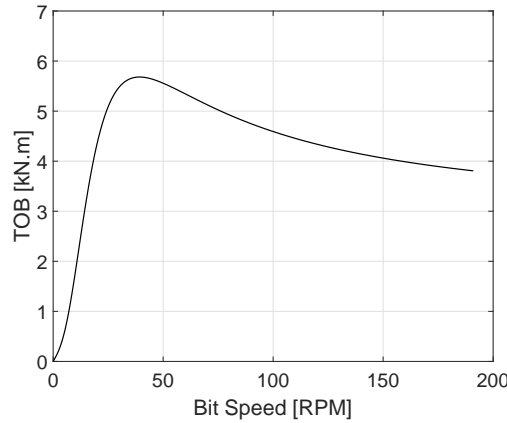


Figure 3.4: Bit-rock interaction model. $\mathcal{W}_{ob} = \bar{W}_{ob} = 100 \text{ kN}$.

In Appendix A, the bit-rock interaction model was experimentally investigated using a test-rig. The limitations and qualities of this model are discussed and it is concluded that this model can represent the drill-string dynamics. However, the main interest of this work is to analyze the deterministic and stochastic dynamics of a real-scale drill-string. Therefore, the calibration proposed by TUCKER and WANG [26] is going to be used, although it does not induce strong hysteric effects or large fluctuations on WOB.

3.4 Boundary conditions

For the simulation of the drilling operation, the boundary condition of a constant speed of Ω at the top is used. This decision is motivated by the fact that most of the drilling rigs use a PID control at the top in order to maintain the rotational speed constant at any costs. This control is very effective for maintaining a constant speed. Some other rigs use different types of control, like Torque-Feedback control [9].

The same strategy used to insert the boundary condition at the calculation of the equilibrium point is used again but with a small change. At first, the 2nd line is removed from all the matrices and vectors. After, the 2nd column of each matrix in the left side goes to the right side of the equation multiplying by the respective derivative of top angular DOF. The mass matrix does not appear on the right side because the speed at the top is constant and thus the acceleration is zero. Finally, the equation becomes:

$$[\bar{M}]\ddot{\bar{\mathbf{u}}}(t) + [\bar{D}]\dot{\bar{\mathbf{u}}}(t) + ([\bar{K}_e] + [\bar{K}_g(\mathbf{u}_s + \mathbf{u}_d(t))])\bar{\mathbf{u}}(t) = \bar{\mathbf{f}}_{\mathbf{T}}(\dot{u}_{bit}(t), \dot{\theta}_{bit}(t)) - \dots \\ \dots [\bar{K}_{gl}(\mathbf{u}_s + \mathbf{u}_d(t))]\mathbf{u}_s - \mathbf{d}_2\Omega - (\mathbf{k}_{e2} + \mathbf{k}_{g2}(\mathbf{u}_s + \mathbf{u}_d(t)))\Omega t, \quad (3.35)$$

where $\bar{\mathbf{u}}(t)$ is the displacement vector $\mathbf{u}_d(t)$ without the second line; $[\bar{M}]$, $[\bar{D}]$, $[\bar{K}_e]$ and $[\bar{K}_g]$ are the mass, damping, linear stiffness, and nonlinear stiffness matrices without the 2nd line and column, $\bar{\mathbf{f}}_{\mathbf{T}}(\dot{u}_{bit}(t), \dot{\theta}_{bit}(t))$ is the bit-rock interaction force without the 2nd line, $[\bar{K}_{gl}(\mathbf{u}_s + \mathbf{u}_d(t))]$ is the nonlinear stiffness matrix without only the 2nd line, and \mathbf{d}_2 , \mathbf{k}_{e2} and $\mathbf{k}_{g2}(\mathbf{u}_s + \mathbf{u}_d(t))$ are vectors composed by the 2nd column of damping, linear stiffness, and nonlinear stiffness matrices already without the 2nd line.

3.5 Reduced-order model

The development of the reduced-order model ignores the nonlinear stiffness matrix because it is concluded in Section 3.6.1 that it does not influence the drill-string dynamics for the model and operational conditions considered in this work. Thus, the nonlinear terms of stiffness matrix in Eq. 3.35 are ignored and the equation of motion becomes:

$$[\bar{M}]\ddot{\bar{\mathbf{u}}} + [\bar{D}]\dot{\bar{\mathbf{u}}} + [\bar{K}_e]\bar{\mathbf{u}} = \bar{\mathbf{f}}_{\mathbf{T}}(\dot{u}_{bit}, \dot{\theta}_{bit}) - \mathbf{d}_2\Omega - \mathbf{k}_{e2}\Omega t, \quad (3.36)$$

The reduction of the model improves the computational costs and, thus, makes stochastic calculations quite faster. The reduction consists in the usage of a more efficient base for the variables of the system. A very common base is the normal

modes of the system and this is the approach adopted in this work.

The first step is to choose the base of normal modes. The first modes to be considered are the rigid modes because drill-string is rotating at a constant speed at the top and it has no boundary condition restraining the axial movement. After the calculation of the rigid modes, the number of flexible modes is specified for axial and torsional vibration separately. It is important to point out that the torsional and axial vibration modes are uncoupled here because the nonlinear stiffness matrix was neglected and thus the coupling in the stiffness matrix does not exist.

To calculate the torsional rigid mode, the full equation of motion described in eq. 3.28 is used. The torsional rigid mode needs to be calculated before imposing the boundary condition of constant speed at the top. The rigid mode for torsional motion is only necessary because the velocity at the top is a constant different from zero. Otherwise, the torsional rigid mode would appear always multiplied by zero. To obtain the normal modes, the following eigenvalue problem is solved:

$$(-[M]\omega^2 + [K_e])\phi = 0 \quad (3.37)$$

The rigid torsional mode (ϕ_{rt}) is identified by testing the two calculated modes with eigenvalue zero. A zero eigenvalue means that the mode is rigid. The torsional rigid mode is the one in which the second row is different from zero because this row corresponds to the torsional dynamics and the modes are uncoupled.

After the computation of the torsional rigid mode, the boundary condition of constant rotational speed at the top is implemented and the second line is removed from all matrices and vectors, including the eigenvector related to rigid torsional mode (ϕ_{rt}). Now, the rest of normal modes are calculated and the new eigenvalue problem need to be solved:

$$(-[\bar{M}]\omega^2 + [\bar{K}_e])\phi = 0 \quad (3.38)$$

There is still one mode with zero natural frequency related to the axial rigid mode. This mode is identified and called by ϕ_{ra} . The rest of the modes are flexible and they are sorted in ascending order of natural frequency. Each mode is then classified as torsional or axial according to the following criteria: if the first element of the eigenvector is zero, the mode is torsional, otherwise, it is axial. After, n_{AM} axial modes and n_{TM} torsional modes are selected to reduce the model. The modes are then assembled into the modal matrix in eq. 3.39 in which $\phi_f^{(i)}$ to $\phi_f^{(n_{TM})}$ are the n_{TM} flexible torsional modes and $\phi_f^{(n_{TM}+1)}$ to $\phi_f^{(n_{TM}+n_{AM})}$ are the n_{AM} flexible axial modes.

$$[\Phi] = \left[\phi_{rt} \quad \phi_{ra} \quad \phi_f^{(1)} \quad \dots \quad \phi_f^{(n_{TM})} \quad \phi_f^{(n_{TM}+1)} \quad \dots \quad \phi_f^{(n_{TM}+n_{AM})} \right] \quad (3.39)$$

The change of variable $\bar{\mathbf{u}} = [\Phi]\mathbf{q}$ is implemented in order to reduce the model. The new variable is substituted in eq. 3.36 and the whole equation is pre-multiplied by $[\Phi]^T$. The new equation of motion is written as:

$$[\Phi]^T[\bar{M}][\Phi]\ddot{\mathbf{q}} + [\Phi]^T[\bar{D}][\Phi]\dot{\mathbf{q}} + [\Phi]^T[\bar{K}_e][\Phi]\mathbf{q} = [\Phi]^T\bar{\mathbf{f}}_T(\dot{u}_{bit}, \dot{\theta}_{bit}) - [\Phi]^T\mathbf{d}_2\Omega - [\Phi]^T\mathbf{k}_{e2}\Omega t. \quad (3.40)$$

The reduced mass matrix is defined by $[m] = [\Phi]^T[\bar{M}][\Phi]$, the reduced damping is $[d] = [\Phi]^T[\bar{D}][\Phi]$ and the reduced stiffness is $[k_e] = [\Phi]^T[\bar{K}_e][\Phi]$. On the right side of equation, the new reduced vectors are $\mathbf{f}_{Tr}(\dot{u}_{bit}, \dot{\theta}_{bit}) = [\Phi]^T\bar{\mathbf{f}}_T(\dot{u}_{bit}, \dot{\theta}_{bit})$, $\mathbf{d}_{2r} = [\Phi]^T\mathbf{d}_2$ and $\mathbf{k}_{e2r} = [\Phi]^T\mathbf{k}_{e2}$.

The damping ratios can be calculated from the damping matrix $[\bar{D}]$. The damping ratios can only be calculated for the flexible modes and they are defined by:

$$\xi_i = \frac{\phi_f^{(i)T}[\bar{D}]\phi_f^{(i)}}{2\omega_i}, \quad (3.41)$$

where ω_i is the natural frequency for flexible mode i . The new reduced equation of motion is finally defined by:

$$[m]\ddot{\mathbf{q}} + [d]\dot{\mathbf{q}} + [k_e]\mathbf{q} = \mathbf{f}_{Tr}(\dot{u}_{bit}, \dot{\theta}_{bit}) - \mathbf{d}_{2r}\Omega - \mathbf{k}_{e2r}\Omega t. \quad (3.42)$$

3.6 Numerical Results

The results in this section were obtained for the properties described in Tab. 3.1. The gravity acceleration is 9.81 m/s^2 . As the bit-rock interaction model proposed by TUCKER and WANG [26] was based on an operation with $\bar{W}_{ob} = 100kN$ and $\Omega = 100RPM$, the values for top rotational speed (Ω) and desired weight-on-bit (\bar{W}_{ob}) must be close to these values in order to use the same calibrated interaction model. The proportional damping coefficients are $\alpha = 0.1$ and $\beta = 0.00008$. The equations of motion were solved using "ode23t" solver in MATLAB. The initial value for rotational speed is set as Ω for the hole drill-string and the axial speed equal to 15 m/h for the hole drill-string as well. The deterministic simulation took less than 7 seconds.

Table 3.1: Drill-string properties.

Property	Drill-pipes	BHA
Length (m)	2250	250
Outside Diameter (mm)	114.3	165.1
Inside Diameter (mm)	97.18	57.15
Young Modulus (GPa)	210	210
Mass Density (kg/m^3)	7850	7850
Poisson's ratio	0.29	0.29

The drill-pipes and BHA are discretized separately using the finite element method and a node is placed at the exact location of transition between drill-pipes and BHA to simplify the discretization. The convergence for the number of elements is achieved for 48 elements in total: 32 for the drill-pipes and 16 for BHA. The convergence analysis considers the relative error in the 20th mode natural frequency calculation. This error is calculated in relation to the previous discretization step. An error on the order of 0.5% was achieved for 48 elements as shown in Fig. 3.5.

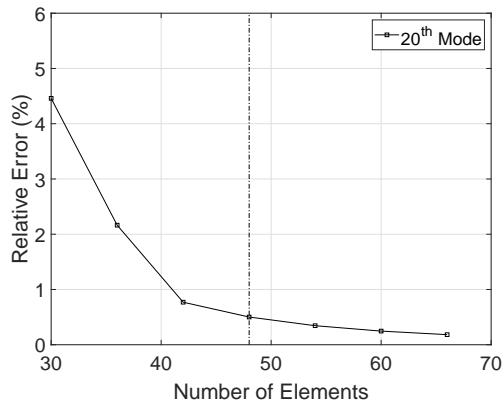


Figure 3.5: Convergence of the 20th natural frequency.

The aim of this study is to analyze stick-slip vibrations, which is a low-frequency vibration. The convergence in 20th vibration mode is enough to assure the convergence of the most important phenomena for this work.

3.6.1 Evaluation of nonlinear stiffness influence

The consideration of nonlinearities in the stiffness matrix is motivated by the works [34, 52]. In [34], some changes in drill-string dynamics were noticed after the consideration of nonlinear stiffness matrix. This section is devoted to evaluating the influence of such nonlinearities in the drill-string dynamical model used in this work.

The simulations of this section consider a rotary table rotational speed of 95.5 RPM (10 rad/s).

The first simulations analyzed in this section considered the full model (i.e. without modal reduction) described in Section 3.1, called model 1. The equation of motion was solved for two cases: the first one considers the nonlinear matrix K_g (as in eq. 3.35) and is called nonlinear; in the second case, the matrix K_g is set to zero (as in eq. 3.36) and this case is called linear.

The results for both linear and nonlinear cases did not show relevant changes in dynamic response for the model chosen above. Figure 3.6 shows the results for both linear and nonlinear cases and the difference between the two responses is only noticed after zooming in. The only difference noticed is a very small phase shift. Thus, the nonlinear stiffness matrix can be ignored in this case.

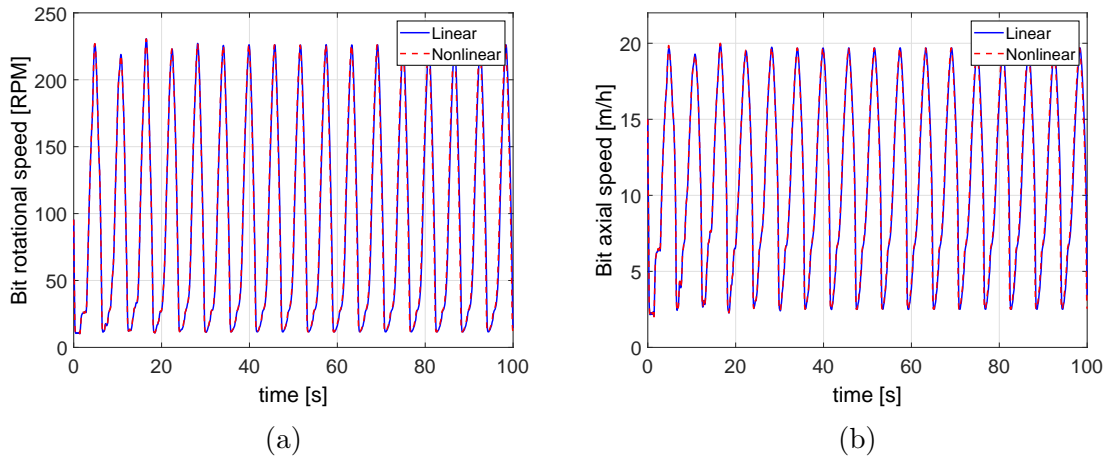


Figure 3.6: Results for model 1 with $\Omega = 95.5$ RPM and $\bar{W}_{ob} = 100$ kN. (a) Rotational speed at the bit; (b) Axial speed at the bit.

In [34], a different model was used for bit-rock interaction. In order to study what caused the high difference between linear and nonlinear responses in [34], the same bit-rock interaction model proposed in [34] was implemented as model 2. The model do not consider changes in axial force at the bit, i.e. $f_{bit} = 0$, and the torque on bit is modeled by:

$$t_{bit} = \mu \bar{W}_{ob} f(\theta_{bit}) \left[\tanh(\dot{\theta}) + \frac{\alpha_1 \dot{\theta}_{bit}}{1 + \alpha_2 \dot{\theta}_{bit}^2} \right], \quad (3.43)$$

where μ is a factor depending on the drill cutter characteristics, α_1 and α_2 are constants and $f(\theta_{bit}) = \frac{1}{1} (1 + \cos(\theta_{bit}))$ is a harmonic function. The values used for the parameters above were the same as in the article: $\mu = 0.04$; $\alpha_1 = \alpha_2 = 1$. At first, the \bar{W}_{ob} was set in 100 kN (different from [34]). The other variables assume the same value as in the simulation of fig. 3.6. In this model, the boundary condition is

also different because the axial displacement at the bit is locked. The initial value for rotational speed is equal to Ω and for axial speed is equal to zero.

In fig. 3.7, it can also be noticed that there are no big differences between linear and nonlinear models for this interaction model with $\bar{W}_{ob} = 100$ kN. The main difference concerns the axial displacement at the top of drill-string. As bit-rock interaction do not consider the coupling between axial and rotational movements, the only coupling in this model is due to nonlinear stiffness matrix, thus there is only axial movement for the nonlinear case. Even so, the axial movement is very small and the rotational speed is not affected.

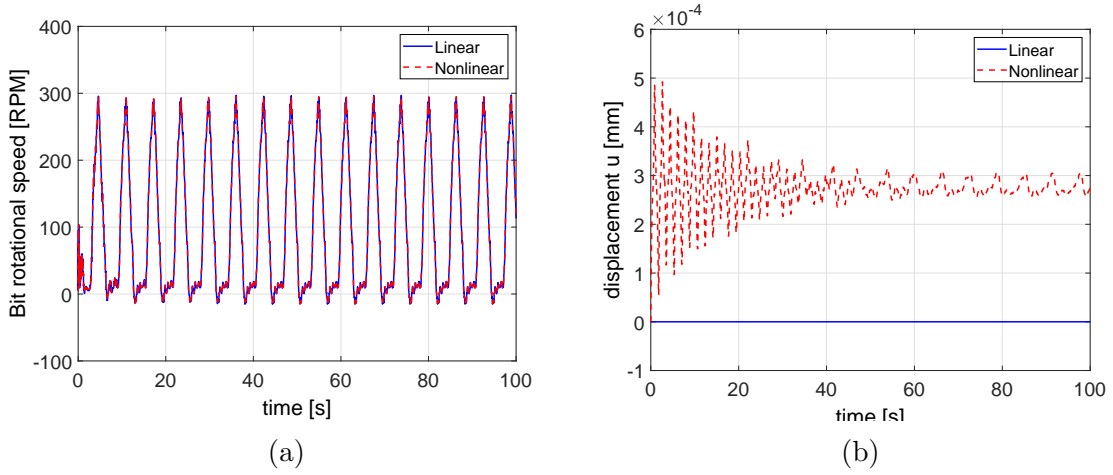


Figure 3.7: Results for model 2 with $\Omega = 95.5$ RPM and $\bar{W}_{ob} = 100$ kN. (a) Rotational speed at the bit; (b) Axial displacement at the bit.

In order to reproduce the same results of [34], the \bar{W}_{ob} was increased to 255 kN. In fig. 3.8a, a higher difference is noticed after some seconds of simulation and, at a first look, it seems that nonlinear stiffness matrix makes difference for a higher \bar{W}_{ob} . The results obtained here are different from the ones obtained in [34]. This difference seems to be related to numerical issues faced during simulations for this case.

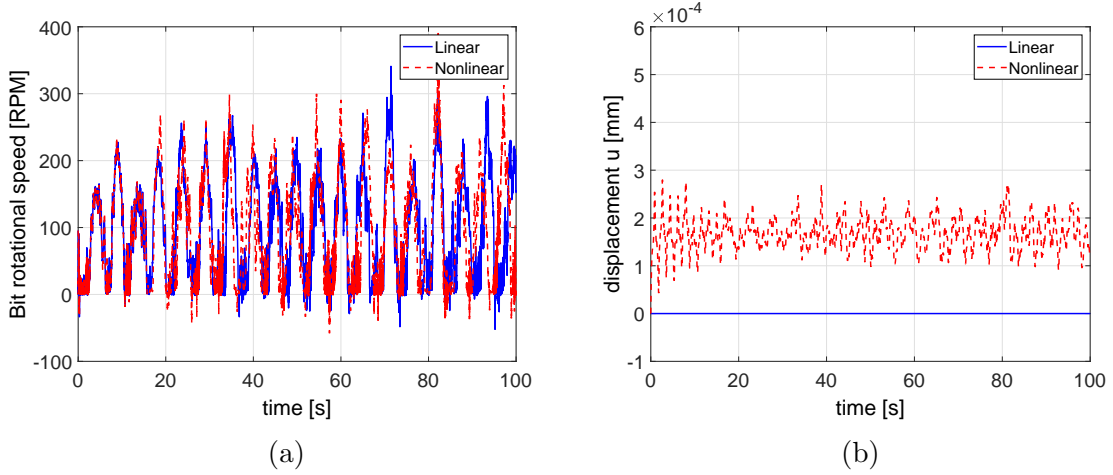


Figure 3.8: Results for model 2 with $\Omega = 95.5$ RPM and $\bar{W}_{ob} = 100$ kN. (a) Rotational speed at the bit; (b) Axial displacement at the bit.

The bit-rock interaction described in section 3.1 was also simulated considering $\bar{W}_{ob} = 255$ kN, but the difference between linear and nonlinear models remained very small and, thus, they are not presented here.

Some attempts to linearize the nonlinear stiffness matrix can be found in literature and, although it was shown that only small and negligible differences are noticed in the case analyzed, the possibility of linearization around an equilibrium configuration was assessed. In fig. 3.9, the axial and angular deformations are plotted against simulation time and each curve corresponds to one element in drill-string. Here, it is not important to identify which line corresponds to each element, but it is important to analyze the overall behavior of both deformations along the time for the whole structure. The graph shows that the linearization is possible for axial deformation because the variations are small around the equilibrium configuration. Otherwise, for the case of angular deformation, the linearization is not recommended due to the high amplitude of variation. For both graphs, the curves with higher magnitude refer to the elements of drill-pipes.

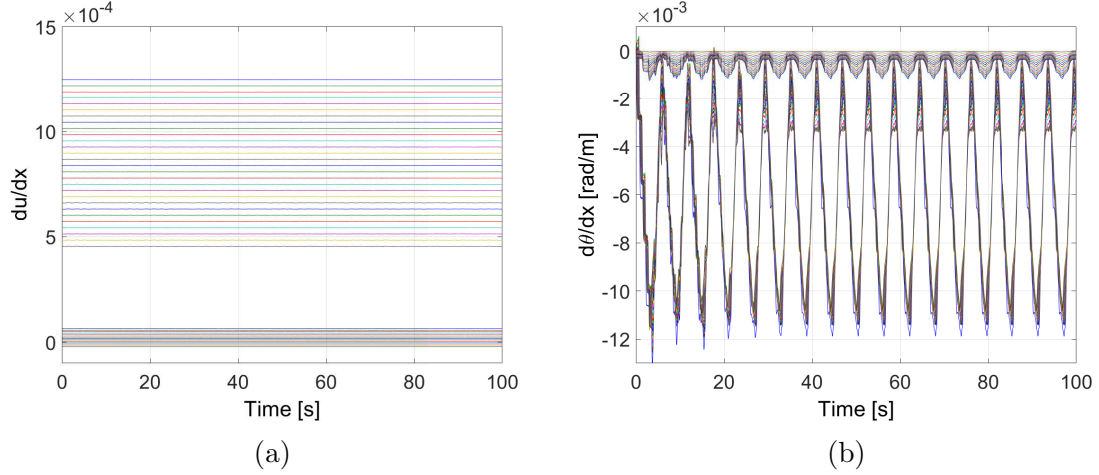


Figure 3.9: Deformation per element through the time. Each line corresponds to one element. (a) Axial deformation; (b) Angular deformation. $\Omega = 95.5$ RPM, $\bar{W}_{ob} = 100$ kN.

After all these analyses, it is concluded that the nonlinear stiffness matrix has negligible influence in the drill-string dynamical model used in this work. Because of this, the nonlinear stiffness matrix will not be considered in the following sections. Thus, the equation of motion resumes to eq. 3.36.

3.6.2 Modal analysis

The vibration modes are calculated according to eq. 3.38 in order to build a reduced-order model. The reduction of the problem saves a lot of processing time. For 100 seconds of simulation, the calculation lasts about 1563 seconds (30 minutes) without the reduction, while it lasts only 25 seconds with the reduction. The model reduction was performed using torsional and axial rigid modes plus 4 axial flexible modes and 7 torsional flexible modes. The number of modes considered are enough to cover all the modes below 4.35 Hz. Figure 3.10 shows the comparison of time response for the bit rotational speed using the complete and reduced-order models. It is noticed that the reduced-order model can represent very well drill-string response despite some vibrations in high frequency. The interest of this study is on low-frequency vibration such as stick-slip. Therefore, the reduced-order model is enough to analyze drill-string dynamics.

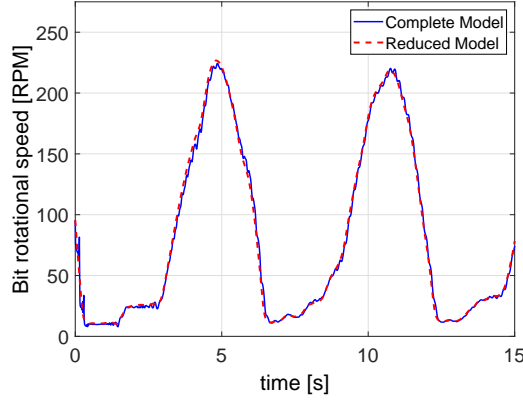


Figure 3.10: Comparison between complete and reduced-order models for the rotational speed at the bit. $\bar{W}_{ob} = 100$ kN, $\Omega = 95.5$ RPM.

The vibration modes that result from eq.3.38 are classified into axial or torsional according to the criteria explained in section 3.5. The rigid modes have zero natural frequency and the mode shape is constant along the drill-string length. Because of this, they are not shown here and only the flexible modes are analyzed. The vibration modes are numbered in ascending order of natural frequency. In table 3.2, the natural frequencies are presented in ascending order and the shapes of the modes are presented below in Figs.3.11, 3.12, 3.13, 3.14, 3.15 and 3.16. Only the flexible modes used in model reduction are shown in those figures and in table 3.2.

Table 3.2: Natural frequencies for drill-string vibration modes used in model reduction.

Mode	Type	Natural Frequency (Hz)
1	Torsional	0.20
2	Torsional	0.78
3	Axial	0.78
4	Torsional	1.46
5	Axial	1.81
6	Torsional	2.17
7	Torsional	2.89
8	Axial	2.93
9	Torsional	3.61
10	Axial	4.06
11	Torsional	4.34

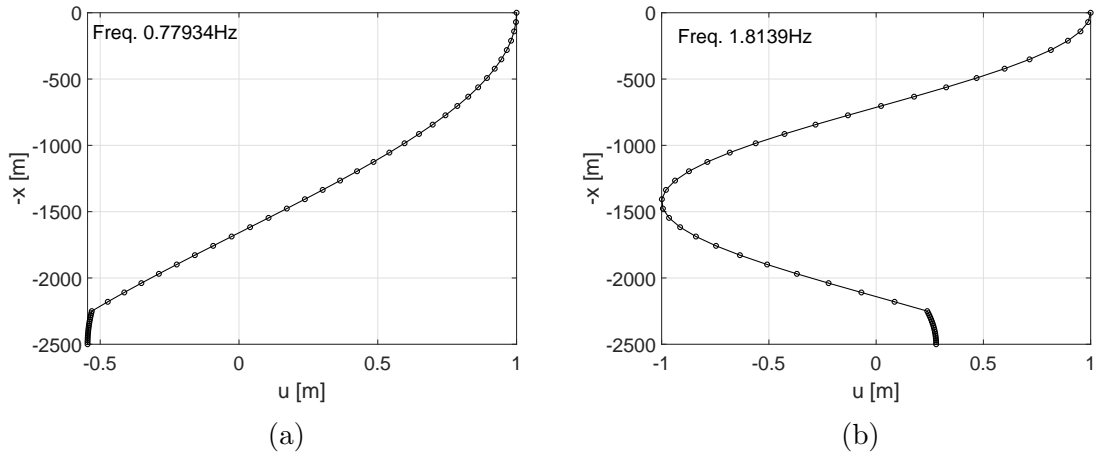


Figure 3.11: Axial vibration modes. (a) 4th mode and (b) 6th mode.

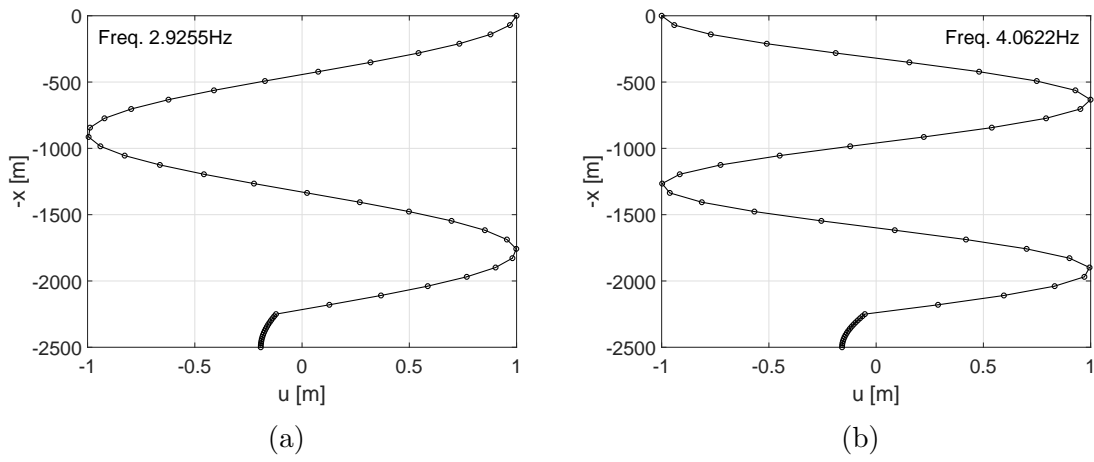


Figure 3.12: Axial vibration modes. (a) 9th mode and (b) 11th mode.

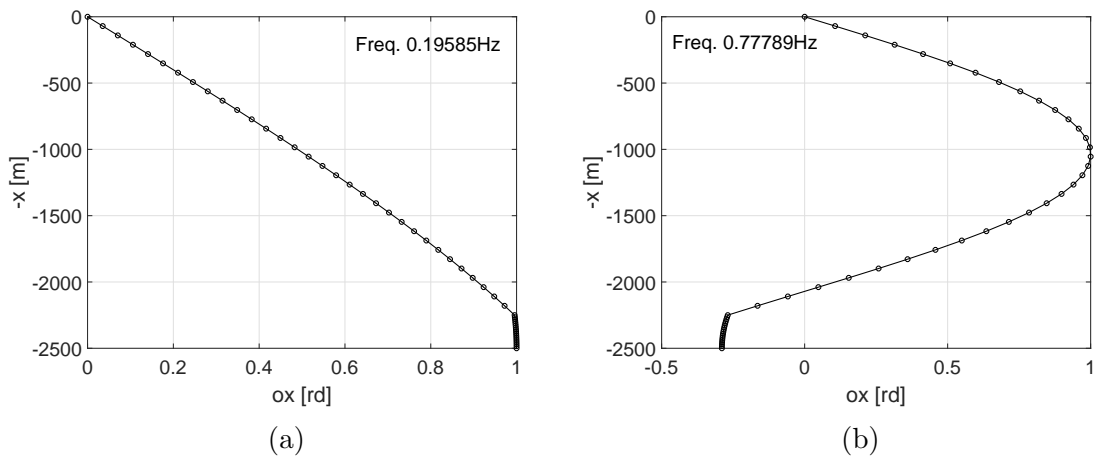


Figure 3.13: Torsional vibration modes. (a) 2nd mode and (b) 3rd mode.

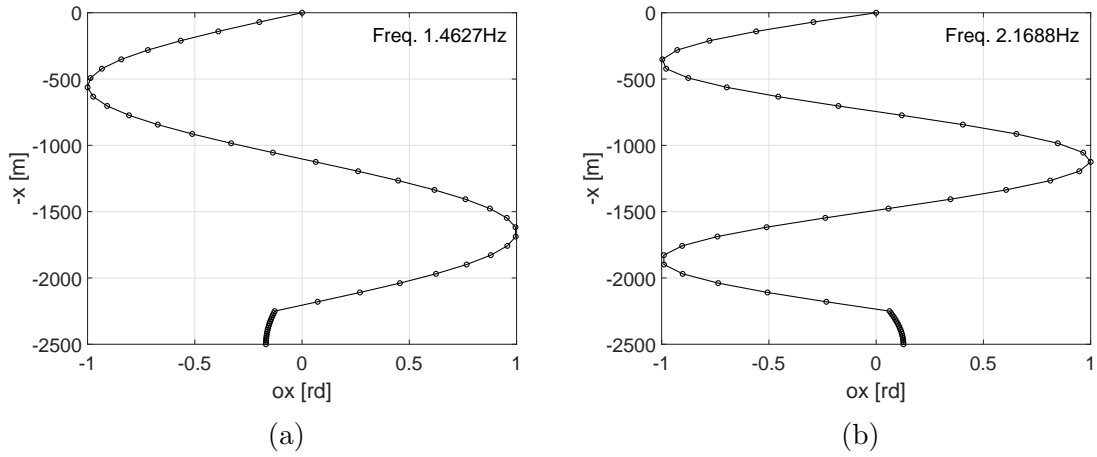


Figure 3.14: Torsional vibration modes. (a) 5th mode and (b) 7th mode.

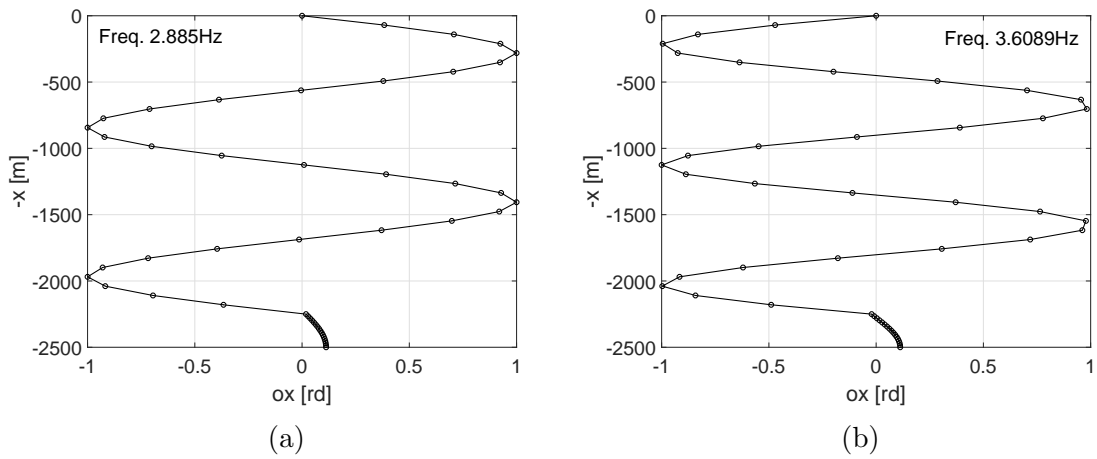


Figure 3.15: Torsional vibration modes. (a) 8th mode and (b) 10th mode.

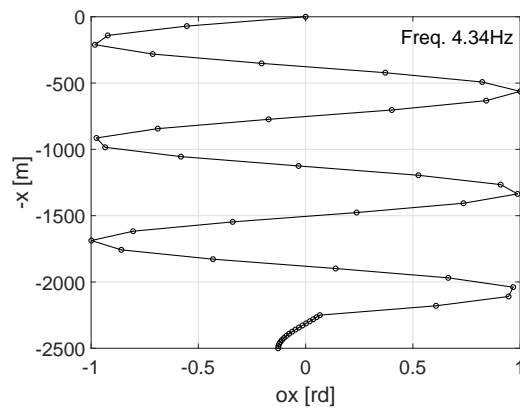


Figure 3.16: Torsional vibration modes. 12th mode.

The first natural frequencies of drill-string are low. It confirms the high flexibility of the structure due to its length. In addition, the analysis of the shape of the

vibration modes suggests that most of the displacement occurs in drill-pipes for the first modes (low frequency). It occurs because the drill-pipes section is much more flexible than BHA section for both axial and torsional vibrations. Therefore, drill-pipes contribute more to low-frequency modes.

With the increase of the natural frequency, the influence of BHA in the shape of vibration modes increases. Figure 3.17 shows one torsional and one axial vibration mode with a higher natural frequency. To calculate these natural frequencies, the drill-string was discretized in 192 elements in order to achieve convergence in such high frequencies. The bigger displacement in BHA section is remarkable. Despite this, there are some modes around the ones shown in Fig. 3.17 that BHA still has a small amplitude when compared to drill-pipes.

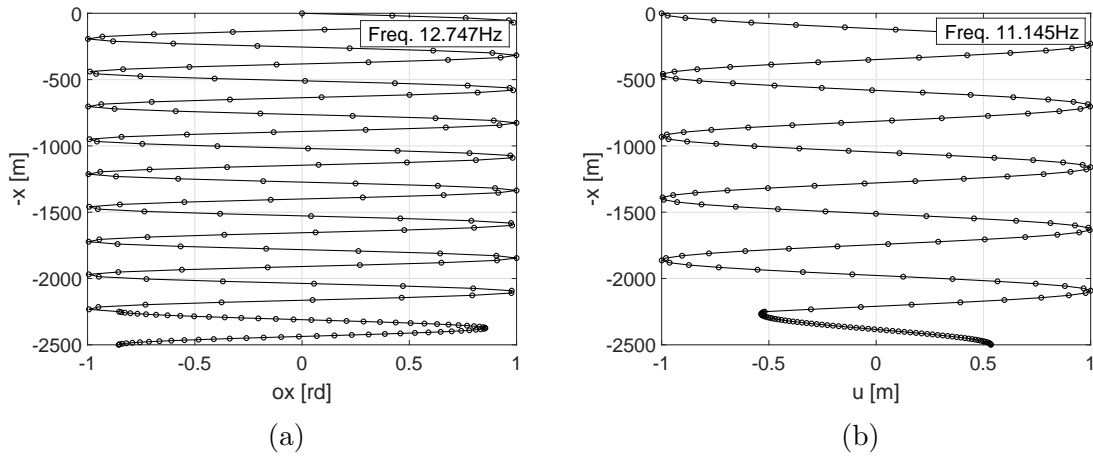


Figure 3.17: Vibration modes. (a) 33th mode (torsional - 12.75Hz) and (b) 29th mode (axial - 11.15Hz).

The modal analysis points out that there is another interesting and important phenomenon in drill-string that can happen in higher frequencies depending on drilling conditions (e.g. HFTO [74]), but the phenomenon of stick-slip, that is going to be studied in this work, is a low-frequency phenomenon and only the low-frequency modes are necessary to describe the dynamics of drill-string in such conditions.

3.6.3 Dynamical response

In this section, the results from deterministic simulation are analyzed. The values of Ω and \bar{W}_{ob} used in this section are chosen in order to reproduce an operation without and with stick-slip. All the plots discussed in this section, consider positive the downward axial movement.

As mentioned in the introduction, only the lowest part of drill-string is operated under compression while the rest of drill-string is under traction. Figure 3.18 shows

the axial deformation along drill-string length for two values of \bar{W}_{ob} . It can be noticed that only the last few meters are under compression. This figure was plotted for the equilibrium configuration calculated in eq. 3.27, but this plot changes very little during simulation time as noticed in Fig. 3.9a. The inclination of the curve is due to the weight of drill-string and the gap between the two lines is exactly at the transition between drill-pipes and BHA. This gap refers to the difference between the stiffness of the two structures.

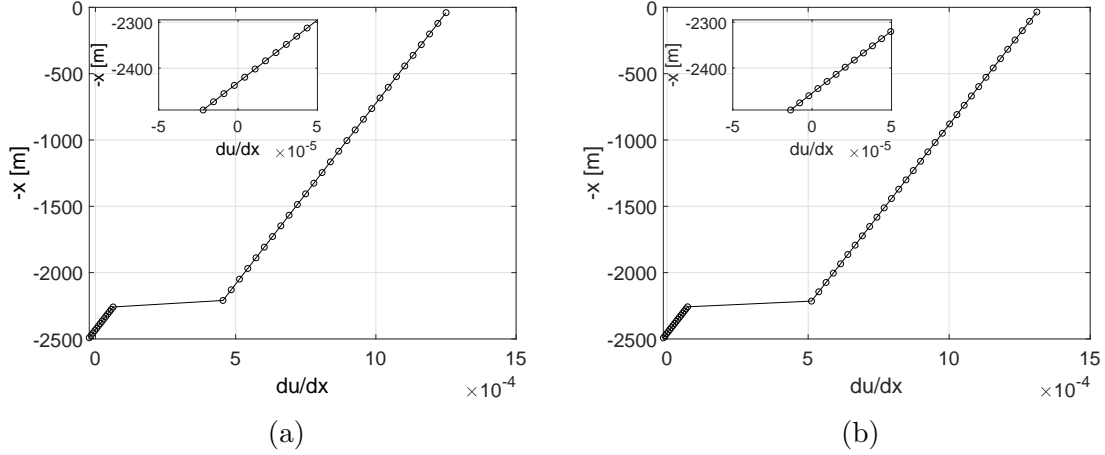


Figure 3.18: Axial deformation du/dx along drill-string length at each position x . (a) $\bar{W}_{ob} = 100$ kN; (b) $\bar{W}_{ob} = 65$ kN.

For $\Omega = 95.5$ RPM and $\bar{W}_{ob} = 65$ kN, Fig. 3.19 shows the axial and rotational speed of the bit. The first seconds are considered as the transient regime and, after that, the bit reaches the steady state. The rotational speed tends to the speed imposed in the rotary table and the bit advances at a constant axial speed.

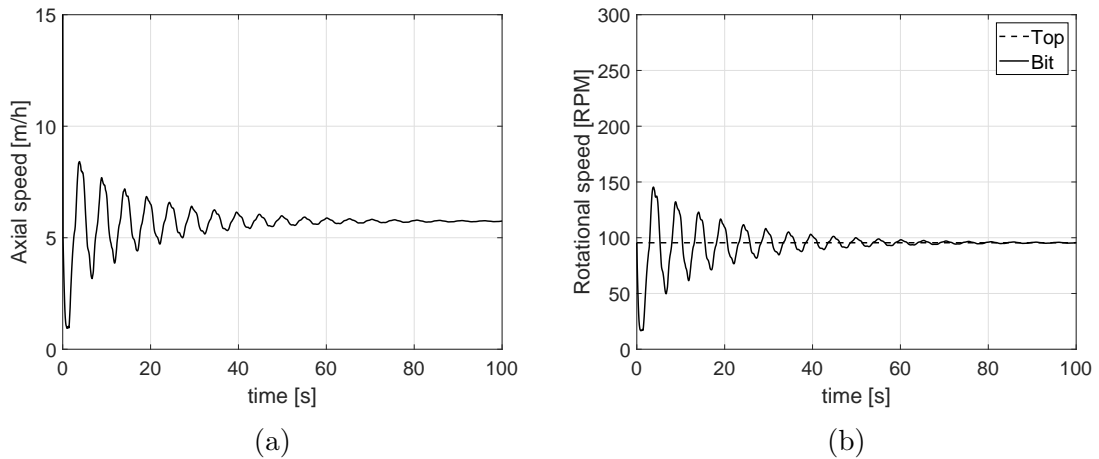


Figure 3.19: (a) Axial speed at the bit; (b) Rotational speed at the top and at the bit. $\bar{W}_{ob} = 65$ kN, $\Omega = 95.5$ RPM.

The difference between the angular position of the top and the bit ($\Delta\theta$) tends

to a constant value, as shown in Fig. 3.20a. This constant value is related to the constant torque applied by bit-rock interaction during steady state (Fig. 3.20b).

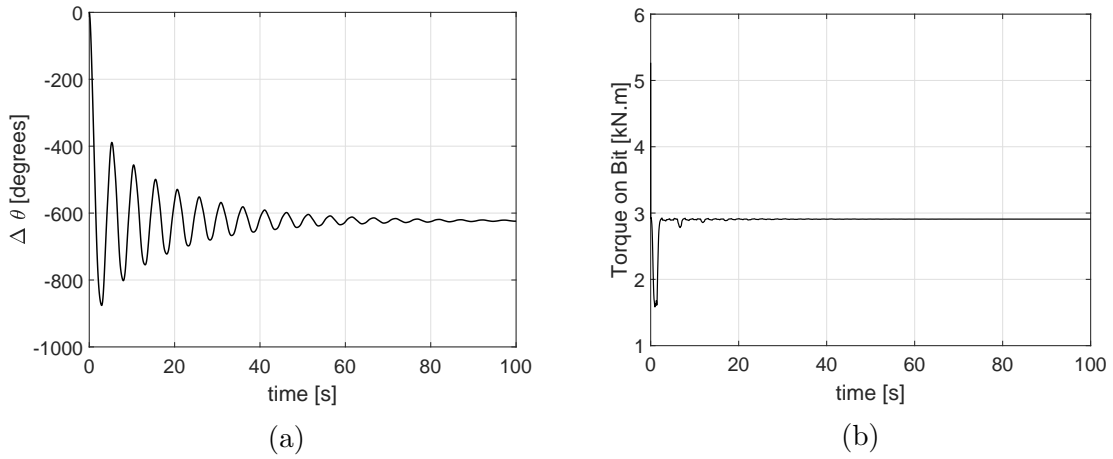


Figure 3.20: (a) Angular relative displacement of the bit with the top angular position as reference. (b) Torque-On-Bit (TOB). $\bar{W}_{ob} = 65$ kN, $\Omega = 95.5$ RPM.

In Fig. 3.21, the Fast Fourier Transform (FFT) of bit rotational speed and bit axial speed are shown. The amplitude of the FFT is scaled to be in Power/Frequency. The highest magnitude occurs around the frequency of 0.19 Hz which is very close to the first natural frequency of the system. Other peaks also appear at multiples of this frequency due to the nonlinearity caused by bit-rock interaction. The peaks occur at the same frequency for either bit rotational and axial speeds, although the first natural frequency is different for each dynamics. It occurs also due to the nonlinearities introduced by bit-rock interaction. The nonlinear interaction forces couple the two dynamics and make the peaks to appear at the same frequency.

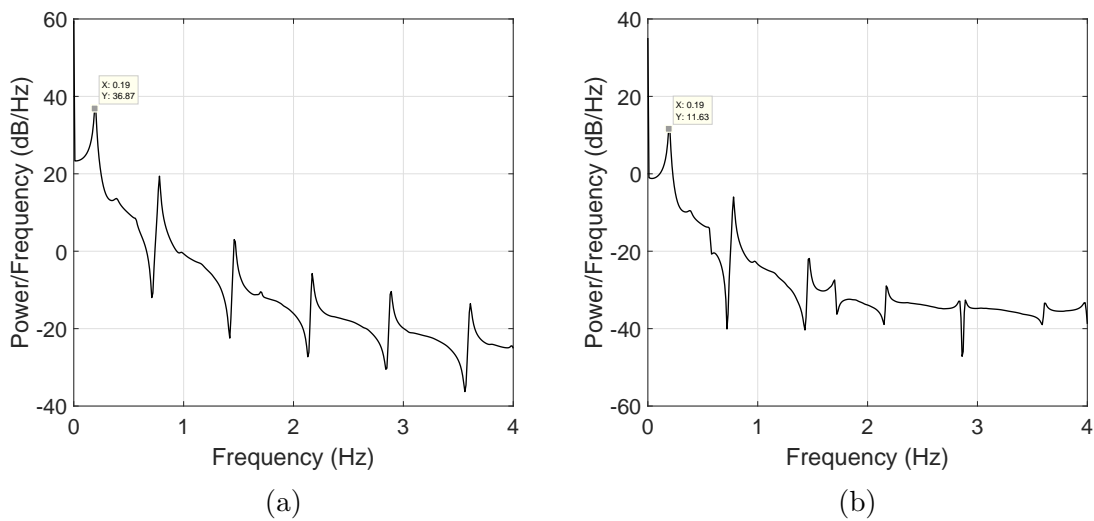


Figure 3.21: Fast Fourier Transform (fft) of (a) Bit rotational speed and (b) Bit axial speed. $\bar{W}_{ob} = 65$ kN, $\Omega = 95.5$ RPM.

With the increase of \bar{W}_{ob} from 65 kN to 100 kN, the stick-slip phenomenon starts to happen. In Fig. 3.22, the axial and rotational speeds are plotted against the time, respectively. Figure 3.22b shows the constant speed applied at the top of drill-string and the speed at the bit indicates the occurrence of stick-slip. This phenomenon is identified when bit achieves zero rotational speed and then is released, reaching values that can be as high as 5 times the speed at the top of drill-string, for example. A limitation of the bit-rock interaction model used is that bit does not achieve zero velocity due to the regularization, but it is not a problem in the analysis done in this work.

At the bit, the axial speed follows up rotational speed behavior as shown in Fig. 3.22a. It occurs because when the bit is stuck, it does not move in any direction considered (rotational nor axial) and a high rotational speed implicates in a faster material removal speed resulting in a higher axial speed. It can also be noticed that axial speed is always positive at the bit thus there is not bit-bounce vibration because the bit never loses contact with borehole bottom.

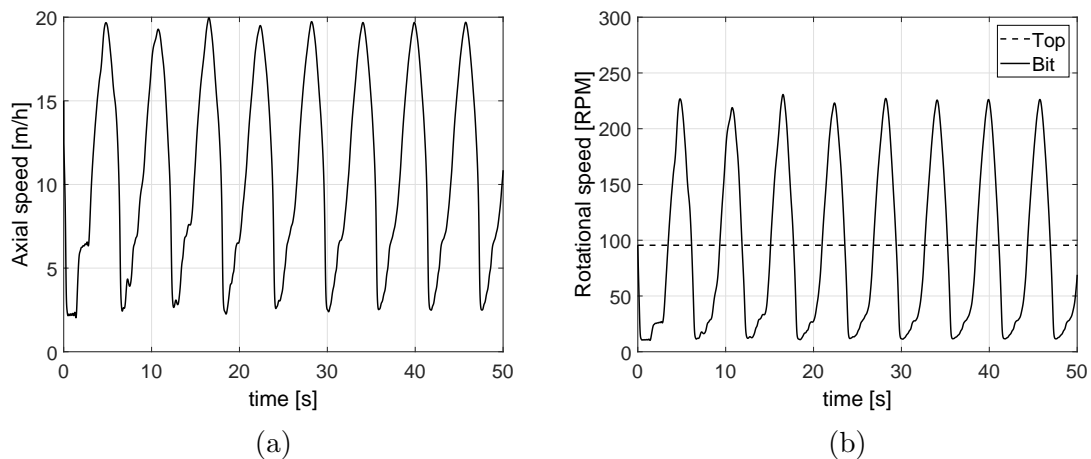


Figure 3.22: (a) Axial speed at the bit; (b) Rotational speed at the top and at the bit. $\bar{W}_{ob} = 100$ kN, $\Omega = 95.5$ RPM.

The phenomenon called stick-slip can be explained a little better with Fig. 3.23 which plots the bit angular speed by time and the torque related to the top-rotary system and bit-rock interaction by time. The torque applied by the rotary table indicates how much energy is stored inside drill-string in the form of torsional deformation. Stick-slip vibration is characterized by the sticking of the bit, indicated by vertical line 1, in which the bit is stick while the top of drill-string continues to rotate and accumulating energy in form of torsional deformation and thus torque. Actually, one can observe that drill-string starts to accumulate torque before the bit sticks because the bit speed is already less than top speed, increasing the torsional deformation. When this accumulated torque is higher than the resistance to movement (due to bit-rock interaction and other dissipative forces) as indicated by

vertical line 2, the bit is released and the accumulated energy is released in form of rotational movement, achieving high speeds. After a big relief of torsional deformation, the torque accumulated in drill-string becomes to a level less than the necessary to make the drilling and the bit starts to decrease its speed until it sticks again, as indicated by vertical line 3.

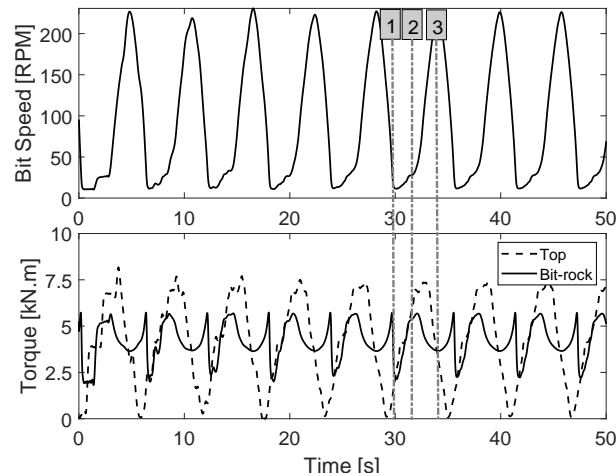


Figure 3.23: Rotational speed at the bit and torque applied by top rotary system compared to the torque on bit due to bit-rock interaction.

The behavior noticed in the bit speed can be translated into axial and rotational displacements, as in Fig. 3.24. The first figure shows that the bit is actually moving downward and drilling the rock, increasing the depth of the hole. The fluctuations on axial speed also appear in axial displacement as well, but the bit never moves in the opposite direction, indicating that bit-bounce is not happening. The second plot shows the linear increase of angular position at the top due to the constant speed imposed. At the bit, the angular position fluctuates due to stick-slip vibration and tries to catch up the angular position at the top.

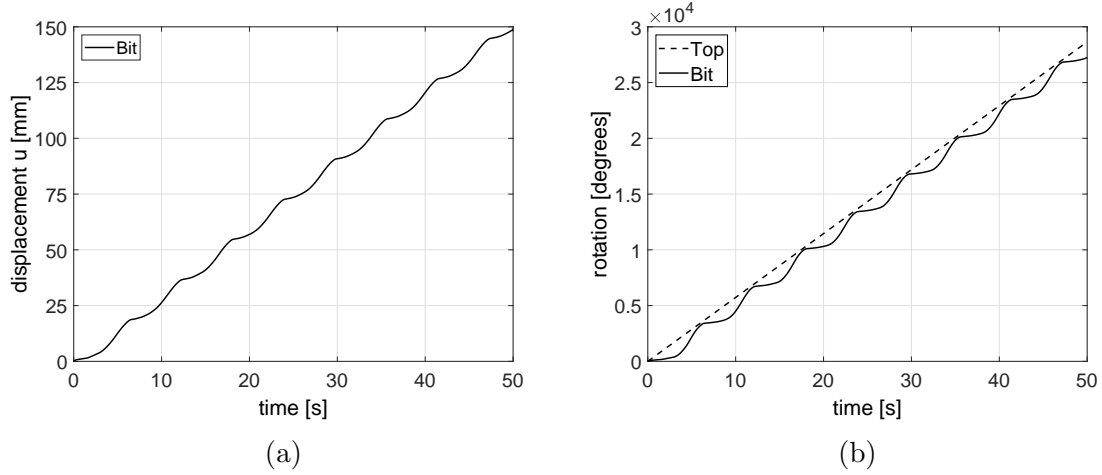


Figure 3.24: (a) Axial displacement of the bit; (b) Torsional displacement at the top and the bit. $\bar{W}_{ob} = 100$ kN, $\Omega = 95.5$ RPM.

The difference in angular position between the top and the bit ($\Delta\theta$) is shown in Fig. 3.25. The initial difference is zero due to the initial condition that imposes rotational position zero along drill-string. The fluctuation refers to the behavior noticed in Fig. 3.24b and elucidates the storage of energy in drill-string during stick-slip cycles.

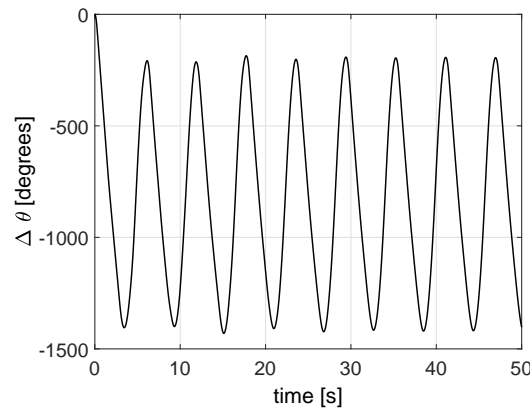


Figure 3.25: Angular relative displacement of the bit with the top angular position as reference. $\bar{W}_{ob} = 100$ kN, $\Omega = 95.5$ RPM.

Another way to analyze stick-slip cycles is by using the phase portrait that plots the rotational speed against angular relative displacement ($\Delta\theta$). The phase portrait of the stick-slip cycles analyzed is plotted in Fig. 3.26. When the bit sticks, the relative displacement starts to increase while the bit has zero speed (or low speed in this case, because of the model limitation). After, the bit is released and the speed significantly increases very fast and thus the relative displacement starts to decrease until the energy is not capable of winning cutting resistance anymore. Therefore, the speed decreases and the bit sticks again. This cycle then repeats according to

Fig. 3.26 in the clockwise direction.

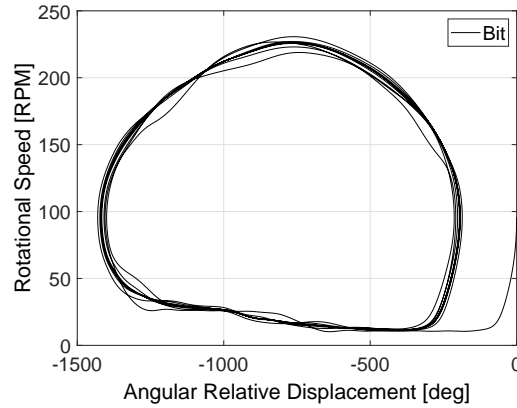


Figure 3.26: Phase Portrait at the bit. $\bar{W}_{ob} = 100$ kN, $\Omega = 95.5$ RPM.

Figure 3.27 shows the phase portrait plotted for one stick-slip cycle in several positions at drill-string length. At the top of drill-string, the phase portrait collapses to a dot, because the rotational speed is fixed at a constant value and it is the reference point to calculate angular relative displacement and thus the angular relative displacement is zero. Along the drill-string, it is possible to see that torsional oscillation attenuates in terms of the speed and angular relative displacement. The higher fluctuations in speed happen at the bottom of the drill-string.

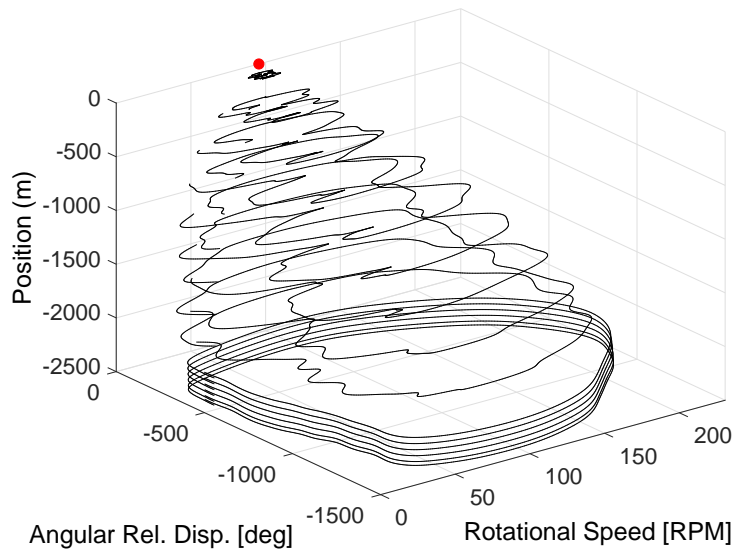


Figure 3.27: Phase Portrait along drill-string length. $\bar{W}_{ob} = 100$ kN, $\Omega = 95.5$ RPM.

Although the torsional vibrations can be undetectable at the surface in terms of the torsional deformation or rotational speed, the fluctuations in the torque applied by top rotary system indicate the occurrence of stick-slip through the high oscillations depicted in Fig. 3.28.

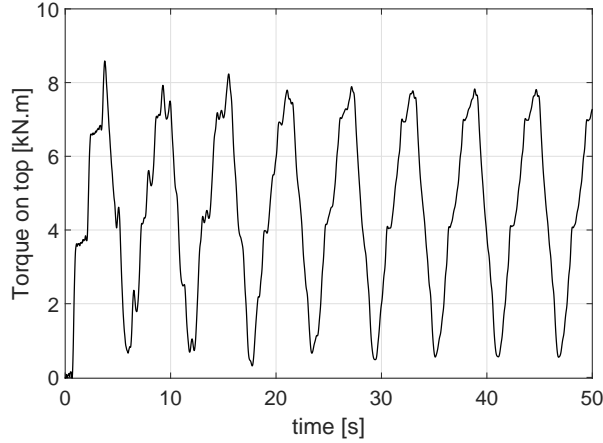


Figure 3.28: Torque applied at the top by the top rotary system (rotary table or top drive). $\bar{W}_{ob} = 100$ kN, $\Omega = 95.5$ RPM.

Figure 3.29 shows the bit rotational speed in the top plot to help the analysis of the other plots. The second plot is about the depth-of-cut (DOC) and it is calculated by the classical definition presented in eq. 2.15. The cutting phenomenon is well represented by this graph because when the bit is stuck, DOC is almost constant and it is in its maximum value, generating the maximum resistance to drilling. When the torque accumulated in drill-string finally wins this resistance, the DOC decreases immediately because of the block of rock in the front of the cutters brakes. After DOC decreases, the bit starts to penetrate the rock again, increasing DOC until it reaches its maximum value again and the cycle repeats.

This behavior is also noticed in the graph that presents the torque on bit (t_{bit}). When the bit sticks, the torque starts to increase in order to match the torque accumulated in drill-string and to maintain the bit stopped. When this torque achieves the maximum torque that represents the maximum rock resistance, the rock breaks and the torque from bit-rock interaction decreases. The bit then starts to penetrate the rock again and the torque from bit-rock interaction increases until bit sticks again and the cycle repeats.

The last plot is about the modulus of axial force at the bit. It can be seen that there are fluctuations around the desired weight-on-bit (\bar{W}_{ob}). The maximum values for axial force happen when the bit sticks because the axial movement is stopped suddenly.

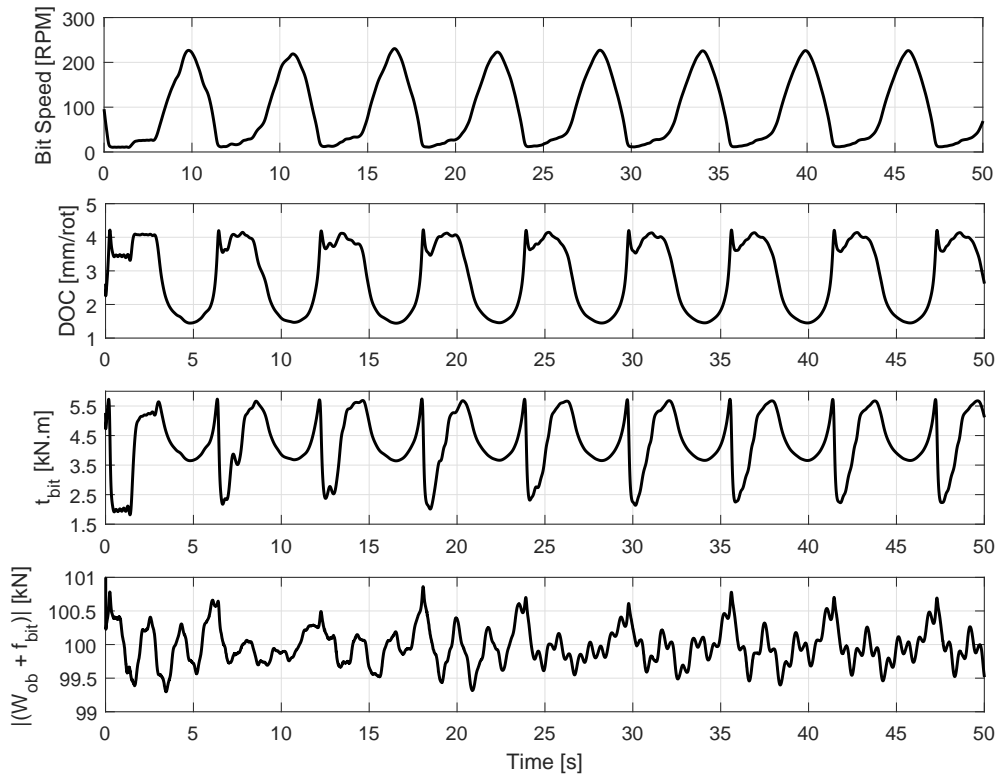


Figure 3.29: Drill-string dynamics and interaction forces. From the top to the bottom, respectively: Rotational speed at the bit (Bit Speed); Depth-of-Cut (DOC); Torque on bit (t_{bit}) and; Axial force on bit (f_{bit}). $\bar{W}_{ob} = 100$ kN, $\Omega = 95.5$ RPM.

Another very common plot is presented in Fig. 3.30. The torque on bit (t_{bit}) is plotted against bit rotational speed and this graph is known as bit-rock interaction graph because it inspired many of the bit-rock interaction models developed in the literature. The same hypothesis from other models are observed here: the torque decays with bit rotational speed and torque has a maximum value that is reached when bit sticks. The difference is that maximum torque is not located at zero speed because of the regularization of the bit-rock interaction model. The other difference is that axial movement includes a variation of the torque for the same bit rotational speed.

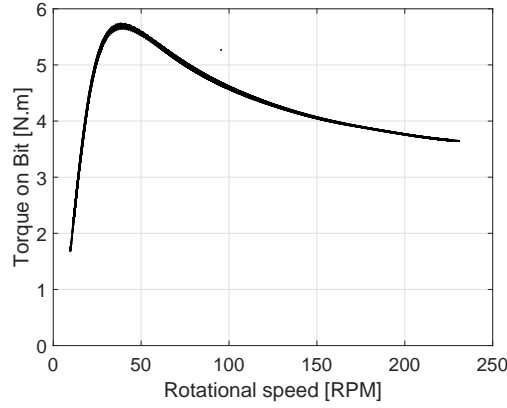


Figure 3.30: Bit-rock interaction. $\bar{W}_{ob} = 100$ kN, $\Omega = 95.5$ RPM.

At last, the Fast Fourier Transform (FFT) of bit rotational speed and bit axial speed are shown in Fig. 3.31. The amplitude is scaled to be in Power/Frequency. The first peak occurs around the frequency of 0.17 Hz which is smaller than the frequency observed in Fig. 3.21. As stick-slip becomes more severe, the frequency tends to decrease because the stick phase lasts longer and thus the period of stick-slip increases. Many more peaks also appear at multiples of this frequency due to the nonlinearity caused by bit-rock interaction. The peaks also occur at the same frequency for either bit rotational and axial speed due to the coupling in bit-rock interaction.

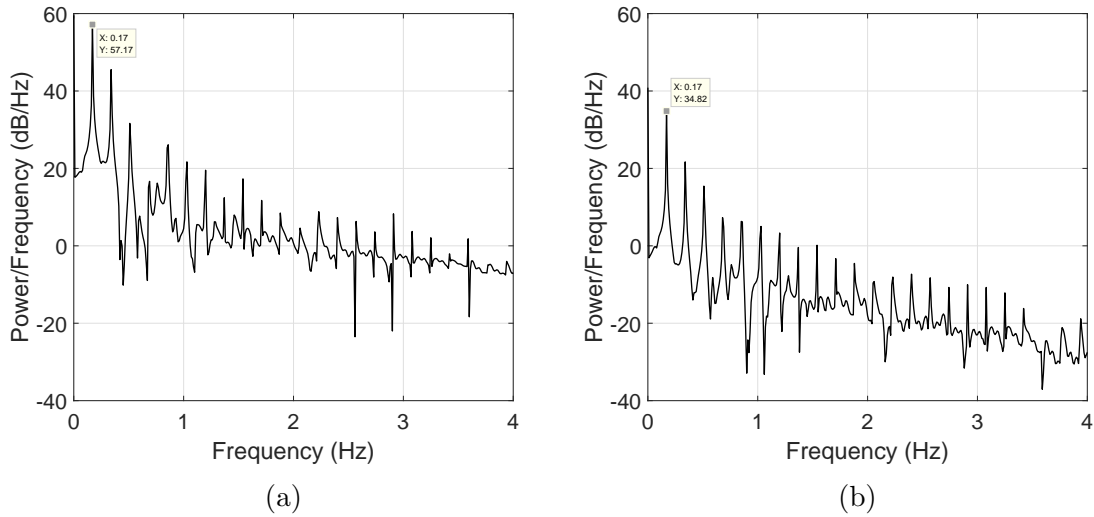


Figure 3.31: Fast Fourier Transform (fft) of (a) Bit rotational speed and (b) Bit axial speed. $\bar{W}_{ob} = 100$ kN, $\Omega = 95.5$ RPM.

3.6.4 Parametric analysis

The aim of this section relies on the evaluation of the impact of changes in the system's parameters on system dynamics. Some of the main challenges regarding

drilling operation simulation are related to the following topics: (i) definition of operational parameters that optimize the drilling efficiency; (ii) Modeling of the interactions between drill-string and environment (e.g. Bit-rock interaction), and; (iii) Modeling of the damping effects along drill-string (e.g. structural damping and damping due to drilling fluid). Therefore, a parametric analysis was performed regarding the variables related to these three topics.

As discussed in section 1.4, the main parameters controlled in drilling operation are: Hook Load (which is directly related to \bar{W}_{ob}); Rotary table speed (Ω), and; Drilling fluid flow rate. In a parametric analysis, the influence of \bar{W}_{ob} and Ω on system dynamics is often assessed through stability maps using the concept of Stick-Slip Severity (S_{ss}) defined as:

$$S_{ss} = \frac{\max(\dot{\theta}_{bit}(t)) - \min(\dot{\theta}_{bit}(t))}{2\Omega} \cdot 100\% \quad (3.44)$$

where $\min(\dot{\theta}_{bit}(t))$ and $\max(\dot{\theta}_{bit}(t))$ are calculated for steady-state regime. Figure 3.32 shows the stability map for the drill-string considered in this chapter. The color gradient represents the Stick-Slip Severity and the stick-slip is considered severe in this work if $S_{ss} > 50\%$. Since the only source of excitement is the bit-rock interaction and there are no uncertainties, the rotational speed at the bit tends to rotary table rotational speed for the cases without stick-slip, and thus $S_{ss} \approx 0$. Therefore, the stability map changes the S_{ss} abruptly in the transition between operation without vibration and with severe stick-slip. The classical behavior in which stick-slip gets worse for higher \bar{W}_{ob} and lower Ω is also noticed.

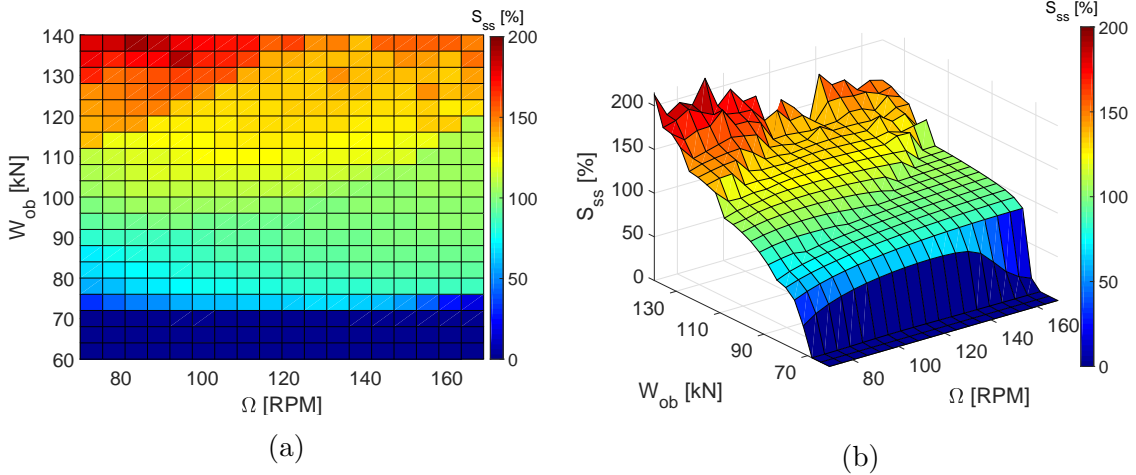


Figure 3.32: Stability map for stick-slip severity. (a) 2D; (b) 3D.

Note that the shape of the stability map presented in Fig. 3.32 is a bit different from what is commonly found in the literature. Although the rotary table speed interferes on the severity of stick-slip, the transition between stick-slip and no stick-

slip is almost flat, i.e. an increase of Ω does not interfere much on the occurrence or not of stick-slip. In literature, it is usual to Ω have a bigger influence on the occurrence of stick-slip. An investigation of the proposed model showed that the damping matrix is capable of increasing the effect of Ω . Figure 3.33 shows a stability map when the proportional coefficients of damping matrix, α and β , are increased, respectively, from 0.1 and 0.00008 to 0.4 and 0.008.

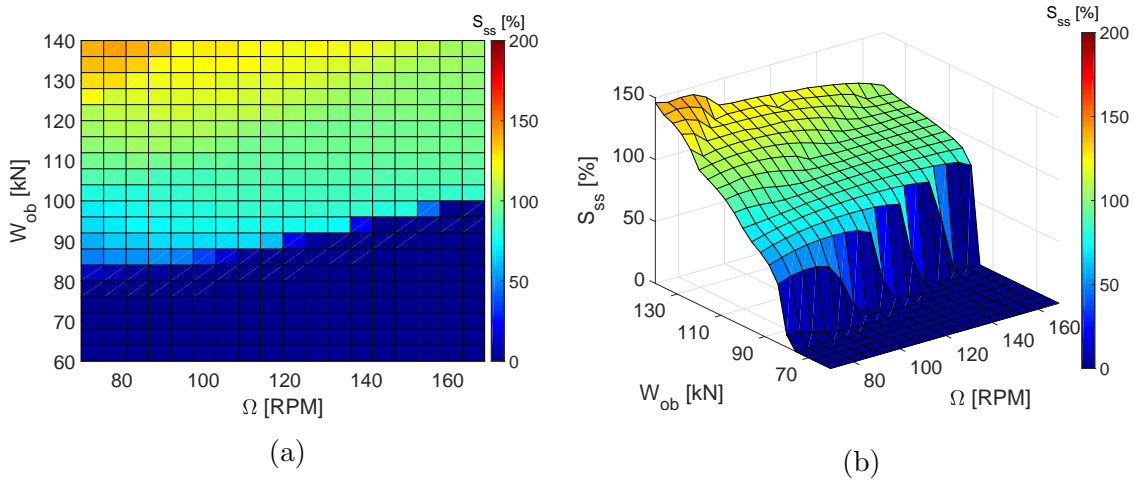


Figure 3.33: Stability map for stick-slip severity. $\alpha = 0.4$ and $\beta = 0.008$. (a) 2D; (b) 3D.

The impact on the transition region is notable. An increase of Ω is now much more relevant in the transition region and it can determine whether the operation will present stick-slip or not. Another important observation is that the severity of stick-slip decreased overall. In Fig. 3.32, the maximum S_{ss} is above 200%, while in Fig. 3.33 the maximum is near 150%. Figure 3.34 illustrates better the difference on stick-slip severity due to damping coefficients. Picking a \bar{W}_{ob} and Ω such that stick-slip happens in both cases, we can see that bit achieves higher speeds in the case with lower damping coefficients, while the bit vibrates with lower amplitudes in the case with higher damping coefficients.

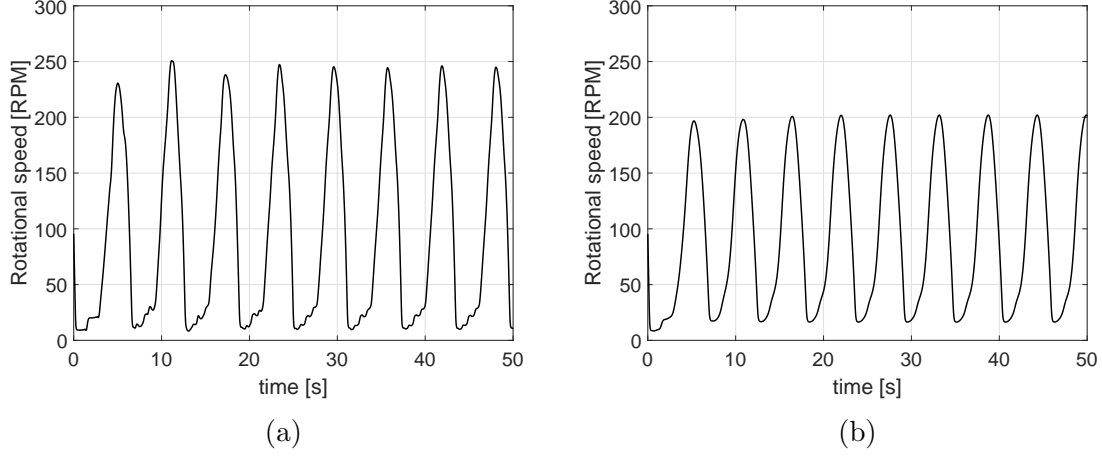


Figure 3.34: Rotational speed at the bit for $\Omega = 95.5$ RPM and $\bar{W}_{ob} = 110$ kN. (a) $\alpha = 0.1$ and $\beta = 0.00008$; (b) $\alpha = 0.4$ and $\beta = 0.008$

The next parametric analysis presented is related to bit-rock interaction model. It is important to verify how changes in model's parameters impact the shape of bit-rock interaction curve and also the consequences in drill-string dynamics. At first, the bit-rock interaction model (Eq. 3.33 and 3.34) is rewritten in order to allow the variation of each component of bit-rock interaction:

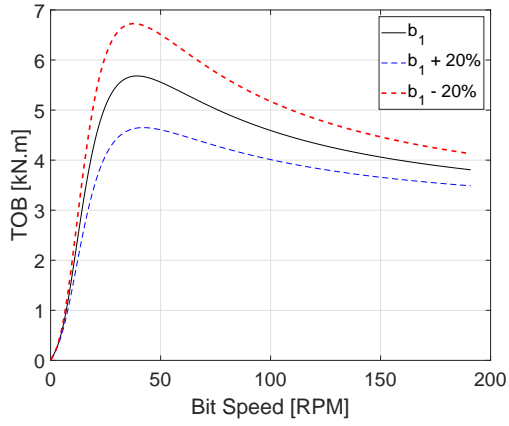
$$f_{bit} = b_1 + \frac{b_2 \dot{u}_{bit}}{Z(\dot{\theta}_{bit})^2} - \frac{b_3 \dot{\theta}_{bit}}{Z(\dot{\theta}_{bit})} - \bar{W}_{ob} \quad (3.45)$$

$$t_{bit} = \frac{\dot{u}_{bit} b_4 Z(\dot{\theta}_{bit})^2}{\dot{\theta}_{bit}} + b_5 Z(\dot{\theta}_{bit}) \quad (3.46)$$

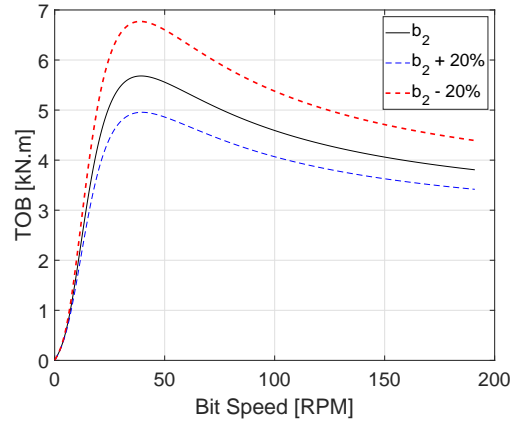
where $b_1 = a_1/a_2$, $b_2 = 1/a_2$, $b_3 = a_3/a_2$, $b_4 = a_4$ and $b_5 = a_5$. Next, a variation of 20% is applied to each parameter in order to evaluate the influence on bit-rock interaction shape. Figures 3.35 to 3.37 show how the shape of bit-rock interaction curve changes for a constant WOB of $\mathcal{W}_{ob} = \bar{W}_{ob} = 100$ kN.

It is intuitive to think that the curves with higher torques would produce more severe stick-slip vibrations. However, this is not entirely true. Previous studies [6, 7, 75] already stated that the difference between the maximum torque and the torque at high speeds is crucial to determine the occurrence and severity of stick-slip vibration in drill-strings. The decrease of the parameter b_4 shown in Fig. 3.36b reduces the torque amplitude and also reduce the difference between the maximum and high-speed torques. Thus, a decrease of b_4 is expected to reduce the severity of stick-slip. Otherwise, a decrease on b_3 (Fig. 3.36a) reduces the torque amplitude but slightly increase the difference between the maximum and high-speed torques. In this case, the stick-slip becomes more severe. This behavior is illustrated in Fig. 3.38.

In Figs. 3.39 and 3.40, some parameters are varied at the same time by the

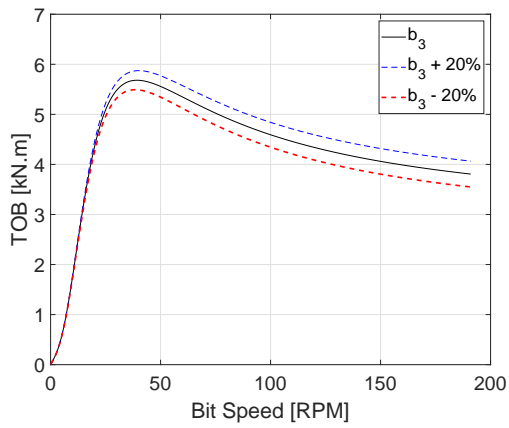


(a)

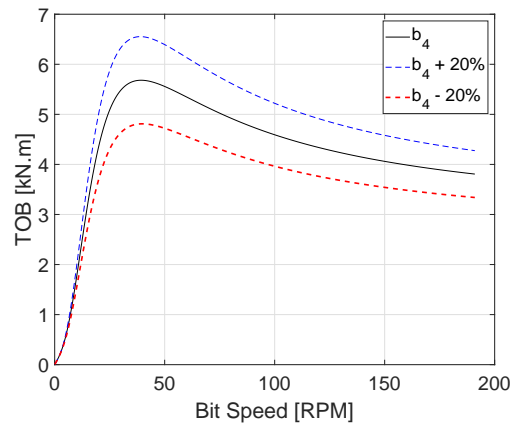


(b)

Figure 3.35: Parametric analysis of bit-rock interaction ($\mathcal{W} = \bar{W}_{ob} = 100$ kN). Varying (a) b_1 ; (b) b_2 .



(a)



(b)

Figure 3.36: Parametric analysis of bit-rock interaction ($\mathcal{W} = \bar{W}_{ob} = 100$ kN). Varying (a) b_3 ; (b) b_4 .

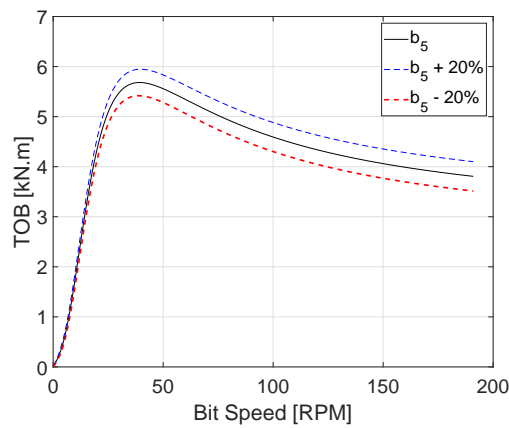


Figure 3.37: Parametric analysis of bit-rock interaction ($\mathcal{W} = \bar{W}_{ob} = 100$ kN). Varying b_5 .

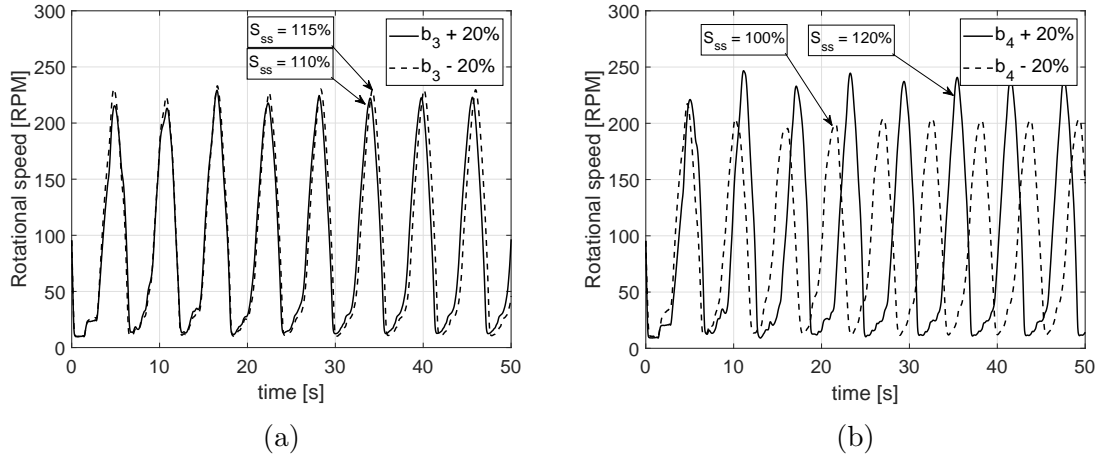


Figure 3.38: Bit rotational speed for $\bar{W}_{ob} = 100$ kN and $\Omega = 95.5$ RPM. Varying (a) b_3 and (b) b_4 .

same factor. It is concluded that if b_2 and b_4 are varied by the same factor, the shape of bit-rock interaction does not change. Also, the variation of b_1 and b_5 affects much more the torque on lower speeds than in higher speeds. In Fig. 3.40, the increase of b_3 and b_4 makes the curve achieve higher values and increase the difference between maximum TOB and high-speed TOB. Otherwise, an increase on b_2 , b_3 and b_4 decreases the difference between maximum TOB and high speed TOB.

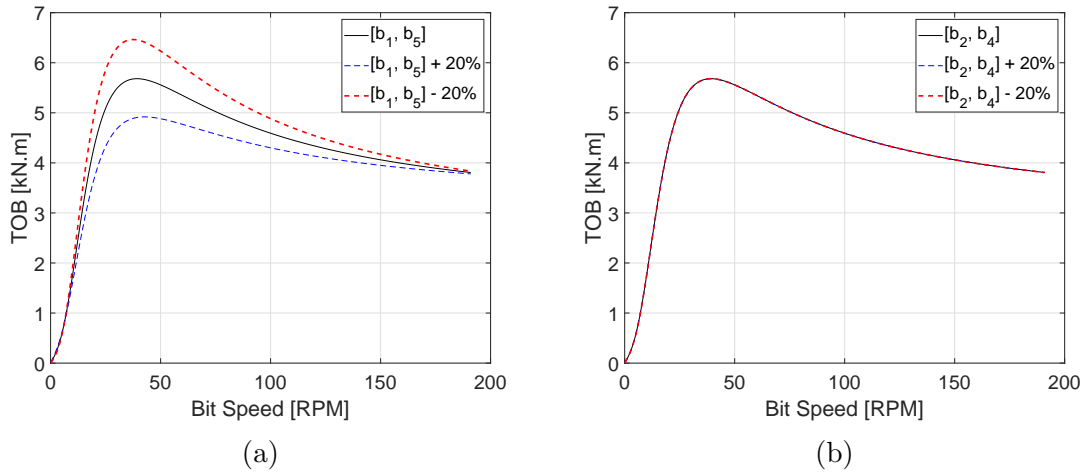


Figure 3.39: Parametric analysis of bit-rock interaction ($\mathcal{W} = \bar{W}_{ob} = 100$ kN). Varying together (a) b_1 and b_5 ; (b) b_2 and b_4 .

Figure 3.41 show the bit rotational speed at the bit when b_2 , b_3 and b_4 are increased. It is concluded that, although a decrease in these parameters results in a decrease in TOB, the bigger difference between max. TOB and high-speed TOB makes the stick-slip worse.

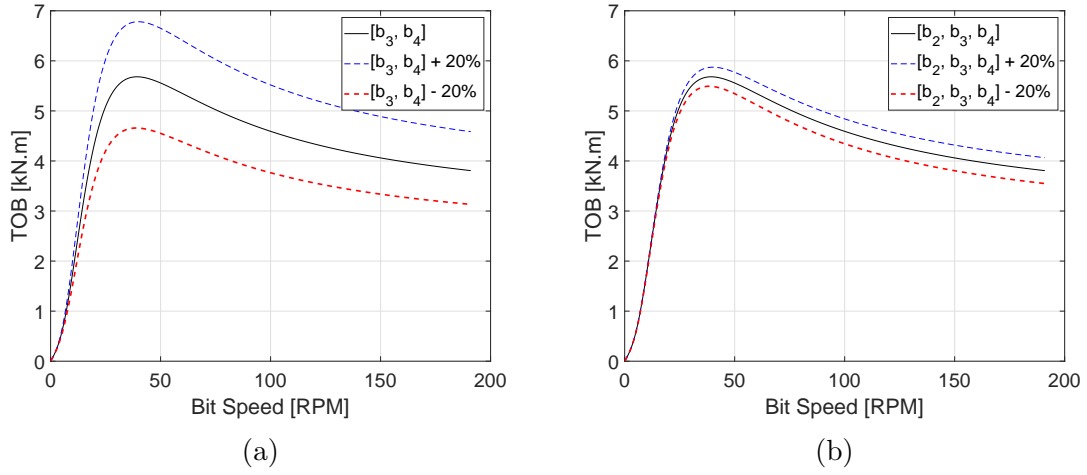


Figure 3.40: Parametric analysis of bit-rock interaction ($\mathcal{W} = \bar{W}_{ob} = 100$ kN). Varying together (a) b_3 and b_4 ; (b) b_2 , b_3 and b_4 .

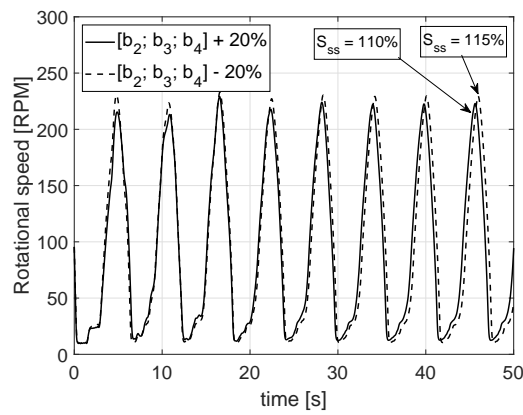


Figure 3.41: Bit rotational speed for $\bar{W}_{ob} = 100$ kN and $\Omega = 95.5$ RPM. Varying (a) b_3 and (b) b_4 .

Chapter 4

Stochastic numerical investigation

As discussed in Sec. 2.3, since 1958, a variety of authors have proposed different probabilistic approaches to study the random vibration of drill-strings. In the majority, the interaction of drill-string with the well was identified to be the main source of uncertainties in drilling operations. Besides, these uncertainties are commonly taken into account in the bit-rock interaction model [37, 53, 55] and associated with the random strength of the rock being cut [14, 55].

Figure 4.1 shows measurements of rock unconfined compressive strength (UCS) by well depth. In Fig. 4.1a, HARELAND and NYGÅRD [76] presents the data from an Italian onshore field [77] for cutting strength obtained by mechanical tests and for a novel approach using ROP. Taking only the cutting strength, which is obtained by mechanical tests, it is clear that UCS presents a high variation along well depth. In Fig. 4.1b, ZAUSA *et al.* [77] presents more data from this same field. It is observed that UCS fluctuates around a mean value during specific depth intervals. Due to this, the stochastic model proposed in this chapter to describe these fluctuations will assume a constant mean over time because the bit is drilling the same rock but with random strength.

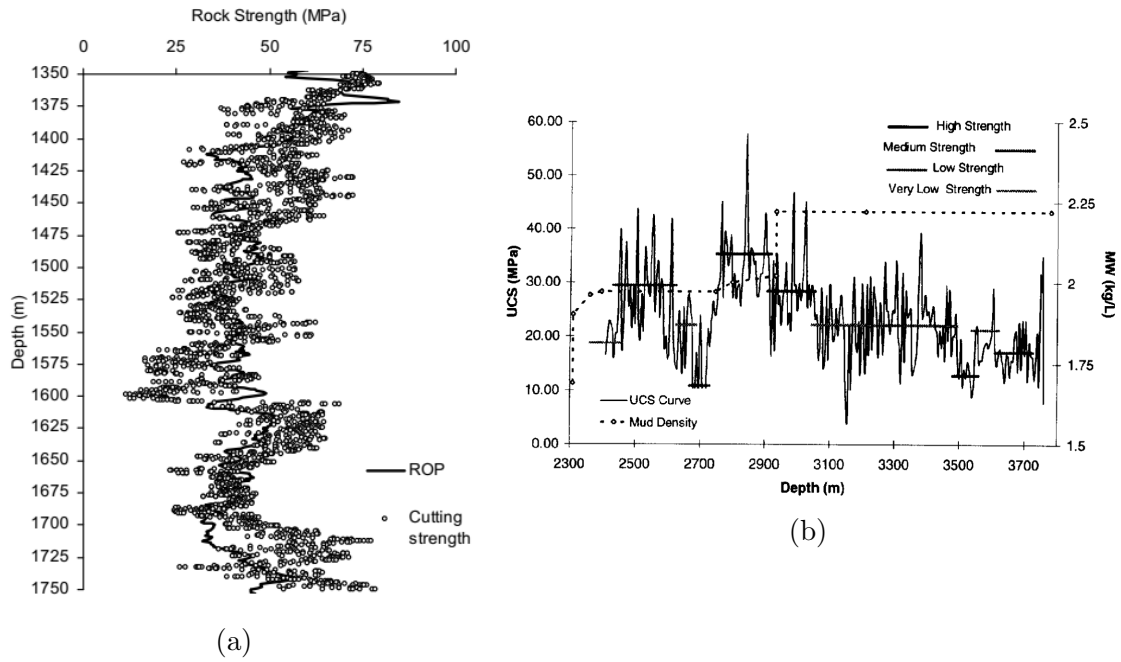


Figure 4.1: Rock Strength by the depth of well. (a) Adopted from [76]; (b) Adopted from [77].

In 1992, DETOURNAY and DEFOURNY [29] associated the UCS to the intrinsic specific energy ϵ . This intrinsic specific energy is interpreted as the amount of energy required to cut a unit volume of rock. Thus, it is directly associated with the cutting components of bit-rock interaction. Figure 4.2 shows the correlation between UCS (q) and ϵ . The dispersion of these variables is associated with stochastic events linked to the failure of rock [29].

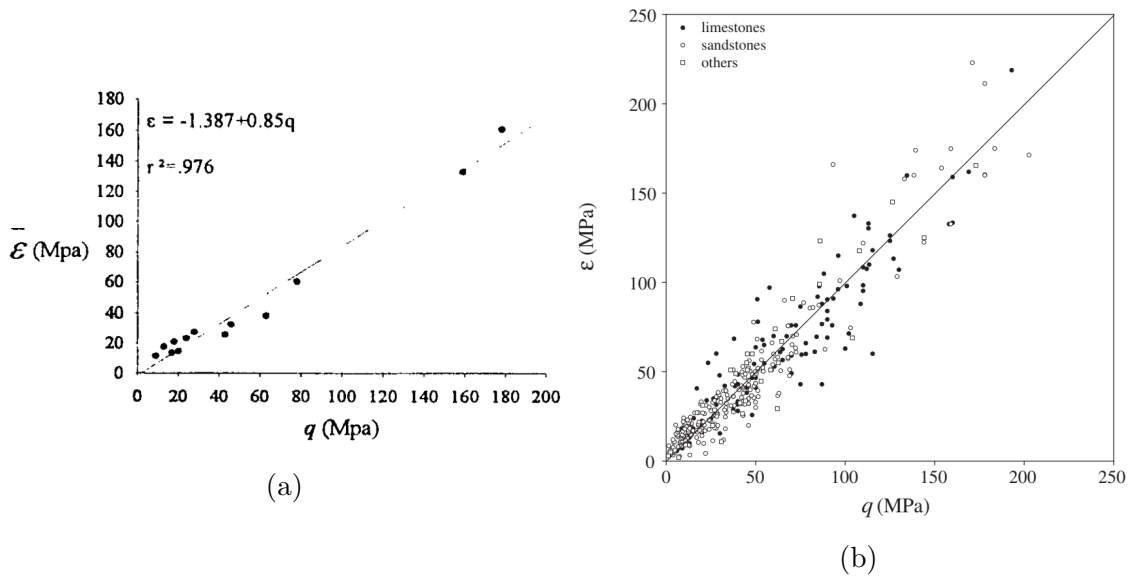


Figure 4.2: Correlation between unconfined compressive strength q and specific energy ϵ . (a) Adopted from [29]; (b) Adopted from [78].

Figure 4.3 shows the intrinsic specific energy calculated during one scratch test. Figure 4.3a depicts a high-frequency content that is associated with stochastic events linked to failure at the scale of the grains or below [29]. In Fig. 4.3b, another test is presented and a moving average is applied with a window of 1.0 cm. The resultant low-frequency content is then associated with heterogeneities or weak zones along the core specimen [79].

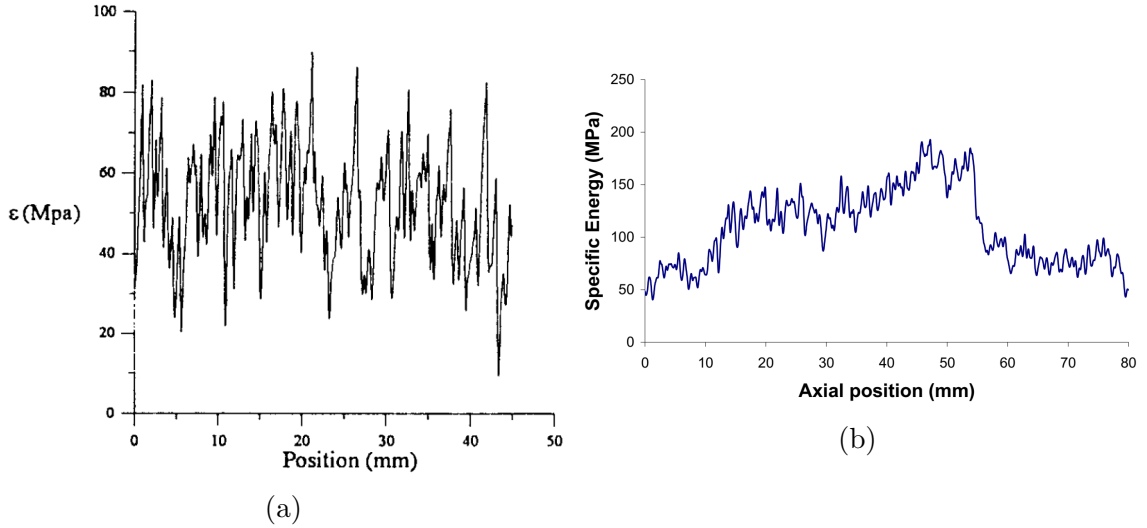


Figure 4.3: Measurements of intrinsic specific energy during a scratch test. (a) Adopted from [29]; (b) Adopted from [79].

In summary, uncertainties related to the specific energy were observed in both laboratory and field tests, corroborating to the motivation of the inclusion of such uncertainties in bit-rock interaction through the cutting components.

4.1 Stochastic model for bit-rock interaction

As discussed in the last section, the uncertainties related to rock strength are associated to the cutting components of bit-rock interaction. Thus, it is necessary to define the cutting component of the bit-rock interaction depicted in Eqs. 3.33 and 3.34, which is [80]:

$$T_c = -a_4 Z (\dot{\theta}_{bit})^2 \frac{\dot{u}_{bit}}{\dot{\theta}_{bit}}, \quad (4.1)$$

where T_c is the cutting component of TOB. In the bit-rock interaction model adopted in this work, there is not a component clearly associated with the cutting process. Since the variation of the axial force is small, the uncertainty in the cutting component of WOB is ignored.

The parameter a_4 is then modeled by a stochastic process $\{\mathbf{A}_4(t), t \in \mathbb{R}\}$ with

values in \mathbb{R}^+ . The stochastic process $\mathbf{A}_4(t) = \{\mathbf{A}_4(t), t \in \mathbb{R}\}$ is constructed according to the following properties:

- i For all t , $\mathbf{A}_4(t) > 0$.
- ii As the idea is to simulate the variation of rock strength within the same rock, the stochastic process $\mathbf{A}_4(t)$ is assumed to be a first-order stationary process (constant first moment over time) which is not Gaussian because the support is $[0, \infty)$.
- iii The second moment of $\mathbf{A}_4(t)$ is finite for all t ($\mathbb{E}\{\mathbf{A}_4^2(t)\} < \infty$) and the first moment is known $\mathbb{E}\{\mathbf{A}_4(t)\} = a_{4m}$, which is independent of time. \mathbb{E} is the linear operator known as mathematical expectation.

The non-Gaussian stochastic process $\mathbf{A}_4(t)$ can be constructed using the methodology presented in [81–83]. Thus, for all $t \in \mathbb{R}$, the stochastic process $\mathbf{A}_4(t)$ is written as:

$$\mathbf{A}_4(t) = a_{4m} (h_a + \mathbf{H}(t))^2 \quad (4.2)$$

where h_a is defined as a constant such that

$$\mathbb{E}\{(h_a + \mathbf{H}(t))^2\} = 1, \quad \mathbb{E}\{(h_a + \mathbf{H}(t))^4\} < \infty. \quad (4.3)$$

Actually, the conditions defined in Eq. 4.3 guarantee the conditions $\mathbb{E}\{\mathbf{A}_4^2(t)\} < \infty$ and $\mathbb{E}\{\mathbf{A}_4(t)\} = a_{4m}$. In addition, notice that the way $\mathbf{A}_4(t)$ is constructed (Eq. 4.2) guarantees that $\mathbf{A}_4(t)$ is always positive if a_{4m} is also positive.

The next step is to define the stochastic process $\mathbf{H}(t)$ to generate $\mathbf{A}_4(t)$. Two different stochastic processes are proposed: Ornstein–Uhlenbeck Process [84] (O-U Process) and a novel Coupled Process (CP Process). The theory used to simulate these stochastic processes is briefly introduced in Appendix B.

4.1.1 Ornstein–Uhlenbeck process

The Ornstein–Uhlenbeck Process ($\mathbf{Y}(t)$) can be used to represent a second-order stationary Gaussian process $\{\mathbf{P}(t), t \in \mathbb{R}\}$, which is centered, mean-square continuous, stationary and ergodic. The power spectral density (PSD) of such a process can then be defined as [82]:

$$S_P(\omega) = \frac{1}{2\pi} \frac{b_2^2}{\omega^2 + b_1^2}, \quad (4.4)$$

where ω is a frequency in rad/s, b_1 and b_2 are positive constants and $S_P(\omega)$ is the PSD in $(\text{rad/s})^{-1}$.

Figure 4.4 shows the PSD of process $\mathbf{P}(t)$ considering several values for b_1 and b_2 . In Fig.4.4a, the $S_P(\omega)$ is plotted against frequency in Hz and in Fig. 4.4b, the PSD is normalized by its maximum value $\max\{S_P\} = \frac{1}{2\pi} \frac{b_2^2}{b_1^2}$ in order to allow the parametric analysis in terms of the decreasing in amplitude with frequency.

Cases 1 and 4 have different amplitudes, but the relative decrease of amplitude with frequency is the same, as in cases 2 and 3. It is observed that a change on b_2 affects only the variance, but not the attenuation over frequencies. This phenomenon occurs because of the definition of $S_P(\omega)$, in which b_2^2 multiplies the whole equation. Otherwise, the parameter b_1 affects directly the attenuation over frequencies. The variance of $\mathbf{P}(t)$ is defined as

$$\sigma_P^2 = \int_{-\infty}^{\infty} \frac{b_2^2}{2\pi(\omega^2 + b_1^2)} d\omega = \frac{b_2^2}{2b_1}. \quad (4.5)$$

It is noticed that, as b_2 affects the amplitude of $S_P(t)$, it will also affect the variance of $\mathbf{P}(t)$. In addition, a change on b_1 also affects the variance, besides the attenuation. Furthermore, the change on b_1 affects more the amplitude near frequency zero and it does not affect much higher frequencies.

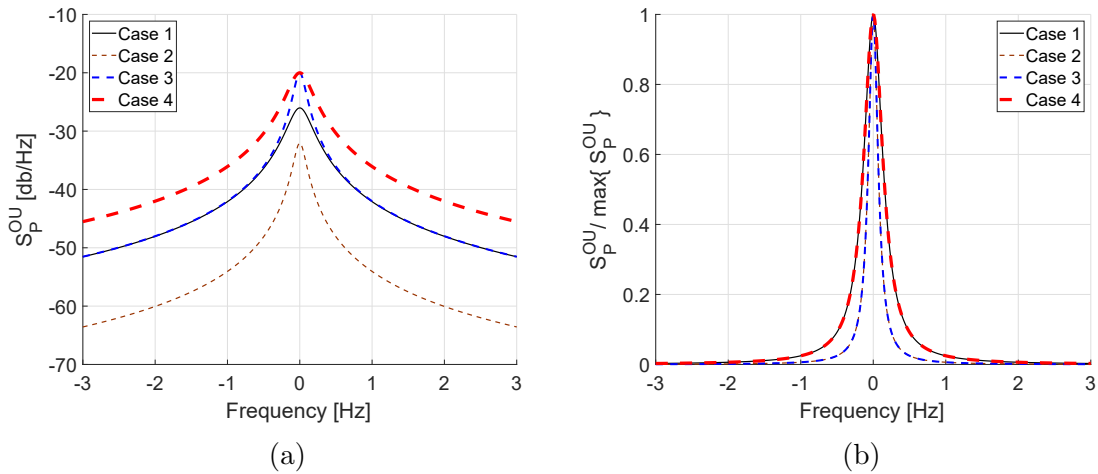


Figure 4.4: Power Spectral Density of process $\mathbf{P}(t)$ for several values of b_1 and b_2 . (a) Without normalization; (b) With normalization. Case 1: $b_1 = 1.0$, $b_2 = 0.05$; Case 2: $b_1 = 0.5$, $b_2 = 0.0125$; Case 3: $b_1 = 0.5$, $b_2 = 0.05$; Case 4: $b_1 = 1.0$, $b_2 = 0.1$.

The stochastic process $\mathbf{P}(t)$ can be interpreted as a linear filtering of the centered Gaussian white noise N_∞ whose PSD is given by

$$S_{N_\infty} = \frac{1}{2\pi}, \quad (4.6)$$

with a linear filter defined by the frequency response function

$$h(\omega) = \frac{b_2}{i\omega + b_1}. \quad (4.7)$$

Thus, the PSD of the filtered signal can be calculated as

$$S_P(\omega) = |h(\omega)|^2 S_{N_\infty}. \quad (4.8)$$

Therefore, the Ornstein–Uhlenbeck Process ($\{\mathbf{Y}(t), t \in \mathbb{R}\}$) can be used to construct the process $\mathbf{P}(t)$ through a linear Itô stochastic differential equation (SDE) known as Langevin’s equation (or Ornstein–Uhlenbeck equation) [84], whose solution is asymptotically stationary. The original application of this equation in physics was as a model for the velocity of a Brownian particle in a fluid. In this work, it is used only to generate a process with the characteristics defined before. This equation works as a linear filter and is defined as:

$$d\mathbf{Y}(t) = -b_1 \mathbf{Y}(t) dt + b_2 d\mathbf{W} , \quad (4.9)$$

where $\mathbf{W}(t)$ is a Wiener process (for more details, see Appendix B). The initial condition for Eq. 4.9 is $\mathbf{Y}(0) = 0$ a.s. (*almost surely*). The analytical solution of Eq. 4.9 is then given by

$$\mathbf{Y}(t) = b_2 \int_0^t e^{-b_1(t-s)} d\mathbf{W} . \quad (4.10)$$

with the first and second moments given by

$$\mathbb{E}[\mathbf{Y}(t)] = 0, \quad \mathbb{E}[\mathbf{Y}^2(t)] = \frac{b_2^2}{2b_1} (1 - e^{-2b_1 t}), \quad (4.11)$$

respectively. The asymptotically stationarity property is noticed in the second moment, which tends to the constant value $\mathbb{E}[\mathbf{Y}^2(t)] = \frac{b_2^2}{2b_1}$, when t is large enough ($t > \tau$).

Next, it is possible to rewrite Eq. 4.2 to consider the O-U process as:

$$\mathbf{A}_4(t) = a_{4m} (h_{OU} + \mathbf{Y}(t))^2 \quad (4.12)$$

where h_{OU} is the deterministic function h_a for the O-U process. To find the function h_{OU} , the first condition defined in Eq. 4.3 must be satisfied, thus:

$$\mathbb{E}[h_{OU}^2] + 2\mathbb{E}[h_{OU} \mathbf{Y}(t)] + \mathbb{E}[\mathbf{Y}^2(t)] = 1 , \quad (4.13)$$

which can be solved by using the moments calculated in Eq. 4.11. This yields:

$$h_{OU}^2 = 1 - \frac{b_2^2}{2b_1}. \quad (4.14)$$

Considering that h_{OU}^2 and b_1 are always positive, Eq. 4.13 yields to the following constraints ([82]):

$$b_1 > 0 \quad \text{and} \quad 0 < b_2 < \sqrt{2b_1}. \quad (4.15)$$

Finally, it is concluded that the statistics of the process $\mathbf{Y}(t)$ generated by Langevin's equation are equivalent to the ones of process $\mathbf{P}(t)$ if τ is chosen large enough to let $\mathbf{Y}(t)$ achieve stationarity.

4.1.2 Coupled process

The second stochastic process is a novel stochastic process that is proposed in this work. It was assumed that a_4 is the stochastic process $\mathbf{A}_4(t)$ because the rock UCS changes while drill-bit drills the rock. However, let's consider the case when drill-string presents torsional oscillations in which drill-bit achieves almost zero speed. The stochastic process $\mathbf{Y}(t)$ generated by the linear SDE defined in Eq. 4.9 will ignore this situation and continues to vary, although the bit is almost not moving. In order to circumvent this problem, a novel Coupled stochastic process (CP process) is proposed.

The proposed process is called coupled because it depends on the drill-string dynamical response. Two hypotheses served as a basis for the construction of this process:

- (i) CP process is the same as the O-U process if drill-bit rotates at the same speed as the top rotary system, and;
- (ii) When the bit rotational speed decreases, the frequency and amplitude of variation of CP process also decreases until CP process remains almost constant over time.

As a first attempt, the right side of Eq.4.9 is multiplied by the bit rotational speed and the constants b_1 and b_2 becomes, respectively, $\nu_1 = \frac{b_1}{\Omega}$ and $\nu_2 = \frac{b_2}{\Omega}$. The SDE would be:

$$d\mathbf{G}(t) = -\nu_1 \dot{\Theta}_{bit}(t) \mathbf{G}(t) dt + \nu_2 \dot{\Theta}_{bit}(t) d\mathbf{W}, \quad (4.16)$$

where \mathbf{W} is a Wiener process and $\dot{\Theta}_{bit}(t)$ is the bit rotational speed, which becomes a stochastic process due to the stochastic bit-rock interaction. The stochastic system of equations will be explained in details in Sec. 4.2. Although this formulation seems very reasonable, the second moment ends up depending on the bit rotational speed, which is not physically true because the uncertainty level on lithology are not related to the bit rotational speed. Thus, a modification of Eq. 4.16 is proposed and the CP stochastic process $\mathbf{G}(t)$ is then constructed by the SDE:

$$d\mathbf{G}(t) = -\nu_1 \dot{\Theta}_{bit}^2(t) \mathbf{G}(t) dt + \nu_2 \dot{\Theta}_{bit}(t) d\mathbf{W}. \quad (4.17)$$

where $\nu_1 = \frac{b_1}{\Omega^2}$ and $\nu_2 = \frac{b_2}{\Omega}$. The initial value for Eq. 4.17 is $\mathbf{G}(0) = 0$ a.s.. Note that Eq. 4.17 is a nonlinear stochastic differential equation, which does not have an analytical solution. Furthermore, there are no explicit formulae for calculating the moments. Thus, in order to simplify the problem and calculate the moments, the rotational speed at the bit is considered as the deterministic result obtained from Eq. 3.42, i.e. $\dot{\Theta}_{bit}(t) = \dot{\theta}_{bit}(t)$. Therefore, Eq. 4.17 becomes a scalar linear equation and the theory presented in Appendix C can be applied to calculate the moments. The first moment $m(t) = \mathbb{E}\{\mathbf{G}(t)\}$ can be obtained by solving the following differential equation:

$$\frac{dm}{dt} = -\nu_1 \dot{\theta}_{bit}^2(t) m(t), \quad m(0) = \mathbf{G}(0) = 0, \quad (4.18)$$

with solution $m = 0$, thus $\mathbb{E}\{\mathbf{G}(t)\} = 0$. It assures the property (ii) that says that $\mathbf{H}(t)$ must be a first-order stationary stochastic process. The second moment $p(t) = \mathbb{E}\{\mathbf{G}^2(t)\}$ is described by the differential equation:

$$\frac{dp}{dt} = -2\nu_1 \dot{\theta}_{bit}^2(t) p(t) + (\nu_2 \dot{\theta}_{bit}(t))^2, \quad p(0) = \mathbf{G}^2(0) = 0, \quad (4.19)$$

which solution can be written as $p(t) = p_h(t) + p_p(t)$, where $p_h(t)$ is the homogeneous solution (Eq. 4.20) and $p_p(t)$ is the particular solution (Eq. 4.21).

$$p_h(t) = c_1 e^{\int_0^t -2\nu_1 \dot{\theta}_{bit}^2(t) dt}, \quad (4.20)$$

$$p_p(t) = \frac{\nu_2^2}{2\nu_1}, \quad (4.21)$$

where c_1 is a constant. Since ν_1 is defined as a positive constant and the term $2\nu_1 \dot{\theta}_{bit}^2(t)$ is always positive, the solution $p_h(t)$ goes to zero after a large enough time ($t > \tau$) and the second moment then becomes

$$\mathbb{E}\{\mathbf{G}^2(t)\} = \frac{\nu_2^2}{2\nu_1}, \quad (4.22)$$

which allows the calculation of h_a in Eq. 4.2 for the CP process. The Eq. 4.2 can be rewritten to consider the CP process as:

$$\mathbf{A}_4(t) = a_{4m} (h_{CP} + \mathbf{G}(t))^2 \quad (4.23)$$

where h_{CP} is the deterministic function h_a for the CP process. This function is calculated such that the first condition defined in Eq. 4.3 is satisfied:

$$\mathbb{E}[h_{CP}^2] + 2\mathbb{E}[h_{CP} \mathbf{G}(t)] + \mathbb{E}[\mathbf{G}^2(t)] = 1 \rightarrow h_{CP}^2 = 1 - \frac{\nu_2^2}{2\nu_1}. \quad (4.24)$$

Considering that h_{CP}^2 and ν_1 are always positive, Eq. 4.24 yields to the following constraints which are very similar to Eq. 4.15:

$$\nu_1 > 0 \quad \text{and} \quad 0 < \nu_2 < \sqrt{2\nu_1}. \quad (4.25)$$

It is important to point out that, although the simplification $\dot{\Theta}_{bit}(t) = \dot{\theta}_{bit}(t)$ is applied here, the calculated properties are validated for the fully coupled case in Sec. 4.3.2. Notice that, if the simplification $\dot{\Theta}_{bit}(t) = \dot{\theta}_{bit}(t)$ was used in Eq. 4.16, the homogeneous and particular solution of Eq. 4.19 would not be trivial to calculate. In order to simplify and demonstrate the dependence of the second moment on drill-string dynamics, let's consider a case in which there is no vibration and the bit rotates at a constant speed $\dot{\Theta}_{bit} = c_s$, where c_s is a positive constant. Considering that the acceleration of the bit is zero, the particular solution of Eq. 4.19 would be:

$$p_{p2} = \frac{c_s \nu_2^2}{2\nu_1}. \quad (4.26)$$

which depends on the bit rotational speed. Furthermore, the homogeneous solution would be $p_h(t) = c_1 e^{\int_0^t -2\nu_1 \dot{\Theta}_{bit}(t) dt}$, which is unstable for negative values of bit rotational speeds.

4.2 Stochastic system of equations

As the parameter a_4 is modeled by a stochastic process $\{\mathbf{A}_4(t), t \in \mathbb{R}\}$, the bit-rock interaction $\bar{\mathbf{f}}_T$ and the displacement vector $\bar{\mathbf{u}}$ defined in Eq. 3.36 also become stochastic processes denoted by $\bar{\mathbf{F}}_T$ and $\bar{\mathbf{U}}$, respectively. The stochastic dynamics equation is then described by:

$$[\bar{M}] \ddot{\bar{\mathbf{U}}}(t) + [\bar{D}] \dot{\bar{\mathbf{U}}}(t) + [\bar{K}_e] \bar{\mathbf{U}}(t) = \bar{\mathbf{F}}_T(\dot{\Theta}_{bit}(t), \dot{\mathbf{U}}_{bit}(t)) - \mathbf{d}_2 \Omega - \mathbf{k}_{e2} \Omega t, \quad (4.27)$$

where $\bar{\mathbf{F}}_T(\dot{\Theta}_{bit}(t), \dot{\mathbf{U}}_{bit}(t)) = \left[0 \quad \dots \quad 0 \quad \mathbf{F}_{bit}(\dot{\Theta}_{bit}(t), \dot{\mathbf{U}}_{bit}(t)) \quad \mathbf{T}_{bit}(\dot{\Theta}_{bit}(t), \dot{\mathbf{U}}_{bit}(t)) \right]^T$ represents now the stochastic forces at the bit due to bit-rock interaction in which $\mathbf{T}_{bit}(\dot{\Theta}_{bit}(t), \dot{\mathbf{U}}_{bit}(t))$ and $\mathbf{F}_{bit}(\dot{\Theta}_{bit}(t), \dot{\mathbf{U}}_{bit}(t))$ are the stochastic processes described in Eqs. 4.28 and 4.29. They describe the torque and axial force variation around the desired value for WOB, respectively.

$$\mathbf{T}_{bit}(\dot{\Theta}_{bit}(t), \dot{U}_{bit}(t)) = -\mathbf{A}_4(t) \mathbf{Z}^2(\dot{\Theta}_{bit}(t)) \frac{\dot{U}_{bit}(t)}{\dot{\Theta}_{bit}(t)} - a_5 \mathbf{Z}(\dot{\Theta}_{bit}(t)), \quad (4.28)$$

$$\mathbf{F}_{bit}(\dot{\Theta}_{bit}(t), \dot{U}_{bit}(t)) = -\frac{\dot{U}_{bit}(t)}{a_2 \mathbf{Z}^2(\dot{\Theta}_{bit}(t))} + \frac{a_3 \dot{\Theta}_{bit}(t)}{a_2 \mathbf{Z}(\dot{\Theta}_{bit}(t))} - \frac{a_1}{a_2} - \bar{W}_{ob}, \quad (4.29)$$

where $\mathbf{A}_4(t)$ is the stochastic process defined in Eq. 4.2; $\Theta_{bit}(t)$ and $\dot{U}_{bit}(t)$ are the stochastic rotational and axial speeds at the bit, respectively, and; $\mathbf{Z}(\dot{\Theta}_{bit}(t))$ is the regularization function defined in Eq. 3.32 that also becomes a stochastic process due to $\dot{\Theta}_{bit}(t)$.

Equation 4.27 can also be reduced in the same way it was presented in Sec.3.5. The reduced stochastic equation of motion becomes:

$$[m]\ddot{Q}(t) + [d]\dot{Q}(t) + [k_e]Q(t) = \mathbf{F}_{Tr}(\dot{\Theta}_{bit}(t), \dot{U}_{bit}(t)) - \mathbf{d}_{2r}\Omega - \mathbf{k}_{e2r}\Omega t, \quad (4.30)$$

where $[m] = [\Phi]^T[\bar{M}][\Phi]$; $[d] = [\Phi]^T[\bar{D}][\Phi]$; $[k_e] = [\Phi]^T[\bar{K}_e][\Phi]$; $\mathbf{F}_{Tr} = [\Phi]^T \bar{\mathbf{F}}_T(\dot{\Theta}_{bit}(t), \dot{U}_{bit}(t))$; $\mathbf{d}_{2r} = [\Phi]^T \mathbf{d}_2$, and; $\mathbf{k}_{e2r} = [\Phi]^T \mathbf{k}_{e2}$. Thus, the stochastic system of equations to be solved in numerical procedure is defined as:

$$\begin{cases} d\mathbf{X}_1(t) = \mathbf{X}_2(t) dt \\ d\mathbf{X}_2(t) = [m]^{-1} \left[-[d]\mathbf{X}_2(t) - [k_e]\mathbf{X}_1(t) + \mathbf{F}_{Tr}(\dot{\Theta}_{bit}(t), \dot{U}_{bit}(t))(\mathbf{X}_1(t), \mathbf{X}_3(t)) \right. \\ \left. - \mathbf{d}_{2r}\Omega - \mathbf{k}_{e2r}\Omega t \right] dt \\ d\mathbf{X}_3(t) = \mathbf{F}(\mathbf{X}, t) dt + \mathbf{B}(\mathbf{X}, t) d\mathbf{W} \end{cases}, \quad (4.31)$$

where $\mathbf{X}(t) = [\mathbf{X}_1(t) \ \mathbf{X}_2(t) \ \mathbf{X}_3(t)] = [\mathbf{U}(t) \ \dot{U}(t) \ \mathbf{H}(t)]$ is the state space variable; $\mathbf{F}(\mathbf{X}(t), t)$ and $\mathbf{B}(\mathbf{X}(t), t)$ are the drift and diffusion coefficients of the stochastic differential equation used to generate $\mathbf{X}_3(t) = \mathbf{H}(t) = \{\mathbf{H}(t), t \in \mathbb{R}\}$ (note that $\mathbf{H}(t)$ can be either $\mathbf{Y}(t)$ (Eq. 4.9) or $\mathbf{G}(t)$ (Eq. 4.17), depending on the stochastic process chosen).

4.3 Stochastic numerical results

The stochastic numerical results are going to be analyzed in three parts. At first, the generation of the stochastic process $\mathbf{A}_4(t)$ through $\mathbf{Y}(t)$ or $\mathbf{G}(t)$ is discussed. Next, the stochastic response of drill-string is analyzed for both stochastic processes considering two operational conditions: one with stick-slip oscillations in the

deterministic case and one without stick-slip. At last, a parametric analysis is performed in order to evaluate the influence of a set of parameters in the stochastic response. The stochastic model was simulated using a Modified Euler's scheme, which is strongly consistent [85]. This method is explained in Appendix D.

4.3.1 Stochastic process generation

Before introducing the stochastic process $\mathbf{A}_4(t)$ in drill-string dynamics, we must understand the characteristics of such process. Therefore, this section will discuss the two stochastic processes proposed in this work.

Ornstein–Uhlenbeck process

The parameters used in the simulation of O-U process are: $a_{4m} = 9.537 \cdot 10^6$ N rad, $b_1 = 1.0$ and $b_2 = 0.05$. We begin with a convergence study of the simulated stochastic process. For this purpose, 120 seconds are simulated and the second moment $\mathbb{E}\{\mathbf{Y}^2(\tau_e)\}$ is calculated at $\tau_e = 120$ seconds. Figure 4.5a shows the convergence of the second moment for the number of simulations. It seems that 200 simulations are enough to achieve convergence in this case. Figure 4.5b shows the convergence of the second moment for the step time size Δt used in the numerical procedure. Although the convergence is achieved for $\Delta t < 10^{-1}$, a step time of 5×10^{-4} is used because of the convergence of the drill-string dynamical response.

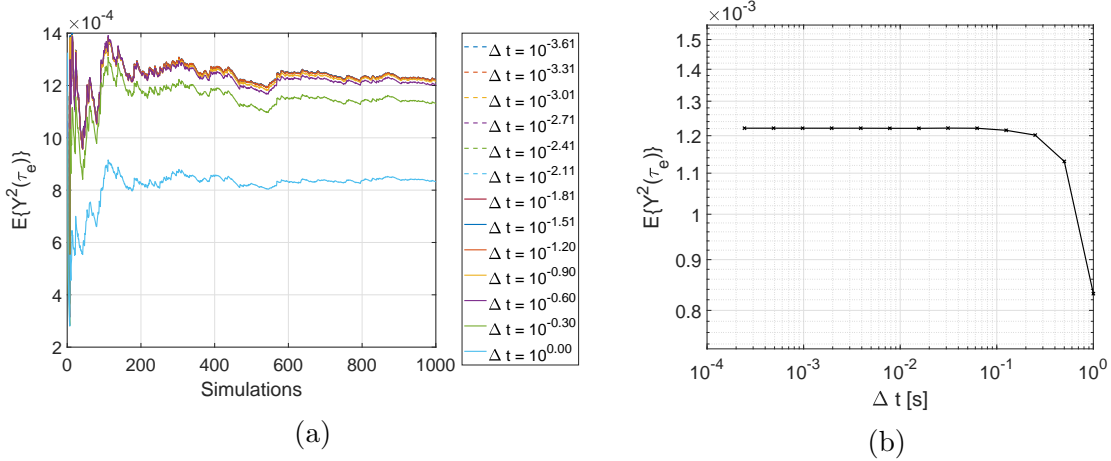


Figure 4.5: Convergence of the second moment of $\mathbf{Y}(t)$: (a) over the number of simulations and step time size Δt , and; (b) over time step size Δt for 1000 simulations.

Figure 4.6 confirms the convergence of stochastic process $\mathbf{A}_4(t)$ for either time step and number of simulations. Note that the curves are closer to each other (i.e. Δt changes less the second moment) and stabilize with fewer simulations (around 100 instead of 200), suggesting that process $\mathbf{A}_4(t)$ converges faster than $\mathbf{Y}(t)$.

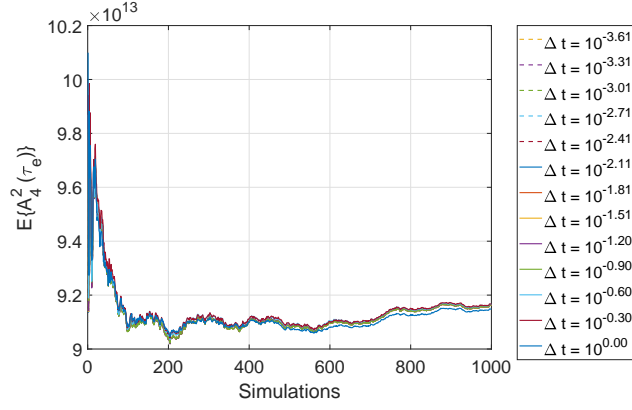


Figure 4.6: Convergence of the second moment of $\mathbf{A}_4(t) = a_{4m}(h_{OU} + \mathbf{Y}(t))^2$ over the number of simulations and step time size Δt .

It was mentioned in Sec. 4.1.1 that process $\mathbf{Y}(t)$ is asymptotically stationary, i.e. it tends to a stationary process. This statement was made because of the second moment $\mathbb{E}\{\mathbf{Y}^2(t)\}$, which has an exponential term that tends to zero with time and makes the second moment to become constant. This behavior is demonstrated in Fig. 4.7a, which plots the second moment calculated over 1000 simulations at each time. It shows that the stochastic process $\mathbf{Y}(t)$ becomes stationary after around 2 seconds. Figure 4.7b shows one simulation of $\mathbf{Y}(t)$ used to calculate the second moment. It is observed that $\mathbf{Y}(t)$ varies around zero and its variation seems to be higher amplitudes in low frequencies.

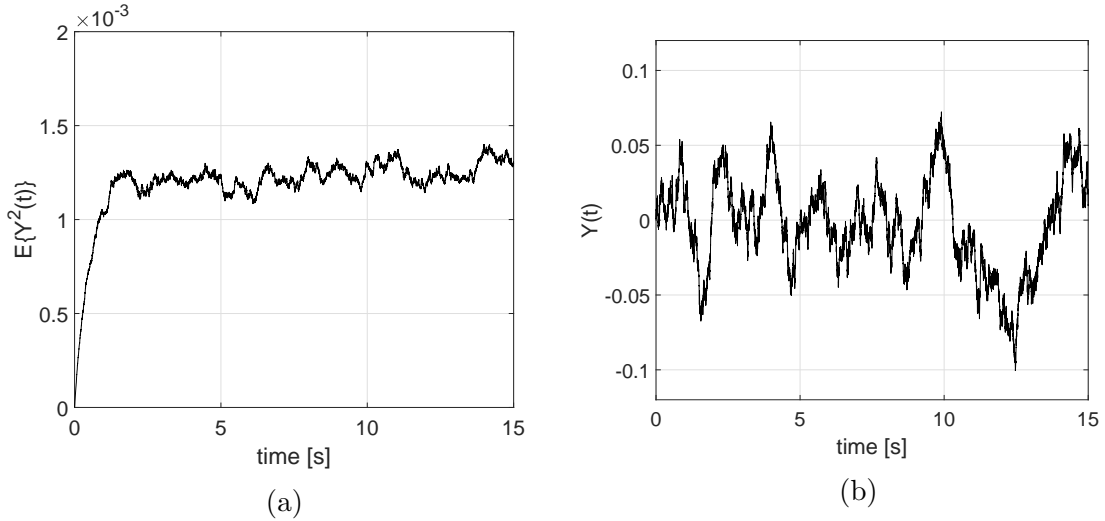


Figure 4.7: (a) Second moment of $\mathbf{Y}(t)$ over time; (b) One realization of stochastic process $\mathbf{Y}(t)$.

A probabilistic envelope of three standard deviations around the mean of process $\mathbf{A}_4(t)$ is plotted in Fig. 4.8a. The mean fluctuates around $a_{4m} = 9.537 \cdot 10^6$, which is expected because $\mathbb{E}\{(h_{OU} + \mathbf{Y}(t))^2\} = 1$. The three standard deviation envelope is about 40% of the mean value a_{4m} , which is acceptable given the variations observed

in experimental data showed in Figs. 4.3, 4.2 and 4.1. The transient of the envelope is related to the time necessary to achieve stationarity. Figure 4.8b shows 5 realizations of process $\mathbf{A}_4(t)$ and a lower variation is observed in the first seconds due to the initial condition that imposes $\mathbf{A}_4(0) = a_{4m}h_{OU}^2$ because $\mathbf{Y}(0) = 0$. This low variation is related to the asymptotically stationarity property.

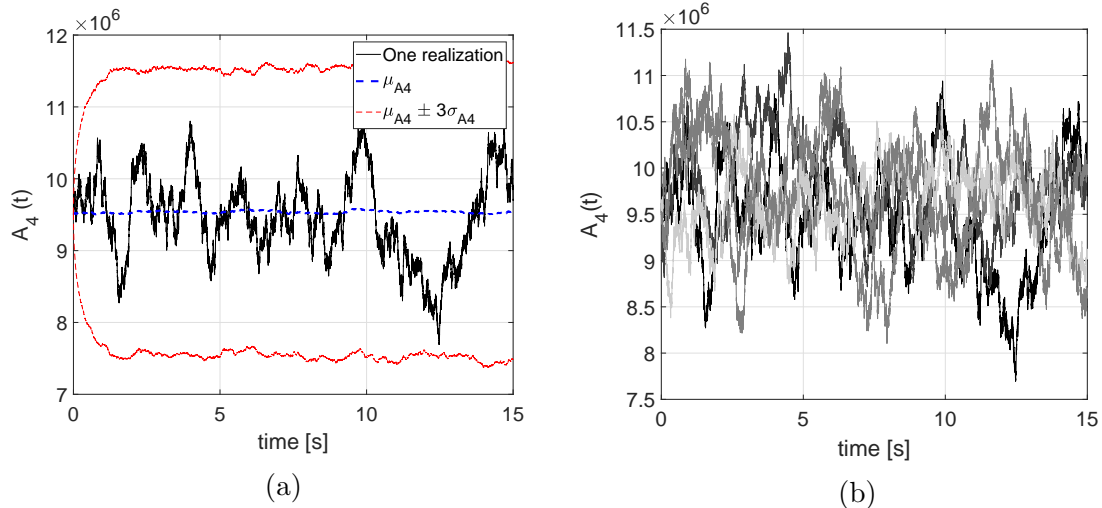


Figure 4.8: (a) Probabilistic envelope of $\mathbf{A}_4(t) = a_{4m}(h_{OU} + \mathbf{Y}(t))^2$ for three times the standard variation σ_{A4} around mean μ_{A4} . (b) Five realizations of the process $\mathbf{A}_4(t) = a_{4m}(h_{OU} + \mathbf{Y}(t))^2$

Next, the Power Spectral Density (PSD) is calculated from the simulated stochastic process and it is compared to the analytical PSD depicted in Eq. 4.4. Figure 4.9 shows the average of the PSDs calculated over 1000 simulations and the analytical PSD. It is concluded that both PSDs fits very well, which indicates that the stochastic process $\mathbf{Y}(t)$ was generated successfully in terms of the PSD.

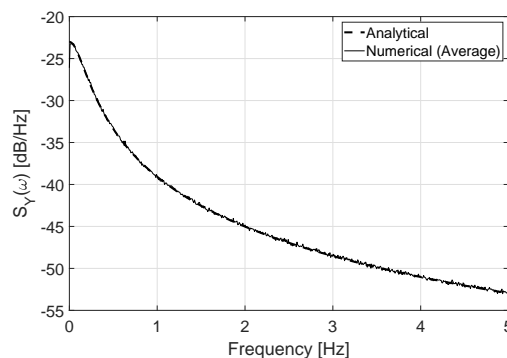


Figure 4.9: Power Spectral Density of process $\mathbf{Y}(t)$ for simulated data and analytical solution.

In order to verify the generation of $\mathbf{A}_4(t)$, the PSD is also evaluated against the analytical result. In order to allow the comparison between the PSDs, they

are normalized by its maximum value. Figure 4.10 shows that the average of PSDs calculated over simulated data fits well the analytical result which indicates that the process $\mathbf{A}_4(t)$ is being constructed correctly.

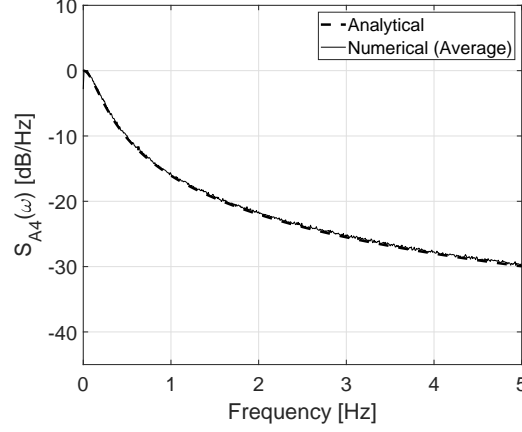


Figure 4.10: Normalized Power Spectral Density of process $\mathbf{A}_4(t) = a_{4m}(h_{OU} + \mathbf{Y}(t))^2$ for simulated data and analytical solution.

Coupled process

The Coupled process (CP process) is simulated in this section. The parameters used in simulation are: $a_{4m} = 9.537 \cdot 10^6$ N rad, $\nu_1 = 0.01$ s²/rad² and $\nu_2 = 0.005$ s/rad. These values were considered in order to allow the comparison with O-U process (note that $b_1 = \nu_1 \cdot 10^2$ and $b_2 = \nu_2 \cdot 10$ for a constant bit speed $\dot{\theta}_{bit} = 95.5$ RPM = 10 rad/s.).

In order to analyze the CP process without the influence of drill-string dynamics, the process $\mathbf{G}(t)$ is simulated without the full coupling with drill-string dynamics at first. For this purpose, the bit rotational speed considered in Eq. 4.17 is set as the deterministic results shown in Fig. 3.22b. In order to wait for process $\mathbf{G}(t)$ to stabilize its second moment before simulation actually begins, 15 seconds are simulated considering a constant bit speed $\dot{\theta}_{bit} = 95.5$ RPM. After these 15 seconds, the simulation restarts using the end of these 15 seconds as the initial condition and the simulation starts to consider the bit speed variations of Fig. 3.22b. Because of the way ν_1 and ν_2 are defined, the results for the first 15 seconds are the same as in Figs. 4.8 and 4.7.

The same way as in the O-U process, the convergence is analyzed in the case of the CP process. Therefore, 120 seconds are simulated and the second moment $\mathbb{E}\{\mathbf{G}^2(\tau_e)\}$ is calculated at $\tau_e = 120$ seconds. Figure 4.11a shows the convergence of the second moment for the number of simulations. It seems that 400 simulations are enough to achieve convergence in this case. Figure 4.11b shows the convergence of the second moment for the step time size Δt used in the numerical procedure.

Although the convergence is achieved for $\Delta t < 10^{-2}$, a step time of 5×10^{-4} is used because of the convergence of drill-string dynamical response.

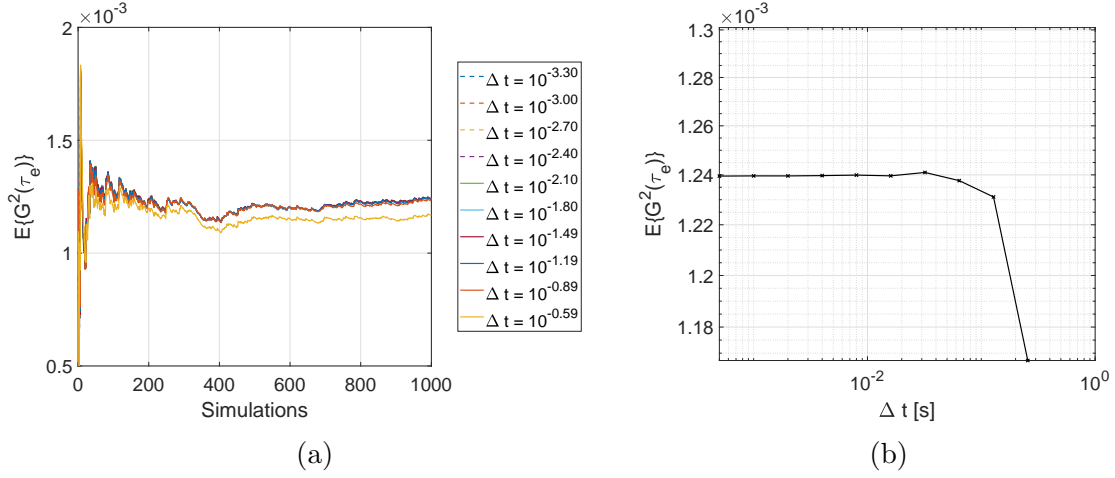


Figure 4.11: Convergence of the second moment of $\mathbf{G}(t)$: (a) over the number of simulations and step time size Δt , and; (b) over time step size Δt for 1000 simulations.

Figure 4.12 confirms the convergence of stochastic process $\mathbf{A}_4(t) = a_{4m}(h_{CP} + \mathbf{G}(t))^2$ for either time step and number of simulations. Note that the curves are closer to each other but it does not stabilize with fewer simulations, as in O-U process.

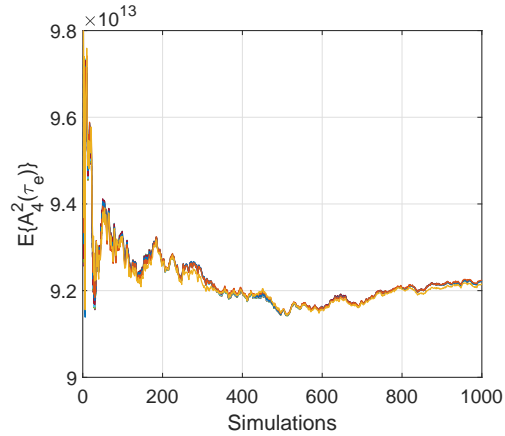


Figure 4.12: Convergence of the second moment of $\mathbf{A}_4(t) = a_{4m}(h_{CP} + \mathbf{G}(t))^2$ over the number of simulations and step time size Δt .

In CP process, the conclusions for both $\mathbf{G}(t)$ and $\mathbf{A}_4(t)$ processes are the same. Because of this, only the graph of $\mathbf{A}_4(t)$ is presented. Figure 4.13 shows a probabilistic envelope of three standard deviations around the mean of process $\mathbf{A}_4(t)$. The mean fluctuates around $a_{4m} = 9.537 \cdot 10^6$, which is also expected because $\mathbb{E}\{(h_{CP} + \mathbf{G}(t))^2\} = 1$. The three standard deviation envelope have almost the same amplitude as in Fig. 4.8a, which permits the comparison between the two

stochastic processes. It is observed a change on the envelope between the phases in which the bit is rotating or almost locked. Also, the envelope fluctuates more during the time bit is rotating. This change on envelope shapes elucidates the homogeneous solution of the second moment (Eq. 4.20). It can also be seen that the changes due to the homogeneous solution are much smaller than in particular solution, which confirms the hypothesis made in Sec. 4.1.2. The green boxes highlight the time intervals in which the bit is almost locked. It is observed that the stochastic process tends to be constant during this time, as expected. The process $\mathbf{A}_4(t)$ does not become strictly constant because of the limitation of the bit-rock interaction model which cannot cause the bit to completely stick, i.e. to achieve zero speed.

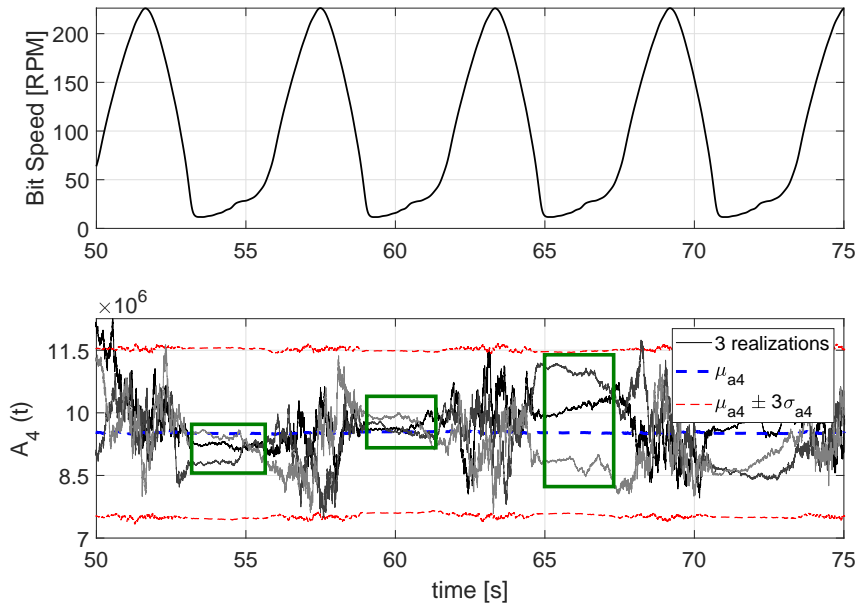


Figure 4.13: Top graph: rotational speed at the bit used as input for the generation of stochastic process $\mathbf{G}(t)$; Bottom graph: 3 realizations and the probabilistic envelope of $\mathbf{A}_4(t) = a_{4m}(h_{CP} + \mathbf{G}(t))^2$ for three times the standard variation σ_{A4} around the mean μ_{A4} . The time intervals in which bit is almost stopped are highlighted by green rectangles.

Since the CP process is not considered wide-sense stationary, it is not possible to calculate its Power Spectral Density. Instead, in Fig. 4.14a, the Fast Fourier Transform (FFT) of process $\mathbf{G}(t)$ is calculated and scaled to make amplitude be in dB/Hz. The FFT is calculated for two distinct time intervals: in one of them, the bit is almost stationary (stick phase) and in the other, the bit is rotating (slip phase). The difference between the spectra is remarkable. In the slip phase, the spectrum presents a smaller attenuation while in stick phase, almost all the energy is concentrated near zero frequency, i.e. the process is almost constant. This behavior can also be noticed in Fig. 4.14b which plots the spectrogram of process $\mathbf{A}_4(t) =$

$a_{4m}(h_{CP} + \mathbf{G}(t))^2$. It is possible to identify the time intervals in which the bit is rotating or almost locked. When the bit is almost locked, the bands are in blue and denote that amplitude is concentrated at frequencies near zero. Otherwise, when the bands are closer to yellow, they have the amplitude distributed over a larger frequency band, which indicates that bit is rotating.

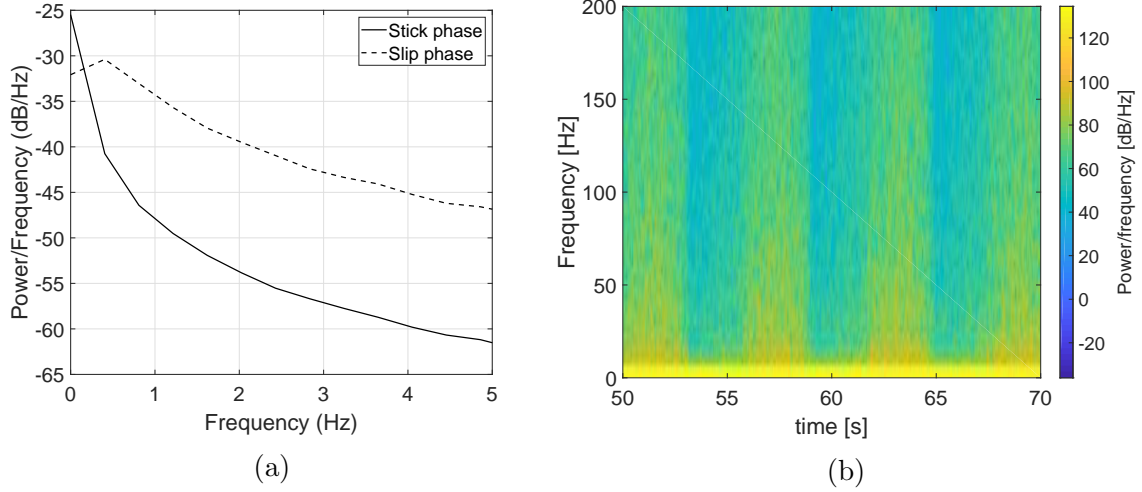


Figure 4.14: (a) Fast Fourier Transform (fft) of process $\mathbf{G}(t)$ for when bit is almost stationary (stick phase) and when bit is rotating (slip phase).; (b) Spectrogram of process $\mathbf{A}_4(t) = a_{4m}(h_{CP} + \mathbf{G}(t))^2$ for simulated data.

4.3.2 Stochastic system response

In this section, the drill-string dynamics is simulated in the presence of the stochastic processes proposed. The parameters used in the simulations are: $a_{4m} = 9.537 \cdot 10^6$ N rad, $b_1 = 1.0$, $b_2 = 0.05$, $\nu_1 = 0.01$ s²/rad² and $\nu_2 = 0.005$ s/rad. The parameters related to drill-string are the same as in Sec. 3.6. The deterministic model is simulated for 250 seconds and the end of the deterministic solution is used as the initial condition of stochastic simulation. The stochastic model is then simulated for more 250 seconds. The solution is obtained by using the solver "ode23t" in MATLAB, for deterministic case, and the stochastic results are obtained by a Modified Euler's scheme. The deterministic solution used as the initial condition for stochastic simulation is shown in Fig. 4.15 in terms of bit rotational speed for two values of WOB. For $\bar{W}_{ob} = 100$ kN, the deterministic result presents a severe vibration at the bit. Otherwise, for $\bar{W}_{ob} = 68$ kN, the bit presents no vibration in steady state.

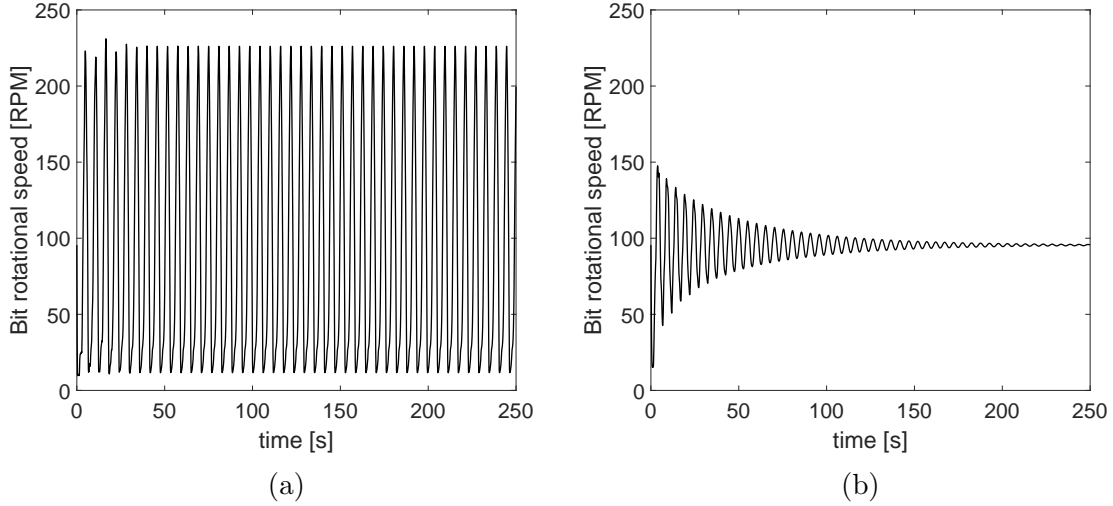


Figure 4.15: Deterministic rotational speed at the bit used as initial condition for stochastic simulation. (a) $\Omega = 95.5$ RPM and $\bar{W}_{ob} = 100$ kN; (b) $\Omega = 95.5$ RPM and $\bar{W}_{ob} = 68$ kN

At first, an investigation is performed in order to evaluate if the model reduction is still working on the stochastic case. Also, the time step Δt of numerical procedure is verified. After the simulation of the deterministic model for 250 seconds, the stochastic model is simulated for more 250 seconds. Figure 4.16 shows the bit rotational speed from 260 to 270 seconds for both proposed stochastic processes. This figure compares the results obtained by the complete model and by the reduced-order model with two time step sizes. It is observed that frequency and amplitude of stick-slip are the same for complete and reduced model, but there is a phase between them. In the case where the complete model is used, it is used in both deterministic and stochastic cases. The same is also true for the reduced model. In deterministic case, a little phase is observed between complete and reduced model. This phase continues to exist in stochastic case, because of the initial condition, and it can increase due to uncertainties. In the complete model, it is possible to detect a higher amplitude of vibration during the stick-slip cycle, but this higher frequency phenomenon does not seem to affect the overall response. In reduced mode, it is also concluded that the time step did not change system response. Thus, the reduced model is going to be used in the following simulations with $\Delta t = 5 \cdot 10^{-4}$.

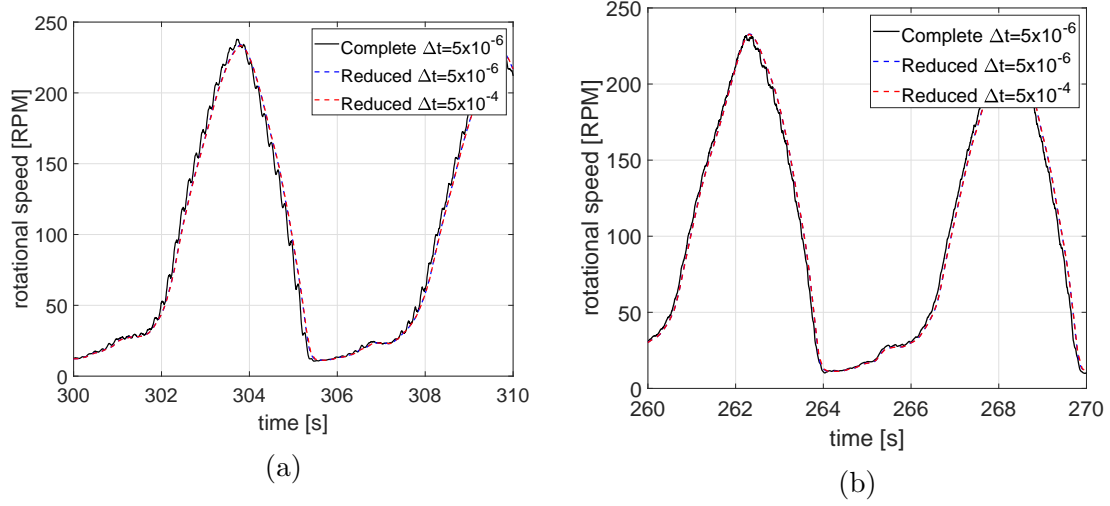


Figure 4.16: Convergence of stochastic drill-string dynamical response. $\Omega = 95.5$ RPM and $\bar{W}_{ob} = 100$ kN. (a) O-U process, and; (b) CP process.

The convergence of the number of simulations (n_s) is also evaluated in terms of the mean square convergence. For this purpose, the function $\text{conv}(n_s)$ is proposed:

$$\text{conv}(n_s) = \frac{1}{n_s} \sum_{i=0}^{n_s} \int_{250}^{500} \dot{\Theta}_{bit}^2(t) dt, \quad (4.32)$$

Figure 4.17 shows that convergence is reached for 400 simulations. However, 1000 simulations are going to be used when possible. This way, the statistics obtained through the stochastic response become smoother and it permits a better visualization of the results.

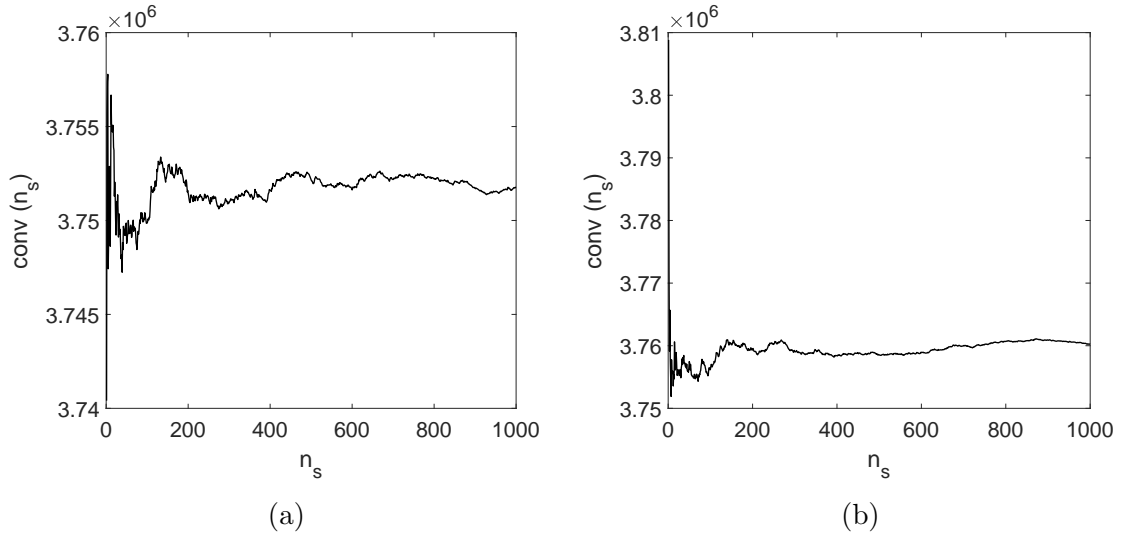


Figure 4.17: Convergence of stochastic drill-string dynamical response for the number of simulations. $\Omega = 95.5$ RPM and $\bar{W}_{ob} = 100$ kN. (a) O-U process, and; (b) CP process.

In Sec. 4.3.1, the CP process is generated considering the bit rotational speed in Fig. 3.22b, but rotational speed is not influenced by stochastic process. Now, the fully coupled system is simulated and the hypotheses are tested again. Figure 4.18 shows one realization of stochastic process $\mathbf{A}_4(t) = a_{4m}(h_{CP} + \mathbf{G}(t))^2$ and its probabilistic envelope for the fully coupled system. It is observed that the mean continues to be constant and equal to a_{4m} and the envelope has constant width, which indicates an almost constant second moment.

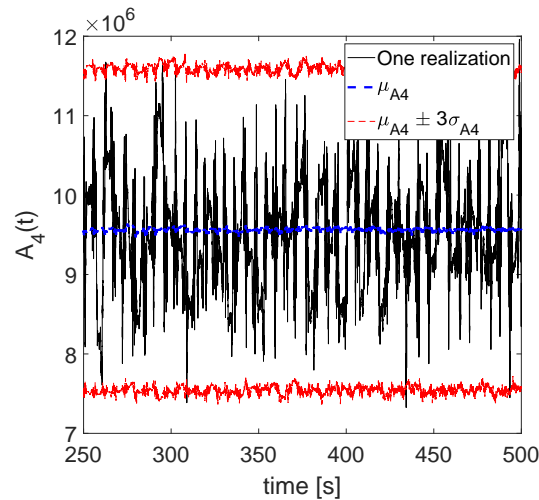


Figure 4.18: Validation of CP Process properties with fully coupled system. One realization and the probabilistic envelope of $\mathbf{A}_4(t) = a_{4m}(h_{CP} + \mathbf{G}(t))^2$ for three times the standard deviation σ_{A4} around mean μ_{A4} . $\Omega = 95.5$ RPM and $\bar{W}_{ob} = 100$ kN.

From now on, the results are going to be presented considering that the uncertainties are modeled by the CP process. In some cases, the results considering the O-U process are also presented for comparison purposes. At first, the case in which stick-slip occurs in the deterministic model is going to be analyzed ($\Omega = 95.5$ RPM and $\bar{W}_{ob} = 100$ kN). Some stochastic simulations resulted in negative axial speeds at the bit, indicating bit-bounce phenomenon. However, a deeper investigation associated these results to numerical issues. Thus, these simulations are aborted and they are not considered in the statistics presented. Figure 4.19 shows that, in 1000 simulations, it occurred 4 times (0.4%) for O-U process and 8 times (0.8%) for CP process.

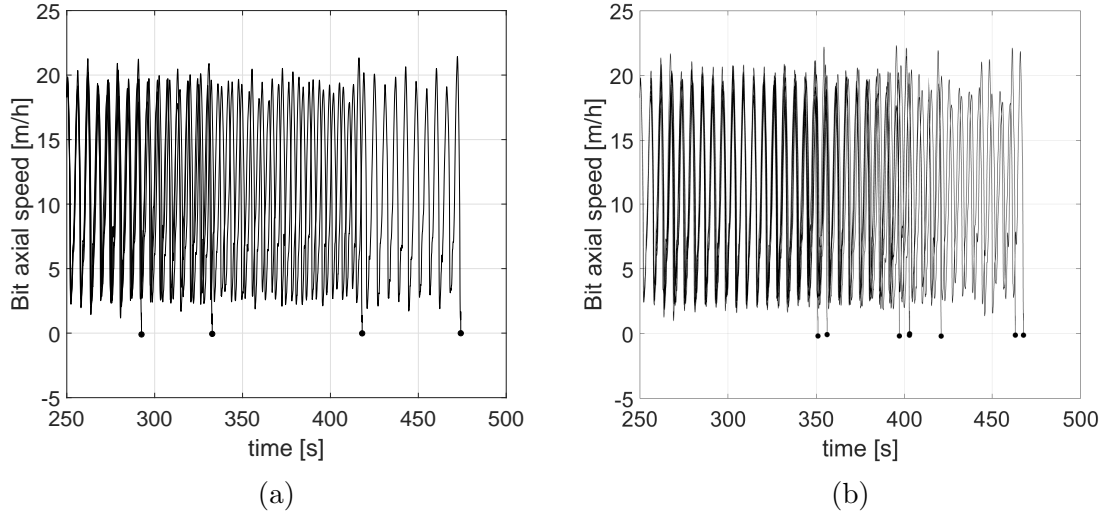


Figure 4.19: Simulations in which the bit achieves negative axial speeds. (a) O-U process, and; (b) CP process.

Figure 4.20 shows the bit rotational and axial speeds for one simulation. Although in the deterministic case the bit vibrates with a constant amplitude, the stochastic results present an amplitude that varies within time. The amplitudes of vibration can achieve higher values, increasing the severity of vibration.

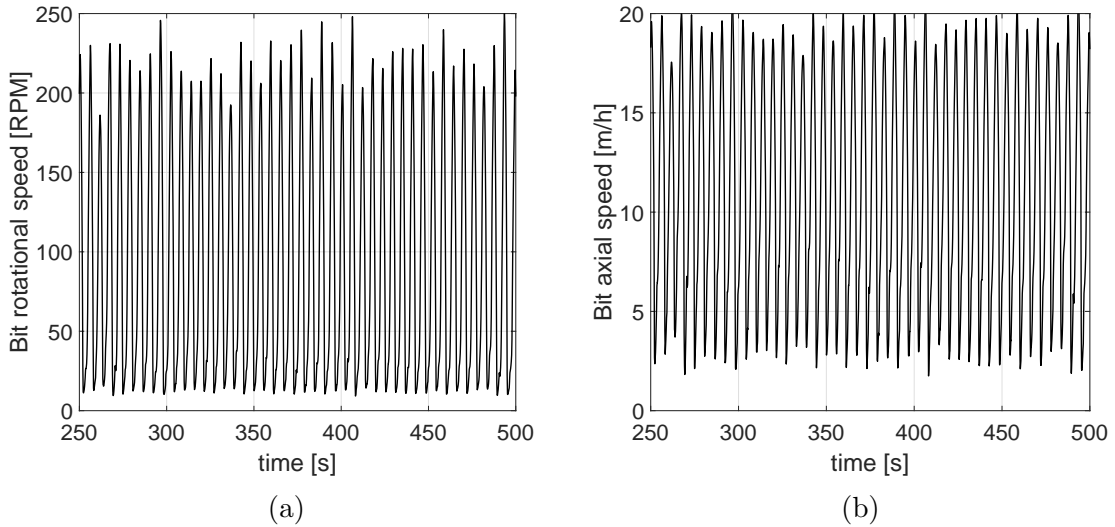


Figure 4.20: One simulation of the stochastic response at the bit with uncertainties modeled by CP Process. (a) Rotational Speed, and; (b) Axial Speed. $\Omega = 95.5$ RPM and $\bar{W}_{ob} = 100$ kN.

The average and the probabilistic envelope of 95% of bit rotational speed are calculated for both stochastic processes over 1000 simulations and shown in Fig. 4.21. In both cases, the probabilistic envelope seems to follow the average at the beginning, and both of them follow the deterministic result. However, after some seconds, the envelope of each cycle starts to sum up until it becomes a great shaded area. This

behavior occurs because the initial condition forces the envelope to be well behaved at the beginning, with a low influence of the uncertainties in stick-slip frequency. After some time, these uncertainties sum up and the cycles start to happen at different times, which causes the envelope to be no more related to the deterministic results and to the average. With time, the average of bit rotational and axial speeds tend to a constant value, which, in rotational case, is very close to surface speed. It also occurs because of the variation in stick-slip frequency. The same phenomenon observed in bit rotational speed is observed in bit axial speed.

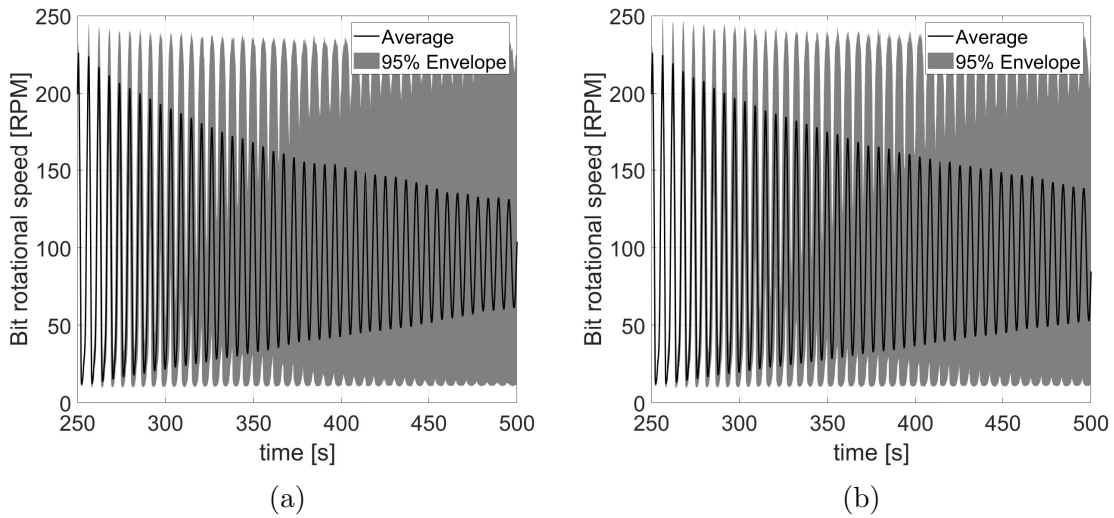


Figure 4.21: Probabilistic envelope of 95% for the rotational speed at the bit. (a) O-U Process; (b) CP Process. $\Omega = 95.5$ RPM and $\bar{W}_{ob} = 100$ kN.

In order to check if the average really goes to a constant value, the stochastic model is simulated for more time (1500 seconds). Figure 4.22 confirms that average goes to a constant value for CP process. The behavior is the same for the O-U process.

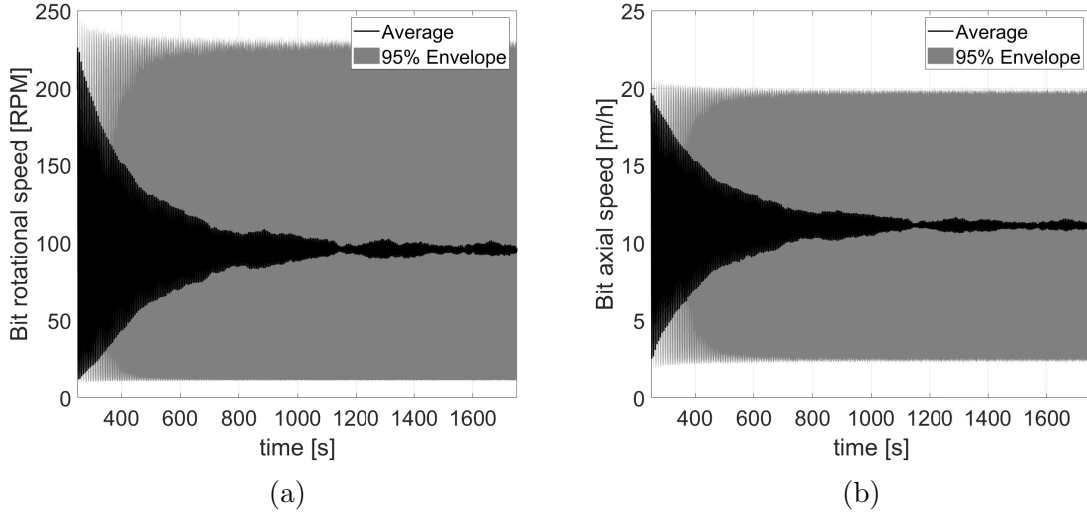


Figure 4.22: Probabilistic envelope of 95% for 1500 seconds of stochastic results with uncertainties modeled by CP Process. (a) Rotational speed, and; (b) Axial speed. $\Omega = 95.5$ RPM and $\bar{W}_{ob} = 100$ kN.

Figure 4.23 presents a zoom on one simulation of the stochastic model with uncertainties modeled by the O-U process and CP process. The difference between the two processes is observed in this graph. In the O-U process, the uncertainties are equally present during all the time, when the bit is almost stuck (blue rectangles) or when it is rotating (red circles). Otherwise, in the CP process, the uncertainties are more relevant when the bit is actually drilling the rock (highlighted by the red circles). Also, the CP process can result in higher variations during stick-slip because the bit achieves rotational speeds much higher than the speed at the top (remember that the parameters used in process simulation are such that they have the same uncertainty level when the bit is rotating at the same speed as in the top rotary system). The graphs in Fig. 4.23 illustrate this very well because, in the CP process, the uncertainties are higher than in the O-U process when the bit is rotating.

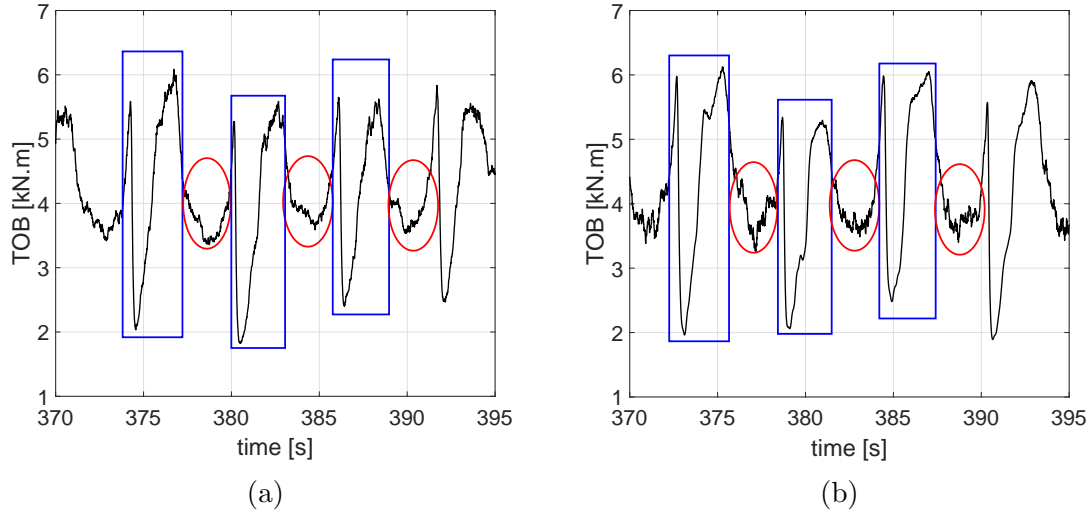


Figure 4.23: One simulation of the TOB by the stochastic model with uncertainties modeled by (a) O-U process and (b) CP process. $\Omega = 95.5$ RPM and $\bar{W}_{ob} = 100$ kN.

The bit-rock interaction graph (TOB vs bit rotational speed) is shown in Fig. 4.24 for the stochastic case. Figure 4.24a shows one simulation of stochastic model and the deterministic result. The variations around deterministic result are noticeable and the graph seems to approximate better reality than the deterministic model. In Fig. 4.24b, the probabilistic envelope is calculated using a moving average approach. It is observed that the average calculated over 1000 simulations lies very close to the deterministic result. Also, the envelope width is higher near the peak and it decreases as bit speeds up. Besides, at low speeds, the envelope is very tight. This behavior is what we expect to obtain according to the parametric analysis performed in Sec. 3.6.4, which presented this behavior in the bit-rock interaction graph for variations in a_4 .

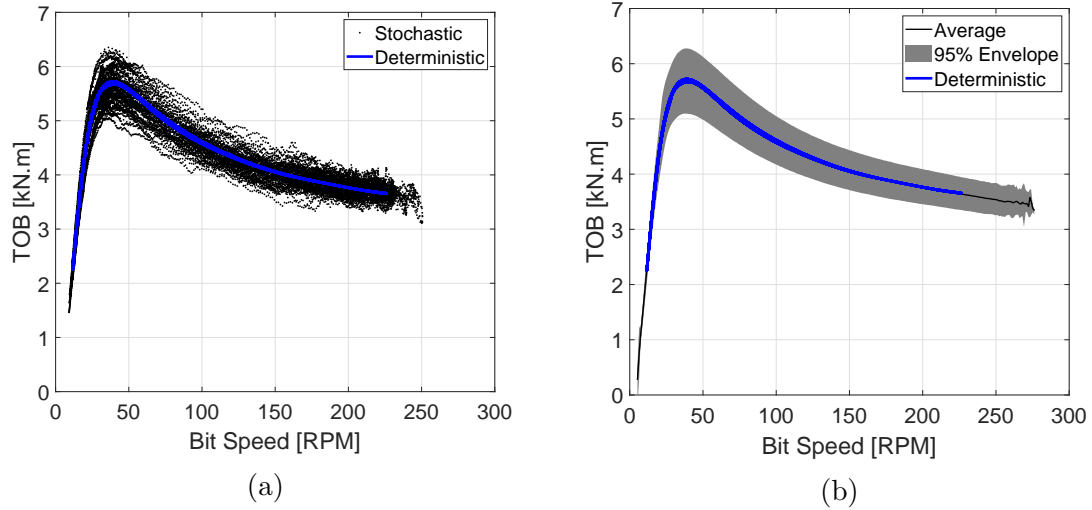


Figure 4.24: Stochastic bit-rock interaction graph with uncertainties modeled by CP Process. (a) One simulation of 250 seconds, and; (b) Probabilistic envelope of 95%. $\Omega = 95.5$ RPM and $\bar{W}_{ob} = 100$ kN.

In order to make an analysis in the frequency domain, a Fast Fourier Transform (FFT) is calculated over the 1000 stochastic simulations. The average FFTs of bit rotational and axial speeds are presented in Fig. 4.25 together with their probabilistic envelope and the deterministic FFTs obtained in Sec. 3.6. The uncertainties on the frequency of the first peak seem to be small and it explains why probabilistic envelope takes a lot of time to become a wide band. It is also noticed that the amplitude of the first peak in the deterministic case is lower than the amplitudes related to the average and to the upper limit of the envelope in stochastic case. It indicates that vibration is worse in stochastic case.

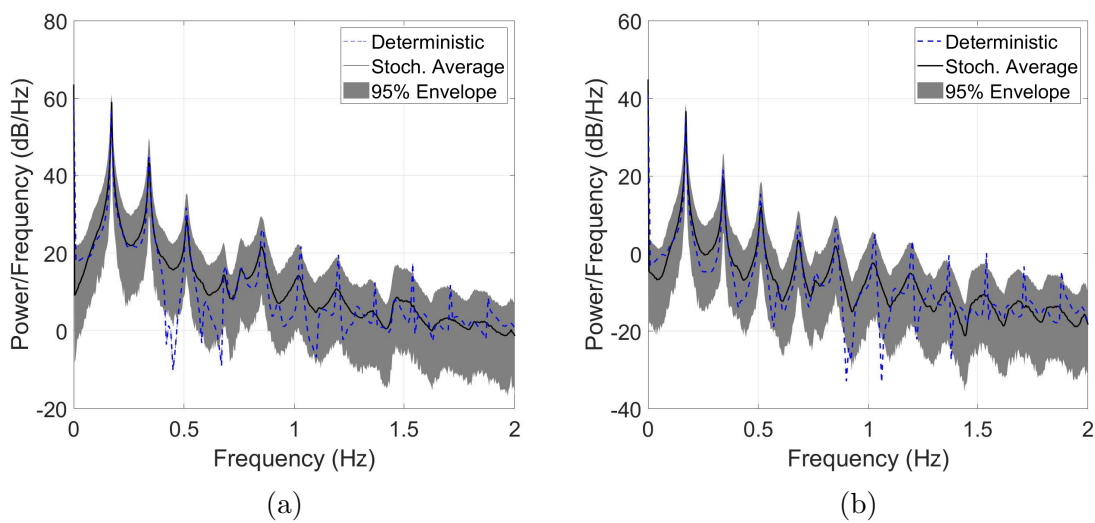


Figure 4.25: Fast Fourier Transform (fft) of stochastic response with uncertainties modeled by CP process. (a) Bit rotational speed, and; (b) Bit axial speed. $\Omega = 95.5$ RPM and $\bar{W}_{ob} = 100$ kN.

By decreasing the \bar{W}_{ob} to 68 kN, it is possible to obtain a deterministic result without vibration in steady state. However, when uncertainties are introduced, the drill-string starts to vibrate. For this value of \bar{W}_{ob} , no simulations presented negative axial speeds at the bit. Figure 4.26 shows one stochastic simulation of bit rotational and axial speed when uncertainties are modeled by CP Process. It is noticed that the amplitude of vibration is small near the beginning because of the initial condition. Nevertheless, the amplitude can increase with time and induce severe vibration at the bit. The probabilistic envelope calculated over 1000 simulations and shown in Fig. 4.27 illustrates pretty well this behavior. Although the average maintains itself near initial condition, the envelope increase with time until reaching a certain amplitude. The same behavior is observed for the cases in which uncertainties are modeled by O-U process, because the difference between the two processes relies mainly on the phases in which bit experiences a high vibration amplitude, such as in stick-slip situations. For this reason, only the results for the CP process are displayed.

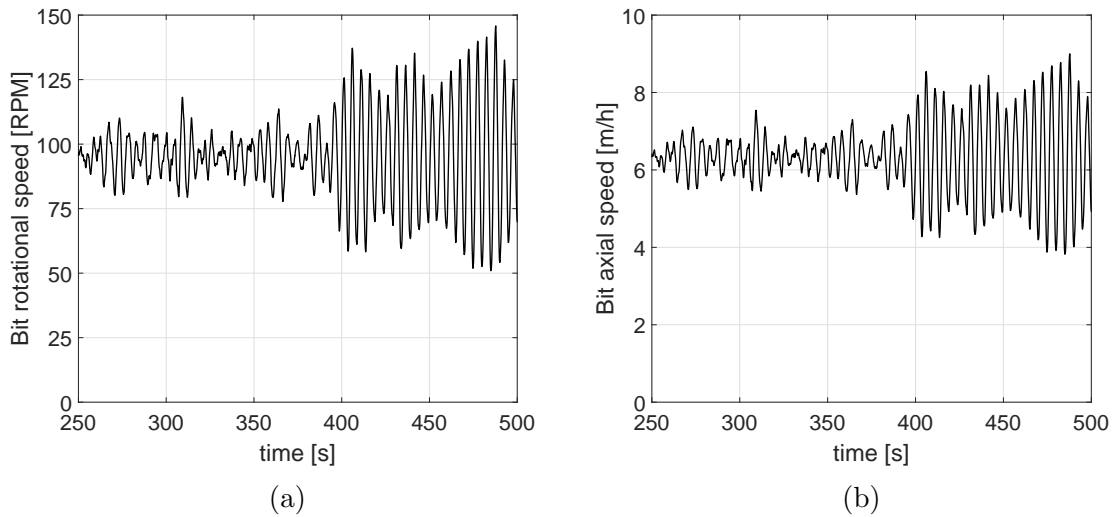


Figure 4.26: One simulation of the stochastic response at the bit with uncertainties modeled by CP Process. (a) Rotational Speed, and; (b) Axial Speed. $\Omega = 95.5$ RPM and $\bar{W}_{ob} = 68$ kN.

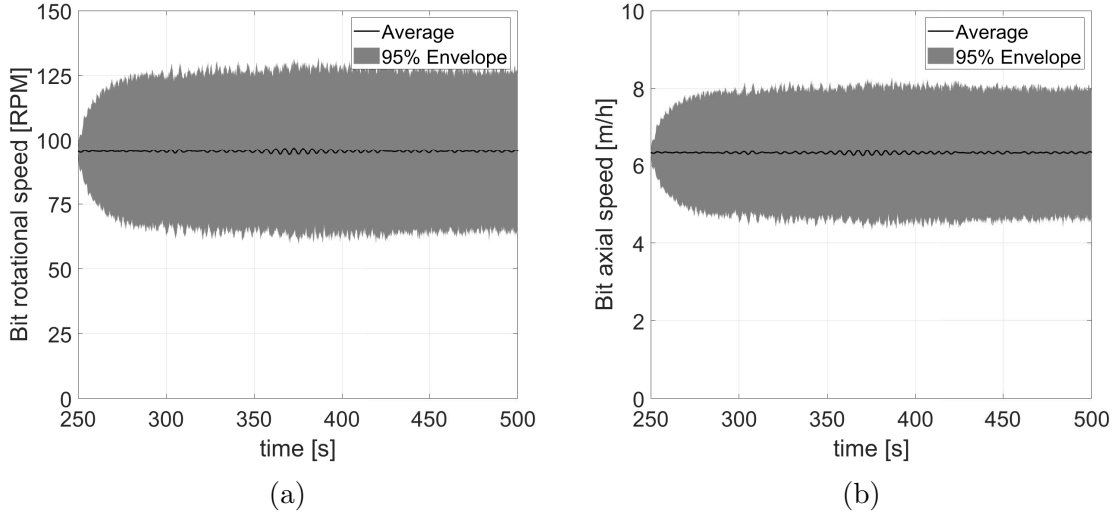


Figure 4.27: Probabilistic envelope of 95% stochastic response with the uncertainties modeled by CP Process. (a) Bit rotational speed, and; (b) Bit axial speed. $\Omega = 95.5$ RPM and $\bar{W}_{ob} = 68$ kN.

The TOB is also analyzed in this case. Figure 4.28 shows that TOB assumes values near a region in bit-rock interaction graph. The usual shape of bit-rock interaction is not recovered in this situation and the results are qualitatively similar to the experimental data available in [45].

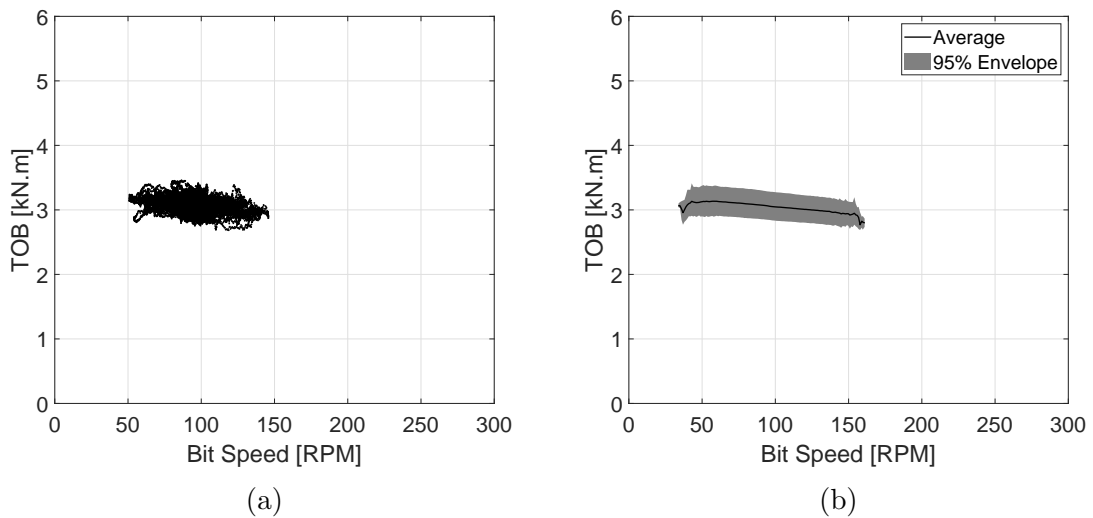


Figure 4.28: Stochastic bit-rock interaction graph with uncertainties modeled by CP Process. (a) One simulation of 250 seconds, and; (b) Probabilistic envelope of 95%. $\Omega = 95.5$ RPM and $\bar{W}_{ob} = 68$ kN.

In the frequency domain, the FFT is calculated for the deterministic result (including transient regime) and for the stochastic result. Figure 4.29 compares the two results. Both responses present peaks at the same frequencies, but the amplitudes are different. It is important to highlight that the deterministic curve is different

from zero only because of the transient regime. Otherwise, the amplitudes of the stochastic curve would be much bigger. However, even considering the transient regime, it is noticed that the magnitude associated with the first peak can reach values in the stochastic case that can be higher than in the deterministic case. It indicates that vibration is more severe when the uncertainties are considered.

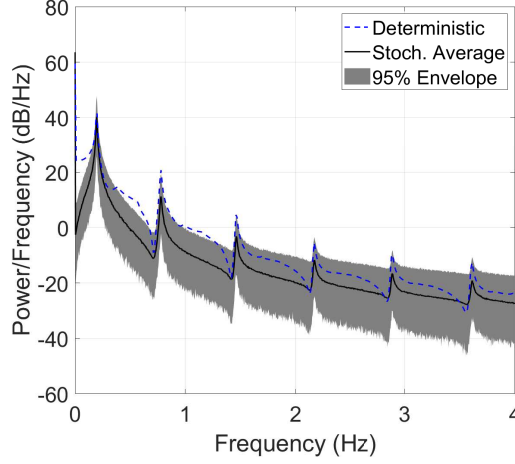


Figure 4.29: Fast Fourier Transform (fft) of stochastic bit rotational speed with uncertainties modeled by CP process. $\Omega = 95.5$ RPM and $\bar{W}_{ob} = 68$ kN.

Figure 4.30 summarizes the effects of the uncertainties on the severity of vibration using the stick-slip severity factor calculated by Eq. 3.44. The empirical cumulative distribution function (cdf) is calculated based on 1000 stochastic simulations and plotted for the two values of \bar{W}_{ob} considered in this section, as well as for the two stochastic processes proposed in this work. The results presented in Fig. 4.30b corroborates that the results are very similar for CP and O-U processes when a small \bar{W}_{ob} is considered. Otherwise, Fig. 4.30a shows that the vibration is more severe when the CP process is applied. The mean of S_{SS} is 125.4% for CP process and 123.5% for O-U process, and the coefficient of variation is 2.85% for CP process and 2.47% for O-U process.

It is also observed that, for both \bar{W}_{ob} values, the mean of S_{SS} do not coincide with the deterministic S_{SS} of $\approx 112\%$ for $\bar{W}_{ob} = 100$ kN and $\approx 0\%$ for $\bar{W}_{ob} = 68$ kN, which are represented by vertical lines in Fig. 4.30. Actually, all the stochastic results presented values higher than the deterministic result. It occurs because the stochastic process can assume different values during the simulation, which can worsen or not the stick-slip oscillations during the same simulation. If the uncertainties were modeled by random variables with the mean as the deterministic value, instead of a stochastic process, the CDF would be much closer to the deterministic result because $\mathbf{A}_4(t)$ would assume values around deterministic value and remain constant over time. Furthermore, the shape of CDF is closely related to the total

time used to calculate S_{SS} because if a very large time is used, the stochastic process would behave in almost all possible ways during this time, generating no big differences between the S_{SS} calculated over different simulations.

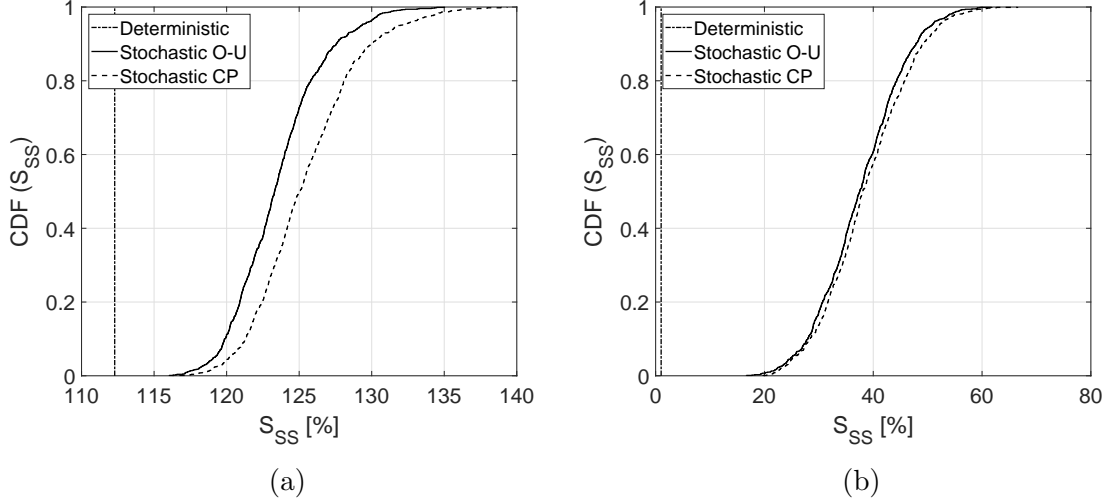


Figure 4.30: Empirical Cumulative Density Function of stick-slip severity factor. $\Omega = 95.5$ RPM. (a) $\bar{W}_{ob} = 100$ kN and; (b) $\bar{W}_{ob} = 68$ kN.

4.3.3 Parametric analysis

A parametric analysis is performed in order to evaluate the influence of some parameter on the statistics of stochastic response. The first parameter analyzed is the applied \bar{W}_{ob} . Figure 4.31a shows the probabilistic envelope of stick-slip severity factor (S_{SS}) compared to the deterministic case for values of \bar{W}_{ob} that range from 60 to 110 kN. The probabilistic envelope was calculated over 450 simulations. The uncertainties are modeled by O-U and CP processes. It is noticed that, for low \bar{W}_{ob} , the deterministic case returns S_{SS} values very close to zero, while stochastic case returns values much higher. Also, the width of the envelope seems to be smaller from 73 to 87 kN. Besides, the statistical envelope is always higher than the deterministic curve, which indicates that uncertainties worsen the vibration experienced at the bit. Comparing the O-U process with the CP process, it is noticed that the CP process generate higher values of S_{SS} and the difference is bigger for higher \bar{W}_{ob} .

Figure 4.31b plots the standard deviation of stochastic S_{SS} against the \bar{W}_{ob} . It is observed that the standard deviation increases from 60 to around 69 kN, where the deterministic case starts to present stick-slip vibrations. It indicates that the influence of uncertainties on stick-slip severity increases in low \bar{W}_{ob} until it reaches the deterministic boundary between operation with and without stick-slip. In the stick-slip zone of the deterministic stability map, the standard deviation of the stochastic case seems to be small from 73 to around 87 kN. From 87 to 110 kN,

the standard deviation increases but it is still much smaller than in the range from 60 to 69 kN. The difference between the two stochastic processes can be noticed again. CP process generates a bigger standard deviation, but this difference is more notable at higher \bar{W}_{ob} . This behavior can be explained because drill-string is usually experiencing worse vibrations at high \bar{W}_{ob} . Thus, the difference between the formulations of the two processes gets more evidence, generating more different results.

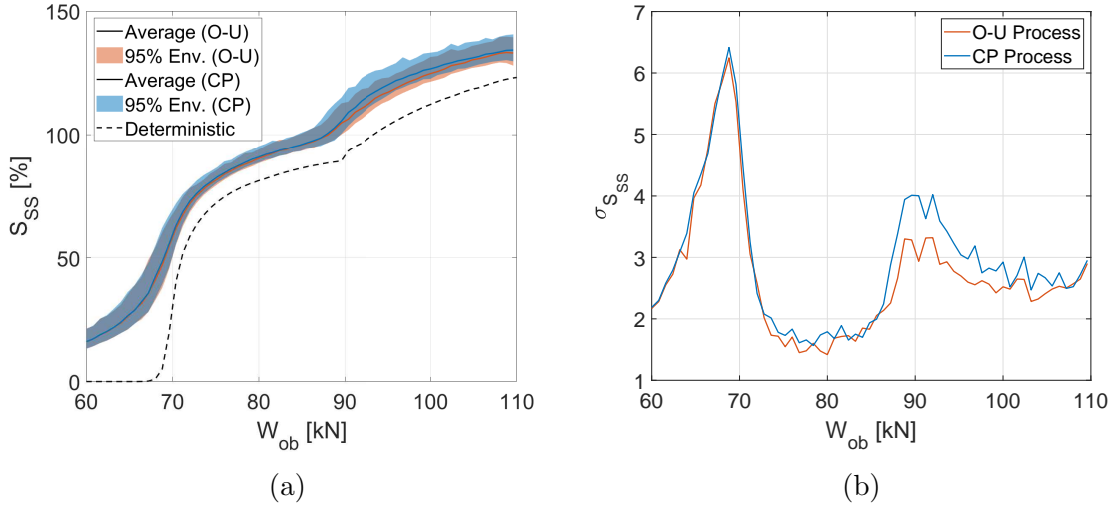


Figure 4.31: (a) Stick-slip severity factor (S_{SS}) for $\Omega = 95.5$ RPM according to the applied \bar{W}_{ob} . (b) Standard deviation of the stick-slip severity according to the applied \bar{W}_{ob} .

As in deterministic parametric analysis, the damping is increased through the parameters α and β in proportional damping matrix. These parameter are increased from $\alpha = 0.1$ and $\beta = 0.00008$ to $\alpha = 0.4$ and $\beta = 0.008$. As in deterministic case, the response in frequency domain is calculated by taking the fft of the results. Figure 4.32a shows the fft of bit rotational speed for $\bar{W}_{ob} = 68$ kN and it is very different from the one presented in Fig. 4.29 because, with a higher damping, only the first peak is evident. For a higher \bar{W}_{ob} , Fig. 4.32b shows that only the first 3 peaks are evident in stochastic case.

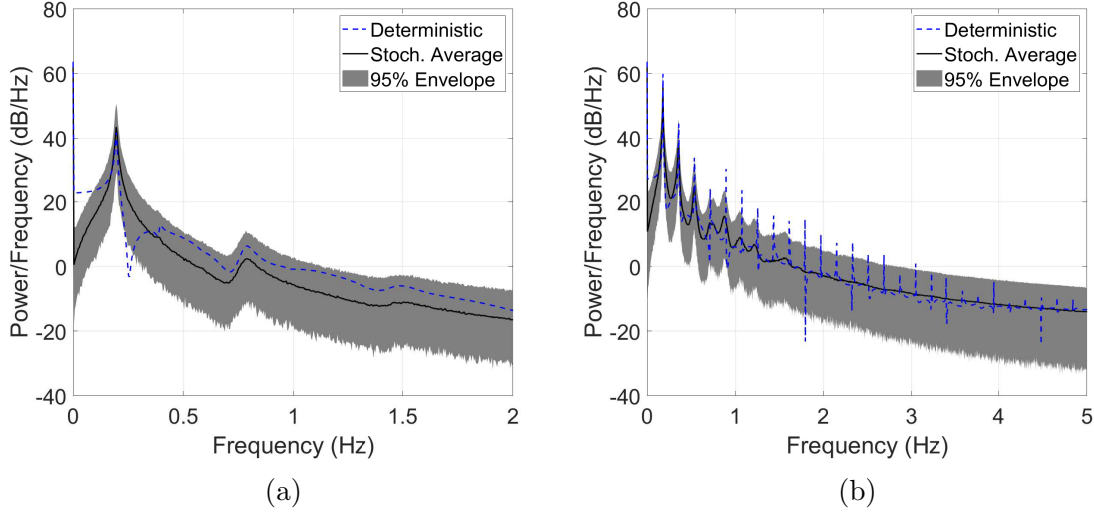


Figure 4.32: Fast Fourier Transform (fft) of bit rotational speed for a bigger damping. $\Omega = 95.5$ RPM, $\alpha = 0.4$ and $\beta = 0.008$. (a) $\bar{W}_{ob} = 82$ kN, and; (b) $\bar{W}_{ob} = 110$ kN.

The empirical cumulative distribution function (CDF) of the S_{SS} is then evaluated using Fig. 4.33. It is important to mention that, as in Fig. 4.32, the \bar{W}_{ob} is different for the two damping cases. For the lower damping, the \bar{W}_{ob} s were maintained in 68 and 100 kN, while for the higher damping, the \bar{W}_{ob} s are 88 and 110 kN. It is done because, as discussed in Sec. 3.6.4, the damping changes the stability map. Thus, the values of \bar{W}_{ob} are reset in order to give a response qualitatively similar.

Figure 4.33a shows the CDF for the case with higher \bar{W}_{ob} . It is noticed that the difference between CP and O-U processes increased for the higher damping. Also, the mean S_{SS} decreased. Despite this, the coefficient of variation increased from 2.47 to 3.47% for O-U process and from 2.85 to 3.89% for CP process. Figure 4.33b shows the CDF for the lower values of \bar{W}_{ob} . In this case, the difference between the processes decreases. The coefficient of variation also increased from 17.50 to 20.56% for O-U process and from 17.65 to 20.73% for CP process.

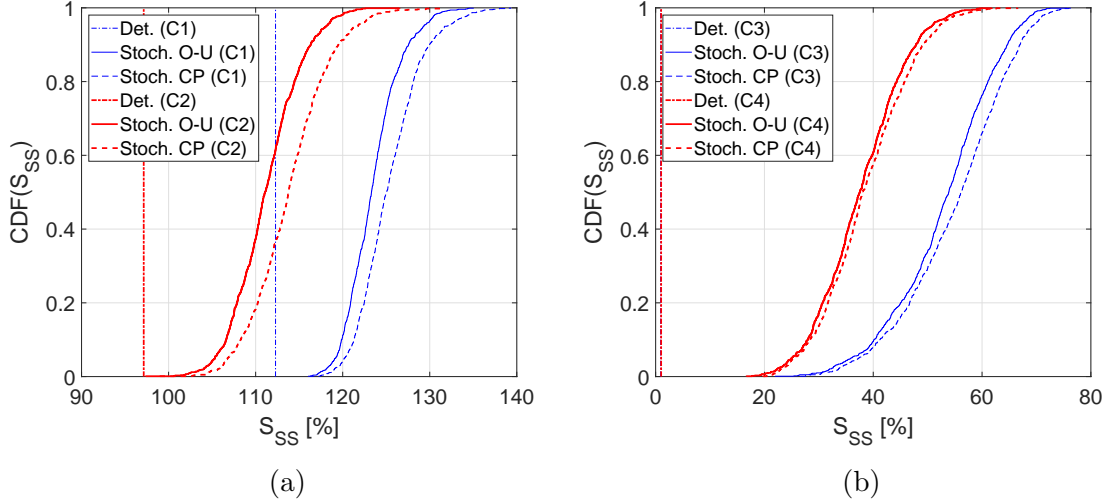


Figure 4.33: Empirical cumulative distribution function (CDF) of the stick-slip severity factor (S_{SS}) for $\Omega = 95.5$ RPM. Case 1 (C1): $\bar{W}_{ob} = 100$ kN, $\alpha = 0.1$ and $\beta = 0.00008$; Case 2 (C2): $\bar{W}_{ob} = 110$ kN, $\alpha = 0.4$ and $\beta = 0.008$; Case 3 (C3): $\bar{W}_{ob} = 68$ kN, $\alpha = 0.1$ and $\beta = 0.00008$; Case 4 (C4): $\bar{W}_{ob} = 88$ kN, $\alpha = 0.4$ and $\beta = 0.008$.

Another investigation performed is related to the parameters of the stochastic process. Three cases are considered and the probabilistic envelopes of the bit-rock interaction graphs are shown in Fig. 4.34 for the three combinations of parameters and two values of \bar{W}_{ob} . The PSDs of the three cases considered are plotted in Fig. 4.4 for O-U process. It is observed that case C3 presented the larger variation on bit-rock interaction for both values of \bar{W}_{ob} . Also, the probabilistic envelope of case C3 is plotted for a larger range of bit rotational speed, which indicates that bit experienced worse vibrations.

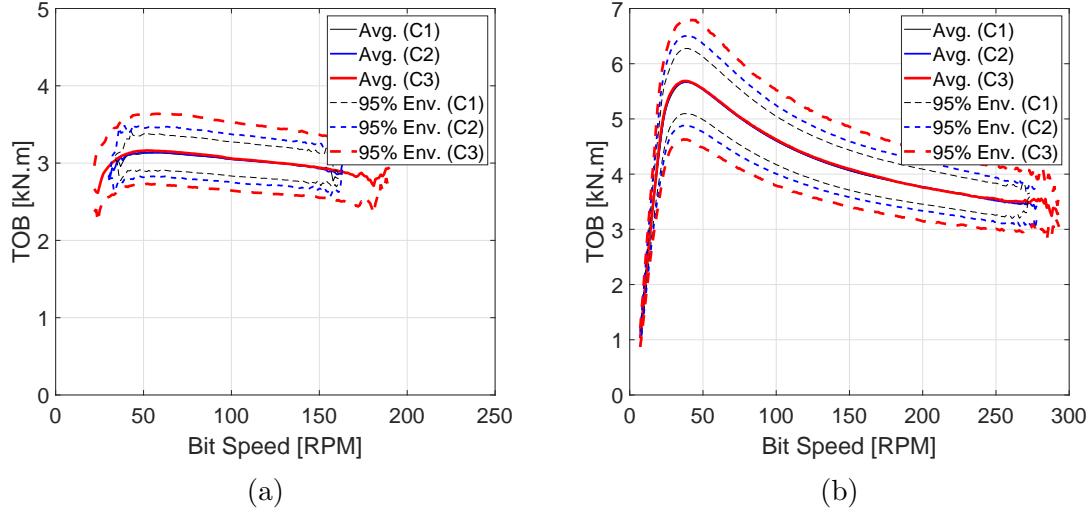


Figure 4.34: Probabilistic envelope of TOB against the bit rotational speed for $\Omega = 95.5$ RPM when the uncertainties are modeled by CP process. Case 1 (C1): $\nu_1 = 0.01$, $\nu_2 = 0.005$; Case 2 (C2): $\nu_1 = 0.005$, $\nu_2 = 0.005$; Case 3 (C3): $\nu_1 = 0.01$, $\nu_2 = 0.01$. (a) $\bar{W}_{ob} = 68$ kN, and; (b) $\bar{W}_{ob} = 100$ kN.

Figure 4.35 shows the empirical CDF for the three cases considered above. It is noticed that, for both \bar{W}_{ob} values, the worst case is case C3 that presents higher values of S_{SS} . The difference between CP and O-U processes increase from case C1 to case C3, as well as the coefficient of variation. Also, a change on b_2 and ν_2 seems to influence much more the stick-slip severity.

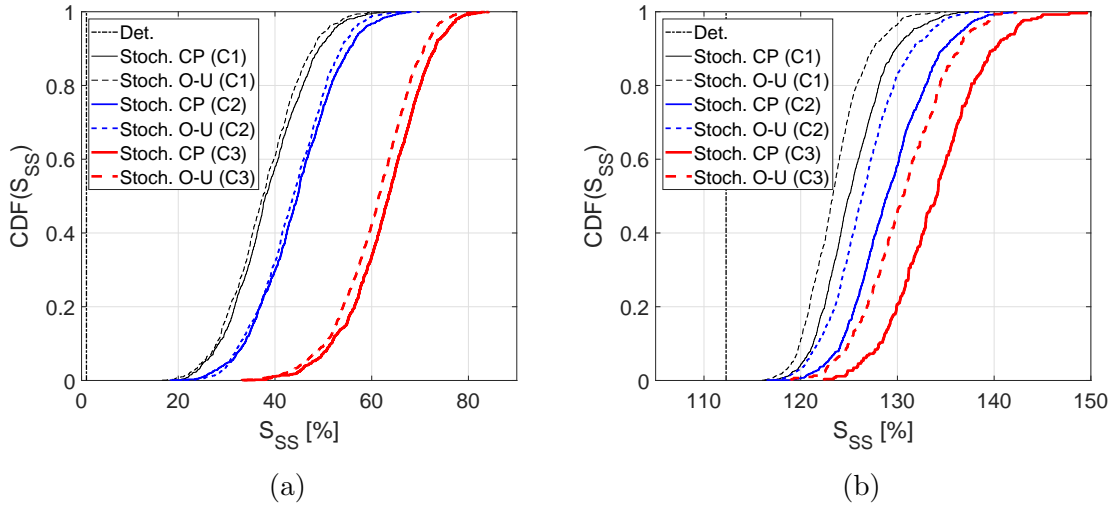


Figure 4.35: Empirical cumulative distribution function (CDF) of stick-slip severity factor (S_{SS}). $\Omega = 95.5$ RPM. Case 1 (C1): $b_1 = 1.0$, $b_2 = 0.05$, $\nu_1 = 0.01$, $\nu_2 = 0.005$; Case 2 (C2): $b_1 = 0.5$, $b_2 = 0.05$, $\nu_1 = 0.005$, $\nu_2 = 0.005$; Case 3 (C3): $b_1 = 1.0$, $b_2 = 0.1$, $\nu_1 = 0.01$, $\nu_2 = 0.01$. (a) $\bar{W}_{ob} = 68$ kN, and; (b) $\bar{W}_{ob} = 100$ kN

Chapter 5

Conclusions

In this work, the axial-torsional coupled dynamics of a drill-string was analyzed in the presence of uncertainties in bit-rock interaction. The drill-string was modeled using extended Hamilton's principle considering geometric nonlinearities. The equations of motions were discretized by the finite element method and the bit-rock interaction model was included. The bit-rock interaction model was validated with experimental data for a laboratory-scale drill-string in order to evaluate its prediction capability. For the numerical investigations, typical geometric parameter values of a real-scale drill-string were used.

At first, the deterministic model is assessed and it is concluded the geometric nonlinearities did not affect the response for the model and the range of parameters considered. The vibration modes were calculated and it was concluded that drill-pipes are more affected in the first modes (low frequency) and the amplitudes at BHA starts to be significant only for higher frequency modes. The model was reduced using the vibration modes and the convergence was assessed. The model could capture typical responses with and without stick-slip. A parametric analysis showed that the stability map is very dependent of the damping level.

After the deterministic investigations, a new stochastic bit-rock interaction model is proposed. This model describes the cutting component of TOB by stochastic processes, which are modeled by using Itô stochastic differential equations. Two stochastic processes were proposed: Ornstein-Uhlenbeck process and a novel coupled process. The stochastic system of equations is simulated by using a modified Euler's method. The bit-rock interaction graphs of stochastic case are much more similar to experimental results found in literature. For the lowest WOB, the stochastic response presents a torsional vibration severity much higher than in deterministic case. The empirical cumulative distribution is calculated for the stick-slip severity factor and shows that all the values obtained in stochastic case are higher than the ones obtained in deterministic case. Also, the difference between the two proposed stochastic processes is more evident with higher WOB.

At last, a parametric analysis is performed. It is observed that the standard deviation of stick-slip severity factor increases with WOB until it reaches its maximum value at the deterministic boundary between operation with and without stick-slip. After this, the standard deviation stays at lower levels. It is also concluded that a higher damping actually increases the coefficient of variation of stick-slip severity factor and the difference between the results from the two stochastic processes for high WOBs. Changes in the diffusion coefficient of the stochastic processes are more detrimental to stick-slip severity.

As future works, three main additional works are proposed:

- Identification of the parameters used in the stochastic process simulation with experimental data in order to validate the stochastic model proposed;
- Improve the experimental test-rig constructed at Laboratório de Acústica e Vibrações (LAVI) in UFRJ - Brazil - in order to include the axial dynamics of drill-string in a more realistic way. It would be done by fixing the test-body and letting the "drill-string" move.
- Use the calibrated bit-rock interaction model proposed by [29] in the dynamical model and consider the cutting components as stochastic variables. This model would allow this consideration for both WOB and TOB. An extensive research is necessary in order to couple delay differential equation with stochastic differential equations.

Bibliography

- [1] MACDONALD, K. A., BJUNE, J. V. “Failure analysis of drillstrings”, *Engineering Failure Analysis*, v. 14, n. 8, pp. 1641–1666, 2007. ISSN: 1350-6307. doi: 10.1016/j.engfailanal.2006.11.073.
- [2] LEINE, R. I., VAN CAMPEN, D. H. “Stick-slip whirl interaction in drillstring dynamics”, *Journal of Vibration and Acoustics*, v. 122, n. April, pp. 287–296, 2002. ISSN: 09250042. doi: 10.1007/1-4020-3268-4-27.
- [3] WU, S. X., PAEZ, L., PARTIN, U., et al. “Decoupling Stick-slip and Whirl to Achieve Breakthrough in Drilling Performance”, *IADC/SPE Drilling Conference and Exhibition*, , n. IADC/SPE 128767, pp. 1–13, 2010. doi: 10.2118/128767-MS.
- [4] DUFÉYTE, M.-P., HENNEUSE, H. “Detection and Monitoring of the Slip-Stick Motion: Field Experiments”, *Proceedings of SPE/IADC Drilling Conference*, pp. 429–438, 1991. doi: 10.2523/21945-MS.
- [5] LIN, Y.-Q., WANG, Y.-H. “Stick-Slip Vibrations of Drill Strings”, *ASME J. Eng. for Industry*, v. 38, n. December 1989, pp. 38–43, 1991.
- [6] DAWSON, R., LIN, Y., SPANOS, P. “Drillstring stick-slip oscillations”. In: *Spring Conference of the Society for Experimental Mechanics*, Houston, TX, 1987.
- [7] SPANOS, P., CHEVALLIER, A. M., POLITIS, N. P., et al. “Oil and Gas Well Drilling : A Vibrations Perspective”, *The Shock and Vibration Digest*, v. 35, n. 2, pp. 85–103, 2003. doi: 10.1177/0583102403035002564.
- [8] NAVARRO-LÓPEZ, E. M., SUÁREZ, R., NAVARRO-LOPEZ, E., et al. “Practical approach to modelling and controlling stick-slip oscillations in oilwell drillstrings”, *Proceedings of the 2004 IEEE International Conference on Control Applications, 2004.*, v. 2, n. October 2004, pp. 1454–1460, 2004. ISSN: 1085-1992. doi: 10.1109/CCA.2004.1387580.

- [9] HALSEY, G., KYLLINGSTAD, A., KYLLING, A. “Torque Feedback Used to Cure Slip-Stick Motion”. In: *SPE Drilling Conference*. Society of Petroleum Engineers - SPE 18049, 1988.
- [10] SCHLUMBERGER. “Drillstring Vibrations and Vibration Modeling Drillstring Vibrations and Vibration Modeling”, pp. 4–7, 2010.
- [11] JANSEN, J. “Non-linear rotor dynamics as applied to oilwell drillstring vibrations”, *Journal of Sound and Vibration*, v. 147, n. 1, pp. 115–135, 1991. doi: 10.1016/0022-460X(91)90687-F.
- [12] BAILEY, J., FINNIE, I. “An Analytical Study of Drill-String Vibration”, *ASME. J. Eng. Ind.*, v. 82, n. 2, pp. 122–127, 1960. doi: 10.1115/1.3663017.
- [13] FINNIE, I., BAILEY, J. “An Experimental Study of Drill-String Vibration”, *ASME. J. Eng. Ind.*, v. 82, n. 2, pp. 129–135, 1960. doi: 10.1115/1.3663020.
- [14] DAREING, D. W., LIVESAY, B. J. “Longitudinal and angular drill-string vibrations with damping”, *Journal of Engineering for Industry*, v. 90, n. 4, pp. 671–679, 1968. doi: doi:10.1115/1.3604707.
- [15] BELOKOBYL, S. V., PROKOPOV, V. K. “Friction-induced self-excited vibrations of drill rig with exponential drag law”, *Soviet Applied Mechanics*, v. 18, n. 12, pp. 1134–1138, 1982. ISSN: 00385298. doi: 10.1007/BF00882226.
- [16] HALSEY, G., KYLLINGSTAD, A., AARRESTAD, T. V., et al. “Drillstring Vibrations: Comparison Between Theory and Experiments on a Full-Scale Research Drilling Rig”, *IADC/SPE Drilling Conference*, , n. IADC/SPE 14760, pp. 311–321, 1986. doi: 10.2118/14760-MS.
- [17] KYLLINGSTAD, Å., HALSEY, G. W. “A Study of Slip/Stick Motion of the Bit”, *SPE Drilling Engineering*, v. 3, n. 4, pp. 369–373, 1988. ISSN: 0885-9744. doi: 10.2118/16659-PA.
- [18] LIN, Y. Q., WANG, Y. H. “New Mechanism in Drillstring Vibration”, *Offshore Technology Conference*, 1990. doi: 10.4043/6225-MS.
- [19] BRETT, J. F. “The Genesis of Torsional Drillstring Vibrations”, *SPE Drilling Engineering*, v. 7, n. 3, pp. 168–174, 1992. ISSN: 0885-9744. doi: 10.2118/21943-PA.

- [20] JANSEN, J. D., VAN DEN STEEN, L. “Active damping of self-excited torsional vibrations in oil well drillstrings”, *Journal of Sound and Vibration*, v. 179, n. 4, pp. 647–668, 1995. ISSN: 0022-460X. doi: 10.1006/jsvi.1995.0042.
- [21] YIGIT, A. S., CHRISTOFOROU, A. P. “Coupled Axial and Transverse Vibrations of Oilwell Drillstrings”, *Journal of Sound and Vibration*, v. 195, n. 4, pp. 617–627, 1996. ISSN: 0022460X. doi: 10.1006/jsvi.1996.0450.
- [22] CHRISTOFOROU, A. P., YIGIT, A. S. “Dynamic Modelling of Rotating Drillstrings With Borehole Interactions”, *Journal of Sound and Vibration*, v. 206, n. 2, pp. 243–260, 1997. ISSN: 0022460X. doi: 10.1006/jsvi.1997.1091.
- [23] TUCKER, W., WANG, C. “An Integrated Model for Drill-String Dynamics”, *Journal of Sound and Vibration*, v. 224, n. 1, pp. 123–165, jul 1999. ISSN: 0022460X. doi: 10.1006/jsvi.1999.2169.
- [24] TUCKER, R. W., WANG, C. “On the Effective Control of Torsional Vibrations in Drilling Systems”, *Journal of Sound and Vibration*, v. 224, n. 1, pp. 101–122, 1999. ISSN: 0022460X. doi: 10.1006/jsvi.1999.2172.
- [25] CHALLAMEL, N. “Rock Destruction Effect on the Stability of a Drilling Structure”, *Journal of Sound and Vibration*, v. 233, n. 2, pp. 235–254, 2000. ISSN: 0022460X. doi: 10.1006/jsvi.1999.2811.
- [26] TUCKER, R. W., WANG, C. H.-T. “Torsional Vibration Control and Cosserat Dynamics of a Drill-Rig Assembly”, *Meccanica*, v. 38, n. 1, pp. 145–161, 2003. ISSN: 1572-9648. doi: 10.1023/A:1022035821763.
- [27] CHRISTOFOROU, A. P., YIGIT, A. S. “Fully coupled vibrations of actively controlled drillstrings”, *Journal of Sound and Vibration*, v. 267, n. 5, pp. 1029–1045, 2003. ISSN: 0022460X. doi: 10.1016/S0022-460X(03)00359-6.
- [28] RICHARD, T., GERMAI, C., DETOURNAY, E. “Self-excited stick-slip oscillations of drill bits”, *Comptes Rendus - Mecanique*, v. 332, n. 8, pp. 619–626, 2004. ISSN: 16310721. doi: 10.1016/j.crme.2004.01.016.
- [29] DETOURNAY, E., DEFOURNY, P. “A phenomenological model for the drilling action of drag bits”, *International Journal of Rock Mechanics and Mining Sciences and*, v. 29, n. 1, pp. 13–23, 1992. ISSN: 01489062. doi: 10.1016/0148-9062(92)91041-3.

- [30] KHULIEF, Y. A., AL-NASER, H. “Finite element dynamic analysis of drill-strings”, *Finite Elements in Analysis and Design*, v. 41, n. 13, pp. 1270–1288, 2005. ISSN: 0168874X. doi: 10.1016/j.finel.2005.02.003.
- [31] YIGIT, A. S., CHRISTOFOROU, A. P. “Stick-Slip and Bit-Bounce Interaction in Oil-Well Drillstrings”, *Journal of Energy Resources Technology*, v. 128, n. 4, pp. 268, 2006. ISSN: 01950738. doi: 10.1115/1.2358141.
- [32] KHULIEF, Y. A., AL-SULAIMAN, F. A., BASHMAL, S. “Vibration analysis of drillstrings with self-excited stick-slip oscillations”, *Journal of Sound and Vibration*, v. 299, n. 3, pp. 540–558, 2007. ISSN: 10958568. doi: 10.1016/j.jsv.2006.06.065.
- [33] ZAMANIAN, M., KHADEM, S. E., GHAZAVI, M. R. “Stick-slip oscillations of drag bits by considering damping of drilling mud and active damping system”, *Journal of Petroleum Science and Engineering*, v. 59, n. 3-4, pp. 289–299, 2007. ISSN: 09204105. doi: 10.1016/j.petrol.2007.04.008.
- [34] SAMPAIO, R., PIOVAN, M. T., VENERO LOZANO, G. “Coupled axial/torsional vibrations of drill-strings by means of non-linear model”, *Mechanics Research Communications*, v. 34, n. 5-6, pp. 497–502, 2007. ISSN: 00936413. doi: 10.1016/j.mechrescom.2007.03.005.
- [35] GERMAÏ, C., DENOËL, V., DETOURNAY, E. “Multiple mode analysis of the self-excited vibrations of rotary drilling systems”, *Journal of Sound and Vibration*, v. 325, n. 1-2, pp. 362–381, 2009. ISSN: 0022460X. doi: 10.1016/j.jsv.2009.03.017.
- [36] RICHARD, T., GERMAÏ, C., DETOURNAY, E. “A simplified model to explore the root cause of stick-slip vibrations in drilling systems with drag bits”, *Journal of Sound and Vibration*, v. 305, n. 3, pp. 432–456, 2007. ISSN: 10958568. doi: 10.1016/j.jsv.2007.04.015.
- [37] RITTO, T. G., SOIZE, C., SAMPAIO, R. “Non-linear dynamics of a drill-string with uncertain model of the bit-rock interaction”, *International Journal of Non-Linear Mechanics*, v. 44, n. 8, pp. 865–876, 2009. ISSN: 00207462. doi: 10.1016/j.ijnonlinmec.2009.06.003.
- [38] LIU, X., VLAJIC, N., LONG, X., et al. “Nonlinear motions of a flexible rotor with a drill bit: Stick-slip and delay effects”, *Nonlinear Dynamics*, v. 72, n. 1-2, pp. 61–77, 2013. ISSN: 0924090X. doi: 10.1007/s11071-012-0690-x.

- [39] KAMEL, J. M., YIGIT, A. S. “Modeling and analysis of stick-slip and bit bounce in oil well drillstrings equipped with drag bits”, *Journal of Sound and Vibration*, v. 333, n. 25, pp. 6885–6899, 2014. ISSN: 10958568. doi: 10.1016/j.jsv.2014.08.001.
- [40] HONG, L., GIRSANG, I. P., DHUPIA, J. S. “Identification and control of stick-slip vibrations using Kalman estimator in oil-well drill strings”, *Journal of Petroleum Science and Engineering*, v. 140, pp. 119–127, 2016. ISSN: 09204105. doi: 10.1016/j.petrol.2016.01.017.
- [41] PAVONE, D. R., DESPLANS, J. P. “Application of High Sampling Rate Down-hole Measurements for Analysis and Cure of Stick-Slip in Drilling”, *SPE Annual Technical Conference and Exhibition*, , n. SPE 28324, pp. 335–345, 1994. doi: 10.2118/28324-MS.
- [42] SPANOS, P. D., SENGUPTA, A. K., CUNNINGHAM, R. A., et al. “Modeling of Roller Cone Bit Lift-Off Dynamics in Rotary Drilling”, *Journal of Energy Resources Technology*, v. 117, n. 3, pp. 197, 1995. ISSN: 01950738. doi: 10.1115/1.2835341.
- [43] DETOURNAY, E., RICHARD, T., SHEPHERD, M. “Drilling response of drag bits: Theory and experiment”, *International Journal of Rock Mechanics and Mining Sciences*, v. 45, n. 8, pp. 1347–1360, 2008. ISSN: 13651609. doi: 10.1016/j.ijrmms.2008.01.010.
- [44] QIU, H., YANG, J., BUTT, S., et al. “Investigation on random vibration of a drillstring”, *Journal of Sound and Vibration*, v. 406, n. October, pp. 74–88, 2017. ISSN: 10958568. doi: 10.1016/j.jsv.2017.06.016.
- [45] RITTO, T. G., AGUIAR, R. R., HBAIEB, S. “Validation of a drill string dynamical model and torsional stability”, *Meccanica*, pp. 1–9, 2017. ISSN: 15729648. doi: 10.1007/s11012-017-0628-y.
- [46] REAL, F. F., BATOU, A., RITTO, T. G., et al. “Hysteretic bit/rock interaction model to analyze the torsional dynamics of a drill string”, *Mechanical Systems and Signal Processing*, v. 111, pp. 222–233, 2018. ISSN: 10961216. doi: 10.1016/j.ymsp.2018.04.014.
- [47] BOGDANOFF, J., GOLDBERG, J. “A New Analytical Approach to Drill Pipe Breakage”. In: *ASME Petroleum Mechanical Engineering Conference*, Denver, Colorado, 1958.

- [48] BOGDANOFF, J. L., GOLDBERG, J. E. “A New Analytical Approach to Drill Pipe Breakage II”, *ASME. J. Eng. Ind.*, v. 83, n. 2, pp. 101–106, 1961. doi: 10.1115/1.3664433.
- [49] KOTSONIS, S. J., SPANOS, P. D. “Chaotic and Random Whirling Motion of Drillstrings”, *Journal of Energy Resources Technology*, v. 119, pp. 1–6, 1997. ISSN: 01950738. doi: 10.1115/1.2794993.
- [50] SPANOS, P., CHEVALLIER, A. M., POLITIS, N. P. “Nonlinear Stochastic Drill-String Vibrations”, *ASME Journal of Vibration and Acoustics*, v. 124, n. October, pp. 512–518, 2002. ISSN: 07393717. doi: 10.1115/1.1502669.
- [51] SOIZE, C. “A Nonparametric Model of Random Uncertainties in Linear Structural Dynamics”, *Probabilistic Engineering Mechanics*, v. 15, pp. 1–28, 2000.
- [52] RITTO, T., SOIZE, C., SAMPAIO, R. “Robust optimization of the rate of penetration of a drill-string using a stochastic nonlinear dynamical model”, *Computational Mechanics*, v. 45, n. 5, 2010. ISSN: 01787675. doi: 10.1007/s00466-009-0462-8.
- [53] QIU, H., YANG, J. “Stochastic and deterministic vibration analysis on drill-string with finite element method”. In: *ASME International Mechanical Engineering Congress and Exposition, Proceedings (IMECE)*, v. 4 A, pp. 1–11, San Diego, California, USA, 2013. ISBN: 9780791856246. doi: 10.1115/IMECE2013-62563.
- [54] PERCY, J. G. *Análise de incertezas em vibrações laterais e de torção acopladas em colunas de perfuração*. Phd Thesis, UFRJ/COPPE, 2014.
- [55] LOBO, D. M., RITTO, T. G., CASTELLO, D. A. “Stochastic analysis of torsional drill-string vibrations considering the passage from a soft to a harder rock layer”, *Journal of the Brazilian Society of Mechanical Sciences and Engineering*, v. 39, n. 6, pp. 2341–2349, 2017. ISSN: 1678-5878. doi: 10.1007/s40430-017-0800-2.
- [56] REAL, F. F., FONTANELA, F., RITTO, T. G., et al. “A probabilistic model of uncertainties in the substructures and interfaces of a dynamical system: application to the torsional vibration of a drill-string”, *Archive of Applied Mechanics*, v. 87, n. 4, pp. 685–698, 2017. ISSN: 14320681. doi: 10.1007/s00419-016-1217-6.

- [57] NOGUEIRA, B. F., RITTO, T. G. “Stochastic torsional stability of an oil drill-string”, *Meccanica*, v. 53, n. 11-12, pp. 3047–3060, 2018. ISSN: 15729648. doi: 10.1007/s11012-018-0859-6.
- [58] DO, K. “Stochastic control of drill-heads driven by Lévy processes”, *Automatica*, v. 103, pp. 36–45, 2019. ISSN: 00051098. doi: 10.1016/j.automatica.2019.01.016.
- [59] DYKSTRA, M. W., CHEN, D. C.-K., WARREN, T. M., et al. “Experimental Evaluations of Drill Bit and Drill String Dynamics”, *Annual Technical Conference and Exhibition of the Society of Petroleum Engineers*, , n. SPE 28323, pp. 319–334, 1994. doi: 10.2118/28323-MS.
- [60] DEILY, F., DAREING, D., PAFF, G., et al. “Downhole Measurements of Drill String Forces and Motions”, *ASME. J. Eng. Ind.*, v. 90, n. 2, pp. 217–225, 1968. doi: 10.1115/1.3604617.
- [61] CUNNINGHAM, R. A. “Analysis of downhole measurements of drill string forces and motions”, *Journal of Engineering for Industry*, v. 90, n. 2, pp. 208–216, 1968. ISSN: 0022-0817. doi: 10.1115/1.3604617.
- [62] MELAKHESSOU, H., BERLIOZ, A., FERRARIS, G. “A Nonlinear Well-Drillstring Interaction Model”, *Journal of Vibration and Acoustics*, v. 125, n. 1, pp. 46, jan 2003. ISSN: 07393717. doi: 10.1115/1.1523071.
- [63] RAYMOND, D. W., ELSAYED, M. A., POLSKY, Y., et al. “Laboratory Simulation of Drill Bit Dynamics Using a Model-Based Servohydraulic Controller”, *Journal of Energy Resources Technology*, v. 130, n. 4, pp. 043103, dec 2008. ISSN: 01950738. doi: 10.1115/1.3000142.
- [64] KHULIEF, Y. A., AL-SULAIMAN, F. A. “Laboratory investigation of drill-string vibrations”, *Proceedings of the Institution of Mechanical Engineers, Part C: Journal of Mechanical Engineering Science*, v. 223, n. 10, pp. 2249–2262, 2009. ISSN: 09544062. doi: 10.1243/09544062JMES1550.
- [65] FRANCA, L. F. P. “Drilling Action of Roller-Cone Bits: Modeling and Experimental Validation”, *Journal of Energy Resources Technology*, v. 132, n. 4, pp. 043101, dec 2010. ISSN: 01950738. doi: 10.1115/1.4003168.
- [66] ESMAEILI, A., ELAHIFAR, B., FRUHWIRTH, R. K., et al. “Laboratory Scale Control of Drilling Parameters to Enhance Rate of Penetration and Reduce Drill String Vibration”, *SPE conference proceeding presented in Al-Khobar, Saudi Arabia*, v. 1, pp. 1–9, apr 2012. doi: 10.2118/160872-MS.

- [67] VLAJIC, N., LIAO, C.-M., KARKI, H., et al. “Draft: Stick-Slip Motions of a Rotor-Stator System”, *Journal of Vibration and Acoustics*, v. 136, n. 2, pp. 021005, dec 2013. ISSN: 0739-3717. doi: 10.1115/1.4025994.
- [68] KAPITANIAK, M., VAZIRI HAMANEH, V., CHÁVEZ, J. P., et al. “Unveiling complexity of drill-string vibrations: Experiments and modelling”, *International Journal of Mechanical Sciences*, v. 101-102, pp. 324–337, 2015. ISSN: 00207403. doi: 10.1016/j.ijmecsci.2015.07.008.
- [69] CAYRES, B., DA FONSECA, C., SANTOS, A., et al. “Analysis of dry friction-induced stick-slip in an experimental test rig modeling a drill string”. In: *Mechanisms and Machine Science*, v. 21, pp. 195–204. Springer, Cham, 2015. ISBN: 9783319065892. doi: 10.1007/978-3-319-06590-8_16.
- [70] WIERCIGROCH, M., NANDAKUMAR, K., PEI, L., et al. “State Dependent Delayed Drill-string Vibration: Theory, Experiments and New Model”. In: *Procedia IUTAM*, v. 22, pp. 39–50. Elsevier, jan 2017. doi: 10.1016/j.piutam.2017.08.007.
- [71] LIU, Y., PÁEZ CHÁVEZ, J., DE SA, R., et al. “Numerical and experimental studies of stick–slip oscillations in drill-strings”, *Nonlinear Dynamics*, v. 90, n. 4, pp. 2959–2978, dec 2017. ISSN: 1573269X. doi: 10.1007/s11071-017-3855-9.
- [72] KAPITANIAK, M., VAZIRI, V., PÁEZ CHÁVEZ, J., et al. “Experimental studies of forward and backward whirls of drill-string”, *Mechanical Systems and Signal Processing*, v. 100, pp. 454–465, feb 2018. ISSN: 10961216. doi: 10.1016/j.ymsp.2017.07.014.
- [73] REAL, F. F., LOBO, D. M., RITTO, T. G., et al. “Experimental analysis of stick-slip in drilling dynamics in a laboratory test-rig”, *Journal of Petroleum Science and Engineering*, v. 170, pp. 755–762, 2018. ISSN: 09204105. doi: 10.1016/j.petrol.2018.07.008.
- [74] ZHANG, Z., SHEN, Y., CHEN, W., et al. “Continuous High Frequency Measurement Improves Understanding of High Frequency Torsional Oscillation in North America Land Drilling”, *Society of Petroleum Engineers*, 2017. doi: 10.2118/187173-MS.
- [75] TANG, L., ZHU, X. “Effects of the Difference Between the Static and the Kinetic Friction Coefficients on a Drill String Vibration Linear Approach”, *Arab J Sci Eng*, v. 40, pp. 3723–3729, 2015. doi: 10.1007/s13369-015-1855-y.

- [76] HARELAND, G., NYGÅRD, R. “Calculating unconfined rock strength from drilling data”, *American Rock Mechanics Association.*, 2007.
- [77] ZAUSA, F., CIVOLANI, L., BRIGNOLI, M., et al. “Real-Time Wellbore Stability Analysis at the Rig-Site”. In: *SPE/IADC Drilling Conference*, n. SPE/IADC 37670, pp. 837–846, 1997. doi: 10.2118/37670-MS.
- [78] RICHARD, T., DAGRAIN, F., POYOL, E., et al. “Rock strength determination from scratch tests”, *Engineering Geology*, v. 148, pp. 91–100, 2012.
- [79] MITAIM, S., DAGRAIN, F., RICHARD, T., et al. “A novel apparatus to determine the rock strength parameters”. In: *The 9th National Convention on Civil Engineering*, 2004.
- [80] SALDIVAR, B., MONDIÉ, S., NICULESCU, S. I., et al. “A control oriented guided tour in oilwell drilling vibration modeling”, *Annual Reviews in Control*, v. 42, pp. 100–113, 2016. ISSN: 13675788. doi: 10.1016/j.arcontrol.2016.09.002.
- [81] SOIZE, C. *Uncertainty Quantification - An Accelerated Course with Advanced Applications in Computational Engineering*. Springer, 2017. doi: 10.1007/978-3-319-54339-0.
- [82] CATALDO, E., SOIZE, C. “Voice Signals Produced With Jitter Through a Stochastic One-mass Mechanical Model”, *Journal of Voice*, v. 31, n. 1, pp. 111.e9–111.e18, 2017. ISSN: 18734588. doi: 10.1016/j.jvoice.2016.01.001.
- [83] CATALDO, E., SOIZE, C. “Stochastic mechanical model of vocal folds for producing jitter and for identifying pathologies through real voices”, *Journal of Biomechanics*, v. 74, pp. 126–133, 2018. ISSN: 18732380. doi: 10.1016/j.jbiomech.2018.04.031.
- [84] OKSENDAL, B. *Stochastic Differential Equations: An Introduction with Applications*. Springer-Verlag, 2010.
- [85] KLOEDEN, P. E., PLATEN, E. *Numerical Solution of Stochastic Differential Equations*. Springer, 1999.
- [86] VANDIVER, K. J., NICHOLSON, J. W., SHYU, R.-J. “Case Studies of the Bending Vibration and Whirling Motion of Drill Collars”, *SPE Drilling Engineering*, v. 5, n. 04, pp. 282–290, 1990. ISSN: 08859744. doi: 10.2118/18652-PA.

- [87] JOGI, P. N., MACPHERSON, J. D., NEUBERT, M. “Field Verification of Model-Derived Natural Frequencies of a Drill String”, *Journal of Energy Resources Technology*, v. 124, n. 3, pp. 154, 2002. ISSN: 01950738. doi: 10.1115/1.1486018.
- [88] SHEN, Y., ZHANG, Z., ZHAO, J., et al. “The Origin and Mechanism of Severe Stick-Slip”, *Society of Petroleum Engineers*, 2017. doi: 10.2118/187457-MS.
- [89] PATIL, P. A., TEODORIU, C. “A comparative review of modelling and controlling torsional vibrations and experimentation using laboratory setups”, *Journal of Petroleum Science and Engineering*, v. 112, pp. 227–238, 2013. ISSN: 09204105. doi: 10.1016/j.petrol.2013.11.008.
- [90] BERLIOZ, A., DERHAGOPIAN, J., DUFOUR, R., et al. “Dynamic behavior of a drill-string: Experimental investigation of lateral instabilities”, *ASME Journal of Vibration and Acoustics*, v. 118, n. 3, pp. 292–298, 1996. ISSN: 1048-9002. doi: 10.1115/1.2888180.
- [91] ELSAYED, M. A. “A Novel Approach to Dynamic Representation of Drill Strings in Test Rigs”, *Journal of Energy Resources Technology*, v. 129, n. 4, pp. 281, 2007. ISSN: 01950738. doi: 10.1115/1.2790979.
- [92] REAL, F. F. *Modeling and experimental identification of drill string torsional dynamics under uncertainties*. D.sc. thesis, Universidade Federal do Rio de Janeiro (UFRJ), 2018.
- [93] YIGIT, A., CHRISTOFOROU, A. “Coupled Torsional and Bending Vibrations of Actively Controlled Drillstrings”, *Journal of Sound and Vibration*, v. 234, n. 1, pp. 67–83, 2000. ISSN: 0022460X. doi: 10.1006/jsvi.1999.2854.
- [94] SAHEBKAR, S. M., GHAZAVI, M. R., KHADEM, S. E., et al. “Nonlinear vibration analysis of an axially moving drillstring system with time dependent axial load and axial velocity in inclined well”, *Mechanism and Machine Theory*, v. 46, n. 5, pp. 743–760, 2011. ISSN: 0094114X. doi: 10.1016/j.mechmachtheory.2010.12.003.
- [95] EVANS, L. C. *An introduction to stochastic differential equations*. American Mathematical Society, 2013.
- [96] HIGHAM, D. “An algorithmic introduction to numerical simulation of stochastic differential equations”, *SIAM Rev.*, v. 43, n. 3, pp. 525–546, 2001. ISSN: 0036-1445. doi: 10.1137/S0036144500378302.

[97] STRANG, G. *Linear Algebra and its applications*. Cengage Learning, 2006.

Appendix A

Bit-rock interaction model validation with experimental data

Many experimental investigations of drill-string vibrations have been reported in the literature. The investigations referring to field measurements approached the vibrations at the surface [13] and near the drill bit [86–88]. Although field tests give a good picture of the vibrations in actual operations, they do not necessarily provide the most appropriate data to corroborate the study of drill-string vibration through mechanical models. There are many uncontrolled variables during the operation, especially the ones associated with the environment.

In order to circumvent these difficulties, many laboratory experimental rigs have been developed to investigate drill-string vibrations. PATIL and TEODORIU [89] have reviewed some of these test-rigs. Most of the experimental setups consist of a slender bar driven at the top by an electric motor, and with a heavy disc attached to the bottom to represent the BHA. The bit-rock interaction is usually emulated by brakes or shakers close to the disc [62, 64, 69, 90]. In contrast to this strategy, only a few test-rigs actually drill rock samples using drill-bits [46, 63, 70, 91].

The experimental test-rig used in this study was designed and constructed at the *Laboratório de Acústica e Vibração (UFRJ)* in collaboration with the *Laboratório de Dinâmica e Vibrações (PUC-RJ)*. This test-rig is a low-cost experimental setup designed based on the work of CAYRES *et al.* [69] with some improvements. The main improvement is the fact that it actually drills a test-body. The construction of the test-rig started at PUC-RJ, where the upper part of the test-rig was constructed. The upper part goes from the top motor to the bit. The test-rig was then moved to UFRJ and assembled. The bottom part of the test-rig was then designed and constructed. Also at UFRJ, the measurement and control systems were designed and implemented. The experimental setup will be briefly explained in the next section, but it is explained in details on [73, 92].

A.1 Experimental set-up

It is desirable to somehow reproduce the complex mechanisms of field drill-string vibrations into a laboratory test-rig in order to allow the investigation of such mechanisms within a more controllable environment. Therefore, an experimental test-rig has been developed at the *Laboratório de Acústica e Vibração (LAVI-COPPE)*. This test-rig is capable of reproducing the torsional vibrations of a drill-string and it is also capable of simulating the coupling between axial and torsional dynamics through bit-rock interaction. The test-rig is shown in Fig. A.1.

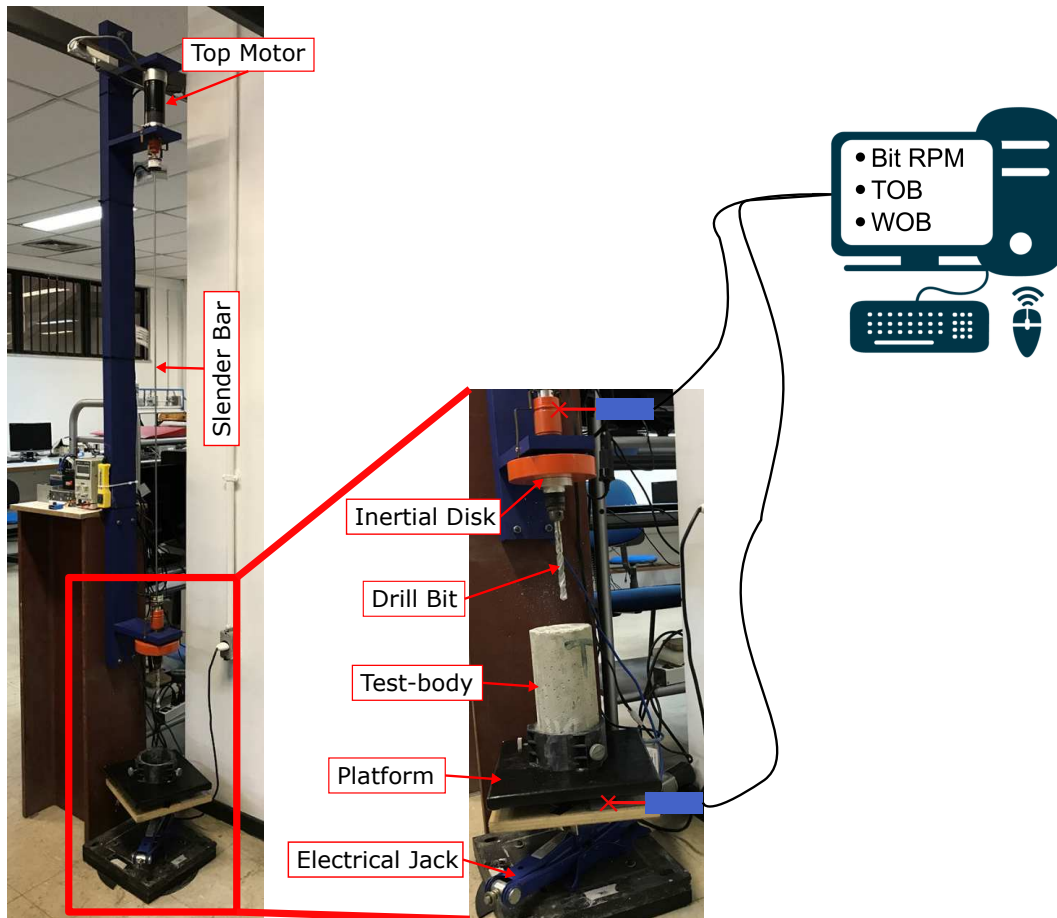


Figure A.1: Experimental test-rig developed and described in [73]. On the left: a general view of the test-rig; On the right: a close view of the bottom part, including the measured variables.

The test-rig consists basically of a DC brushless motor at the top that drives a slender circular bar with 1530 mm length and 5 mm diameter. At the bottom, there is an inertial disc with 28.4 mm thickness and 138 mm diameter with a mandrel that holds a drill-bit, which is a common masonry bit. The penetration is simulated by an electrical jack the lifts a concrete test-body against the drill-bit. The test-body is held by a support printed in 3D printer, that is connected to a platform which is assembled to the electrical jack. Due to the lack of test-bodies, the same sample

was drilled several times as shown in Fig. A.2.



Figure A.2: Concrete test-body after experiment.

In addition, a set of sensors are used to measure the variables of our interest. The platform is composed of two wood plates with load cells between them to measure the weight-on-bit (WOB). A cantilever load cell is connected between the bottom plate of the platform and the electrical jack in order to measure the torque on bit (TOB). In addition, the rotational displacement of the bit and at the top are measured by quadrature encoders. The rotational speed of the bit (Bit RPM) is calculated from the rotational displacement using finite difference method. Attempts were made to measure the axial displacement of the concrete sample using optical sensors. However, the measurements were not satisfactory due to the instabilities of the platform connected to the electrical jack. The measurements are done using the portable data acquisition platform cDAQ-9174 together with the modules NI-9223 and NI-9237 from National Instruments. Labview graphical interface is used to manage the acquisition system and allows real-time response monitoring as well as data recording.

The masonry bits used in experimental tests have 10 mm and 12 mm of diameter. The test-body is made of ordinary concrete (30 fck, diameter of 100 mm, 200 mm of length). The electrical jack is manually controlled by maintaining the input voltage constant and using a power switch. The average speed of the top motor is maintained almost constant during the test by an electronic speed control. However, oscillations of 40% on top speed are often observed and this is a limitation of the test-rig.

In total, 140 data experimental tests were performed (70 for each bit diameter). The average speed set on top motor ranged from 40 to 140 RPM. The slender bar and inertial discs are made of steel and they are considered to represent the drill-pipes and BHA, respectively. For more details about the construction of this test-rig, please refer to [73, 92].

A.2 Mechanical model

The mechanical model proposed for the validation of bit-rock interaction is constructed by means of a lumped parameter approach considering axial and torsional dynamics. The geometric coupling between these two dynamics is not considered. Therefore, the equations are derived separately and the coupling is done by the bit-rock interaction model. A schematic view of the mathematical model is presented in Fig. A.3 and the equations of motion are:

$$I\ddot{\theta}_{bit} + c_t\dot{\theta}_{bit} + k_t\theta_{bit} = -t_{bit} + c_t\Omega + k_t\Omega t , \quad (\text{A.1})$$

$$M\ddot{U} = H_0 - M g - \mathcal{W}_{ob} , \quad (\text{A.2})$$

where θ_{bit} is the rotation at the bit; U is the axial displacement of test-body; Ω is the rotational speed of the top motor, that is supposed to be almost constant; I is the mass moment of inertia of the drill-string, c_t is the torsional damping of the drill-string, k_t is the torsional stiffness of the drill-string, t_{bit} is the Torque On Bit (TOB), M is the mass of the concrete test-body, H_0 is the axial force applied by electrical jack, \mathcal{W}_{ob} is the Weight-On-Bit (WOB) and g is the gravity acceleration. Note that the properties used in axial dynamics are related to the concrete test-body because the drill-string does not move axially. The axial movement is done by the concrete test-body. Furthermore, the axial equation of motion neglects the stiffness and damping because of the boundary condition, which is free-free. The equations of motion are in agreement with [36].

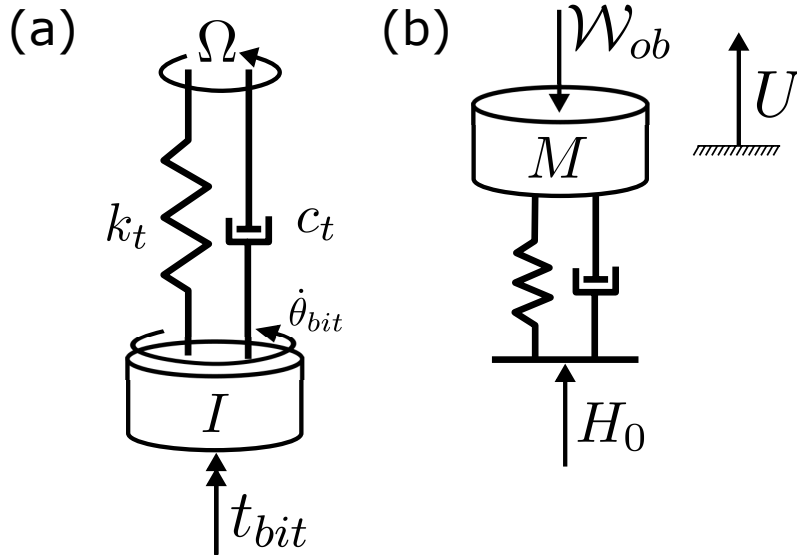


Figure A.3: Schematic view of mechanical model for (a) torsional dynamics and (b) axial dynamics.

The lack of a control strategy for the electrical jack complicates the modeling of

the boundary condition associated with this component. Neither the displacement nor the force are constants, thus it is necessary to propose a function for the force applied by electrical jack. It is experimentally identified that the force applied by the electrical jack varies harmonically around a mean value. Thus, the force H_0 is modeled as:

$$H_0 = \bar{H}_0(1 + h \cos(\omega t)) , \quad (\text{A.3})$$

where H_0 varies around \bar{H}_0 , i.e. the mean value of the applied force; h is a constant related to the amplitude of the fluctuating part, and; ω is the frequency of variation. Inspired by the references [32, 93, 94] and by the fact that the force applied by electrical jack is closely related to the interaction between the bit and the rock, the use of the following function is proposed:

$$H_0 = \bar{H}_0(1 + h \cos(n_b \theta_{bit})) . \quad (\text{A.4})$$

where n_b is the number of cutting blades on the bit (in this case, 2). The TOB (t_{bit}) and WOB (\mathcal{W}_{ob}) are defined by the bit-rock interaction model defined in Sec. 3.3 and reproduced below:

$$t_{bit} = a_4 Z^2(\dot{\theta}_{bit})d(t) + a_5 Z(\dot{\theta}_{bit}) \quad (\text{A.5})$$

$$\mathcal{W}_{ob} = -\frac{\dot{U}}{a_2 Z^2(\dot{\theta}_{bit})} + \frac{a_3}{a_2} Z(\dot{\theta}_{bit}) \dot{\theta}_{bit} - \frac{a_1}{a_2} \quad (\text{A.6})$$

where the depth-of-cut $d(t)$ is defined as:

$$d(t) = \frac{\dot{U}(t)}{n_b \dot{\theta}_{bit}(t)} , \quad (\text{A.7})$$

and the regularization function $Z(\dot{\theta}_{bit})$ is

$$Z(\dot{\theta}_{bit}) = \frac{\dot{\theta}_{bit}}{\sqrt{\dot{\theta}_{bit}^2 + e^2}} . \quad (\text{A.8})$$

A.3 Experimental results

In this section, the sample 105 is selected among the 140 tests performed and investigated. For this sample, the bit diameter is 12 mm and the average rotational speed of the top motor is 78 RPM. At first, the general behavior of sample 105 is analyzed for all the 59 seconds. Then, a time interval of 3 seconds is chosen in order to permit the analysis of stick-slip mechanism and the calibration of the proposed

mechanical model.

Figure A.4 shows the bit rotational speed, the TOB and WOB for sample 105 during all experiment time. The presence of stick-slip oscillations is noticed during almost all the time. In certain time intervals, the bit speed goes to zero and keeps at zero or a longer time. It occurs because the TOB is too high and the top motor does not have enough torque to overcome this resistance. In these situations, the top motor stops and the WOB is relieved in order to decrease the torque and allow the top motor to rotate again.

The manual control applied to the electrical jack is also noticeable by looking at the WOB curve. This curve is made of small time intervals in which the average WOB decreases. It occurs due to the lack of a control strategy to WOB. When the average WOB decreases enough, the electrical switch is turned off and on again in order to increase the power with the starting current and restore the average applied WOB.

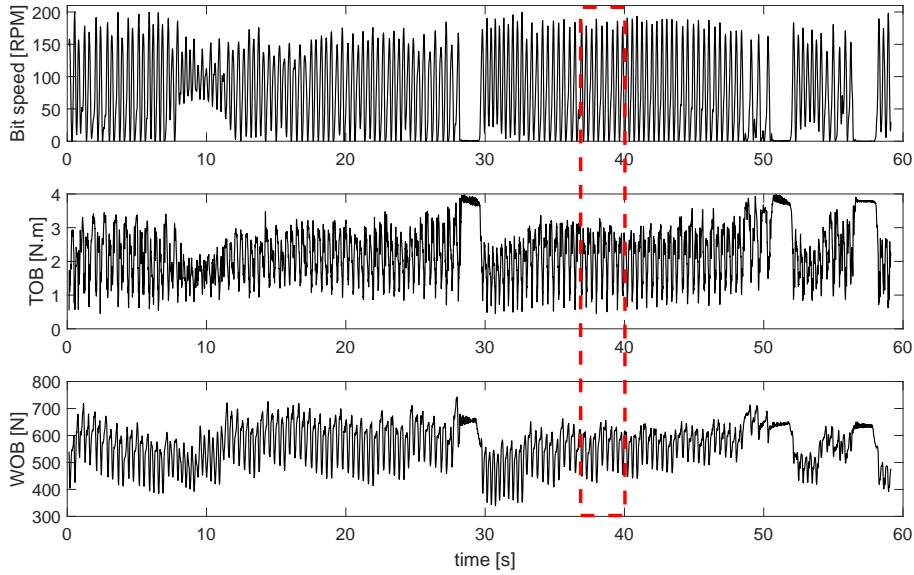


Figure A.4: Experimental data for one experimental run of 60 seconds (sample 105) with an average top rotational speed of 78 RPM and bit diameter of 12 mm. The red box is related to the 3s time interval taken for analysis.

A time interval of 3 seconds is selected in Fig. A.4 from 37 to 40 seconds in order to make a detailed analysis of the stick-slip phenomenon. In Fig. A.5, this time interval is plotted together with six vertical lines that indicate the occurrence of several interesting phenomena. These lines are chosen the same way as in [88], where the authors did a deep analysis of stick-slip mechanism using experimental data from a real-scale drilling rig. The explanation for each point highlighted in Fig. A.5 is presented as follow:

1. At this point, the bit is not rotating and the deformation energy accumulated in drill-string starts to increase as well as the TOB in order to keep the bit stuck.
2. The bit starts to rotate again and TOB achieves its maximum value, which is related to the maximum resistance against cutting. WOB is approximately at the same level.
3. Bit speed is increasing and reaches the average top motor speed. Therefore, deformation energy decreases, the TOB decreases and WOB is maximum locally and starts to decrease.
4. Bit achieves its maximum speed, while TOB achieves its minimum value. It confirms the relation between TOB and bit speed. WOB is also near its minimum value.
5. After the bit achieves its maximum speed, it starts to slow down. WOB starts to increase, indicating that DOC is increasing.
6. Bit sticks again and the stick-slip cycle restarts. The TOB increases to near its maximum value and starts to decrease to a new level, which is related to the enough torque to maintain bit stopped.

This analysis highlights the coupling between axial and torsional dynamics through the interaction force at the bit: TOB and WOB.

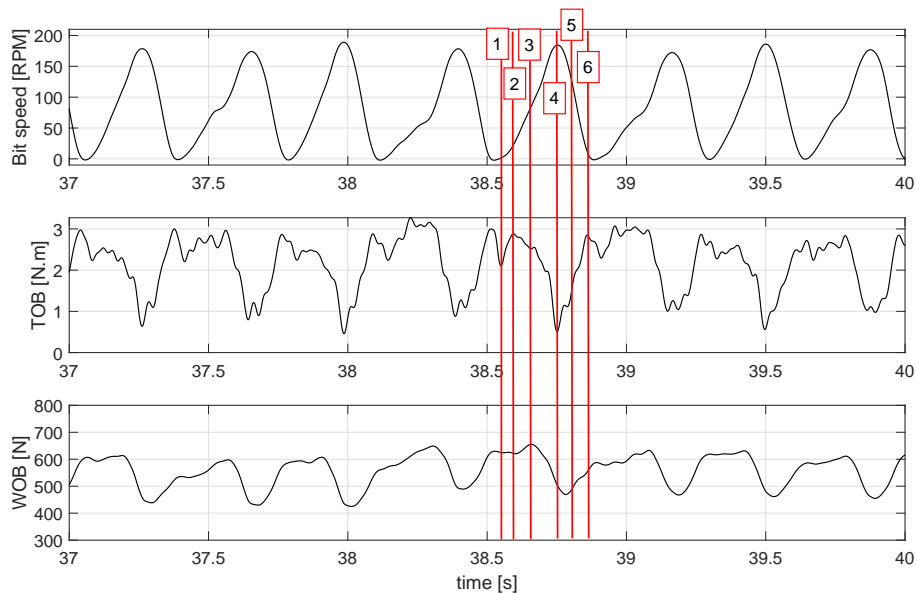


Figure A.5: Experimental data from sample 105 for the time interval of 37 to 40 seconds.

Figure A.6 shows two graphs plotting the interaction forces TOB and WOB against the bit rotational speed. The red arrows indicate the direction of the curve during acceleration and deceleration. It is observed that, in both graphs, the path during acceleration is different from the one when speed is decreasing. This phenomenon was first mentioned in literature in [41] and modeled in [40, 46] for pure torsional models. In Fig.A.6a, the velocity weakening effect is noticed because TOB decreases as the bit rotational speed increases. The cycles shown in Fig. A.6b are far from each other due to change on average WOB provoked by the lack of a control strategy for the electrical jack.

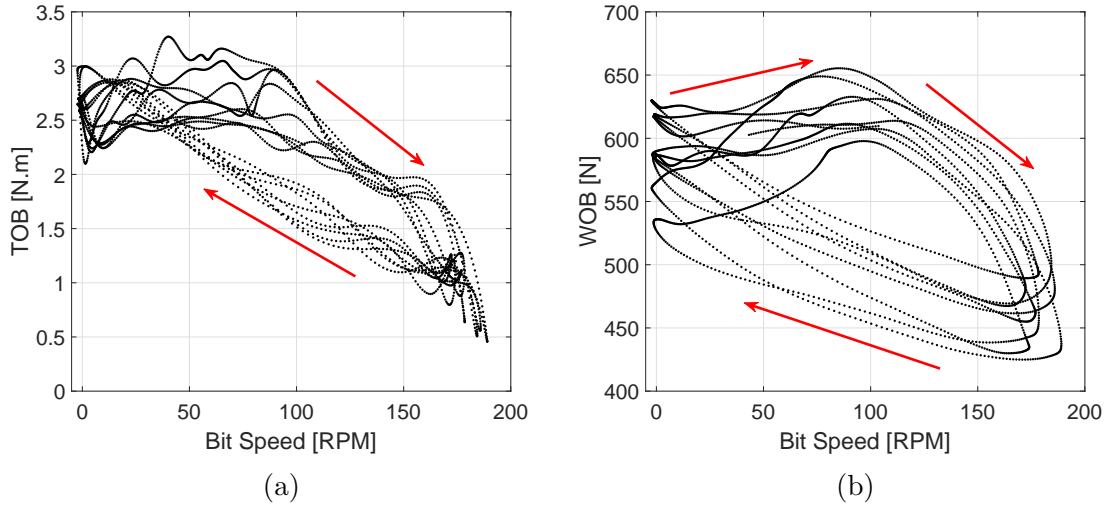


Figure A.6: Bit-rock interaction graphs for sample 105 ($37 < t < 40$). (a) TOB versus Bit speed (b) WOB versus Bit speed. The red arrows show the path direction during acceleration and deceleration.

A.4 Numerical results

The mathematical model is solved using the solver "ode23t" from MATLAB. The parameters used in the simulations are disposed at Tab. A.1. The parameters were calculated using the following equations:

$$I = I_{BHA} + \frac{I_{DP}}{3}, \quad (\text{A.9})$$

$$k_t = \frac{G J_{DP}}{L_{DP}}, \quad (\text{A.10})$$

where the subscript DP denotes the slender bar and BHA is the inertial disk plus the mandrel; G is the shearing modulus; L is the length, and J is the polar moment of inertia. The DP and BHA are considered to be made of steel. The value for stiffness is then adjusted in order to give a natural frequency near to the experimental one (3 Hz [92]). The values for c_t , M , h and \bar{H}_0 are defined using experimental data. The

rotational speed at the top motor Ω is set as 82 RPM, i.e. the average rotational speed during only the 3 seconds under analysis (37 to 40 seconds).

Parameter	Value
I	0.0081 kg.m ² /s ²
c_t	0.036 N.m.s
k_t	2.77 N.m
M	4.419 kg
g	9.81 m/s ²
h	0.17
H_0	524.42 N
n_b	2
Ω	82 RPM

Table A.1: Parameters used in the simulations on experimental investigation.

Before analyzing the 2-DOF model proposed in Sec. A.2, a classical 1-DOF torsional model is implemented. This model is governed by Eq. A.1 with the torque from bit-rock interaction modeled by:

$$t_{bit} = b_0 \mathcal{W}_{ob} \left(\tanh(b_1 \dot{\theta}_{bit}) + \frac{b_2}{1 + b_3 \dot{\theta}_{bit}^2} \right), \quad (\text{A.11})$$

where \mathcal{W}_{ob} is constant and equal to 550 N because only torsional dynamics is considered. The parameter b_0 to b_3 are manually calibrated. Figure A.7 shows the bit rotational speed, TOB and WOB within the time for numerical and experimental results. It is observed that the amplitude of torsional vibration is very similar. However, the shapes of the TOB curve are different. In experimental data, the decay of TOB with speed in higher speeds are much more evident than in lower speeds, but in numerical results, it is not true. As the model considered is pure torsional, WOB does not vary within time.

The behavior of TOB is more evident in Fig. A.8a. In lower speeds, the simulated TOB decays much more than the experimental one. Also, in simulated data, the TOB decays to almost the same level in high and low speeds. This is a limitation of the bit-rock interaction model considered. Furthermore, the hysteric cycles observed in experimental results are also not captured by the 1-DOF torsional model. To capture this phenomenon in pure torsional models, some authors proposed hysterical bit-rock interaction laws [40, 46] which are not implemented here because the objective is to evaluate if this phenomenon occurs because of the axial-torsional coupling. Figure. A.8b shows the FFT of the bit rotational speed for both numerical and experimental results. It is observed that the dominant frequency is the same for both results.

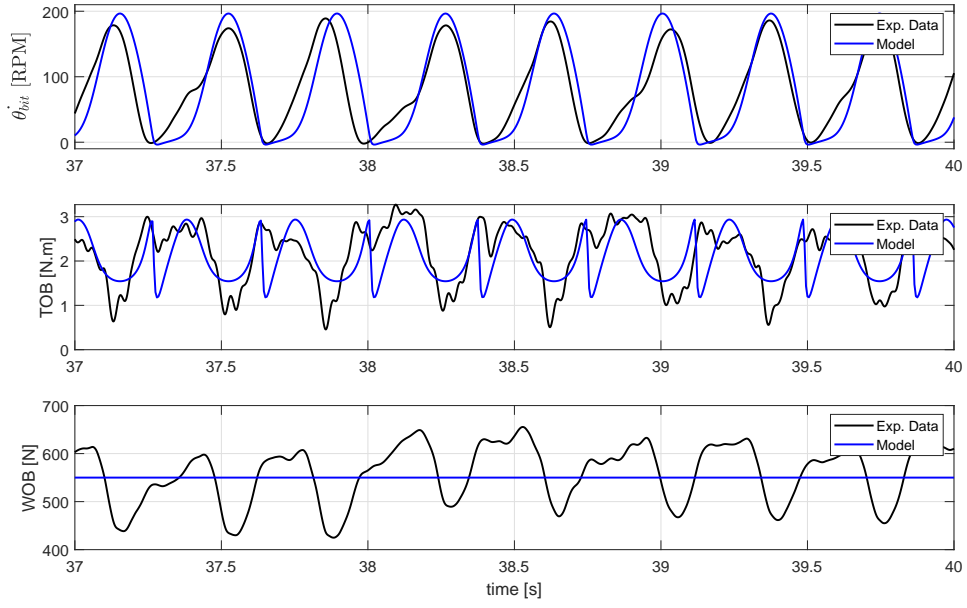


Figure A.7: Numerical results for the 1-DOF model compared to experimental data from 37 to 40 seconds. $b_0 = 0.0022$ m, $b_1 = 1.5$ s/rad, $b_2 = 1.5$ and $b_3 = 0.01$ s²/rad².

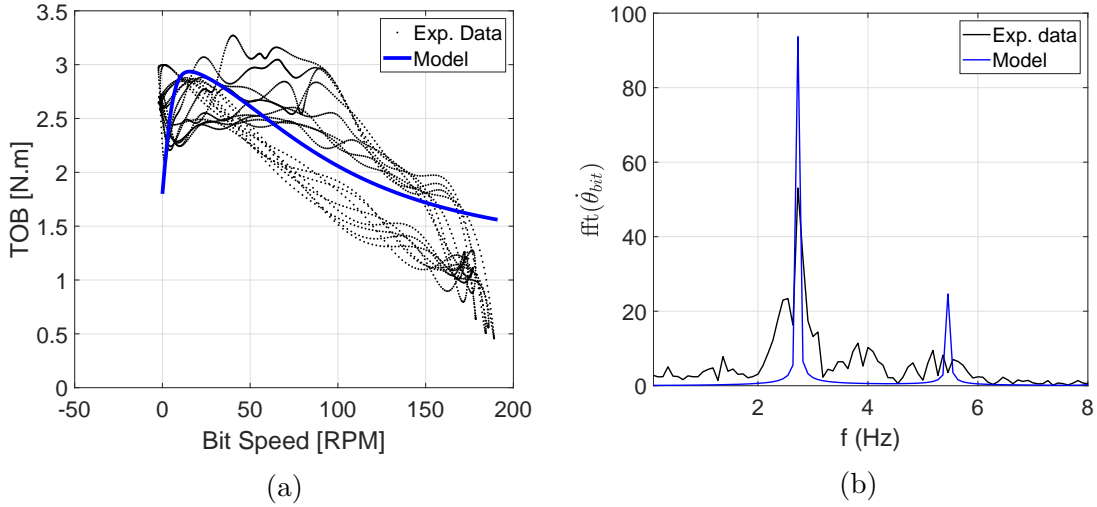


Figure A.8: (a) TOB versus Bit speed and (b) Fast Fourier Transform (fft) of the bit rotational speed for the numerical results of the 1-DOF model compared to experimental data from 37 to 40 seconds. $b_0 = 0.0022$ m, $b_1 = 1.5$ s/rad, $b_2 = 1.5$ and $b_3 = 0.01$ s²/rad².

To conclude, the 1-DOF model can capture the overall behavior of drill-string but it is still not capable of describing the details of the dynamics and neither the fluctuations of WOB. Therefore, the 2-DOF model proposed in Sec. A.2 is simulated and compared to experimental data in order to investigate the gains with an axial-torsional model.

Figure A.9 shows the bit rotational and axial speeds, TOB and WOB for one calibration of the 2-DOF model. The amplitude of the torsional vibration in terms of bit rotational speed is also compatible with experimental results. In this case, it is also possible to obtain the bit axial speed which presents realistic values for the test-rig but it could not be compared to experimental results because of the problems with the measurement system. The TOB presented lower variations but the decrease with bit rotational speed is also the same for high and low speeds. The fluctuations on WOB are now captured by the model. Furthermore, the variation of the applied force H_0 is found to affect much more the WOB than the forces due to the bit-rock interaction model.

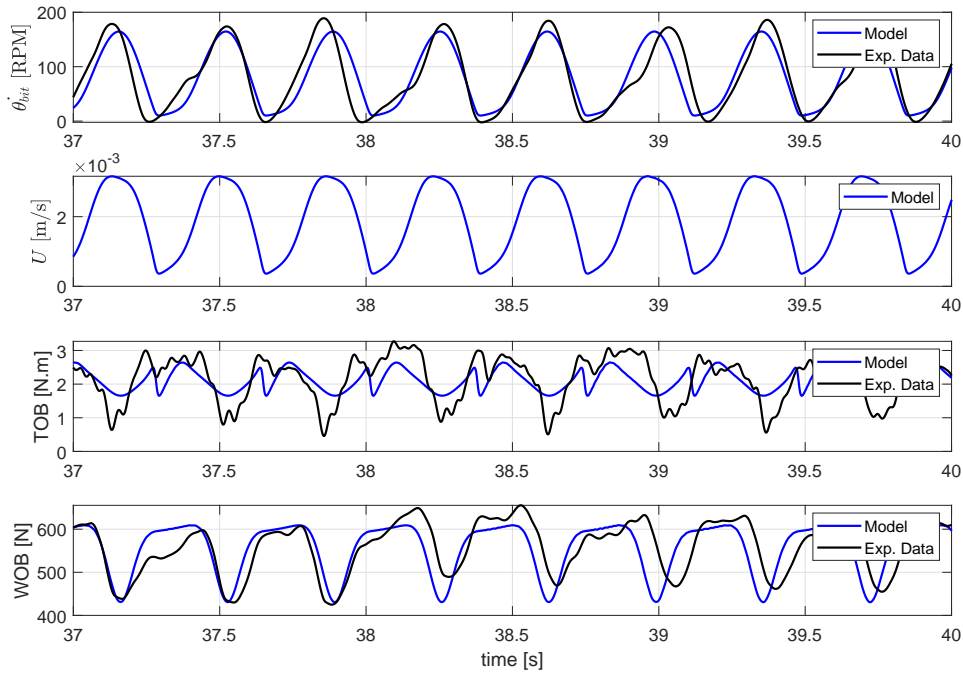


Figure A.9: Numerical results for the 2-DOF model compared to experimental data from 37 to 40 seconds. $a_1 = 0.0026$ m/s, $a_2 = 5 \times 10^6$ m/s/N, $a_3 = 2.0610 \times 10^{-4}$ m/rad, $a_4 = 8751.6$ N.rad, $a_5 = 0.0875$ N.m, $e = 1$ rad²/s².

The frequency of variation of the bit rotational speed is also assessed by the FFT. Figure A.10 shows that the 2-DOF model also represents pretty well the experimental bit rotational speed in the frequency domain.

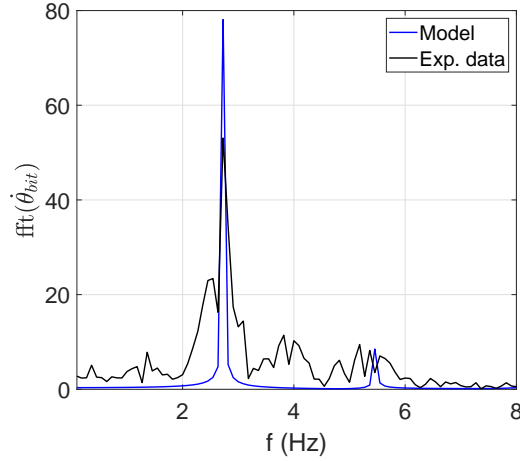


Figure A.10: Fast Fourier Transform (fft) of the bit rotational speed for the numerical results of the 2-DOF model compared to experimental data from 37 to 40 seconds. $a_1 = 0.0026$ m/s, $a_2 = 5 \times 10^6$ m/s/N, $a_3 = 2.0610 \times 10^{-4}$ m/rad, $a_4 = 8751.6$ N.rad, $a_5 = 0.0875$ N.m, $e = 1$ rad²/s².

The most interesting phenomenon observed in the 2-DOF model results is the hysteric effect on TOB and WOB versus bit rotational speed. Figure A.11 shows that, although the amplitudes are not the same, the 2-DOF model can capture the hysteric effect observed in experimental data, including the direction of acceleration and deceleration paths (highlighted by red arrows for the model and green arrows for experimental data).

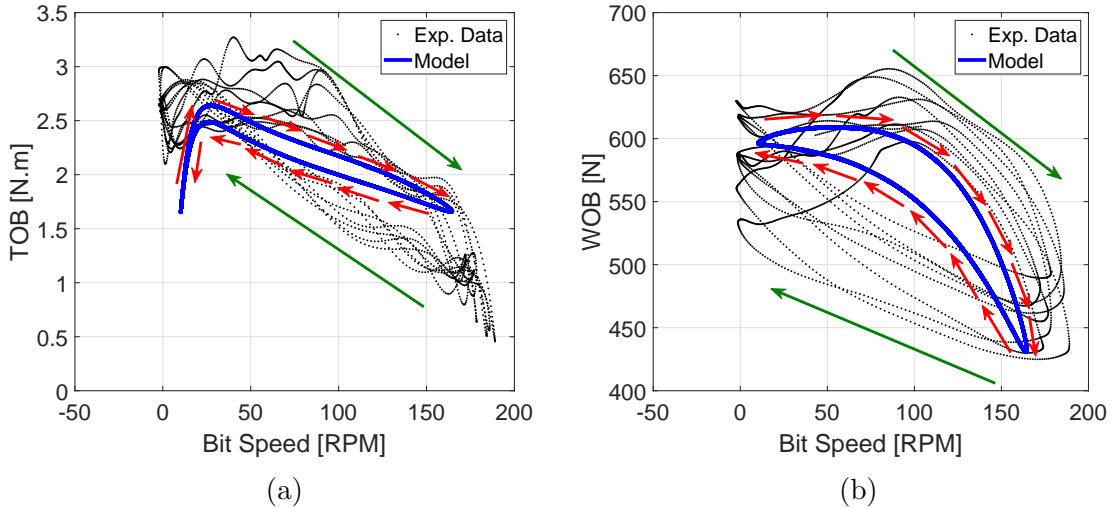


Figure A.11: (a) TOB versus Bit speed and (b) WOB versus Bit speed for the numerical results of the 2-DOF model compared to experimental data from 37 to 40 seconds. $a_1 = 0.0026$ m/s, $a_2 = 5 \times 10^6$ m/s/N, $a_3 = 2.0610 \times 10^{-4}$ m/rad, $a_4 = 8751.6$ N.rad, $a_5 = 0.0875$ N.m, $e = 1$ rad²/s². The arrows show the path direction during acceleration and deceleration. The green arrows are for the experimental data and the red ones are for the numerical results.

A variety of calibrations were tested for the bit-rock interaction. Some of these combinations resulted in bit-rock interaction curves that were more similar to experimental results, as in Fig. A.12. However, the direction of the paths is the opposite of the experimental data. This difference can also be observed in Fig. A.13, where the bit rotational speed continued to be in good agreement (amplitude and frequency) but the TOB and WOB present results qualitatively different from experimental data. For example, the maximum WOB occurs when the bit is accelerating for experimental data, while it occurs when bit achieves its maximum speed for the numerical result.

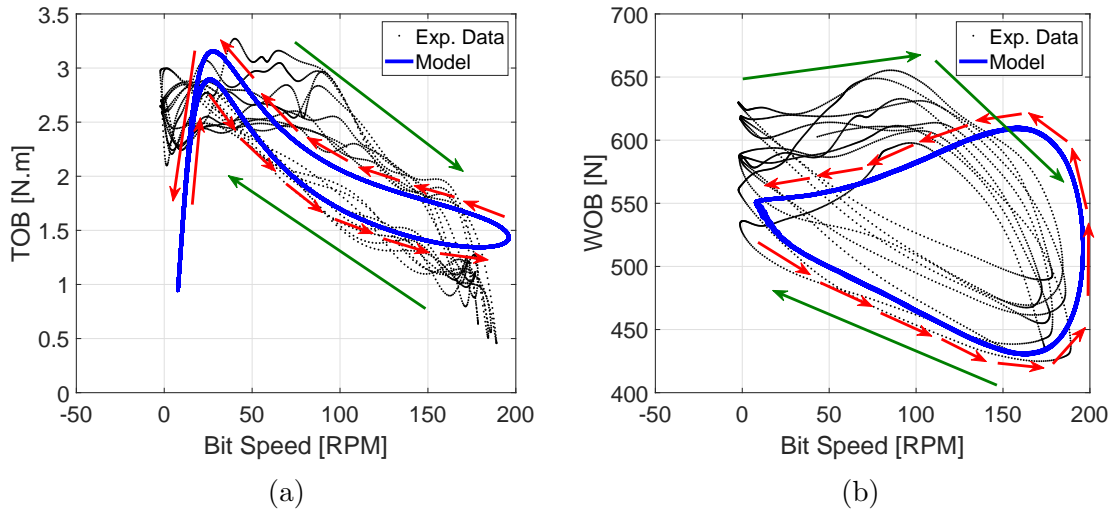


Figure A.12: (a) TOB versus Bit speed and (b) WOB versus Bit speed for the numerical results of the 2-DOF model compared to experimental data from 37 to 40 seconds. $a_1 = 0.0011$ m/s, $a_2 = 5 \times 10^6$ m/s/N, $a_3 = 9.16 \times 10^{-5}$ m/rad, $a_4 = 6732$ N.rad, $a_5 = 0.3471$ N.m, $e = 1.5$ rad²/s². The arrows show the path direction during acceleration and deceleration. Green arrow are for experimental data and the red ones are for numerical results.

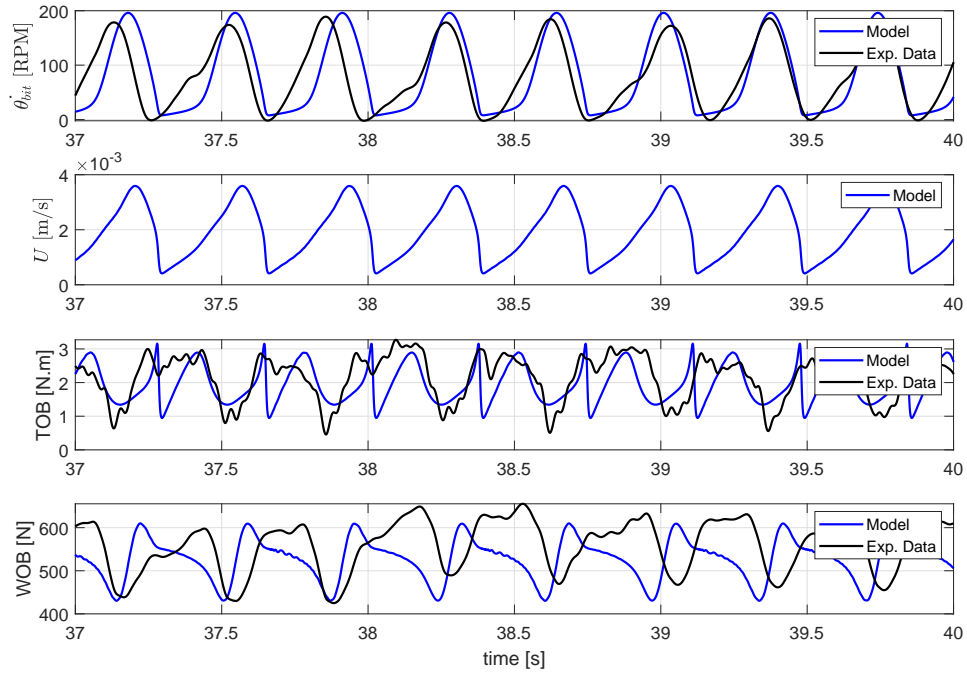


Figure A.13: Numerical results for the 2-DOF model compared to experimental data from 37 to 40 seconds. $a_1 = 0.0011$ m/s, $a_2 = 5 \times 10^6$ m/s/N, $a_3 = 9.16 \times 10^{-5}$ m/rad, $a_4 = 6732$ N.rad, $a_5 = 0.3471$ N.m, $e = 1.5$ rad²/s².

In summary, the 2-DOF model can capture some dynamical effects that the 1-DOF model is not capable of, including: the axial speed of the bit, which is a direct measure of the efficiency of operation; variations of WOB during drilling, and; hysteric effects on bit-rock interaction.

Appendix B

An introduction to stochastic differential equations (SDE)

This appendix is devoted to a brief introduction of stochastic differential equations. The subject is discussed assuming that the reader has a fair base on probability theory. Most of the proofs and theorems are omitted in order to simplify this introduction. For those who want to study SDE in more details, the books from OKSENDAL [84] and EVANS [95], which were used as a base for this text, are recommended. Most of the numerical examples and the codes presented in this chapter were base on the work developed by HIGHAM [96].

Ordinary differential equations (ODE) are often used to model systems of interest in many engineering applications. However, the experimentally measured variables of systems modeled by ODEs do not behave precisely as predicted. If the model is adequate, the variables seem to behave more or less as expected but they are often subject to random fluctuations. Depending on the system characteristics, this random behavior can have a significant influence on the system response as illustrated by the example presented at the end of this chapter. One way to model a system using SDE is to allow some randomness in some coefficients of the ODE. Consider the following example:

EXAMPLE 1: Consider the following simple population growth model taken from [84]:

$$\frac{dX}{dt} = a(t)X(t), \tag{B.1}$$

where $X(t)$ is the population size and $a(t)$ is the relative growth coefficient. Suppose now that $a(t)$ is not precisely known and it is influenced by random environmental effects. Thus, this coefficient can be interpreted as:

$$a(t) = r(t) + \xi(t), \tag{B.2}$$

where $r(t)$ is a deterministic function and $\xi(t)$ is a Gaussian white noise process. The inclusion of the noise factor in eq. B.1 transforms it into a stochastic differential equation. Substituting eq.B.2 into B.1 results in the following SDE:

$$\frac{dX}{dt} = r(t)X(t) + \alpha X(t)\xi(t),, \quad (\text{B.3})$$

For the case $r(t) = 0$ and $\alpha X(t) = 1$, the solution turns out to be a Brownian motion (or Wiener process), denoted by $W(t)$. It introduces the idea that white noise is in fact the time derivative of Brownian motion. Thus,

$$\frac{dW}{dt} = \xi(t). \quad (\text{B.4})$$

Finally, the SDE B.3 can be written in the classical derivative form as:

$$dX(t) = r(t)X(t)dt + \alpha X(t)dW. \quad (\text{B.5})$$

In a more general perspective, a SDE is expressed by:

$$\begin{cases} d\mathbf{X}(t) = \mathbf{b}(\mathbf{X}(t))dt + [B(\mathbf{X}(t))]d\mathbf{W}(t) \\ \mathbf{X}(0) = \mathbf{x}_0 \end{cases}, \quad (\text{B.6})$$

where bold indicates a vector and [B] indicates that B is a matrix. The terms $d\mathbf{X}$ and $[B(\mathbf{X})]d\mathbf{W}$ are called stochastic differentials. Taking the integral of Eq. B.6 from 0 to t and considering that $\int_0^t d\mathbf{X}(t) = \mathbf{X}(t) - \mathbf{x}_0$, we can write the SDE in integral form:

$$\mathbf{X}(t) = \mathbf{x}_0 + \int_0^t \mathbf{b}(\mathbf{X}(s)) ds + \int_0^t [B(\mathbf{X}(s))] d\mathbf{W} \quad (\text{B.7})$$

where s is a dummy variable (integration variable).

B.1 Brownian Motion

DEFINITION: A Brownian motion (or Wiener process) is a stochastic process with the following properties:

- (i) $W(0) = 0$, almost surely,
- (ii) $dW = W(t) - W(s) \sim N(0, t - s)$ for all $t \geq s \geq 0$,
- (iii) for all times $0 < t_1 < t_2 < \dots < t_n$, the random variables $W(t_1)$, $W(t_2) - W(t_1)$, \dots , $W(t_n) - W(t_{n-1})$ are independent ("independent increments").

Considering the second property and taking $s = 0$, it gives that $W(t) \sim N(0, t)$. It means that $E[W(t)] = 0$, $E[W^2(t)] = t$ and, thus, the probability density function of $W(t)$ is

$$f(W, t) = \frac{1}{\sqrt{2\pi t}} e^{-\frac{W^2}{2t}} \quad (\text{B.8})$$

It is also possible to prove that the autocorrelation function for $t \geq s \geq 0$ is given by

$$\begin{aligned} E[W(t)W(s)] &= E[\{W(s) + (W(t) - W(s))\}W(s)] \\ &= E[W^2(s)] + E[(W(t) - W(s))W(s)] \\ &= s + 0 = s \end{aligned} \quad (\text{B.9})$$

It can be shown that, for the case where $s \geq t \geq 0$, the autocorrelation becomes $E[W(t)W(s)] = t$. Thus, we conclude that $E[W(t)W(s)] = \min\{t, s\}$

In Fig. B.1a, three sample paths of a Brownian motion (Eq. B.4) are simulated in MATLAB using the code in Listing B.1 and presented. The simulation of a Brownian motion is performed by simulating M increments with time step dt using Monte Carlo and summing them until time $t = Mdt$.

In Fig. B.1b, the eq. B.10 is simulated and five individual sample paths are plotted as well as the average of $U(t)$ along 1000 simulations. Actually, eq. B.10 is the solution of a SDE and the average $U(t)$ is expressed as $E[U(t)] = \exp(9/8t)$ and coincides to the deterministic solution this SDE. Further, in this chapter, this equation will be presented and studied.

$$U(t) = \exp\left(t + \frac{1}{2}W(t)\right) \quad (\text{B.10})$$

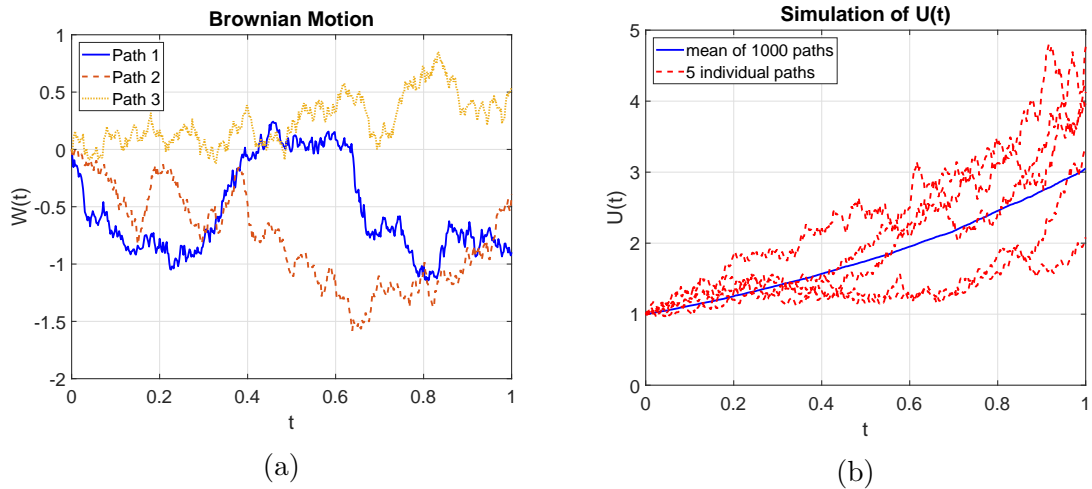


Figure B.1: (a) Three sample paths of brownian motion with $dt = 0.002s$. (b) Five paths of $U(t)$ and mean value with $dt=0.002s$.

Listing B.1: Code to generate Brownian motion

```

1  %% Brownian path simulation
2
3  T = 1;           % Simulation total time
4  N = 500;        % Number of time steps
5  dt = T/N;       % Time step
6  t = [dt:dt:T];  % Time Vector (t0 is added later)
7
8  dW = sqrt(dt)*randn(3,N); % Brownian motion increments
9  W = cumsum(dW,2); % Construct Brownian motion ...
    (cumulative sum)
10
11 figure(1)
12 plot([0:dt:T],[zeros(size(W,1),1),W]) % Include t0 here
13 legend('Path 1','Path 2','Path 3')
14 title('Brownian Motion')
15 xlabel('t')
16 ylabel('W(t)')
17 grid on
18
19 M = 1000;        % M paths simultaneously
20 dW = sqrt(dt)*randn(M,N); % Brownian motion increments
21 W = cumsum(dW,2); % Construct Brownian motion
22 U = exp(repmat(t,[M 1]) + 0.5*W); % Evaluate function U
23 % (repmat transforms t into a matrix)
24 Umean = mean(U); % Evaluate mean(U)
25
26 figure(2)
27 plot([0,t],[1,Umean],'b-'), hold on % plot mean ...
    over M paths
28 plot([0,t],[ones(5,1),U(1:5,:)],'r--'), hold off % plot 5 ...
    individual paths
29 xlabel('t','FontSize',16)
30 ylabel('U(t)','FontSize',16)
31 grid on
32 legend('mean of 1000 paths','5 individual paths')
33
34 averr = norm((Umean - exp(9*t/8)),'inf') % sample error

```

B.2 Stochastic Integrals

In order to solve stochastic differential equations of the form of eq. B.6, it is necessary to comprehend the concept of stochastic integrals. Taking the general integral form of a SDE, as represented by eq. B.7, we define as stochastic integral the term

$\int_0^t [B(\mathbf{X}(s))]d\mathbf{W}$, where $[B(\mathbf{X}(s))]$ is a stochastic process. Note that this integral is not about a deterministic variable, like the time for example, but about a stochastic process. As the Brownian motion is not differentiable, the interpretation of stochastic integrals is not trivial. One of the first definitions of stochastic integral was proposed by Paley-Wiener-Zygmund for the 1-D case:

DEFINITION (Paley-Wiener-Zygmund): Suppose a deterministic continuously differentiable function $g : [0, T] \rightarrow \Re$ with $g(0) = g(T) = 0$. We define

$$\int_0^T g dW = - \int_0^T g' W dt \quad (\text{B.11})$$

where $g' = \frac{dg}{dt}$. Note that, although $\int_0^T g dW$ is random, g is a deterministic function. The formulation above gives rise to the following properties:

- (i) $E \left(\int_0^T g dW \right) = 0$
- (ii) $E \left(\left(\int_0^T g dW \right)^2 \right) = \int_0^T g^2 dt$

Proof:

$$(i) \ E \left(\int_0^T g dW \right) = E \left(- \int_0^T g' W dt \right) = - \int_0^T g' E(W(t)) dt = 0$$

$$\begin{aligned} (ii) \ E \left(\left(\int_0^T g dW \right)^2 \right) &= E \left(\int_0^T g'(s)W(s) ds \int_0^T g'(t)W(t) dt \right) \\ &= E \left(\int_0^T \int_0^T g'(s)W(s)g'(t)W(t) ds dt \right) \\ &= \int_0^T \int_0^T g'(s)g'(t) E(W(s)W(t)) ds dt \end{aligned}$$

Separating the integral in ds for $s < t$ and $s > t$, we get

$$= \int_0^T g'(t) \left(\int_0^t g'(s)s ds + \int_t^T g'(s)t ds \right) dt$$

Integrating by parts with $g(0) = g(T) = 0$,

$$\begin{aligned} &= \int_0^T g'(t) \left(tg(t) - \int_0^t g(s) ds - tg(t) \right) dt \\ &= \int_0^T g'(t) \left(- \int_0^t g(s) ds \right) dt \end{aligned}$$

Integrating by parts again with $g(0) = g(T) = 0$,

$$= \int_0^T g^2(t) dt$$

Although this definition is very useful for the cases in which g is deterministic and satisfies $g(0) = g(T) = 0$, it is demanded a definition that covers a wider class of functions of the type

$$\int_0^t B(X, s) dW \quad (\text{B.12})$$

where $B(X, s)$ is a stochastic process. Actually, the wider definition proposed by Ito returns to the formulation of Paley-Wiener-Zygmund (Eq. B.11) for the case considered by them.

B.2.1 Riemann Sums

The Riemann sums can help us to interpret stochastic integrals with random integrands. The idea relies on understanding this type of integral through Riemann sums and then (if possible) pass it to limits. Let's consider the stochastic integral of a Brownian motion, for example:

$$R = \int_0^T W dW. \quad (\text{B.13})$$

A partition P in $[0, T]$ is defined as a collection of discrete point, including the boundaries, such as: $P = \{0 = t_0 < t_1 < \dots < t_m = T\}$ with a mesh size $|P| = \max_{0 \leq k \leq m-1} |t_{k+1} - t_k|$. For a fixed $0 \leq \lambda \leq 1$ and a partition P , we can define a point τ_k lying withing the subinterval $[t_k, t_{k+1}]$ for $k = 0, 1, 2, \dots, m - 1$ such as:

$$\tau_k = (1 - \lambda)t_k + \lambda t_{k+1}. \quad (\text{B.14})$$

Finally, we can interpret the integral in eq. B.13 as a Riemann sum with $|P| \rightarrow 0$ for a given partition P :

$$R = R(P, \lambda) = \sum_{k=0}^{m-1} W(\tau_k) [W(t_{k+1}) - W(t_k)]. \quad (\text{B.15})$$

Next, we take the limit when mesh size goes to zero. Then, it is possible to prove that

$$\lim_{|P| \rightarrow 0} R(P, \lambda) = \frac{W^2(T)}{2} + \left(\lambda - \frac{1}{2} \right) T, \quad \text{in } \mathcal{L}^2(0, T). \quad (\text{B.16})$$

where $\mathcal{L}^2(0, T)$ is the space of all real-valued, progressively measurable stochastic processes $G(\cdot)$ such that $E[\int_0^T G^2 dt] < \infty$. For details and proof, please refer to [95]. Note that this result depends on the choice of the intermediate point τ_k . Two definitions are often used in the literature: Itô ($\lambda = 0$) and Stratonovich ($\lambda = \frac{1}{2}$):

$$\int_0^T W dW = \frac{W^2(T)}{2} - \frac{T}{2} \quad (\text{It\^o integral}), \quad (\text{B.17})$$

$$\int_0^T W dW = \frac{W^2(T)}{2} \quad (\text{Stratonovich integral}). \quad (\text{B.18})$$

The main advantage of selecting $\lambda = 0$ and choosing It\^o definition relies on the calculation of the integrand at point t_k within the subinterval $[t_k, t_{k+1}]$. It allows the definition for a wide class of "nonanticipating" stochastic processes $G(\circ)$ as depicted in eq. B.19. The idea relies on the fact that, since we do not know what $G(\circ)$ will do in $[t_k, t_{k+1}]$, it is better to use the known value of $G(t_k)$.

$$\int_0^T G dW \sim \sum_{k=0}^{m-1} G(\tau_k) [W(t_{k+1}) - W(t_k)]. \quad (\text{B.19})$$

In Fig. B.2, the stochastic integral of a Brownian motion defined as the function $F(t) = \int_0^t W dW$ is plotted against time for the definitions proposed by It\^o and Stratonovich using the code in Listing B.2 written in MATLAB. The numerical results were obtained by solving the Riemann sum with 100 points in time interval $t \in [0, 1]$ and the analytical results follow eq. B.17 and B.18. It is observed that numerical results tend to the analytical solution. Actually, if the number of points is increased, the precision of numerical results improves. The differences between the approach by It\^o and Stratonovich can be noticed. According to [95], there is no evidence on which interpretation is physically correct.

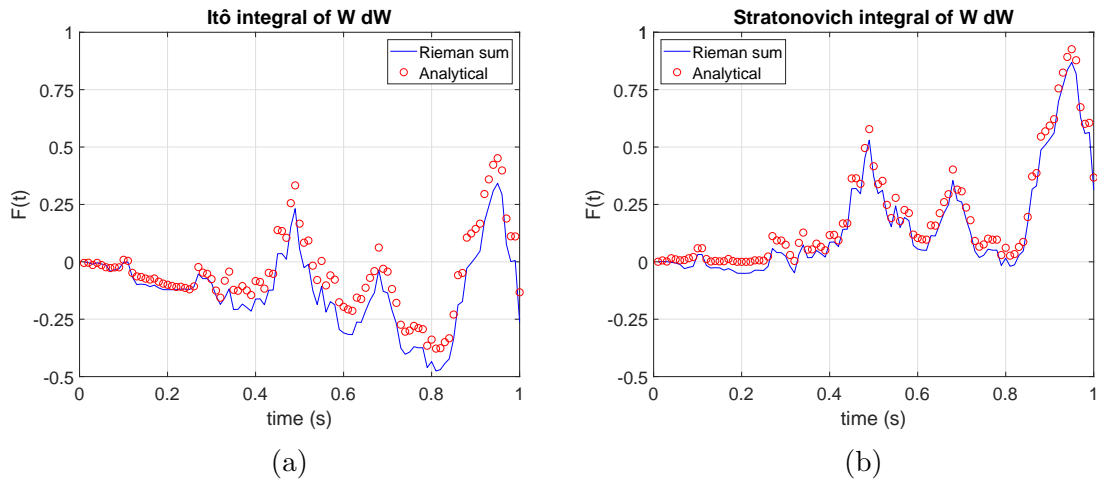


Figure B.2: Stochastic integrals of $W dW$ following (a) It\^o definition and (b) Stratonovich definition.

Listing B.2: Code to calculate Ito and Stratonovich integral of $W dW$

```

1 %% Ito and Stratonovich integrals of W dW
2
3 T = 1;           % Simulation total time
4 N = 100;        % Number of time steps
5 dt = T/N;       % Time step
6 t = [dt:dt:T];  % Time Vector (t0 is added later)
7
8 dW = sqrt(dt)*randn(1,N); % Brownian motion increments
9 W = cumsum(dW);  % Construct Brownian motion ...
    (cumulative sum)
10
11 % Solve stochastic integral by Ito
12 ito = cumsum([0,W(1:end-1)].*dW);
13 % Solve stochastic integral by Stratonovich
14 strat = cumsum((0.5*([0,W(1:end-1)]+W) + ...
    0.5*sqrt(dt)*randn(1,N)).*dW);
15
16 figure(3) % Plot Ito stochastic integral
17 plot(t,ito,'b'),hold on % Rieman Sum
18 plot(t,0.5*(W.^2-t),'ro'), hold off % Analytical
19 grid on
20 legend('Rieman sum','Analytical')
21 xlabel('time (s)')
22 ylabel('F(t)')
23 title('Ito integral of W dW')
24
25 figure(4) % Plot Stratonovich stochastic integral
26 plot(t,strat,'b'),hold on % Rieman Sum
27 plot(t,0.5*(W.^2),'ro'), hold off % Analytical
28 grid on
29 legend('Rieman sum','Analytical')
30 xlabel('time (s)')
31 ylabel('F(t)')
32 title('Stratonovich integral of W dW')
33
34 % Error of Rieman sum approximation at the last point
35 itoerr = abs(ito(end) - 0.5*(W(end)^2-T))
36 straterr = abs(strat(end) - 0.5*W(end)^2)

```

In summary, according to [95], the advantages of each definition of the stochastic integral are:

- Itô integral

(i) Simple formulas:

$$E \left(\int_0^t G dW \right) = 0, \quad E \left(\left(\int_0^t G dW \right)^2 \right) = E \left(\int_0^t G^2 dt \right).$$

(ii) $I(t) = \int_0^t G dW$ is a martingale (see [84, 95]).

• **Stratonovich integral**

(i) Ordinary chain rule holds.

(ii) Solutions of stochastic differential equations interpreted in the Stratonovich sense are stable with respect to changes in random terms.

B.2.2 Itô integral

Although both interpretations of stochastic integrals have advantages, the Itô approach was chosen in the present work because it is valid for a wider class of integrands. Thus, this approach will be discussed in details. The first step is to define what are nonanticipating stochastic processes in order to clarify the main advantage of Itô interpretation.

Let $W(\circ)$ be a 1-D Brownian motion defined in the probability space (Ω, \mathcal{U}, P) . The σ -algebra $\mathcal{W}(t) = \mathcal{U}(W(s) | 0 \leq s \leq t)$ is called the history of Brownian motion up to time t and $\mathcal{W}^+(t) = \mathcal{U}(W(s) - W(t) | s \geq t)$ is the future of Brownian motion beyond time t .

DEFINITION: A family \mathcal{F} of σ -algebras $\subseteq \mathcal{U}$ is called nonanticipating if:

- (i) $\mathcal{F}(t) \supseteq \mathcal{F}(s)$ for $t \geq s \geq 0$,
- (ii) $\mathcal{F}(t) \supseteq \mathcal{W}(t)$ for $t \geq 0$,
- (iii) $\mathcal{F}(t)$ is independent of $\mathcal{W}^+(t)$ for $t \geq 0$.

$\mathcal{F}(\circ)$ is sometimes called filtration and it is interpreted as all the information we have up to time t . A process $G(\circ)$ is called nonanticipating if it is $\mathcal{F}(t)$ -measurable for $t \geq 0$.

In the sequence, we define stochastic integral according to Itô interpretation. For this purpose, let's define what are step processes.

DEFINITION: A stochastic process $G(\circ)$ is called step process if there exist a partition $P = \{0 = t_0 < t_1 < \dots < t_m = T\}$ such as:

$$G(t) = G_k, \quad \text{for } t_k \leq t < t_{k+1} \quad (k = 0, 1, \dots, m-1) \quad (\text{B.20})$$

Therefore, G_k is $\mathcal{F}(t)$ -measurable and $G(\circ)$ is nonanticipating. Thus, we can use Riemann sums to calculate the stochastic integral using Itô:

$$\int_0^T G dW = \sum_{k=0}^{m-1} G_k (W(t_{k+1}) - W(t_k)) \quad (\text{B.21})$$

LEMMA: If $G \in \mathcal{L}^2(0, T)$, there exist a sequence of bounded step processes $G^n \in \mathcal{L}^2$ such as:

$$E \left(\int_0^T |G - G^n|^2 dt \right) \rightarrow 0. \quad (\text{B.22})$$

This states that we can approximate a stochastic process as a sequence of step processes. Then, in the limit,

$$\int_0^T G dW = \lim_{n \rightarrow \infty} \int_0^T G^n dW \quad (\text{B.23})$$

The proof can be checked out in [84, 95]. Therefore, the following properties can be verified if we use the approximation by step processes:

Properties of Itô stochastic integral

- (i) $\int_0^T (aG + bH) dW = a \int_0^T G dW + b \int_0^T H dW$
- (ii) $E \left(\int_0^T G dW \right) = 0$
- (iii) $E \left(\left(\int_0^T G dW \right)^2 \right) = E \left(\int_0^T G^2 dt \right)$
- (iv) $E \left(\int_0^T G dW \int_0^T H dW \right) = \int_0^T GH dt$

Note that the properties (ii) and (iii) are identical to the ones provided by Paley-Wiener-Zygmund definition.

Itô's chain rule

The chain rule in stochastic differentials is different from the deterministic case. In deterministic case, let's consider the following differential equation

$$\frac{dx}{dt} = F(x, t), \quad (\text{B.24})$$

and suppose that $y(t) = u(x, t)$, where $u : \mathcal{R} \rightarrow \mathcal{R}$ is a deterministic function. The derivative $\frac{dy}{dt}$ can be calculated using deterministic chain rule that can be proved by

writing the increment in function $u(x, t)$ using Taylor theorem as in Eq B.25.

$$u(x + \Delta x, t + \Delta t) - u(x, t) = u_x \Delta x + u_t \Delta t + o(|\Delta x|^2 + |\Delta t|^2) \quad (\text{B.25})$$

where $\Delta x = (x(t + dt) - x(t))$, $u_x = \frac{\partial u}{\partial x}$ and $u_t = \frac{\partial u}{\partial t}$. Taking the limit when $\Delta t \rightarrow 0$,

$$u(x(t + dt), t + dt) - u(x, t) = u_x \frac{dx}{dt} dt + u_t dt + o(dt^2) \quad (\text{B.26})$$

Dividing this equation by dt and taking the limit $dt \rightarrow 0$, the term $o(dt^2)$ vanishes and we get the multivariable chain rule for deterministic case:

$$\frac{dy}{dt} = u_x \frac{dx}{dt} + u_t \rightarrow dy = u_x dx + u_t dt. \quad (\text{B.27})$$

Otherwise, the Itô stochastic differential equations are written as

$$dX = F(X, t)dt + G(X, t)dW, \quad (\text{B.28})$$

and the chain rule acquires a new term as it is going to be demonstrated. At first, it is possible to verify (for proof, refer to [84, 95]) that

$$\sum_{k=0}^{m-1} (W(t_{k+1}) - W(t_k))^2 \rightarrow b - a = \sum_{k=0}^{m-1} (t_{k+1} - t_k), \quad (\text{B.29})$$

where $t_0 = a$ and $t_m = b$. This leads to the heuristic idea that

$$dW^2 \approx dt. \quad (\text{B.30})$$

Next, we suppose a twice continuously differentiable function $U : \mathcal{R} \rightarrow \mathcal{R}$ such that $Y(t) = U(X(t), t)$. Using again Taylor theorem and keeping all the terms of order less or equal to Δt and considering the idea of Eq. B.30, we get:

$$U(X(t + \Delta t), t + \Delta t) - U(X, t) = U_x \Delta X + U_t \Delta t + \frac{1}{2} U_{xx} (\Delta X)^2 + \dots \quad (\text{B.31})$$

where $U_{xx} = \frac{\partial^2 U}{\partial X^2}$. Note that the term of order $(\Delta X)^2$ was included in Eq. B.31. The reason is going to be explained ahead. Now, taking the limit when $\Delta t \rightarrow 0$, we can write $\Delta t = dt$ and $\Delta X = dX$, and substitute Eq. B.28 into Eq. B.31 to result in

$$\begin{aligned} \Delta U &= U_x dX + U_t dt + \frac{1}{2} U_{xx} (F dt + G dW)^2 + \dots \\ \Delta U &= U_x dX + U_t dt + \frac{1}{2} U_{xx} (F^2 (dt)^2 + 2FG(dt)(dW) + G^2 (dW)^2) + \dots \end{aligned} \quad (\text{B.32})$$

where $\Delta U = U(X(t + dt), t + dt) - U(X, t)$, $F = F(X, t)$ and $G = G(X, t)$ are used

to simplify the notation. Using Eq. B.30 and keeping only the terms of order less or equal to dt , we get

$$\Delta U = U_x dX + U_t dt + \frac{1}{2} U_{xx} G^2 dt + o(dt^{\frac{3}{2}}) \quad (\text{B.33})$$

Note that the term $(\Delta X)^2$ maintained in Eq. B.31 gave rise to the term $\frac{1}{2} U_{xx} G^2 dt$ which has order dt due to the relation established in Eq. B.30. Dividing Eq. B.33 by dt and taking $dt \rightarrow 0$, the terms of order higher than dt vanishes and we get the Itô formula (or Itô chain rule):

$$\frac{dU}{dt} = U_x \frac{dX}{dt} + U_t + \frac{1}{2} U_{xx} G^2 \quad (\text{B.34})$$

Now, substituting Eq. B.28 into Eq. B.34 and writing in differential form, we get the Itô chain rule in the classical form

$$dU = \left(U_x F(X, t) + U_t + \frac{1}{2} U_{xx} G^2(X, t) \right) dt + U_x G(X, t) dW \quad (\text{B.35})$$

(Itô's chain rule)

The above demonstration of Itô chain rule above omits most of the details. For the formal proof, please refer to [84].

EXAMPLE 2: Let's consider the SDE

$$dX(t) = (\alpha - X(t))dt + \beta \sqrt{X(t)} dW(t), \quad X(0) = 1, \quad (\text{B.36})$$

where α and β are positive constants. Taking a function $Y(t) = u(X(t)) = \sqrt{X(t)}$ and applying Itô's chain rule using Eq. B.35, we get

$$dY = \left(\frac{4\alpha - \beta^2}{8Y(t)} - \frac{1}{2} Y(t) \right) dt + \frac{1}{2} \beta dW \quad (\text{B.37})$$

In Fig.B.3, three plots are presented using the code in ListingB.3 written in MATLAB. The Direct solution is obtained by solving Eq. B.36 numerically by Euler-Maruyama method (explained further) and applying the square root to the results. Itô's chain rule solution is obtained by solving Eq. B.37 by the same numerical method. Finally, the deterministic chain rule solution solves Eq. B.37 but ignoring the Itô's correction term. Is noticed that Itô's chain rule solution matches direct solution very well and deterministic chain rule solution is not capable of describing the direct solution. Although deterministic chain rule solution approximates the direct solution in the beginning, the error increases with time.

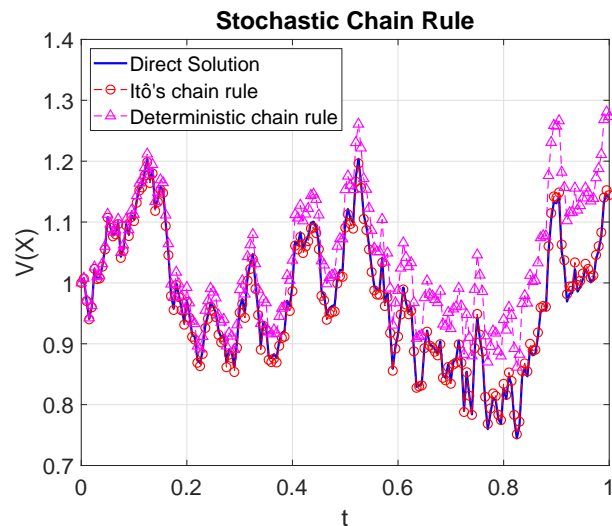


Figure B.3: Stochastic chain rule demonstration.

Listing B.3: Code to test Ito's chain rule

```

1 %% Test stochastic Chain Rule
2
3 T = 1;           % Simulation total time
4 N = 100;        % Number of time steps
5 dt = T/N;       % Time step
6
7 alpha = 2; beta = 1;           % SDE coefficients
8 Xzero = 1; Xzero2 = sqrt(Xzero); % Initial values
9
10 Xem1 = zeros(1,N); Xem2 = zeros(1,N); Xem3 = zeros(1,N);
11 Xtemp1 = Xzero; Xtemp2 = Xzero2; Xtemp3 = Xzero;
12 for j = 1:N
13 Winc = sqrt(dt)*randn; % Brownian increments
14
15 % Direct Solution
16 f1 = (alpha-Xtemp1);
17 g1 = beta*sqrt(abs(Xtemp1));
18 Xtemp1 = Xtemp1 + dt*f1 + g1*Winc;
19 Xem1(j) = Xtemp1;
20
21 % Ito's Chain Rule
22 f2 = (4*alpha-beta^2)/(8*Xtemp2) - Xtemp2/2;
23 g2 = beta/2;
24 Xtemp2 = Xtemp2 + dt*f2 + g2*Winc;
25 Xem2(j) = Xtemp2;
26
27 % Deterministic chain rule
28 f3 = (4*alpha)/(8*Xtemp2) - Xtemp2/2;

```

```

29 g3 = beta/2;
30 Xtemp3 = Xtemp3 + dt*f3 + g3*Winc;
31 Xem3(j) = Xtemp3;
32 end
33
34 figure(5)
35 plot([0:dt:T],[sqrt([Xzero,abs(Xem1)])], 'b-', [0:dt:T],...
36 [Xzero,Xem2], 'ro--', [0:dt:T],[Xzero,Xem3], 'm^--')
37 legend('Direct Solution', "Ito's Chain Rule", "Deterministic chain ...
        rule")
38 xlabel('t')
39 ylabel('V(X)')
40 grid on
41
42 % Norm of the difference between direct solution and Ito's chain rule
43 Xdiff = norm(sqrt(Xem1) - Xem2, 'inf')

```

Itô's product rule

As in chain rule, the product rule also has one additional term. To demonstrate this, we are going to study the deterministic case first. Suppose two deterministic variables $x(t)$ and $y(t)$. We are interested in determining the derivative or differential of the product between those two variables, i.e. $\frac{d(xy)}{dt}$ or $d(xy)$. To do so, let's consider the same differential equation presented in Eq. B.24 and suppose a function $u(x) = x^2$. Applying the deterministic chain rule presented in Eq. B.27 in function $u(x)$, we get

$$du = 2xdx. \quad (\text{B.38})$$

Now, we can rewrite the differential $d(xy)$ as

$$d(xy) = d\left(\frac{1}{2}((x+y)^2 - x^2 - y^2)\right) = \frac{1}{2}(d(x+y)^2 - dx^2 - dy^2). \quad (\text{B.39})$$

In the sequence, we apply Eq. B.38 to solve $d(x+y)^2$:

$$d(x+y)^2 = 2(x+y)d(x+y) = 2(x+y)(dx+dy) = 2(xdx+xdy+ydx+ydy). \quad (\text{B.40})$$

Applying Eq. B.38 on the other two terms of Eq. B.39 and substituting Eq. B.40 in Eq. B.39, we get

$$d(xy) = \frac{1}{2}(2(xdx+xdy+ydx+ydy) - 2xdx - 2ydy), \quad (\text{B.41})$$

which yields the deterministic product rule described by

$$d(xy) = xdy + ydx. \quad (\text{B.42})$$

For the stochastic case, let's consider the variable $X(t)$ and $Y(t)$ together with the stochastic differential equations

$$dZ = Fdt + GdW, \quad (\text{B.43})$$

where $Z = \{X, Y\}$, $F = \{F_1, F_2\}$ and $G = \{G_1, G_2\}$. Supposing $U(Z) = Z^2$ and applying Itô's chain rule described in Eq. B.37, we get

$$d(Z^2) = 2ZdZ + G^2dt. \quad (\text{B.44})$$

Now, we apply Eq. B.44 in the first term of Eq. B.39. To do so, we consider that $d(X + Y) = dX + dY = (F_1 + F_2)dt + (G_1 + G_2)dW$, where the diffusion coefficient G becomes $G_1 + G_2$. Therefore,

$$d(X + Y)^2 = 2(X + Y)d(X + Y) + (G_1 + G_2)^2dt. \quad (\text{B.45})$$

Next, we substitute Eq. B.45 in Eq. B.39 and apply Eq. B.44 in the last two terms of Eq. B.39 to obtain

$$\begin{aligned} d(XY) &= \frac{1}{2} (2(X + Y)d(X + Y) + (G_1 + G_2)^2dt - (2XdX + G_1^2dt) - (2YdY + G_2^2dt)) \\ &= \frac{1}{2} (2(X + Y)d(X + Y) + 2G_1G_2dt - 2XdX - 2YdY) \\ &= \frac{1}{2} (2XdX + 2YdX + 2XdY + 2YdY + 2G_1G_2dt - 2XdX - 2YdY) \\ &= \frac{1}{2} (2YdX + 2XdY + 2G_1G_2dt), \end{aligned} \quad (\text{B.46})$$

which yields the Itô's product rule as described below:

$$d(XY) = XdY + YdX + G_1G_2dt \quad (\text{Itô's product rule}). \quad (\text{B.47})$$

EXAMPLE 3: Consider the following SDE for $i = 1, 2$,

$$dX_i = \lambda_i X_i dt + \mu_i X_i dW, \quad X(0) = X_0 \quad (\text{B.48})$$

where λ_i and μ_i are positive constants. Now, suppose one would like to calculate the product $X_1 X_2$ with parameters $X_0 = 1$, $\lambda_1 = 2$, $\mu_1 = 1$, $\lambda_2 = 3$ and $\mu_2 = 1.5$. Applying Eq. B.47 to obtain the product $X_1 X_2$, we get:

$$\begin{aligned}
d(X_1X_2) &= X_2dX_1 + X_1dX_2 + G_1G_2dt \\
&= X_2(\lambda_1X_1dt + \mu_1X_1dW) + X_1(\lambda_2X_2dt + \mu_2X_2dW) + (\mu_1\mu_2)dt \quad (\text{B.49}) \\
&= (\lambda_1 + \lambda_2 + \mu_1\mu_2)X_1X_2dt + (\mu_1 + \mu_2)X_1X_2dW.
\end{aligned}$$

If we substitute X_1X_2 by X_3 , Eq. B.49 turns out to be the same type of Eq. B.48 with $i = 3$, $\lambda_3 = \lambda_1 + \lambda_2 + \mu_1\mu_2$ and $\mu_3 = \mu_1 + \mu_2$.

In Fig. B.4a, both X_1 and X_2 are plotted against time. The solutions for X_1 and X_2 are obtained by analytically solving Eq. B.48 using the technique presented in section B.3.1, which results in $X_i = X_0 \exp((\lambda_i - \frac{1}{2}\mu^2)t + \mu_iW)$. In Fig. B.4b, again three plots are shown: the direct solution, that is obtained by simply multiplying X_1 and X_2 ; the Itô's product rule solution, which is obtained by solving Eq. B.49 analytically in the same way as for Eq. B.48 considering $Z = X_1X_2$; and the deterministic product rule solution that ignores the Itô correction term G_1G_2dt in Eq. B.47. The difference between the solutions indicates that the use of deterministic product rule is not correct. The results of Fig. B.4 were simulated using the code in Listing B.4 written in MATLAB.

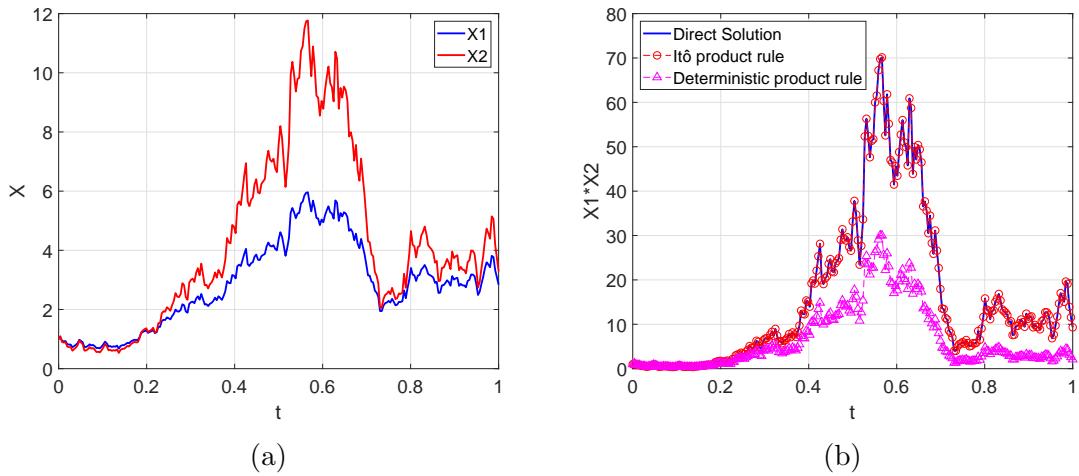


Figure B.4: (a) Simulation of X_1 ($\lambda_1 = 2$; $\mu_1 = 1$) and X_2 ($\lambda_2 = 3$; $\mu_2 = 1.5$). (b) Solutions for X_1X_2

Listing B.4: Code to test Ito's product rule

```

1 %% Test Ito Product Rule
2
3 T = 1;           % Simulation total time
4 N = 2^8;        % Number of time steps
5 dt = T/N;       % Time step
6 Xzero = 1;      % Initial value

```

```

7
8 dW = sqrt(dt)*randn(1,N); % Brownian motion increments
9 W = cumsum(dW); % Construct Brownian motion ...
    (cumulative sum)
10
11 % Approximate X_1
12 lambda1 = 2; mu1 = 1; % SDE coefficients
13 XTrue1 = [Xzero Xzero*exp((lambda1-0.5*mu1^2)*([dt:dt:T])+mu1*W)];
14
15 % Approximate X_2
16 lambda2 = 3; mu2 = 1.5; % SDE coefficients
17 XTrue2 = [Xzero Xzero*exp((lambda2-0.5*mu2^2)*([dt:dt:T])+mu2*W)];
18
19 % Solve X_1*X_2 by Ito chain rule
20 lambda = lambda1 + lambda2 + mu1*mu2; mu = mu1 + mu2; % SDE ...
    coefficients
21 XTrue3 = [Xzero Xzero*exp((lambda-0.5*mu^2)*([dt:dt:T])+mu*W)];
22
23 % Solve X_1*X_2 by deterministic chain rule
24 lambda = lambda1 + lambda2; mu = mu1 + mu2; % SDE coefficients
25 XTrue4 = [Xzero Xzero*exp((lambda-0.5*mu^2)*([dt:dt:T])+mu*W)];
26
27 figure(6) % Plot X_1 and X_2
28 plot([0:dt:T],XTrue1,'b-',[0:dt:T],XTrue2,'r-')
29 legend('X1','X2')
30 xlabel('t')
31 ylabel('X')
32 grid on
33
34 figure(7) % Plot solutions for X_1*X_2
35 plot([0:dt:T],XTrue1.*XTrue2,'b-',t3,XTrue3,'ro--',t4,XTrue4,'m^--')
36 xlabel('t')
37 ylabel('X1*X2')
38 grid on
39 legend('Direct Solution','Ito product rule','Deterministic ...
    product rule')

```

Itô's integration by parts

The integration by parts of stochastic variables also includes an extra correction term. Let's begin with the deterministic case: if we integrate the product rule in Eq.B.42, we obtain

$$\int_s^r d(xy) = x(r)y(r) - x(s)y(s) = \int_s^r (xdy + ydx). \quad (\text{B.50})$$

Reordering the equation above, we get the deterministic integration by parts

described by

$$\int_s^r xdy = x(r)y(r) - x(s)y(s) - \int_s^r ydx. \quad (\text{B.51})$$

In the stochastic case, we integrate Itô's product rule (Eq. B.47) to obtain the Itô's integration by parts:

$$\int_s^r X_2dX_1 = X_1(r)X_2(r) - X_1(s)X_2(s) - \int_s^r X_1dX_2 - \int_s^r G_1G_2dt \quad (\text{B.52})$$

(Itô's integration by parts)

If G_1 or G_2 is zero, Eq. B.52 returns to deterministic product rule. Note that if $G_2 = 0$ and $X_2(0) = X_2(T) = 0$, Paley-Wiener-Zygmund definition described in Eq. B.11 is recovered.

B.3 Stochastic Differential Equations

Consider a m-dimensional Brownian motion $\mathbf{W} = [W_1(t), W_2(t), \dots, W_m(t)]^T$ and a n-dimensional random variable \mathbf{X}_0 . Also, for $t > 0$, consider the functions $b : \mathcal{R}^n \times [0, T] \rightarrow \mathcal{R}$ and $B : \mathcal{R}^n \times [0, T] \rightarrow \mathcal{M}^{n \times m}$. These functions can also be expressed as

$$b = (b^1, b^2, b^3, \dots, b^n) \quad , \quad [B] = \begin{bmatrix} b^{11} & \dots & b^{1m} \\ \vdots & \ddots & \vdots \\ b^{n1} & \dots & b^{nm} \end{bmatrix} \quad (\text{B.53})$$

Therefore, we can define a n-dimensional stochastic process $\mathbf{X}(t)$ that is the solution of the following stochastic differential equation:

$$\begin{cases} d\mathbf{X}(t) = \mathbf{b}(\mathbf{X}, t)dt + [B(\mathbf{X}, t)]d\mathbf{W} \\ \mathbf{X}(0) = \mathbf{x}_0 \end{cases} \quad , \quad (\text{B.54})$$

In case of differential equation in higher orders, the representation in state space can be used:

$$\mathbf{X}(t) = \begin{bmatrix} Y(t) \\ Y^{(1)}(t) \\ \vdots \\ Y^{(n-1)}(t) \end{bmatrix} = \begin{bmatrix} X_1(t) \\ X_2(t) \\ \vdots \\ X_n(t) \end{bmatrix} \quad , \quad (\text{B.55})$$

where $Y^{(i)}$ is the i-th derivative of Y. This way, the stochastic differential equation

becomes:

$$d\mathbf{X}(t) = \begin{bmatrix} X_2(t) \\ \vdots \\ X_n(t) \\ b(\mathbf{X}, t) \end{bmatrix} dt + \begin{bmatrix} 0 \\ \vdots \\ 0 \\ B(\mathbf{X}, t) \end{bmatrix} d\mathbf{W} \quad (\text{B.56})$$

Note that the equation above were developed for a higher order stochastic differential equation with a 1-D stochastic process $Y(t)$. If a stochastic process with a higher dimension is considered, it must be included in vector $\mathbf{X}(t)$ as usual in state space representation.

B.3.1 Solutions of SDE

A stochastic differential equation can be solved either numerically or analytically. Stochastic differential equations do not have as many analytical solutions as deterministic differential equations. The most common analytical and numerical strategies are going to be presented further, but first, we have to establish the following theorem of existence and uniqueness for stochastic differential equations.

THEOREM: For $T > 0$, let $b : \mathcal{R}^n \times [0, T] \rightarrow \mathcal{R}$ and $B : \mathcal{R}^n \times [0, T] \rightarrow \mathcal{M}^{n \times m}$ be measurable functions such that

$$|\mathbf{b}(\mathbf{X}, t)| + |[B(\mathbf{X}, t)]| \leq C(1 + |\mathbf{X}|), \quad \mathbf{X} \in \mathcal{R}^n, t \in [0, T] \quad (\text{B.57})$$

for some constant C, (where $|[B]| = \sqrt{\sum |[B]_{ij}|^2}$ and $|\mathbf{b}| = \sqrt{\sum |\mathbf{b}_i|^2}$) and

$$|\mathbf{b}(\mathbf{X}, t) - \mathbf{b}(\mathbf{Y}, t)| + |[B(\mathbf{X}, t)] - [B(\mathbf{Y}, t)]| \leq D|\mathbf{X} - \mathbf{Y}|, \quad \mathbf{X}, \mathbf{Y} \in \mathcal{R}^n, t \in [0, T] \quad (\text{B.58})$$

for some constant D. Also, let $\mathbf{X}_0 \in \mathcal{R}^n$ be a random variable such that $E(|\mathbf{X}_0|^2) \leq \infty$ and \mathbf{X}_0 is independent of $\mathcal{W}^+(0)$. Then the stochastic differential equation

$$\begin{cases} d\mathbf{X}(t) = \mathbf{b}(\mathbf{X}, t)dt + [B(\mathbf{X}, t)]d\mathbf{W} \\ \mathbf{X}(0) = \mathbf{X}_0 \end{cases}, \quad (\text{B.59})$$

has a unique t-continuous solution $X(t)$ with the property that

$$E \left[\int_0^T |X_t|^2 dt < \infty \right]. \quad (\text{B.60})$$

For more details, properties and proofs, refer to [84, 95].

Application of Eq. (B.57): In order to illustrate this theorem, consider the deterministic equation

$$dx = x^2 dt, \quad x_0 = 0, \quad (\text{B.61})$$

in which $b(x) = x^2$. This ODE has the unique solution

$$x = \frac{1}{1-t}, \quad x(0) = 0, 0 \leq t < 1.$$

Note that X explodes if $t = 1$. This equation does not satisfy Eq. B.57 and thus it is not possible to find a solution X for all t . Therefore, Eq. B.57 assures that the solution does not tend to ∞ in a finite time.

Application of Eq. (B.58): Now, consider the equation

$$dx = 3x^{2/3} dt, \quad x(0) = 0. \quad (\text{B.62})$$

This equation has more than one solution. Then, supposing a a positive constant, the function

$$x = \begin{cases} 0 & \text{for } t \leq a \\ (t-a)^3 & \text{for } t > a \end{cases}$$

solves Eq. B.62 for any $a > 0$. In this case, $b = 3x^{2/3}$ do not satisfy Eq. B.58. To prove this, we calculate the left side of Eq. B.58 as

$$\begin{aligned} |b(x_1, t) - b(x_2, t)| &= |x_1^{2/3} - x_2^{2/3}| \\ &= \frac{|x_1^{1/3} + x_2^{1/3}|}{|x_1^{2/3} + x_1^{1/3}x_2^{1/3} + x_2^{2/3}|} |x_1 - x_2|, \end{aligned}$$

and set x_2 to zero to obtain

$$|b(x_1, t) - b(0, t)| = \frac{1}{|x_1^{1/3}|} |x_1|.$$

It can be noticed that when x_1 approaches zero, the coefficient $\frac{1}{|x_1^{1/3}|}$ goes to ∞ and Eq. B.58 is not valid for a finite constant D near $x = 0$. As the solution is not unique, we conclude that Eq. B.58 is related to the uniqueness of solution.

Analytical solutions

One method to obtain the solution of many stochastic differential equations is by using the Itô Formula. This method consists on eliminating the dependence of $X(t)$ on the right side of the equation by a change of variables. The next examples will demonstrate this technique.

EXAMPLE 4: Let us consider again the SDE introduced in Eq. B.5 about population growth and set $r(t)$ as constant. Rewriting this equation, we can obtain:

$$dX = rXdt + \alpha XdW \rightarrow \frac{dX}{X} = rdt + \alpha dW \quad (\text{B.63})$$

Integrating the above equation, we obtain

$$\int_0^t \frac{dX}{X} = rt + \alpha W. \quad (\text{B.64})$$

To solve this equation, we have to solve the remaining integral. To do so, we choose a function $g(t, x)$ in a smart way in order to remove the dependence on X in the integrand by using Itô formula (Eq. B.35). Therefore, in this case, the function $g(t, X) = \ln X$ for $X > 0$ is used to obtain, through Eq. B.35,

$$d(\ln X) = \frac{1}{X}dX + \frac{1}{2}\left(-\frac{1}{X^2}\right)(\alpha X)^2dt = \frac{1}{X}dX - \frac{1}{2}\alpha^2dt. \quad (\text{B.65})$$

Note that $\frac{dN_t}{N_t}$ can now be written in function of two terms whose integrand doesn't depend on X. Now, substituting $\frac{dN_t}{N_t}$ in Eq. B.64 by the result above and integrating from 0 to t, we obtain

$$\ln \frac{X(t)}{X_0} = (r - \frac{1}{2}\alpha^2)t + \alpha W(t), \quad (\text{B.66})$$

or

$$X(t) = X_0 \exp\left((r - \frac{1}{2}\alpha^2)t + \alpha W(t)\right), \quad (\text{B.67})$$

that is the solution. The expected value of this solution can be calculated, but the difficulty relies on the calculation of $E[X_0 \exp(\alpha W)]$. Supposing that X_0 and W are independent, the problem is concentrated on calculating $E[e^{\alpha W}]$. To do so, we used Itô formula again to try to rewrite this expression. Assuming a function $Y = U(Z) = e^Z$ where $Z = \alpha W$ and thus $dZ = \alpha dW$, we apply Itô formula (Eq. B.35) to obtain

$$dY = \alpha e^{\alpha W} dW + \frac{1}{2}\alpha^2 e^{\alpha W} dt, \quad (\text{B.68})$$

which can be integrated as

$$Y_t = Y_0 + \alpha \int_0^t e^{\alpha W} dW + \frac{1}{2}\alpha^2 \int_0^t e^{\alpha W} dt. \quad (\text{B.69})$$

Next, we can calculate the expected value of both sides and use the Itô's property that $E[\int_0^t GdW] = 0$ to obtain

$$E[Y_t] = E[Y_0] = \frac{1}{2}\alpha^2 E[Y_t], \quad E[Y_0] = 1. \quad (\text{B.70})$$

Taking the time derivative of the above equation, it is possible to find that

$E[Y_t] = e^{\frac{1}{2}\alpha^2 t}$ and, therefore, we obtain

$$E[N_t] = E[N_0]e^{rt}. \quad (\text{B.71})$$

EXAMPLE 5: Consider the following SDE that describes the charge $Q(t)$ at time t at a point in an electric circuit:

$$LQ''(t) + RQ'(t) + \frac{1}{C}Q(t) = F(t), \quad Q(0) = Q_0, Q'(0) = I_0, \quad (\text{B.72})$$

where L is inductance, R is resistance, C is capacitance and $F(t)$ is the potential source at time t . Now, consider the potential source is actually a stochastic process such as $F(t) = G(t) + \alpha\xi$, where $G(t)$ is a deterministic function, α is a positive constant and ξ is a white noise. Rewriting Eq. B.72 using state space representation and introducing the vector $\mathbf{X}_t = (X_1, X_2)^T = (Q_t, Q'_t)^T$, we get

$$\begin{cases} X_1' &= X_2 \\ LX_2' &= -RX_2 - \frac{1}{C}X_1 + G_t + \alpha W_t, \end{cases} \quad (\text{B.73})$$

or, in matrix notation,

$$d\mathbf{X}_t = [A]\mathbf{X}_t dt + \mathbf{H}_t dt + \mathbf{K} dW_t, \quad (\text{B.74})$$

where

$$d\mathbf{X}_t = \begin{bmatrix} dX_1 \\ dX_2 \end{bmatrix}, \quad [A] = \begin{bmatrix} 0 & 1 \\ -\frac{1}{CL} & -\frac{R}{L} \end{bmatrix}, \quad \mathbf{H}_t = \begin{bmatrix} 0 \\ \frac{1}{L}G_t \end{bmatrix}, \quad \mathbf{K} = \begin{bmatrix} 0 \\ \frac{\alpha}{L} \end{bmatrix}. \quad (\text{B.75})$$

Thus, the second order system in Eq. B.72 is represented as a 2-dimensional stochastic differential equation. Now, let us pre-multiply the Eq. B.74 by $\exp(-[A]t)$ to get

$$\exp(-[A]t)d\mathbf{X}_t - \exp(-[A]t)[A]\mathbf{X}_t dt = \exp(-[A]t) [\mathbf{H}_t dt + \mathbf{K} dW_t]. \quad (\text{B.76})$$

Note that we are taking the exponential out of a matrix here (for details, see [97]). To solve this, we use again Itô formula (Eq. B.35) in the function $u = \exp(-[A]t)\mathbf{X}_t$ to obtain

$$d(\exp(-[A]t)\mathbf{X}_t) = (-[A]) \exp(-[A]t)\mathbf{X}_t dt + \exp(-[A]t)d\mathbf{X}_t. \quad (\text{B.77})$$

Substituting Eq. B.77 into Eq. B.76 and integrating from 0 to t , we get

$$\exp(-[A]t)\mathbf{X}_t - \mathbf{X}_0 = \int_0^t \exp(-[A]s)\mathbf{H}_s ds + \int_0^t \exp(-[A]s)\mathbf{K} dW_s. \quad (\text{B.78})$$

Finally, using integration by parts in the term $\int_0^t \exp(-[A]t) \mathbf{K} dW_t$, the solution becomes

$$\mathbf{X}(t) = \exp([A]t) \left[\mathbf{X}_0 + \exp(-[A]t) \mathbf{K} W_t + \int_0^t \exp(-[A]s) [\mathbf{H}(s) + [A] \mathbf{K} W_s] ds \right]. \quad (\text{B.79})$$

Numerical solutions

Only a few SDE can be solved analytically using the techniques discussed in this work. Thus, numerical methods are demanded in order to approximate these equations numerically. This way, the solution $X(t)$ is interpreted as the random variable that arises when the time step goes to zero. The numerical methods consist of discretizing the time intervals and approximate the continuous solution $X(t_j)$ by the discrete solution X_j . One of the simplest time discrete approximations is the Euler-Maruyama approximation.

Let us consider the following 1-dimensional SDE in differential form:

$$dX = F(X, t)dt + G(X, t)dW, \quad X(0) = X_0, \quad 0 \leq t \leq T. \quad (\text{B.80})$$

For a given time discretization $0 = t_0 < t_1 < \dots < t_j < \dots < t_N = T$ of time interval $[0, T]$, the Euler-Maruyama method (EM) takes the form

$$X_j = X_{j-1} + F(X_{j-1}, t_{j-1})\Delta t + G(X_{j-1}, t_{j-1})\Delta W, \quad j = 1, 2, \dots, N \quad (\text{B.81})$$

where $\Delta t = t_j - t_{j-1}$ is the time increment and $\Delta W = W_j - W_{j-1}$ is the Brownian motion increment such that $\Delta W \rightarrow N(0, \delta t)$. Note that the discretization presented in Eq. B.81 assumes Ito interpretation because the functions $F(X, t)$ and $G(X, t)$ are evaluated at t_{j-1} over the interval $[t_{j-1}, t_j]$. To demonstrate the EM method, consider the following example.

EXAMPLE 6: Consider the same linear stochastic differential equation used in example 3:

$$dX = \lambda X dt + \mu X dW, \quad X(0) = X_0, \quad (\text{B.82})$$

which the solution is expressed as $X(t) = X_0 \exp((\lambda - \frac{1}{2}\mu^2)t + \mu W)$. In Fig. B.5, the approximated solution by EM method is plotted together with the analytical solution using the code in Listing B.5 together with the functions in the Listings B.6 and B.7. There was used 258 time increments for the analytical solution and 64 increments for EM approximation. It is noticed that the numerical solution tends to the solutions obtained by the analytical method.

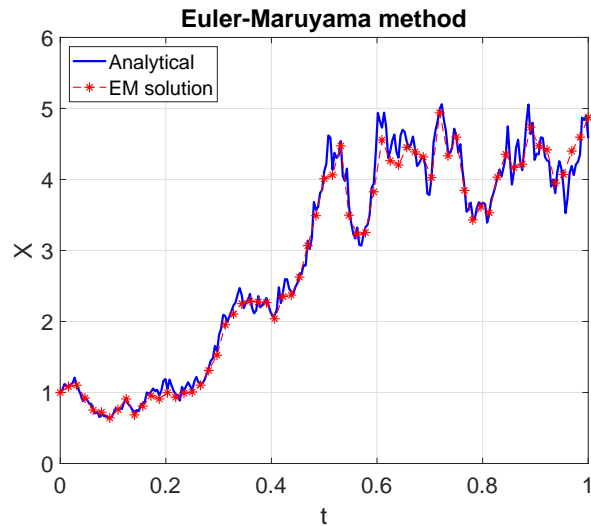


Figure B.5: Euler-Maruyama method demonstration.

Listing B.5: Code to simulate of Euler-Maruyama method

```

1 %% Euler-Maruyama Method
2
3 T = 1;           % Simulation total time
4 N = 2^8;        % Number of time steps
5 dt = T/N;      % Time step
6 Xzero = 1;     % Initial value
7 lambda = 2; mu = 1; % SDE coefficients
8
9 dW = sqrt(dt)*randn(1,N); % Brownian motion increments
10 W = cumsum(dW); % Construct Brownian motion ...
    (cumulative sum)
11
12 % Analytical Solution
13 XTrue1 = [Xzero Xzero*exp((lambda-0.5*mu^2)*([dt:dt:T])+mu*W)];
14
15 % Numerical Solution
16 R = 4; Dt = R*dt; % EM steps of size Dt = R*dt
17 dW2 = sum(reshape(dW,R,[],1),1); % Reshape Brownian Motion to ...
    Dt = R*dt
18 [t1,Xem1] = sde_em(@(t,y,dW,dt)em_test(t,y,dW,Dt,[lambda mu]),...
19 0:Dt:T,Xzero,dW2); % Solve using Euler-Maruyama
20
21 figure(8)
22 plot([0:dt:T],XTrue1,'b-',[0:Dt:T],Xem1,'r*--')
23 legend('Analytical','EM solution')
24 xlabel('t')
25 ylabel('X')
26 grid on

```

```
27 title('Euler-Maruyama method')
```

Listing B.6: Function sde_em

```
1 function [t,y] = sde_em(fun,t,y0,dW)
2 % Solves stochastic differential equations by using Euler-Maruyama
3 % approximation.
4 % dY = fun(t,y,dW,dt) = F dt + G dW
5
6 y = zeros(length(y0),length(t)); % Preallocate in memory
7
8 y(:,1) = y0; % Initial value
9 for i = 2:length(t)
10 dt = t(i) - t(i-1); % time step
11 y(:,i) = y(:,i-1) + fun(t(i-1),y(:,i-1),dW(:,i-1),dt);
12 end
13
14 y = y';
15 t = t';
```

Listing B.7: Function em_test

```
1 function dy = em_test(t,y,Winc,dt,par)
2 % Function to describe the stochastic differential equation
3 % dY = lambda X dt + mu X dW
4
5 lambda = par(1); mu = par(2); % SDE coefficients
6 dy = dt*lambda*y + mu*y.*Winc;
```

Next, we need a criterion to judge whether a time discrete approximation is accurate or not. Basically, there are two types of objects related to the solution of stochastic differential equations. The first consists of the pathwise approximation and is related to the strong convergence of numerical methods. The second one focus on approximating the expectations of functionals of the Ito process, such as its probability function and moments. This is very relevant because, in many problems, the functionals cannot be determined explicitly. The second objective is related to the weak convergence of the method.

The strong convergence (i.e. pathwise approximation) is evaluated by assessing how EM solution matches the true solution (i.e. analytical solution) by taking the expected value of the difference between the two solutions. Keeping in mind that $X(t_j)$ is the true solution and X_j is the approximated solution, a method is said to

converge strongly with order $\gamma > 0$ at time T if there exists a constant C such that

$$E[|X_N - X(T)|] \leq C\Delta t^\gamma \quad (\text{B.83})$$

The weak convergence (i.e. approximation of expectations) says how the expectation of approximated method approaches the expectation of the true solution. It is calculated taking the difference between the two expectations, thus

$$|E[p(X_j)] - E[p(X(t_j))]| \leq C\Delta t^\gamma. \quad (\text{B.84})$$

Taking p as the identity function and calculating the convergence at the end point T , we get

$$|E[X_N] - E[X(T)]| \leq C\Delta t^\gamma. \quad (\text{B.85})$$

In Fig. B.6, the strong and weak convergences are plotted in log-log scale for the SDE considered in example 6 using the codes in Listings B.8 and B.9. For the strong convergence, 1000 simulations were performed for each time step size. The expectation was calculated as a sample average and the red line represents a linear curve with an inclination of $-\frac{1}{2}$, showing that the strong order of convergence is $\gamma = \frac{1}{2}$ for EM method. In the case of weak convergence, 5000 simulations were performed for each time step size. The expected value for the true solution at time T can be calculated and it is equal to $\exp(\lambda T)$. The difference on the average value at time T for EM simulations and the true solution was calculated and the weak order of convergence is found to be $\gamma = 1$, following the inclination of the second red line.

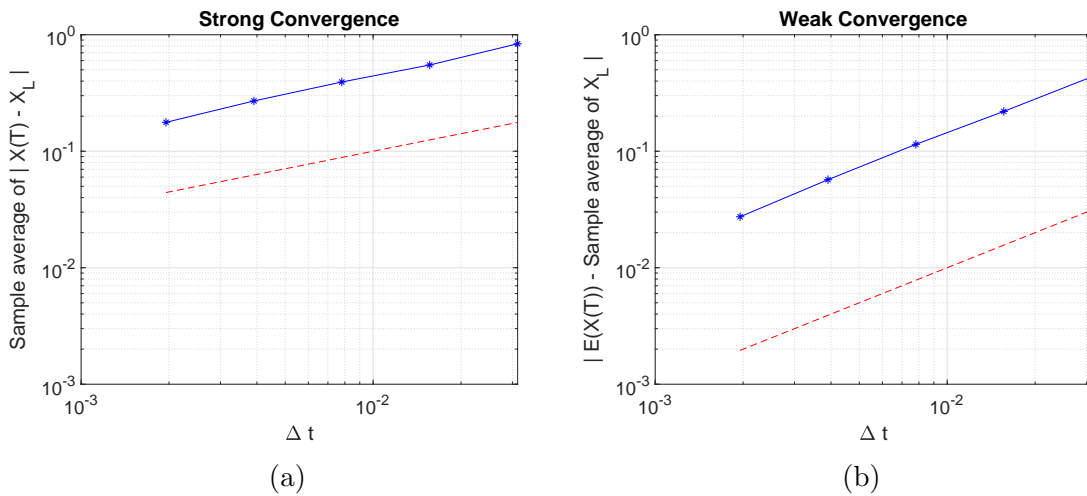


Figure B.6: (a) Strong and (b) weak convergence of EM method.

Listing B.8: Code to test strong convergence of EM method.

```

1 %% Test Strong convergence of Euler-Maruyama
2
3 T = 1; % Simulation total time
4 N = 2^9; % Number of time steps
5 dt = T/N; % Time step
6 Xzero = 1; % Initial value
7 lambda = 2; mu = 1; % SDE coefficients
8
9 M = 1000; % number of paths sampled
10 dW = sqrt(dt)*randn(M,N); % Brownian motion increments
11 W = cumsum(dW,2); % Construct Brownian motion ...
    (cumulative sum)
12
13 % True Solution
14 Xtrue = ...
    Xzero*ones(M,1).*exp((lambda-0.5*mu^2)*ones(M,1)+mu*W(:,end));
15
16 % Numerical Solution
17 Xerr = zeros(M,5); % preallocate memory
18 for p = 1:5
19 R = 2^(p-1); Dt = R*dt; L = N/R; % L Euler steps of size Dt ...
    = R*dt
20
21 % Reshape dW to size Dt = R*dt
22 dW2 = zeros(M,N/R);
23 for i = 1:M
24 dW2(i,:) = sum(reshape(dW(i,:),R,[],1));
25 end
26
27 % Solve using EM
28 [t2,Xtemp] = sde_em(@(t,y,dW,dt)em_test(t,y,dW,dt,[lambda mu]),...
29 0:Dt:T,Xzero*ones(M,1),dW2);
30 Xerr(:,p) = abs(Xtemp(end,:) - Xtrue); % Store the error at t ...
    = T
31 end
32
33
34 Dtvals = dt*(2.^([0:4]));
35 figure(9)
36 loglog(Dtvals,mean(Xerr),'b*-'), hold on
37 loglog(Dtvals,(Dtvals.^(.5)),'r--'), hold off % reference slope ...
    of 1/2
38 xlabel('\Delta t'), ylabel('Sample average of | X(T) - X.L |')
39 title('emstrong.m','FontSize',10)
40
41 %%% Least squares fit of error = C * Dt^q %%%

```



```

42 A = [ones(5,1), log(Dtvals)']; rhs = log(mean(Xerr)');
43 sol = A\rhs; q = sol(2)
44 resid = norm(A*sol - rhs)

```

Listing B.9: Code to test weak convergence of EM method.

```

1 %% Test Weak convergence of Euler-Maruyama
2
3 T = 1; % Simulation total time
4 Xzero = 1; % Initial value
5 lambda = 2; mu = 0.11; % SDE coefficients
6
7 M = 50000; % number of paths sampled per time step size Dt
8
9 Xem = zeros(5,1); % Preallocate memory
10 for p = 1:5
11 Dt = 2^(p-10); % Time step
12 L = T/Dt; % Number of time steps
13 Winc = sqrt(Dt)*randn(M,L); % Brownian motion increments
14
15 % Solve using EM
16 [t,Xtemp] = sde_em(@(t,y,dW,dt)em_test(t,y,dW,dt,[lambda mu]),...
17 0:Dt:T,Xzero*ones(M,1),Winc);
18 Xem(p) = mean(Xtemp(end,:)); %Calculate the mean value at t=T
19 end
20
21 % Evaluate the error at t=T
22 % exp(lambda*T) is the deterministic solution
23 Xerr = abs(Xem - exp(lambda*T));
24
25 Dtvals = 2.^([1:5]-10);
26 figure (10)
27 loglog(Dtvals,Xerr,'b*-'), hold on
28 loglog(Dtvals,Dtvals,'r--'), hold off % reference slope of 1
29 xlabel('\Delta t'), ylabel('| E(X(T)) - Sample average of X.L |')
30 title('emweak.m','FontSize',10)
31
32 %%% Least squares fit of error = C * dt^q %%%
33 A = [ones(p,1), log(Dtvals)']; rhs = log(Xerr);
34 sol = A\rhs; q = sol(2)
35 resid = norm(A*sol - rhs)

```

B.3.2 Applications of SDE

In the following, several examples of stochastic differential equations are presented. Here, it is not intended to present the solution procedure but it follows the technique presented in the subsection about analytical solutions. The objectives of this subsection are to present several types of stochastic processes that can be generated by using Itô stochastic differential equations and discuss their characteristics.

EXAMPLE 7: Let $m = n = 1$ and suppose g is a continuous function. The only solution of the SDE

$$dX = gXdW, \quad X(0) = 1$$

is

$$X(t) = \exp\left(-\frac{1}{2} \int_0^t g^2 ds + \int_0^t g dW\right) \quad (\text{B.86})$$

To prove this, we can set $Y(t) = -\frac{1}{2} \int_0^t g^2 ds + \int_0^t g dW$ and take the derivative to obtain $dY = -\frac{1}{2}g^2 dt + g dW$. Then, we apply the Itô's chain rule for $X = u(Y) = \exp(Y)$ to obtain

$$\begin{aligned} dX &= u' dY + \frac{1}{2} u'' g^2 dt \\ &= e^Y \left(\frac{1}{2} g^2 dt + g dW + \frac{1}{2} g^2 dt \right) \\ &= gX dW \end{aligned}$$

EXAMPLE 8: The solution of the SDE

$$\begin{cases} dB = \frac{-B}{T-t} dt + dW \\ B(0) = 0 \end{cases} \quad (0 \leq t \leq T),$$

is

$$B(t) = (T-t) \int_0^t \frac{1}{T-s} dW$$

Note that $\lim_{t \rightarrow 1^-} B(t) = 0$. The solution $B(t)$ is called Brownian bridge between times 0 and T . The expected value is zero, with variance $\frac{t(T-t)}{T}$ and the covariance of $B(s)$ and $B(t)$ is $\frac{s(T-t)}{T}$ for $s < t$. The increments on a Brownian Bridge are not independent

This stochastic process is often used when there is already a generated Wiener process path and we want to interpolate between two already generated points. This way we have to assure that interpolation assumes the values of the already generated points at the ends. A sample path of a Brownian Bridge is shown in Fig. B.7 for $T = 1$.

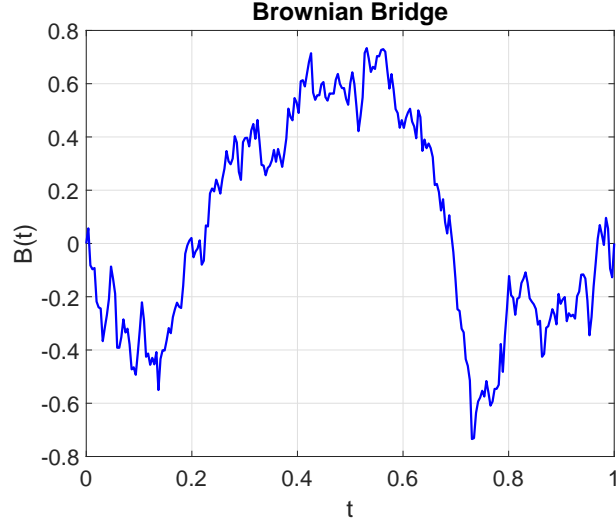


Figure B.7: One sample path of a Brownian Bridge.

EXAMPLE 9: It is possible to model viscous friction forces considering uncertainties through the SDE

$$\dot{X} = -bX(t) + \sigma\xi(t)$$

where ξ is a white noise, $b > 0$ is the friction coefficient and σ is the diffusion coefficient. This equation can be rewritten as

$$\begin{cases} dX = -bXdt + \sigma dW \\ X(0) = X_0 \end{cases}$$

where X_0 can be a random variable independent of Brownian motion. This equation is called the Langevin's equation. $X(t)$ is interpreted as the velocity of a Brownian particle. The solution of this equation is

$$X(t) = e^{-bt}X_0 + \sigma \int_0^t e^{-b(t-s)}dW, \quad (t \geq 0)$$

It is possible to calculate the first and second moment of $X(t)$. To do this, the properties of stochastic integrals are used.

$$E(X(t)) = e^{-bt}E(X_0)$$

$$\begin{aligned} E(X^2(t)) &= E\left(e^{-2bt}X_0^2 + 2\sigma e^{-bt}X_0 \int_0^t e^{-b(t-s)}dW + \sigma^2 \left(\int_0^t e^{-b(t-s)}dW\right)^2\right) \\ &= e^{-2bt}E(X_0^2) + 2\sigma e^{-bt}E(X_0)E\left(\int_0^t e^{-b(t-s)}dW\right) + \sigma^2 \int_0^t e^{-2b(t-s)}ds \\ &= e^{-2bt}E(X_0^2) + \frac{\sigma^2}{2b}(1 - e^{-2bt}) \end{aligned}$$

From this, we obtain the variance:

$$\begin{aligned} V(X(t)) &= E(X^2(t)) - (E(X(t)))^2 \\ &= e^{-2bt}V(X_0) + \frac{\sigma^2}{2b}(1 - e^{-2bt}) \end{aligned}$$

Note that when $t \rightarrow \infty$, the variable $X(t)$ tends to a distribution $N(0, \frac{\sigma^2}{2b})$. It means that, independent of the initial distribution of X_0 , the solution of this SDE goes to zero and varies around this as a result of the balance between disturbing force ($\sigma\xi$) and damping force ($-bX(t)$). One sample path of $X(t)$ is shown in Fig. B.8 for $b = 2$ and $\sigma = 0.4$.

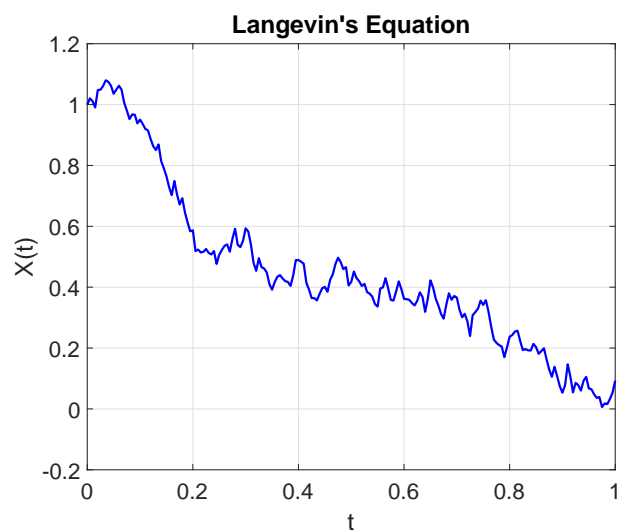


Figure B.8: One sample path of Langevin's equation.

Appendix C

Scalar linear stochastic differential equations

The stochastic differential equations can be classified into two large groups: linear SDEs and nonlinear SDEs. Furthermore, they are also distinguished between scalar and vectorial SDEs. This appendix is devoted to discussing a very particular group of SDEs: scalar linear SDEs. The stochastic processes generated in this work are classified into this category. A scalar linear SDE can be written as [85]:

$$dX = (A(t)X(t) + a(t)) dt + \sum_{i=1}^N (B_i(t)X(t) + b_i(t)) dW_i(t) , \quad (\text{C.1})$$

where $A(t)$, $a(t)$, $B_i(t)$ and $b_i(t) \in \mathbb{R}$; $W_i(t) \in \mathbb{R}$ is a Brownian motion, and; $X(0) = x_0$. The solution of linear SDEs like Eq. C.1 is well established in literature as [85]:

$$X(t) = \Phi(t) \left(x_0 + \int_0^t \Phi^{-1}(s) \left[a(s) - \sum_{i=1}^N B_i(s)b_i(s) \right] ds + \sum_{i=1}^N \int_0^t \Phi^{-1}(s) b_i(s) dW_i(s) \right) , \quad (\text{C.2})$$

where $\Phi(t)$ is the fundamental matrix defined by

$$\Phi(t) = \exp \left(\int_0^t \left[A(s) - \sum_{i=1}^N \frac{B_i^2(s)}{2} \right] ds + \sum_{i=1}^N \int_0^t B_i(s) dW_i(s) \right) , \quad (\text{C.3})$$

There are sometimes that $A(s)$, $a(s)$, $B_i(s)$ and $b_i(s)$ are complicated functions and the integrals in Eq. C.2 become very difficult to calculate analytically. Thus, the calculation of the moments from the solution is compromised. In order to circumvent this, the expectation $m(t) = \mathbb{E}[X(t)]$ and second moment $P(t) = \mathbb{E}[X^2(t)]$ can be calculated directly from differential equation. Taking the expectation on both sides of Eq. C.1 and considering that $X(t)$ and $dW(t)$ are independent, we obtain:

$$\begin{aligned}\mathbb{E}[dX(t)] &= \mathbb{E} \left[(A(t)X(t) + a(t)) dt + \sum_{i=1}^N (B_i(t)X(t) + b_i(t)) dW_i(t) \right], \\ \mathbb{E}[dX(t)] &= dm(t) = (A(t)\mathbb{E}[X(t)] + a(t)) dt \\ &\quad + \sum_{i=1}^N \mathbb{E}[(B_i(t)X(t) + b_i(t)) \mathbb{E}[dW_i(t)]] \overset{0}{},\end{aligned}$$

which leads to the following ODE describing the expectation of $X(t)$:

$$dm(t) = (A(t)m(t) + a(t)) dt. \quad (\text{C.4})$$

In order to calculate the second moment, we define a new variable $Y(t) = X^2(t)$ and apply Itô's chain rule (Eq. B.35) to obtain the following SDE:

$$\begin{aligned}dY(t) &= \left[2X(t)(A(t)X(t) + a(t)) + \sum_{i=1}^N (B_i(t)X(t) + b_i(t))^2 \right] dt \\ &\quad + 2X(t) \sum_{i=1}^N (B_i(t)X(t) + b_i(t))^2 dW_i(t), \\ dY(t) &= \left[2A(t)X^2(t) + 2a(t)X(t) + \sum_{i=1}^N B_i^2(t)X^2(t) + 2B_i(t)b_i(t)X(t) + b_i^2(t) \right] dt \\ &\quad + 2X(t) \sum_{i=1}^N (B_i(t)X(t) + b_i(t))^2 dW_i(t).\end{aligned}$$

Taking the expectation on both sides, we obtain:

$$\begin{aligned}\mathbb{E}[dY(t)] &= dP(t) = \left[2A(t)\mathbb{E}[X^2(t)] + 2a(t)\mathbb{E}[X(t)] + \sum_{i=1}^N B_i^2(t)\mathbb{E}[X^2(t)] \right. \\ &\quad \left. + 2B_i(t)b_i(t)\mathbb{E}[X(t)] + b_i^2(t) \right] dt \\ &\quad + \mathbb{E}[2X(t) \sum_{i=1}^N (B_i(t)X(t) + b_i(t))^2 \mathbb{E}[dW_i(t)]] \overset{0}{},\end{aligned}$$

which results in the following ODE to describe the second moment:

$$dP(t) = \left[2A(t)P(t) + 2a(t)m(t) + \sum_{i=1}^N B_i^2(t)P(t) + 2B_i(t)b_i(t)m(t) + b_i^2(t) \right] dt .$$

(C.5)

Appendix D

Numerical integration method

The numerical integration method used to solve the stochastic system of differential equations is based on a generalization of the Heun method, or the modified Euler method. Consider a stochastic differential equation of the form

$$dX = f(X, t)dt + g(X, t)dW , \quad (\text{D.1})$$

where $f(X, t)$ and $g(X, t)$ are the drift and diffusion coefficients, respectively; and W is a Brownian motion. A formal generalization of the Heun scheme for ordinary differential equations to the stochastic differential equations is

$$\begin{aligned} X_{i+1} = X_i + \frac{1}{2} [f(X_i, t_i) + f(X_i + f(X_i, t_i)\Delta_i + g(X_i, t_i)\Delta W_i, t_i)] \Delta_i \\ + \frac{1}{2} [g(X_i, t_i) + g(X_i + f(X_i, t_i)\Delta_i + g(X_i, t_i)\Delta W_i, t_i)] \Delta W_i , \end{aligned} \quad (\text{D.2})$$

where $X_i = X(t_i)$ with $t_{i+1} = t_i + \Delta_i$; $X_0 = X(0)$ is the initial condition, and; ΔW_i is the increment on Brownian motion. Although the formally generalized Heun method presented in Eq. D.2 seems acceptable, it is only strongly consistent if $g(X, t) = \text{constant}$ [85], i.e. otherwise, the solution does not converge. Thus, a modification of this method is applied:

$$X_{i+1} = X_i + \frac{1}{2} [f(X_i, t_i) + f(X_i + f(X_i, t_i)\Delta_i + g(X_i, t_i)\Delta W_i, t_i)] \Delta_i + g(X_i, t_i)\Delta W_i , \quad (\text{D.3})$$

which is strongly consistent [85].

Appendix E

Program structure

The program developed in this work is coded in MATLAB and it consists of more than 20 files and several thousand lines. In order to present the structure of the program in a simplified way, the flowcharts in Figs. E.1, E.2, E.3 and E.4 are presented. The main program, which calls all the others, is called PRINCIPAL.m (Fig. E.1). Here, the user specifies the rotational speed at the top (Ω), the WOB (\bar{W}_{ob}), the simulation time and the number of stochastic simulations (N_s). Then, it calls the DRILLDYN.m (Fig. E.2) to solve deterministic model (stoch = 0). After this, the stochastic model is solved (stoch = 1) inside a loop to generate N_s stochastic simulations. Finally, the statistics are calculated and plotted.

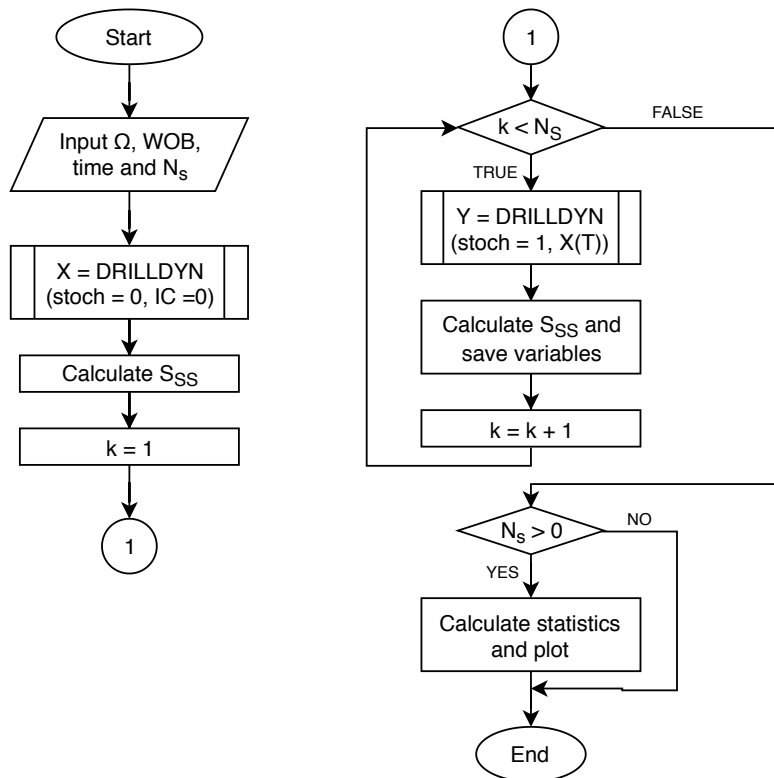


Figure E.1: Simplified structure of program PRINCIPAL.m.

In DRILLDYN.m, all the other parameters are inputted, the matrices are calculated with sub_normalmodes.m (Fig E.3) and the equations are solved in sub_dyn.m (Fig E.4). The boundary condition BC 1 fixes the rotation at the top and the axial movement at the bottom, while BC 2 only imposes a rotational speed at the top. In stochastic case, the initial condition is set as the deterministic solution at time $t = T$ ($X(T)$) for drill-string dynamics and as the end point of the pre-simulation for the stochastic process generation.

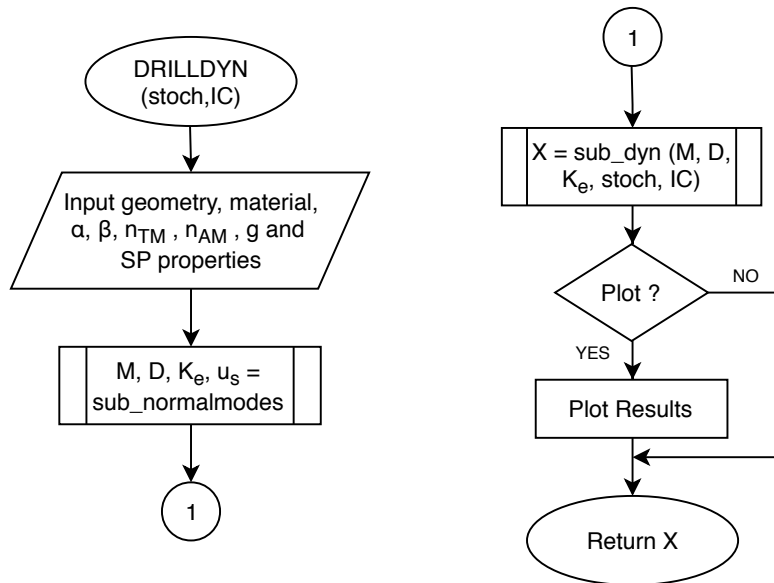


Figure E.2: Simplified structure of program DRILLDYN.m.

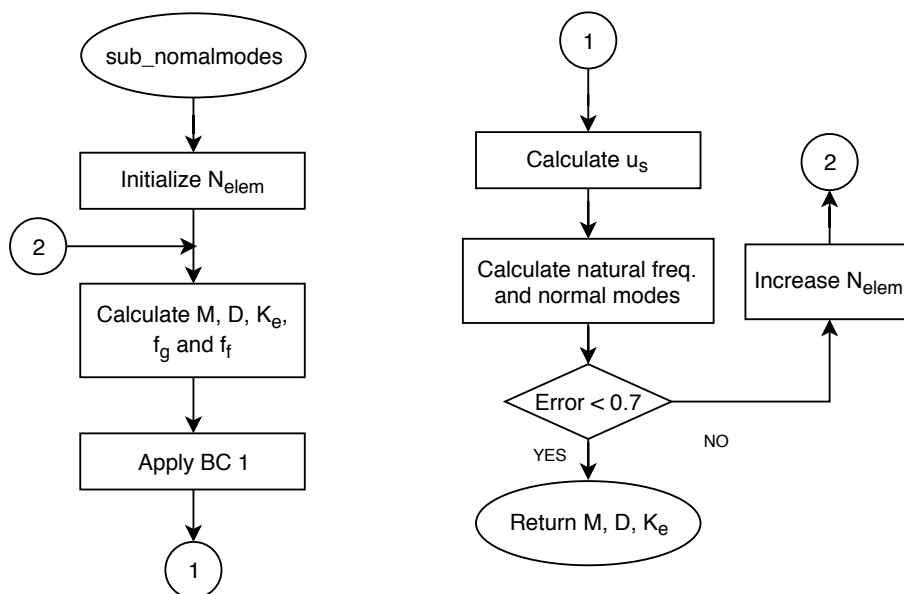


Figure E.3: Simplified structure of program sub_normalmodes.m.

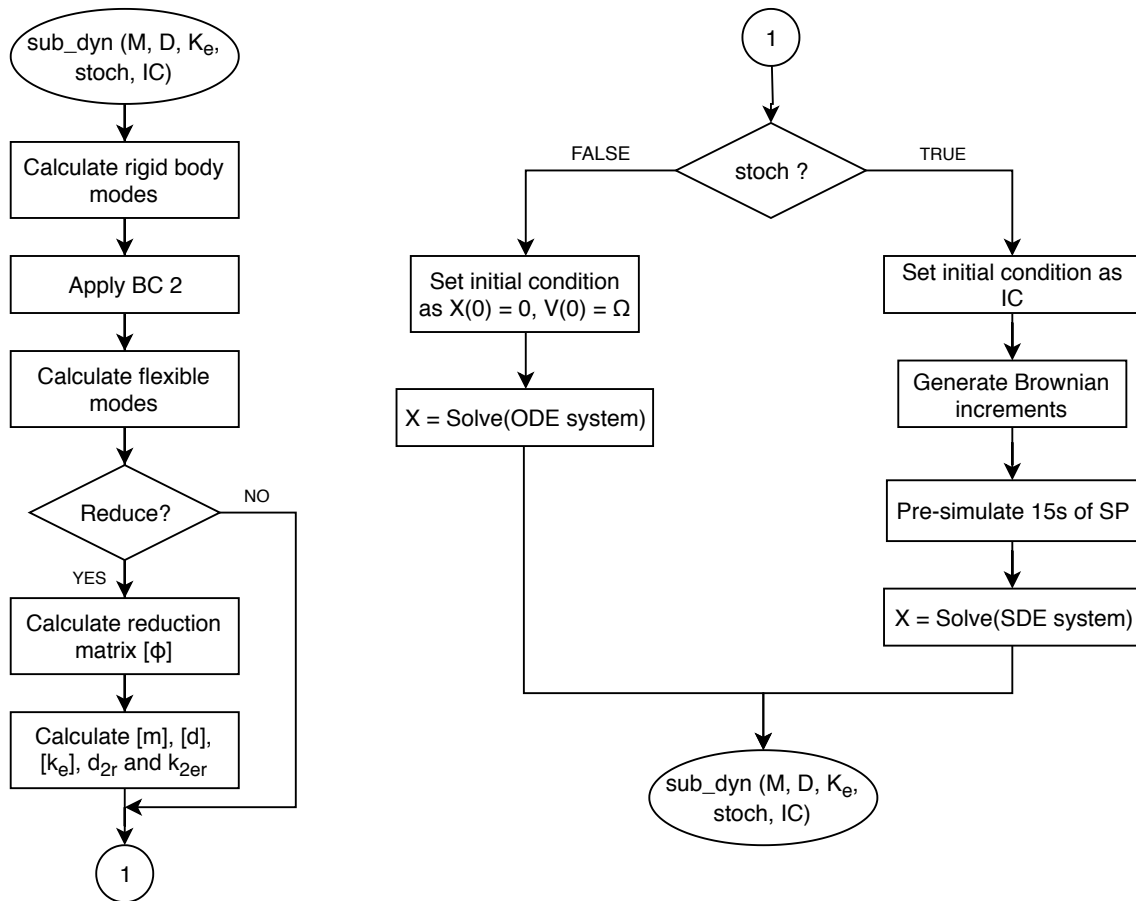


Figure E.4: Simplified structure of program sub_dyn.m.